

Final Report  
for the period  
October 1, 1988  
through March 31, 1990

Approved for public release;  
distribution unlimited.

OFFICE OF SCIENTIFIC RESEARCH (AFSC)

Department of Aerospace Engineering  
College Station, Texas 77843-3141

Research Division

# Analytical and Experimental Research on Large Angle Maneuvers of Flexible Structures

AD-A226 679

Prepared by:  
J. L. Junkins  
T. C. Pollock  
Z. H. Rahman

Texas A&M Research Foundation  
Texas A&M University System  
Department of Aerospace Engineering  
College Station, Texas 77843-3141

Contract Number  
F49620-87-C-0078

May 1990

DTIC  
SELECTED  
SEP 25 1990  
S D CS D

Prepared for: U. S. Air Force, AFSC Code FQ8671

Air Force Office of Scientific Research  
Bolling Air Force Base, DC 20332-6448

**DISTRIBUTION STATEMENT A**  
Approved for public release  
Distribution Unlimited

Unclassified

SECURITY CLASSIFICATION OF THIS PAGE

### REPORT DOCUMENTATION PAGE

Form Approved  
OMB No. 0704-0188

1a. REPORT SECURITY CLASSIFICATION <b>UNCLASSIFIED</b>		1b. RESTRICTIVE MARKINGS	
2a. SECURITY CLASSIFICATION AUTHORITY		3. DISTRIBUTION / AVAILABILITY OF REPORT Approved for Public Release; Distribution Unlimited	
2b. DECLASSIFICATION / DOWNGRADING SCHEDULE			
4. PERFORMING ORGANIZATION REPORT NUMBER(S) TAMURF - AERO- 90-5-1		5. MONITORING ORGANIZATION REPORT NUMBER(S) <b>AFOSR-TR- 90 0919</b>	
6a. NAME OF PERFORMING ORGANIZATION Texas A&M Research Foundation	6b. OFFICE SYMBOL (if applicable)	7a. NAME OF MONITORING ORGANIZATION <b>AFOSR/NA</b>	
6c. ADDRESS (City, State, and ZIP Code) Texas A&M University College Station, Texas 77843		7b. ADDRESS (City, State, and ZIP Code) <b>Bolling AFB</b> <b>DC 20332-6448</b>	
8a. NAME OF FUNDING / SPONSORING ORGANIZATION Air Force Office of Scientific Research	8b. OFFICE SYMBOL (if applicable) <b>NA</b>	9. PROCUREMENT INSTRUMENT IDENTIFICATION NUMBER F 49620-87-C-0078	
8c. ADDRESS (City, State, and ZIP Code) Bolling AFB, D. C. 20322-6448		10. SOURCE OF FUNDING NUMBERS	
		PROGRAM ELEMENT NO. <b>63 221C</b>	PROJECT NO. <b>0812</b>
		TASK NO. <b>K1</b>	WORK UNIT ACCESSION NO.
11. TITLE (Include Security Classification) Analytical and Experimental Research on Large Angle Maneuvers of Flexible Structures <b>(U)</b>			
12. PERSONAL AUTHOR(S) John L. Junkins, Thomas C. Pollock, Zahidul H. Rahman			
13a. TYPE OF REPORT Final	13b. TIME COVERED FROM <u>8810</u> TO <u>9003</u>	14. DATE OF REPORT (Year, Month, Day) 900504	15. PAGE COUNT 308
16. SUPPLEMENTARY NOTATION			
17. COSATI CODES		18. SUBJECT TERMS (Continue on reverse if necessary and identify by block number)	
FIELD	GROUP	SUB-GROUP	
		Flexible space Structures, on-orbit identification, control design, large angle maneuvers <b>(U)</b>	
19. ABSTRACT (Continue on reverse if necessary and identify by block number) <i>are presented</i> We present new methods for structural system identification and control of large angle maneuvers. Both analytical and experimental results are presented. Globally stable control laws for flexible body maneuvers are derived and validated experimentally. Stereo triangulation methods are proposed and tested experimentally for structural identification. <i>Keywords:</i>			
20. DISTRIBUTION / AVAILABILITY OF ABSTRACT <input checked="" type="checkbox"/> UNCLASSIFIED/UNLIMITED <input checked="" type="checkbox"/> SAME AS RPT. <input checked="" type="checkbox"/> DTIC USERS		21. ABSTRACT SECURITY CLASSIFICATION UNCLASSIFIED	
22a. NAME OF RESPONSIBLE INDIVIDUAL G. K. Haritos, S. Wu, <i>A. Das</i>		22b. TELEPHONE (Include Area Code) (202) 767-4987	22c. OFFICE SYMBOL AFOSR/NA

000

(U)

---

Final Report  
for the period  
October 1, 1988  
through March 31, 1990

## **Analytical and Experimental Research on Large Angle Maneuvers of Flexible Structures**

Prepared by:

J. L. Junkins  
T. C. Pollock  
Z. H. Rahman

Texas A&M Research Foundation  
Texas A&M University System  
Department of Aerospace Engineering  
College Station, Texas 77843-3141

Contract Number  
F49620-87-C-0078

May 1990

---

Prepared for: U. S. Air Force, AFSC Code FQ8671

Air Force Office of Scientific Research  
Bolling Air Force Base, DC 20332-6448

# Contents

	Summary .....	2
1	Introduction .....	3
2	Technical Accomplishments: .....	5
2.1	A Novel Approach for Designing Globally Stable Control Laws for Distributed Parameter Systems .....	6
2.1.1	Analytical Results for Flexible Structure Maneuvers .....	6
2.1.2	Experimental Results .....	11
2.2	A Stereo Triangulation Approach to Structural Identification .....	11
2.2.1	Stereo Triangulation Approach to Deformation Measurements .....	11
2.2.2	System Identification Approach .....	12
2.2.3	Description of Experimental Results .....	13
2.3	Other Research Results .....	13
2.3.1	Sensitivity of the Singular Value Decomposition .....	13
2.3.2	A Star Pattern Recognition Approach for Autonomous Spacecraft Attitude Determination .....	14
2.3.3	Analytical/Computational Results for Tethered Satellite Retrieval .....	14
2.3.4	Singularity Avoidance in Control Moment Gyros (CMGs) ..	14
3	Concluding Remarks: .....	16
4	References .....	17
5	Attachment Index .....	18
6	Attachments .....	19

## SUMMARY

This document represents the final report on research performed under Contract No. F49620-87-C-0078 from the Air Force Office of Scientific Research to Texas A&M University. The period covered by this report is from October 1, 1988 through March 31, 1990.

Significant progress is reported on analytical, computational, and experimental methodology applicable to sensing, actuation, identification, and control of flexible structures. Especially significant are the following: (i) We have developed new analytical, numerical, and experimental results pertaining to optimal large angle maneuvers of flexible structures. (ii) We have successfully demonstrated a stereo optical sensing method for measuring structural response, and developed an associated new method for updating an a priori model to be consistent with experimental measurements of the free and forced vibratory behavior of the actual structure. (iii) We have developed several test articles, implemented appropriate sensors, actuators, data acquisition and computer systems, and have implemented a first version of the overall system identification method, as well as a most significant near-minimum-time large angle maneuver experiment. (iv) We have developed some important analytical and numerical results which give new insight into avoidance of well-known singularities encountered when using single-gimbal Control Moment Gyros to impart attitude maneuver control torques. The maneuver results are especially significant because we have formulated and implemented successfully the most complete flexible body maneuver theory available for robust near-minimum-time maneuvers

The Investigators for this effort were as follows: J. L. Junkins served as Project Director and Principal Investigator; he played the leading role in the analytical and computational aspects of this research. T.C. Pollock served as Co-Principal Investigator; he played the leading role in design of experiments, actuator and sensor systems. The project benefited significantly from the excellent analytical contributions of S.R. Vadali. Research Engineer Z.H. Rahman contributed many important ideas and played the central role in carrying out the experimental research on large angle maneuvers. Six Graduate Research Assistants participated in this project: David Anderson, Robert Byers, Johnny Hurtado, Steven Morgan, Matilda McVay, and George James. Byers and Morgan completed Masters theses, while James finished a Ph.D. dissertation; Byers and the remaining three students will complete their Ph. D. programs in the near future. The technical monitors for the Air Force Office of Scientific Research were Drs. G.K. Haritos S. Wu, and A.K. Amos of the Directorate of Aerospace Sciences; their support and constructive interactions are most appreciated.

Organization of this report is as follows. We have elected to present most of the detailed technical results as attachments to this report. We have written the body of this report as a guided tour; following a brief introduction in Section 1, the sub-sections of Section 2 overview the essence of the several contributions with reference to the attachments. Section 2 provides only a macroscopic summary of the research results discussed in detail in the attachments. Section 3 provides concluding remarks and discusses some promising avenues for extending the research discussed in this report.



Also discussed in this report are several sets of research results which have not been complemented by experimental studies. Attachments 4-5 discuss analytical and numerical results we have developed for improved optimization and sensitivity analysis of linear feedback structural control laws. Attachment 13 present new results on Control Moment Gyro steering laws which gives insight into avoidance of singularities. Attachment 12 discusses nonlinear feedback control for stable deployment and retrieval of tether-connected structures. Attachment 12 may at first glance seem loosely related with the results in Attachments 1-3. However, a close examination reveals that Liapunov stability theory underlies all of the results in Attachments 1-3, 4, 12, and together with the background problem area of space structure dynamics and control, we see that a strong unifying thread runs through all of the research contained herein.

We discuss an on-going research analytical/experimental effort which makes use of star sensing and pattern recognition to determine spacecraft pointing. This work is on-going, but we have demonstrated that sub five arc-second attitude can be determined, on-board, in real time, with an all solid state system. Attachment 14 describes our experimental laboratories; this is a unique facility developed for control/structure interaction research. The results reported span a wider scope and achieved a much higher level of technical maturity than could be expected based upon the the proposal and contractual requirements. This fortuitous circumstance is the result of the truly extraordinary productivity of the excellent corps of graduate students who worked on this project.

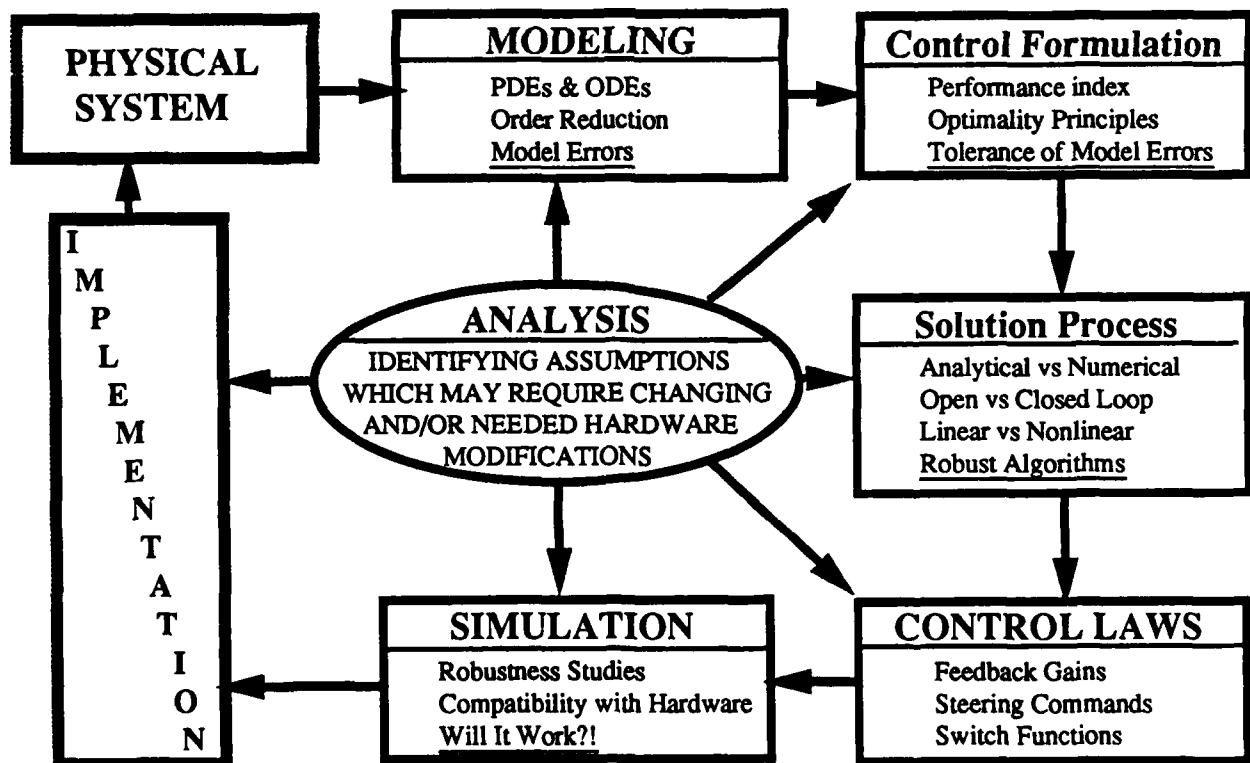


Figure 1 A Roadmap for Dynamical Modeling, Control Analysis/Design and Implementation of Closed Loop Control on Large Flexible Structures

## 2 Technical Accomplishments

With reference to Figure 1, we overview the research contributions in the context of this roadmap of activities for dynamics and control of space structures. In this project we have contributed new control law design and system identification methodology, and we have implemented several of the new concepts in successful laboratory experiments. In Sub-sections 2.1-2.3, we overview these contributions with reference to the Attachments which discuss the contributions in detail.

The most significant accomplishments of this research project are discussed in Section 2.1. We have developed an important method for designing globally stable control laws for near-minimum-time maneuvers of flexible spacecraft. The control law includes a provision for a user-optimized feed-forward reference maneuver and the large motion control law blends smoothly into a constant gain terminal controller for fine pointing and vibration suppression. Both analytical and experimental results are summarized which conclusively demonstrate the validity and some of the salient features of this approach. Since the results of Section 2.1 are judged to be of exceptional significance, we summarize the main features of these contributions in the body of this report. The remaining contributions are discussed in a briefer overview fashion, with all details relegated to the attachments.

In Section 2.2, we present the results of our research into structural system identification. We develop an improved approach for updating our available a priori structural model so that it is in best agreement with free and forced response measurements. We develop a new approach to structural sensing using stereo triangulation. We present both analytical and experimental results. The stereo triangulation system makes stereo images of >20 light emitting (or reflecting) targets on the vibrating structure @ 200 frames/sec; the three dimensional deflections of these points are determined by ray intersection. This stereo measurement approach represents an advance over the ideas successfully demonstrated in the 1984 Shuttle/SAFE experiment. Whereas several man-weeks of post processing were required to extract useful information from the SAFE video data, our image processing and triangulation software reduces this task to a fraction of an hour of interactive processing (in a laboratory computer interfaced directly to an analog video processor).

In Section 2.3, we overview four other sets of contributions made during this project. The first of these is purely analytical. We developed the first and second order sensitivity of the singular value decomposition. This will find widespread applications in control design studies. The second area of research contributions is in the area of control law design for tethered satellite deployment and retrieval; these are overviewed in Section 2.3.2. The design methodology is similar to the Liapunov methods used in the control laws discussed in Section 2.1 and Attachments 1-3; we show that small thrusting on the sub-satellite can greatly reduce oscillations and lead to significant reduction in retrieval times. The third set of results is discussed in Section

2.3.3; we have developed an improved method for avoiding singularities when using Control Moment Gyroscopes (CMGs) to generate attitude control torques.

The final topic (Section 2.3.4) is analytical and experimental research on spacecraft pointing determination using star pattern identification. This work was partially supported by a research grant from the Texas Advanced Technology Program (ATP); it includes both analytical and experimental aspects. The experimental work is still in progress and will be brought to maturity during this calendar year under ATP support.

## 2.1 A Novel Approach for Designing Globally Stable Control Laws for Distributed Parameter Systems

With reference to Figure 2 and Attachments 1-3, we discuss the research contributions we have made for designing globally stable control laws. The results involve both new analytical/theoretical developments and also several successful laboratory experiments. We have established that this approach applies to a wide class of dynamical systems described by coupled ordinary, partial, and integro-differential equations. We first discuss the analytical results in an overview fashion.

### 2.1.1 Analytical Results for Flexible Structure Maneuvers

The equations of motion for the structure in Figure 2 are discussed in Attachment 1; under usual approximations discussed in the attachments, the dynamics of this structure are described by the following system of coupled ordinary and partial integro-differential equations:

$$\begin{aligned}
 I_{hub} \frac{d^2 \theta}{dt^2} &= u + 4(M_o - S_o l_o) \\
 -(M_o - S_o l_o) &= \int_{l_o}^l \rho x \left( \frac{\partial^2 y}{\partial t^2} + x \frac{d^2 \theta}{dt^2} \right) dx + ml \left( l \frac{d^2 \theta}{dt^2} + \frac{\partial^2 y}{\partial t^2} \Big|_l \right) + HOT \\
 \rho \left( \frac{\partial^2 y}{\partial t^2} + x \frac{d^2 \theta}{dt^2} \right) + EI \frac{\partial^4 y}{\partial x^4} &= 0 + HOT
 \end{aligned} \tag{1}$$

We will overview a method we have developed for designing globally stable control laws for distributed parameter systems such as Eq. (1). The method does not rely upon the use of spatial (or temporal) discretization/approximations, and known nonlinearities can be accommodated readily. It can be verified that for zero control torque ( $u = 0$ ) the total energy of the system is rigorously conserved:

$$2E = I_{\omega} \left( \frac{d\theta}{dt} \right)^2 + 4 \left[ \int_{l_0}^l \rho \left( \frac{\partial y}{\partial t} + x \frac{d\theta}{dt} \right)^2 dx + \int_{l_0}^l EI \left( \frac{\partial^2 y}{\partial x^2} \right)^2 dx + m \left( l \frac{d\theta}{dt} + \frac{\partial y}{\partial t} \Big|_l \right)^2 \right] = \text{constant} \quad (2)$$

This motivates introducing the following error energy (Liapunov) function to measure the departure of the actual, generally disturbed motion (using an arbitrary control  $u(t)$ ) from the open-loop trajectory  $( )_r$ , which is the rigorous solution of the equations of motion, Eq. (1), corresponding to using a pre-optimized shaped control torque history  $u_{ref}(t)$ :

$$2U = a_1 I_{\omega} \delta\dot{\theta}^2 + a_2 \delta\theta^2 + 4a_3 \left\{ \int_{l_0}^l \rho \left[ \delta \frac{\partial y}{\partial t} + x \delta\dot{\theta} \right]^2 dx + \int_{l_0}^l EI \left( \delta \frac{\partial^2 y}{\partial x^2} \right)^2 dx + m \left[ l \delta\dot{\theta} + \delta \frac{\partial y}{\partial t} \Big|_l \right]^2 \right\} \quad (3)$$

where we use the departure motion notation  $\delta( ) \equiv ( ) - ( )_r$ . The second term is introduced because the energy integral is indefinite in the cyclic coordinate  $\theta$ ; note that  $U$  assumes its global minimum value of zero everywhere along the  $( )_r$  trajectory. Also note that choosing values for the positive weights  $a_i$  allow us to place relative emphasis upon three subsets of the error energy. In Attachment 1, we show that using the following feedback control law

$$u = u_{ref}(t) - \left\{ g_1 (\theta - \theta_r) + g_2 (\dot{\theta} - \dot{\theta}_r) + g_3 [(l_0 S_0 - M_0) - (l_0 S_0 - M_0)_r] \right\} \quad (4)$$

with any values of the gains which satisfy  $g_1 \equiv a_2/a_1 > 0$ ,  $g_2 > 0$ ,  $g_3 \equiv 4(a_3 - a_1)/a_1 > -4$ , makes the Liapunov error function of Eq. (3) become everywhere non-increasing, and in fact, results in all motions being globally attracted to the  $( )_r$  trajectory. Therefore the control law of Eq. (4) guarantees global Liapunov stability with respect to the  $( )_r$  path. Note that this is a rigorous result in the sense that we have proven it using the original system of ordinary and partial differential equations. *We have furthermore showed that the same control law of Eq. (4) stabilizes the obvious generalizations of the model (including rotational stiffening geometric nonlinearities, rotary inertia, shear deformation, and aerodynamic drag). In short the stability of the system using the control law of Eq. (4) has been found very forgiving of modeling assumptions.* A significant practical problem arises because this control law requires pre-computation of the open-loop solution of the full partial differential equations of motion to obtain the  $( )_r$  quantities. This difficulty can be avoided by introducing approximations which yield a simpler system of reduced order equations whose solution  $( )_{ref}$  is both sufficiently accurate and computable in near real time. In Attachment 1, we show that these ideas lead to the feedback law

$$u = u_{ref}(t) - \left\{ g_1 (\theta - \theta_{ref}) + g_2 (\dot{\theta} - \dot{\theta}_{ref}) + g_3 [(l_0 S_0 - M_0) - (l_0 S_0 - M_0)_{ref}] \right\} \quad (5)$$

which is globally stable in the sense that the motion is globally attracted to a small  $\Delta$  neighborhood near the  $( )_{ref}$  motion; this region is defined by a simple inequality. The control of Eq. (5) causes the error energy function of Eq. (3) to be strictly decreasing everywhere that the following

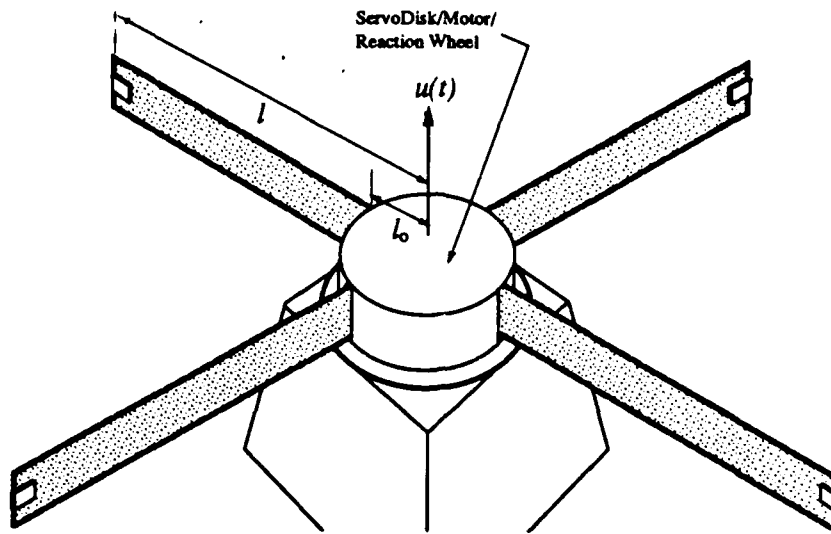


Figure 2 Texas A&M Maneuverable Flexible Structure Experiment

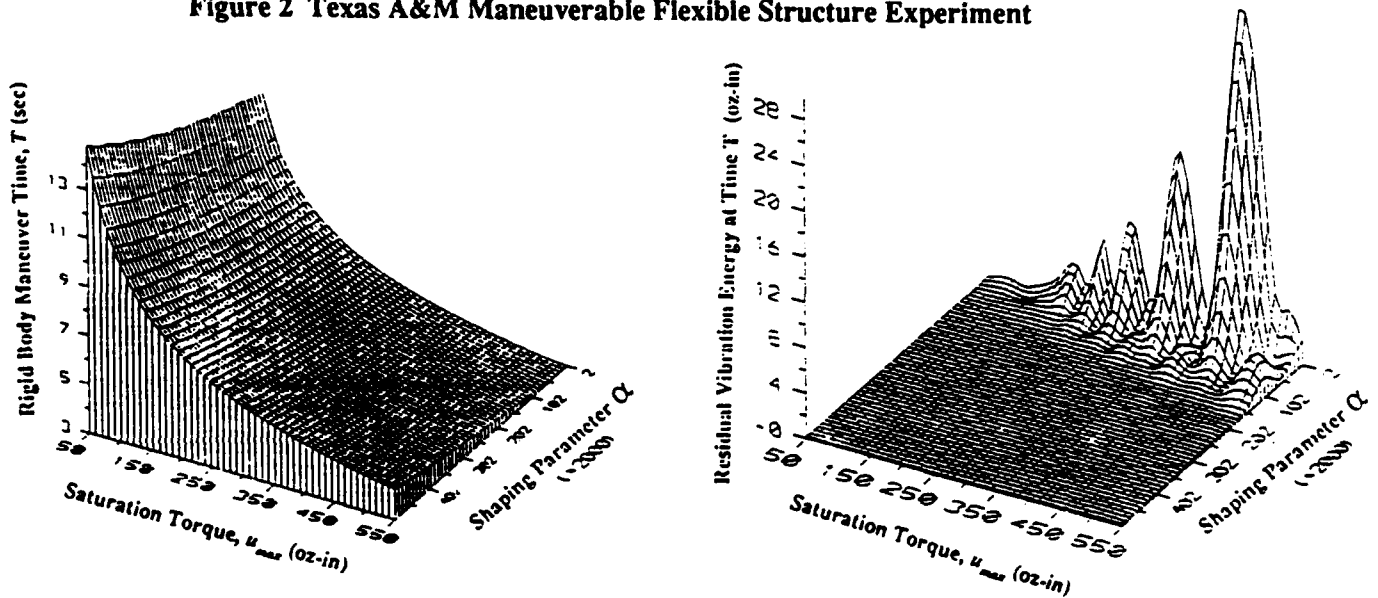


Figure 3 Residual Vibration Energy At Nominal Rigid Body Maneuver Completion Time (as a function of the torque shape parameters  $u_{max}$  and  $\alpha$ )

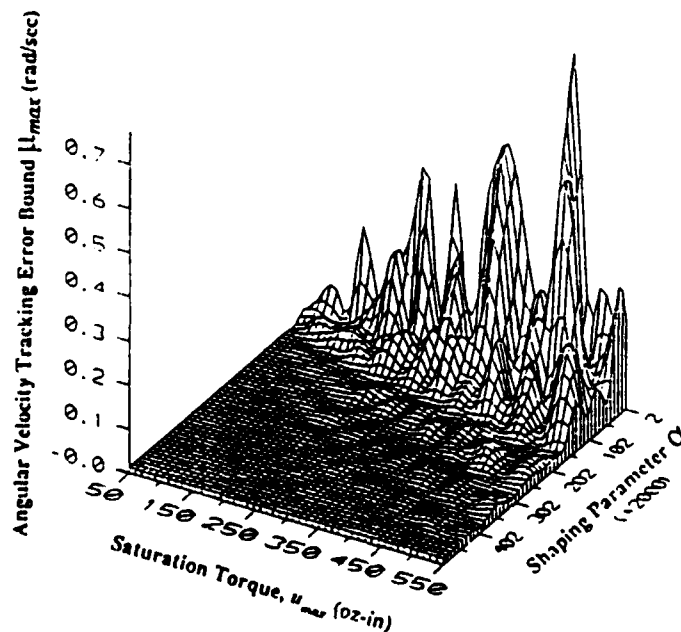
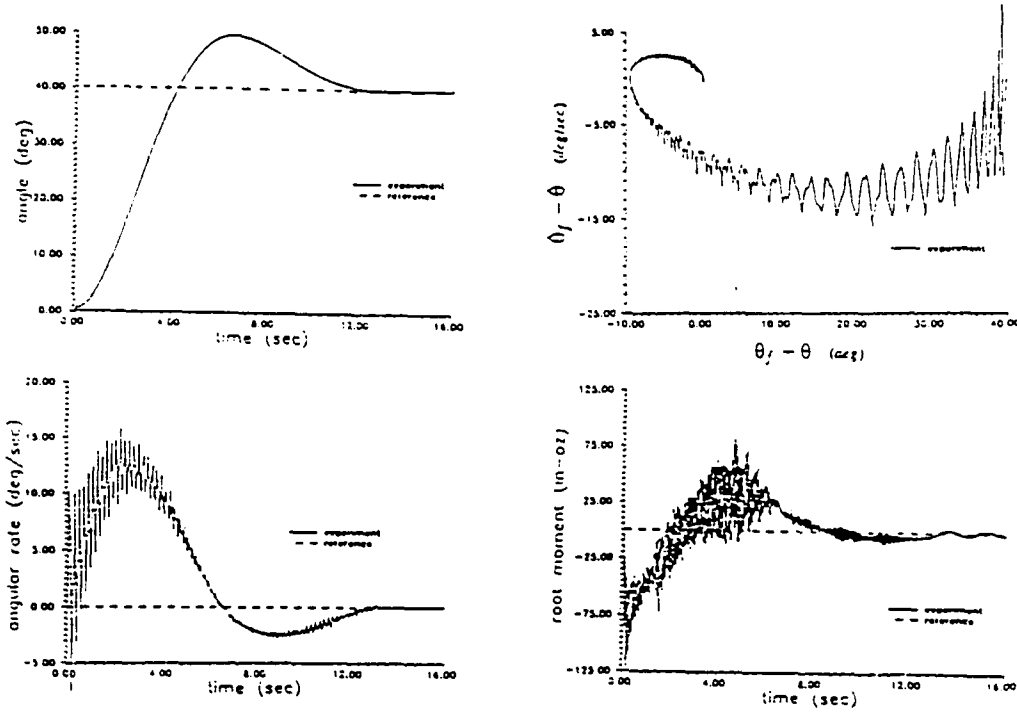


Figure 4 Bound on the  $\Delta$  Region Near the Rigid Body Motion (to which all motion is globally attracted, as a function of  $u_{max}$  and  $\alpha$ )

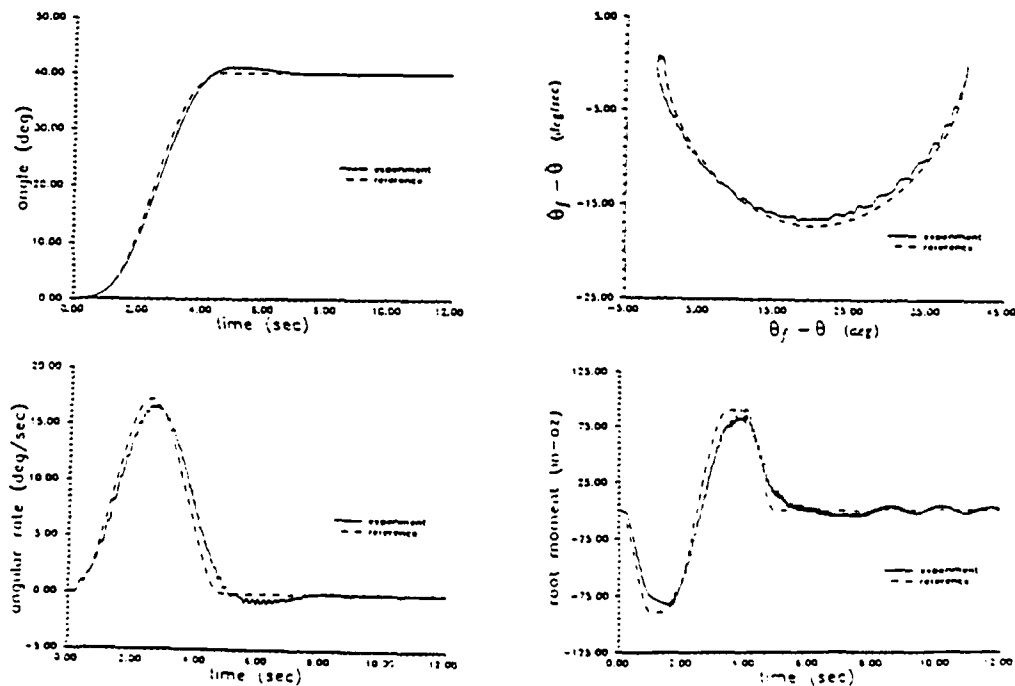
**Figure 5a Experimental Results Using Conventional Linear Output Feedback**

control gains:  $g_1 = 600$  oz-in/rad,  $g_2 = 800$  oz-in/rad/s,  $g_3 = 0$



**Figure 5b Experimental Results Using Globally Liapunov Stable Tracking Control with a Torque-Shaped Reference Trajectory**

torque shape parameter:  $\alpha = 0.2$ , control gains:  $g_1 = 600$  oz-in/rad,  $g_2 = 800$  oz-in/rad/s,  $g_3 = 0$



condition is satisfied:

$$|\hat{\theta} - \hat{\theta}_r| > \mu \equiv \frac{1}{g_2} |g_1 \Delta\theta + g_2 \Delta\dot{\theta} + g_3 \Delta(l.S. - M.)| \quad (6)$$

Since the  $\Delta(\ ) = (\ )_r - (\ )_{ref}$  quantities are differences between two open loop motions {which ensue from  $u_{ref}(t)$ }, it is easy to bound the  $\Delta(\ )$ 's by directly by a priori simulation study (Figures 3, 4) and therefore establish a measure of how near the closed loop motion stays to the  $(\ )_{ref}$  trajectory. We also prove that if the  $(\ )_{ref}$  trajectory is designed to spline smoothly into the fixed target state at time  $t_f$ , then after  $t_f$ , the control law of Eq. (5) provides unqualified global Liapunov (asymptotic) stability with respect to the fixed target state. Note that the  $\Delta(\ )$  quantities are simply interpreted as measures of how nearly the approximate  $(\ )_{ref}$  motion satisfies the system equations of motion, Eq. (1), and therefore if the region defined by Eq. (6) is not sufficiently small, then the reduced order model underlying the  $(\ )_{ref}$  trajectory can be revised appropriately or,  $u_{ref}(t)$  can be modified. Physically, it is obvious that a single actuator cannot make all infinity of degrees of freedom of a flexible structure behave exactly like, for example, a rigid body, and the tracking errors are functions of (i) how well the assumptions underlying the  $(\ )_{ref}$  motion models the actual system, and how aggressively one attempts to maneuver the structure (one would expect, for example, that a very smooth, small reference torque input should result in the flexible structure motion approaching the rigid body idealization, as is evident in Figures 3 and 4).

If the reference open-loop control  $u_{ref}(t)$  is parameterized simply, then an a priori global parameter study can provide complete visibility of these issues. For example, for the particular family of near-minimum-time control laws studied in Attachments 1-3,  $u_{ref}(t)$  depends upon a torque-shape parameter  $\alpha$   $\{0 \leq \alpha \leq 0.25, \alpha$  controls the sharpness of the control switches with  $\alpha=0$  corresponding to the zero-rise-time bang-bang case} and a parameter  $u_{max}$  which is the saturation torque. An a priori parameter study led to Figures 3 and 4; these provide visibility of the open-loop residual vibration energy (Figure 3) and the maximum value of the tracking bound  $\mu$  (Figure 4, Eq. (6)) which describes the size of the region near the  $(\ )_{ref}$  motion in which asymptotic stability cannot be guaranteed. Note that while Figure 4 bounds the closed loop stability, only open loop solutions of the differential equations are required to construct this surface; however selection of particular feedback gains is required. It is apparent that there is a triangular region in  $(\alpha, u_{max})$  space wherein both of these surfaces approach zero. The near-bang region, especially for large  $u_{max}$ , rings the structure badly. In the detailed examples studied in Attachments 1-3, it is shown that a maneuver in the attractive (sufficiently small  $\mu$ ) region can be selected with only a modest penalty on overall maneuver time (including time for vibration settling), as compared to the minimum maneuver time for an equivalent rigid body.

## 2.1.2 Experimental Results

In Attachments 1-3, we report several successful experiments; these results provide convincing evidence that the above-discussed concepts are both valid and can be readily implemented. As noted in Attachment 1, we achieved approximately a 100% reduction in overall maneuver and vibration settling time as compared to a conventional constant gain feedback law to perform a  $40^\circ$  maneuver of the structure in Figure 2. The analytical and experimental results were in excellent agreement. The experimental hardware is described in Reference 1 and Attachments 1-3, and 14. One of the experimental maneuvers led to the results displayed in Figure 5. Note that the dashed line is a rigid body  $(\cdot)_{ref}$  predicted solution using the reference torque  $u_{ref}(t)$  {with the parameter choices taken as  $(\alpha, u_{max}) = (0.2, 400 \text{ oz-in})$ }, whereas the solid line is the experimental results. The shaped torque rigid body maneuver was used as the target (reference) motion, even though it was obvious that finite tracking errors would (and did) occur during the mid-course phase of this maneuver. In Attachments 1-3, numerous other experimental results are documented, including a comparison to a constant gain output feedback controller which incurred much larger vibrations and required over 12 seconds to do the same maneuver shown in Figure 5. As described in Attachment 1, the presence of bearing nonlinearities, sensor noise and other non ideal effects provided significant unintended robustness tests for the method; the highly successful experiments confirmed that this approach to near-minimum-time control of distributed parameter systems is valid, highly attractive, and physically realizable.

## 2.2 A Stereo Triangulation Approach to Structural Identification

### 2.2.1 Stereo Triangulation Measurement of Structural Deformation

In Attachments 6, 8-11 we present concepts and results of a non-contacting structural sensing approach which involves intersecting rays from two or more synchronized high speed, high resolution video cameras to targets on the vibrating structure. We have successfully demonstrated that this approach can be used to measure the inertial motion of more than twenty targets 200 times per second with an application-dependent spatial resolution (typically a few mm). The primary advantage of this approach is that non-intrusive, non-contacting inertial measurements of the global vibration of the structure can be made, and the approach works best precisely in the low frequency bandwidth (0 to 20 Hz) where conventional sensors such as accelerometers are least accurate. The primary disadvantage is that the limited spatial resolution usually means that only the participation lowest frequency modes can be observed in the measurements. The dissertation by George James, Ref. [2] details several advances of this approach to optical sensing, including the use of analog video processing to detect edges and extract image centroids, calibration of camera geometry and sensor model parameters from static measurements. The results in James' dissertation are representative of the state of the art in the use of video camera data to make structural vibration measurements.

## 2.2.2 System Identification Approach

Based upon the ideas we published in Ref. [3], a new approach has been established to update the a priori finite element model using measurements of structural response. The key ingredients in the approach are the enforcement of two fundamental constraints when updating a structural model, for the purpose of control design, based upon dynamical response measurements:

- (1) To the extent possible, the parameterization implicit in the a priori model should be preserved, unless there is evidence of a serious modeling error, as a minimal requirement the symmetry, sparsity, and coupling patterns of the a priori model's mass and stiffness characterization should be preserved to the extent possible in the updated model.
- (2) The updated model should be brought into "best agreement" with both (i) free vibration measurements, as well as (ii) forced response measurements.

To the extent that the first constraint must be abandoned (to obtain a good fit of the structure's behavior), we obtain insight to the validity of the modeling process, on the other hand, not attempting to enforce this constraint precludes learning very much about the shortcomings of the original model. Furthermore the particular measurement process is often found to embody some poorly understood issues, therefore one should be equally skeptical of both the model and the measurements. The second constraint reflects the truth that the two basic approaches to structural vibration measurements (free vs forced vibrations) are complimentary and we believe both data types should be used simultaneously to obtain updated models of highest fidelity. The fact that an infinity of updated models can yield exactly the same measured free vibration results (i. e., an infinity of mass and stiffness matrices lead to identical natural frequencies and mode shapes) has not deterred the development of a large number of ad hoc ("nearest neighbor") approaches which compute non-unique model updates using only free vibration measurements. We believe that these methods are hazardous to the health of closed loop controllers and do not provide a reliable basis for feedback control design purposes. Since feedback control involves, by definition, forced response, the model update should ideally be based upon measurements of forced response; it is also evident that the model uniqueness criticism is alleviated on sound physical grounds by using the forced response data (e. g., the frequency response function) to impose the proper scaling on the system mass and stiffness characteristics.

In Attachments 6-10, we present some preliminary details of our formulations based upon this approach, but the most complete and definitive results are contained in references [2,3]. In these references, we establish a linear parameterization of the mass and stiffness matrices upon linear scaling of the contributions of  $n$  substructures to the global mass and stiffness matrices. The best linear scaling is determined to fit available free and forced response measurements; the

definition/selection of substructures remains subjective, but we show that the spatial distribution of energy (in the modes which lie in the frequency range where the poorest match between model and measurements) provides some insight in this process.

### **2.2.3 Description of Experimental Results**

In Attachments 8-11, and references [2,3], we apply the above methodology to both simulated and actual measurements. In reference [2], we detail the analytical and experimental results for an end-to-end application of the stereo-triangulation measurement system, and the free/forced measurement model update system which we first proposed in Reference [3]. The experimental test article is a 5' x 5' aluminum grid; we used 20 light emitting targets (fibre optic light guides) for stereo triangulation. We imaged these targets 200 times per second and also utilized six strain gauges and three accelerometers. We used several forms of actuation, including on-board reaction wheels (driven by Clifton Precision motors with  $\pm 20$  Oz-in torque), impulse hammers, and a conventional harmonic shaker). We were able to establish a fairly complete demonstration of the analytical and experimental methodology, albeit using a small laboratory structure (modeled by a 60 degree of freedom finite element model).

## **2.3 Other Research Results**

In this section, we briefly describe four other subsets of research results. Except for the final item (Section 2.3.4), these represent analytical/computational research results related to spacecraft dynamics and control analysis. The final topic is addressed to experimental research on spacecraft navigation by star sensing/star pattern recognition. Each of these research contributions are subsets of recent or on-going Ph. D. dissertations.

### **2.3.1 Sensitivity of the Singular Value Decomposition**

The singular value decomposition (SVD) represents the singular most important advance in computational linear algebra of the past two decades. Its applications in dynamics and control of aerospace structures are rapidly growing. In Attachment 5, we make a fundamental contribution of analytical partial derivatives for the singular values and singular vectors; these promise to be of widespread utility. Both first and second order sensitivities are presented; the analytical results have been verified by finite differences to nine digits. In Attachment 12, we use these sensitivities to design a robust linear feedback law for a simple structure. Y. Kim is currently nearing completion of his Ph. D. dissertation which extends these results, develops new controller/structure formulations, and applies these ideas to optimization of actuator locations for large flexible structures (Attachment 4).

### **2.3.2 Analytical/Computational Results for Tethered Satellite Retrieval**

In Attachment 12, we present new research results on control of three dimensional tethered satellite deployment and retrieval. Feedback control laws with guaranteed closed loop stabilizability are obtained using the second method of Liapunov. First a coordinate transformation is presented that partially uncouples the in-plane and out-of-plane dynamics. A combination of tension control as well as out-of-plane thrusting is shown to be adequate for a speedy retrieval. Next, a unified control design method based on an integral of the nonlinear motion (related to the Hamiltonion of the coupled system) is presented. It is shown that the controller designed by the latter method is superior to that of the former primarily from the out-of-plane thrust usage point of view. A detailed analysis of stability of the closed loop system is presented and the existence of limit cycles is ruled out if out-of-plane thrusting is used in conjunction with tension control. Finally, a tether rate control law is also developed using the integral of motion mentioned above. These control laws can also be used for station-keeping. Current studies are focused upon evaluating the modification of these results to accommodate tether flexibility and extension effects as well account for aerodynamics and other external disturbances.

### **2.3.3 Singularity Avoidance Steering for Control Moment Gyros (CMGs)**

In Attachment 13, we present a novel approach to singularity avoidance steering for single gimbal CMGs. These actuators are attractive for maneuvering large spacecraft as they provide torque amplification and are mechanically simpler than double gimbal CMGs. A method based on back integration of the CMG torque equation from the desired final state is utilized to determine a family of initial gimbal angles that avoid internal singularities. Each member of this family is defined as a preferred initial gimbal angle set. The pseudo-inverse steering law is used during the numerical integrations. A feedback control scheme based on "null motion" is also developed to position the gimbals at preferred locations. These results are a significant contribution to the CMG singularity avoidance literature, because this is the first time the existence of these preferred angles has been noted and their implications studied.

### **2.3.4 A Star Pattern Recognition Approach for Autonomous Spacecraft Attitude Determination**

In Reference [5], we describe an analytical study and our experimental evaluation of a novel method for spacecraft attitude determination from star pattern recognition. The idea is very simple, two or more star cameras are fixed to the main body of a spacecraft, as stars pass through the field of view their patterns are matched by reference to an on-board catalog and logic is employed to answer the question "how must the spacecraft be pointing so that the cameras see

the stars they are actually imaging?" We seek to answer this question (with essentially probability 1) without making use of rate gyros or other electro-mechanical systems; we are seeking a real-time, all stellar system which can operate continuously even in the presence of realistic mis-matches expected between the sets of cataloged and imaged stars (due to uncertainty of the cameras' spectral characteristics and the cataloged information, especially the spectral data for fainter stars, electronic noise, and pixel granularity-induced centroiding errors). In Reference [6], we published several years ago the essential ideas which we have extended in the present research project; these ideas have been implemented in several successful ground-based-computations for spacecraft attitude determination (e. g. the S<sup>3</sup> DoD system). The star pattern recognition ideas are based upon the fact that the instruments under discussion are fairly accurate (<5 arc seconds), so the angles between pairs of measured stars can be accurately determined from the measurements. The measured interstar angles can be compared with angles between candidate pairs of stars from the catalog; we have shown that when three or more measured interstar angles match cataloged interstar triplets, in each of two fields of view, to within 5 arc seconds, then it is essentially the certain event that the measured stars have been correctly identified with cataloged stars. All measured and cataloged stars in the field of view which were not successfully matched are simply deleted. To achieve an on-board, real-time version of this approach requires considerable sophistication of the formulation and algorithms, and the evaluation of many salient issues are best addressed in a combined analytical/experimental study.

This project included a general development of the algorithms and a sharply focused experimental study. The experimental study was approached assuming that most of the sensor-related issues could be resolved with a single camera. We mounted a two axis CCD camera (512 x 512 pixel format) on a Contraves air bearing. The air bearing has a 1 arc second angle encoder and therefore the inertial pointing could be determined independently of the estimated attitude based upon the attitude sensing and pattern identification process. The "stars" imaged were actually a simulated starfield consisting of over 100 light emitting diodes arranged on inner surface of a quarter cylinder with the air bearing and camera systems at the center of the cylinder. The analytical/computational/experimental results were consistent with the conclusion that sub-five-arc-second attitude determination can indeed be reliably achieved from an all stellar system, as an on-board, real-time process. We encountered and solved many problems associated with the fact that our laboratory experiment involved close-range photogrammetry, whereas the stars lie at practical infinity in actual in-space implementations (i. e., errors in the calibrated relative position in linear displacement of the camera with respect to the cylinder cause apparent angular displacements of the simulated starfield). These difficulties made our laboratory experiments more difficult than actual spacecraft attitude determination. Even though we have not engaged in an extensive hardware development and associated experimental studies, we feel that we have brought these ideas to a fairly mature stage of development. The Ph.D. dissertation by D. Anderson will be completed during the current calendar year; this dissertation will include a complete discussion of the analytical and experimental aspects of this research. On-board implementation of these ideas on a spacecraft appears relatively straight-forward.

### 3 Concluding Remarks

During the course of this research, we have engaged in several parallel research efforts. Coordinated analytical, numerical, and experimental studies have been undertaken in the following four areas:

1. Design of control laws for nonlinear systems (Attachments 1-3, 11-13)
2. Structural Identification (Attachments 6-10)
3. Spacecraft attitude determination (Reference 5)
4. Structure/Control design optimization (Attachments 4, 5)

In all four areas we have made significant advances and have engaged in both theoretical developments and computational studies. In the first three areas, we have also engaged in successful hardware implementations and experimental studies. We have gained an unusually excellent closure in the sense that innovative theoretical research has proceeded aggressively and in parallel with the successful proof-of-concept experimental research. The elapsed time from idea conception to hardware implications/feasibility evaluations has been greatly shortened as a consequence of this research. The most significant conclusion is that progress in analytical and experimental research can constructively co-exist and be significantly accelerated only if the principal investigators are broadly involved in both the analytical research and experiment design. The feedback loops are therefore efficiently closed around both the experiment and the analysis.

The most significant of our innovations is believed to be the Liapunov stable control laws we have developed for controlling nonlinear distributed parameter systems [Attachments 1-3, 11-13]. These ideas promise many new applications and provide a branch point for a diverse set of research direction implementations including, but not limited to the following:

New methods for globally controlling nonlinear distributed parameter systems.

New methods for spacecraft deployment dynamics and control.

New methods for stable control of flexible multi-body systems.

## References

1. Morgan, S., "Identification and Open Loop Control of a Simulated Flexible Space Structure Experimentally Verified with a Real Flexible Structure", M. S. Thesis, Aerospace Texas Engineering, Texas A&M University, College Station, Texas, 1989.
2. James, G. H. III, "An Experimental and Analytical Study of Structural Identification", Ph. D. dissertation, Aerospace Texas Engineering, Texas A&M University, College Station, Texas, 1989.
3. Creamer, N. G., "Identification of Linear Structural Models", Ph. D. dissertation, Engineering Science and Mechanics, Virginia Polytechnic Institute, Blacksburg, Va, 1987.
4. Creamer, N. G., and J. L. Junkins, "Identification Method for Lightly Damped Structures," *AIAA J. of Guidance, Control and Dynamics*, Vol 11, No. 6, Nov-Dec 1988, pp 571-576.
5. Anderson, D. S., T. C. Pollock, and J. L. Junkins, "A Testbed for Autonomous Star Pattern Recognition and Attitude Determination", Texas A&M University, August, 1990.
6. Junkins, J.L., White, III, C.C., and Turner, J.D., "Star Pattern Recognition for Real Time Attitude Determination," *Journal of the Astronautical Sciences*, Vol 25, No. 3, (September 1977, appeared June 1978), pp. 2512-270.

## Attachment Index

No	Authors	Title	Page
1	Junkins, Rahman, & Bang	"Near-Minimum-Time Maneuvers of Flexible Vehicles: A Liapunov Control Design Method" .....	20
2	Junkins, Rahman, & Bang	"Stable Maneuver Control Laws for Distributed Parameter Systems" .....	34
3	Junkins, Rahman, & Bang	"Near-Minimum-Time Maneuvers of Flexible Vehicles: Analytical and Experimental Results" .....	56
4	Junkins & Kim	"A Measure of Controllability for Actuator Placement" .....	95
5	Junkins & Kim	"First and Second Order Sensitivity of the Singular Value Decomposition" .....	129
6	James & Junkins	"Novel Sensing and Structural Identification Methods: Preliminary Analytical and Experimental Results" .....	148
7	Creamer & Junkins	"Identification Methods for Lightly Damped Structures" .....	166
8	Junkins & James	"A Stereo-Triangulation Approach to Structural Identification" .....	174
9	Junkins & James	"Identification of Flexible Structures Using Stereo Triangulation" .....	188
10	Junkins, James Pollock & Rahman	"A Stereo Triangulation System for Structural Identification: Analytical and Experimental Results" .....	203
11	Junkins, Pollock & Rahman	"Control-Structure-Interaction Sensing and Control: Analytical Experimental Results" .....	215
12	Vadali & Kim	"Feedback Control of Tethered Satellites Using Liapunov Stability Theory" .....	255
13	Vadali, Oh, & Walker	Gimbal Angles for Single Gimbal Control Moment Gyros" .....	274
14	Pollock	"Dynamics and Control Laboratory Facilities" .....	305

# ATTACHMENTS

ATTACHMENT 1

**Near-Minimum-Time Maneuvers of Flexible Vehicles:  
A Liapunov Control Law Design Method**

*J. Junkins  
Z. Rahman  
H. Bang*

Texas A&M University  
Dept. of Aerospace Engineering  
College Station, Texas 77843

*AIAA Dynamics Specialist Conference  
Paper No. 90-1222  
Long Beach, California  
April 5-6, 1990*



**AIAA-90-1222**

**Near-Minimum-Time Maneuvers of Flexible  
Vehicles: A Liapunov Control Law Design  
Method**

J. Junkins, Z. Rahman and H. Bang  
Texas A&M Univ.  
College Station, TX

**AIAA DYNAMICS SPECIALIST CONFERENCE**

**LONG BEACH, CA / APRIL 5-6, 1990**

For permission to copy or republish, contact the American Institute of Aeronautics and Astronautics  
370 L'Enfant Promenade, S.W., Washington, D.C. 20024

## Near-Minimum-Time Maneuvers of Flexible Vehicles: A Liapunov Control Law Design Method

J. L. Junkins Z. H. Rahman H. Bang  
 Department of Aerospace Engineering  
 Texas A&M University  
 College Station, Texas 77843

## Abstract

An approach for designing globally stable feedback control laws for maneuvers of distributed parameter structural systems is presented. The analytical developments and results are supported by experimental results.

## I. Introduction

Considerable recent research has been directed toward the problem of maneuvering a flexible spacecraft. The present paper grew out of our recent study [1]. In [2], we present a fairly comprehensive treatment of this family of problems up through 1985. Other analytical and experimental investigations<sup>3-13</sup> have been carried out to evaluate: (i) feedback control laws based upon minimizing quadratic indices, (ii) near-minimum time, switching-type controllers, and (iii) implementation issues. The main configuration of interest in the present discussion is a hub-appendage structure similar to the configuration of the Vander Velde and He study<sup>13</sup>, however, we address the use of variable torque actuation via a reaction wheel instead of on-off thrusters, and utilize Lyapunov control design approaches and establish stable tracking-type control laws for distributed parameter systems.

## II. Maneuvers and Vibration Control for Distributed Parameter Systems

With reference to Figures 1 - 3, we consider single-axis maneuvers of a rigid hub with four cantilevered flexible appendages. In [1], we present an analogous control law for nonlinear three dimensional maneuvers. In [3], Wie, et al develop similar globally stable laws for rigid body maneuvers. For the present discussion, we consider in-plane vibration and the appendages are assumed to be identical uniform flexible beams. We further invoke the Euler-Bernoulli assumptions of negligible shear deformation and distributed rotary inertia. Each beam is cantilevered rigidly to the hub and has a finite tip mass. All motion is restricted to the horizontal plane, and a control torque  $u(t)$  acting on the hub is the only external effect considered at this stage of the developments. We subsequently address rejection of disturbances and discuss generalizations to accommodate other modeling assumptions.

We are interested in a class of rest-to-rest maneuvers and under the above assumptions, we can show that the beams will deform in the anti-symmetric fashion (Figure 1) with the configuration's instantaneous mass center remaining at the hub's geometrical center. Due to the anti-symmetric deformation of the beams, we need concern ourselves only with the deformation  $y(x,t)$  of a single beam. We adopt the continuum viewpoint and avoid introducing spatial approximations in the application of Liapunov concepts; the resulting control law and stability arguments will therefore apply rigorously to the distributed parameter system. The hybrid system of ordinary and partial differential equations governing the dynamics of this system are

$$I_{hub} \frac{d^2 \theta}{dt^2} = u + 4(M_o - S_o l_o) - (M_o - S_o l_o) = \int_{l_o}^l \rho x \left( \frac{\partial^2 y}{\partial t^2} + x \frac{d^2 \theta}{dt^2} \right) dx + ml \left( l \frac{d^2 \theta}{dt^2} + \frac{\partial^2 y}{\partial t^2} \Big|_l \right) \quad (1)$$

+HOT

$$\rho \left( \frac{\partial^2 y}{\partial t^2} + x \frac{d^2 \theta}{dt^2} \right) + EI \frac{\partial^4 y}{\partial x^4} = 0 + HOT$$

where

$\rho$  is the constant mass/unit length of the beams,  
 $EI$  is the assumed constant beam bending stiffness,  
 $(M_o, S_o)$  denote bending moment and shear force, at the root of the beams,  
 $\theta$  denotes hub inertial rotation,  
 $m$  denotes the mass of the tip mass, and  
 $(l, l_o)$  denote the distance from the hub center to the beam tip and the hub radius.

We denote higher order terms by *HOT* to indicate other known linear and nonlinear effects (such as rotational stiffening, shear deformation, etc.). The most fundamental of the developments given here do not consider these higher order effects, however, we selectively discuss these generalizations as well. The boundary conditions on Eqs. (1) are

$$\begin{aligned} \text{at } x = l_o: y(t, l_o) = \frac{\partial y}{\partial x} \Big|_{l_o} = 0 \\ \text{at } x = l: \frac{\partial^2 y}{\partial x^2} \Big|_l = 0, \frac{\partial^3 y}{\partial x^3} \Big|_l = \frac{m}{EI} \left( l \frac{d^2 \theta}{dt^2} + \frac{\partial^2 y}{\partial t^2} \Big|_l \right) \end{aligned} \quad (2)$$

The total energy of the system (constant in the absence of control or disturbances) is:

$$2E = I_{\omega} \left( \frac{d\theta}{dt} \right)^2 + 4 \left[ \int_0^l \rho \left( \frac{\partial y}{\partial t} + x \frac{d\theta}{dt} \right)^2 dx + \int_0^l EI \left( \frac{\partial^2 y}{\partial x^2} \right)^2 dx + m \left( l \frac{d\theta}{dt} + \frac{\partial y}{\partial t} \Big|_l \right)^2 \right] \quad (3)$$

Motivated by the recent work of Fujii<sup>5</sup> and Vadali<sup>9</sup>, and in view of the energy integral of the open loop system, we investigate the Liapunov function

$$2U = a_1 I_{\omega} \dot{\theta}^2 + a_2 (\theta - \theta_f)^2 + 4a_3 \left[ \int_0^l \rho \left( \frac{\partial y}{\partial t} + x \dot{\theta} \right)^2 dx + \int_0^l EI \left( \frac{\partial^2 y}{\partial x^2} \right)^2 dx + m \left( l \dot{\theta} + \frac{\partial y}{\partial t} \Big|_l \right)^2 \right] \quad (4)$$

where the positive weighting coefficients  $a_i$  are introduced to allow relative emphasis upon the three sets of contributors to the "error energy" of the system. We anticipate that only two of these weight parameters really matter, since we can scale Eq. (4) by an arbitrary constant without changing the location of the global minimum. Notice that the open loop system energy integral of Eq. (3) does not depend upon the rigid body displacement coordinate  $\theta$ . In addition to introducing weights on subsets of the system energy, to construct a meaningful Lyapunov function [Eq. (4)] for the closed loop system, we have modified the open loop energy integral by adding the second term  $a_2 (\theta - \theta_f)^2$  to make the desired final state

$$(\theta, \dot{\theta}, y(x,t), \frac{\partial y(x,t)}{\partial t})_{desired} = (\theta_f, 0, 0, 0)$$

be the global minimum of  $U$ . It is obvious by inspection that the logical requirement that  $a_i > 0$  guarantees that  $U \geq 0$ , and that indeed the global minimum of  $U=0$  occurs only at the desired state. Differentiation of Eq. (4), substitution of the equations of motion (Eqs. (1), (2)), and some calculus leads to

$$\dot{U} = \dot{\theta} \left[ a_1 \dot{u} + a_2 (\theta - \theta_f) + 4(a_3 - a_1)(l.S. - M.) \right] \quad (5)$$

Since we require that  $\dot{U} \leq 0$  to guarantee stability, we set the [ ] term to  $-a_4 \dot{\theta}$  and this leads to  $\dot{U} = -a_4 \dot{\theta}^2$  and the control law

$$u = -\frac{1}{a_1} \left[ a_2 (\theta - \theta_f) + a_4 \dot{\theta} + 4(a_3 - a_1)(l.S. - M.) \right] \quad (6)$$

or, we see that the following *linear, spatially discrete* output feedback law globally stabilizes this distributed parameter system:

$$u = - \left[ g_1 (\theta - \theta_f) + g_2 \dot{\theta} + g_3 (l.S. - M.) \right]; \quad (7)$$

*with  $g_1 \geq 0, g_2 \geq 0, g_3 \geq -4$ , for global stability.*

This control law is elegant. Notice that controllers based upon this output feedback law are easy to implement since no state estimation is required. The root shear and bending moment can be measured by conventional strain gauges. The value and sign of the shear/moment feedback gain  $g_3 = 4(a_3 - a_1)/a_1$ , depends upon whether we wish to emphasize dissipation of the beam energy (for  $a_3 > a_1$ ), or the motion of the hub (for  $a_3 < a_1$ ), as is evident from Eq. (4).

Note  $\dot{U} = -a_4 \dot{\theta}^2$  is only negative semi-definite, since it is not an explicit function of the subset of state variables  $(\theta, y(x,t), \frac{\partial y(x,t)}{\partial t})$ ; the stability arguments therefore implicitly depend upon the truth that all infinity of modes of motion of this structure, under the assumption of anti-symmetric deflections, have generally non-zero hub angular velocity ( $\dot{\theta}$ ).

It is of significance that the linear feedback law of Eq. (7) maintains it's globally stabilizing character even when the Euler/Bernoulli assumptions are relaxed to include additional linear and nonlinear effects; in particular, closed loop stability is maintained when we include the following effects neglected above: rotational stiffening, coriolis kinematic coupling terms, aerodynamic drag, shear deformation, beam rotary inertia, and finite rotational inertia of the tip mass. The verification of these truths requires appropriate modifications of the kinetic and potential energy functions, and of course, the differential equations of motion must be generalized consistently. *In short, global stability of the system using the simple linear control law of Eq. (7) has been found very forgiving of modeling assumptions and therefore modeling errors.*

On the other hand, the overall performance measures (time constants, required energy, rms output errors, etc.) of the system versus our simulations are generally not as forgiving as the most fundamental performance measure (stability). While we can guarantee stability for a large family of model errors, it should be apparent that *performance predictions are generally very sensitive to modeling errors*. With appropriate system modeling and selection of the feedback gains, however, we have found numerically and experimentally, that this feedback law works well

over finite regions of the state and gain space, and in the presence of typical model errors.

While the constant gain linear feedback works well for terminal pointing and vibration suppression, we have found it to be a poor law for carrying out both large angle maneuvers and terminal pointing/vibration suppression. In fact, it is evident from both analytical and experimental studies that gain scheduling is needed to use the linear feedback law of Eq. (7) to efficiently control both the large maneuvering motions and the small terminal motions. This is because the large gains required for effective vibration suppression and disturbance rejection near the target state typically differ by several orders of magnitude from the smaller ones needed far from the target state (i., e., large gains appropriate for terminal vibration suppression, when used during a large angle maneuver typically result in actuator saturation and significant  $\theta$  overshoots). To obtain a control law more appropriate for large angle maneuvers with vibration suppression, we can modify the above developments; a stable tracking-type feedback control law is presented in the following discussion.

### III. Near-Minimum-Time Maneuvers of Distributed Parameter Systems

Consider the near-minimum-time, single axis maneuver of a rigid body. We know that the strict minimum time control is a bang-bang law<sup>2</sup>, which for the rest-to-rest maneuver-to-the-origin case, saturates negatively during the first half of the maneuver and positively during the last half of the maneuver. However, the switch times for arresting many modes of a vibrating structure are sensitive to model errors; we prefer to adopt an approach which is inherently smoother and more robust. Note that discontinuous controls will almost certainly excite higher frequency modes as well as fail to perfectly arrest the lower frequency modes. We seek to generalize the above vibration suppression approach which does not require we control the structure mode-by-mode, so that it permits the user to shape the overall maneuver as well as incorporate vibration suppression feedback.

Recently, an attractive family of controllably smooth approximations of the sign (*sgn*) function which arises in time-optimal control has been introduced. The

smoothed control approximations presented in Ref. [1, 8] has been studied in the context of near-minimum-time maneuvers of flexible bodies. These studies motivate the use of a smoothly switching family of controls for single axis maneuvers. The approach involves applying a judiciously shaped torque profile to a rigid body to provide a nearly achievable target trajectory for the flexible body maneuver. One such smooth family of rigid body maneuvers for near minimum time control is generated as follows:

$$I\ddot{\theta} = u = \pm u_{max} f(\Delta t, t_f, t) \quad (8)$$

where

$u_{max}$  is the saturation torque,

$t_f$  is the maneuver time, we choose the + sign if  $\theta_f > \theta_o$ .

$$t_1 = \frac{t_f}{2} - \Delta t, \quad t_2 = \frac{t_f}{2} + \Delta t, \quad t_3 = t_f - \Delta t,$$

$\Delta t$  is the rise time, and the smooth torque shape function adopted is

$$f(\Delta t, t_f, t) \begin{cases} = (\frac{t}{\Delta t})^2 [3 - 2(\frac{t}{\Delta t})], & \text{for } 0 \leq t \leq \Delta t \\ = 1, & \text{for } \Delta t \leq t \leq t_1 \\ = 1 - 2\left(\left(\frac{t-t_1}{2\Delta t}\right)^2 [3 - 2\left(\frac{t-t_1}{2\Delta t}\right)]\right), & \text{for } t_1 \leq t \leq t_2 \\ = -1, & \text{for } t_2 \leq t \leq t_3 \\ = -1 + \left(\frac{t-t_3}{\Delta t}\right)^2 [3 - 2\left(\frac{t-t_3}{\Delta t}\right)] & \text{for } t_3 \leq t \leq t_f \end{cases}$$

Adopting the positive sign, Eq. (8) integrates to yield

$$\theta(t) = \theta_o + \frac{u_{max}}{T} \int_{t_o}^t f(t_1, t_f, \tau) d\tau \quad (9)$$

$$\theta(t) = \theta_o + \theta_o(t-t_o) + \frac{u_{max}}{T} \int_{t_o}^t \int_{t_o}^{\tau_1} f(t_1, t_f, \tau_2) d\tau_2 d\tau_1$$

The integrations indicated in Eq. (9) can be carried out in terms of elementary functions which are not presented here for brevity. Figure 4 shows the maneuver resulting from these integrations for a typical selection of parameters. For rest-to-rest maneuvers, we can impose the boundary conditions

$$\text{at } t_o = 0: \quad \theta(0) = \theta_o, \quad \dot{\theta}(0) = 0; \quad (10)$$

$$\text{at } t_f = T: \quad \theta(T) = \theta_f, \quad \dot{\theta}(T) = 0$$

and upon carrying through the integrations of Eqs. (9), we find the useful relationship

$$\theta_f - \theta_o = \frac{u_{max}}{T} \left[ \frac{1}{4} - \frac{1}{2}\alpha + \frac{1}{10}\alpha^2 \right] T^2, \quad (11)$$

$$\text{with } t_1 = \Delta t = \alpha T, \quad 0 < \alpha < \frac{1}{4}$$

$$\text{or } T = \left[ \frac{I(\theta_f - \theta_o)}{u_{max} \left( \frac{1}{4} - \frac{1}{2}\alpha + \frac{1}{10}\alpha^2 \right)} \right]^{1/2} \quad (12)$$

In Eq. (12) we see the rigid body tradeoff between torque shaping ( $\alpha$ ), maneuver time ( $T$ ), maneuver angle ( $\theta_f - \theta_o$ ), and maximum angular acceleration ( $u_{max}/I$ ). Obviously, Eq. (11) can be inverted for any of these as a function of the remaining parameters. If we set  $\alpha = t/T = 0$ , of course, we obtain the special case result  $\{T^2 = 4I(\theta_f - \theta_o)/u_{max}\}$  expressing the well-known square-root relationship between the minimum time, maneuver angle, inertia, and saturation torque for bang-bang control.

Figure 5 shows the rigid body maneuver time ( $T$ ) versus  $\alpha$  and  $u_{max}$ . Notice that the maneuver time is strongly dependent upon  $u_{max}$ , but varies much less as a function of  $\alpha$ . However, we find when the torque  $u_{ref}(t) = u_{max} f(\alpha T, T, t)$  of Eq. (8) is applied to a flexible body, the reverse is true vis-a-vis the residual vibration energy at time  $T$ . To illustrate this point, we approximated the solution of Eqs. (1) by introducing a Galerkin expansion (of the beam deflection in terms of the first ten clamped-free cantilever mode shapes times time varying generalized coordinates). The forced response of the resulting 20th order system was judged adequately converged. Using this solution, we applied the same family of torques used for the rigid body results of Figure 5 and computed the flexible body open loop response for each choice of  $\alpha$  and  $u_{max}$ . Figure 6 shows the total energy of the flexible body system at time  $T$  for this same family of maneuvers. As is evident, the vibration energy vanishes for sufficiently small  $u_{max}$  and is significantly reduced for any given  $u_{max}$  by increasing  $\alpha$ . Notice the triangular region (large  $\alpha$ , small  $u_{max}$ ) for which the vibration energy at time  $T$  is negligible. We will subsequently see that measures of the largest errors with which the closed-loop-controlled flexible body system can track the rigid body maneuvers of Figure 5 behave in a qualitatively similar way.

The above results and those of Ref. [1, 6, 7, 8] support the intuitively obvious truth that applying judiciously

"smoothed bang-bang" open-loop controls such as Eq. (8) to generate maneuvers of a flexible body results in moderate structural vibration, for sufficiently slow and smooth maneuvers (small  $u_{max}$  and large  $\alpha$ ). Of course unmodeled disturbances, control implementation errors, and model errors negate some of these apparent gains, especially without feedback. For relatively small penalties in maneuver time<sup>1,7</sup>, actual torque-shaped maneuvers enjoy several orders of magnitude reduction in residual vibration, even without feedback, although some offset in rigid body position usually results. Thus overall maneuver time, including vibration arrest, can be reduced dramatically by modest torque shaping, as compared to simply using bang-bang control augmented by vibration suppression. Also of significance, we find that it is usually desirable to select the torque profile (e.g.,  $u_{max}$ ,  $\alpha$ , etc.) to consider the sensor and actuator dynamics and thereby make the commanded torque history more nearly physically achievable. More generally, however, we can use any reference maneuver (not necessarily a rigid body torque-shaped maneuver).

Suppose we adopt a reference open-loop rigid body maneuver denoted by the subscript *ref* as  $\{\theta_{ref}(t), \dot{\theta}_{ref}(t), \ddot{\theta}_{ref}(t) = u_{ref}/I\}$  and satisfying Eqs. (8-12). Note  $I$  is the undeformed moment of inertia, and we have implicitly selected the torque shaping parameters  $\alpha$ ,  $u_{max}$ , and thereby established the corresponding target maneuver time  $T$  from Eq. (12) for specified initial and final angle. Motivated by the issues discussed above and the quadratic regulator perturbation feedback controllers in refs. [2, 11, 13], we hypothesize the following structure for the control law

$$u = u_{ref}(t) - [g_1(\theta - \theta_{ref}) + g_2(\dot{\theta} - \dot{\theta}_{ref}) + g_3((I_s - M_s) - (I_s - M_s)_{ref})] \quad (13)$$

where the root moment for the reference (rigid body) motion is proportional to the angular acceleration:  $(I_s - M_s)_{ref} = [\rho(I^3 - I_o^3)/3 + m l^2] \ddot{\theta}_{ref}(t)$ .

We wish to gain insight on the stability characteristics of the flexible body's closed-loop departure dynamics [from the target (*ref*) rigid body motion (for  $t < T$ ), and from the fixed target state (for  $t \geq T$ )], and we will

provide an analytical justification for the tracking control law of Eq. (13). Let us denote by the subscript  $r$  the state variables along the open-loop flexible body solution of Eqs. (1) when driven by the torque  $u_{ref}(t)$  of Eqs. (8-12). The instantaneous displacement of the open-loop flexible body solution from the open loop rigid body motion is denoted  $\Delta() = ()_r - ()_{ref}$ ; for example,  $\Delta\theta(t) = \theta_r(t) - \theta_{ref}(t)$ . Variables without subscripts represent the actual instantaneous closed-loop controlled solution variables. Consider the candidate error energy Liapunov function

$$2U = a_1 I_{hub} (\dot{\theta} - \dot{\theta}_r)^2 + a_2 (\theta - \theta_r)^2 + 4a_3 \left[ \int_0^t \rho \left( \frac{\partial y}{\partial t} - \frac{\partial y_r}{\partial t} \right) + x(\theta - \theta_r) \right]^2 + \int_0^l EI \left( \frac{\partial^2 y}{\partial x^2} - \frac{\partial^2 y_r}{\partial x^2} \right)^2 dx + m \left[ l(\dot{\theta} - \dot{\theta}_r) + \left( \frac{\partial y}{\partial t} \Big|_l - \frac{\partial y_r}{\partial t} \Big|_l \right) \right]^2 \quad (14)$$

Assuming the actual control is some general, to-be-determined  $u(t)$ , and that the actual motion satisfies Eqs. (1), we have investigated the time derivative of  $U$  of Eq. (14) and found that it is given by the following equation

$$\dot{U} = a_1 (\dot{\theta} - \dot{\theta}_r) \left[ \dot{u} - \dot{u}_{ref} + \frac{a_2}{a_1} (\dot{\theta} - \dot{\theta}_r) + 4 \frac{a_3 - a_1}{a_1} [(l, S_o - M_o) - (l, S_o - M_o)_r] \right] \quad (15)$$

Analogous to the logic leading to Eq. (5), we see that we could determine a globally stabilizing  $u(t)$  by setting the bracketed term to a positive quantity  $g_2$

times  $-(\dot{\theta} - \dot{\theta}_r)$  (i. e., this makes  $\dot{U}$  a negative definite function of the error in hub angular velocity), and gives the globally stabilizing control law

$$u = u_{ref}(t) - \left[ g_1 (\dot{\theta} - \dot{\theta}_r) + g_2 (\dot{\theta} - \dot{\theta}_r) + g_3 [(l, S_o - M_o) - (l, S_o - M_o)_r] \right] \quad (16)$$

with  $U = -a_1 g_2 (\dot{\theta} - \dot{\theta}_r)^2$  and we introduced the gain definitions as  $g_1 \equiv a_2/a_1$ , and  $g_3 \equiv 4(a_3 - a_1)/a_1$ . Notice, to guarantee global stability, that  $g_1$  and  $g_2$  must be positive, but as before  $g_3$  must be greater than  $-4$ . The only difficulty with this control law is that it requires pre-computing the flexible body solution, which is generally infeasible in an on-line implementation. Obviously, we'd prefer a tracking law which requires a much simpler (e., g., rigid body) maneuver to be pre-computed. Let us pursue this objective. Since Eq. (15) holds for an arbitrary  $u(t)$ , we introduce instead of Eq. (16) the control law of Eq. (13), and investigate it's stability characteristics. Using the

notation  $\Delta() = ()_r - ()_{ref}$ , Eq. (15) simplifies to

$$\dot{U} = -a_1 (\dot{\theta} - \dot{\theta}_r) \left\{ g_2 (\dot{\theta} - \dot{\theta}_r) + [g_1 \Delta\dot{\theta} + g_2 \Delta\dot{\theta} + g_3 \Delta(l, S_o - M_o)] \right\} \quad (17)$$

A sufficient condition characterizing the region where  $\dot{U} \leq 0$  is the dominance of the first term in the  $\{\}$  of Eq. (17), this gives the inequality

$$|\dot{\theta} - \dot{\theta}_r| > \frac{1}{g_2} |g_1 \Delta\dot{\theta} + g_2 \Delta\dot{\theta} + g_3 \Delta(l, S_o - M_o)| \equiv \mu \quad (18)$$

It is further apparent that the  $\Delta$  quantities on the right hand side of Eq. (18) are finite and (pre-) computable differences between the open loop flexible and rigid body motions, thus an upper bound can be established directly by a one-time family of a priori simulations of the two open loop motions, and using a particular set of feedback gains. Equation (18) thus determines an angular velocity boundary region. Note that large motions are globally attracted to the region bounded by  $\mu$  of Eq. (18). Thus the control law of Eq. (13) is almost globally stabilizing, and the only region where asymptotic stability cannot be guaranteed is a boundary layer region near the target trajectory. Furthermore, note the right hand side of Eq. (18) is essentially a weighted measure of how nearly the target trajectory satisfies the flexible body equations of motion; further note that judicious choice of the torque shaping parameters defining the target trajectory can result in  $\mu$  being arbitrarily small.

A bounded-input/bounded-output viewpoint of stability can also be considered, based upon the departure motion differential equations obtain by differencing Eqs. (1) evaluated at each instant along the flexible body closed loop trajectory and along the flexible body open loop  $()_r$  motion. Upon formulating these equations, we find departure motion is governed by an otherwise asymptotically stable system of differential equations forced by the known  $\Delta()$  terms which appear in Eqs. (18). Since these forcing terms can be bounded by direct calculation, the resulting departure motion can also be bounded. Since the actual numerical bounds on the  $\Delta$  quantities can be made arbitrarily small (depending upon how nearly the user defined reference trajectory is made to satisfy the open loop equations of motion), we have a very attractive theoretical and practical situation vis-a-vis stability of the closed loop tracking motion. *We see that the closed-loop motion is globally attracted to the controllably small region near the target trajectory*

which violates the inequality of Eq. (18), and considering the motions within this small region, we have bounded-input, bounded-output stability.

The above discussion can probably be generalized for any smooth target trajectory, but we find that it is attractive to use a torque-shaped rigid body reference trajectory, such as Eqs. (8)-(12). Note that Eqs. (8)-(13) result in a  $C^1$  continuous transition:  $\{\theta_{ref}(t), \dot{\theta}_{ref}(t), \ddot{\theta}_{ref}(t), M_{\theta_{ref}}(t), S_{\theta_{ref}}(t)\} \Rightarrow \{0, \theta_f, 0, 0, 0\}$  as  $t \Rightarrow T$ ; so that for  $t > T$ , only the three feedback terms of Eq. (13) are contributing to the terminal fine-pointing/vibration arrest control. Thus the controls blend continuously from the large angle tracking law into a constant gain controller (for  $t > T$ ) identical to the globally stable fixed point output feedback case of Eq. (7).

#### IV. Simulated Results: Large Angle Maneuvers Experiment

Returning to the family of  $40^\circ$  open loop maneuvers used to generate the energy surface of Figure 6, we computed the velocity tracking bound  $\mu$  for Liapunov stability [as given by Eq. (18)] and found the maximum value ( $\mu_{max}$ ) of  $\mu(t)$  along each trajectory. Figure 7 displays this worst case tracking bound (maximum value of  $\mu$ ) surface  $\mu_{max}(\alpha, u_{max})$  over the same  $(\alpha, u_{max})$  region used to generate Figures 5, 6. The closed-loop tracking error bound has a roughly analogous behavior to the open-loop residual vibration energy surface of Figure 6. Recall that outside the region bounded by the inequality of Eq. (18), we have guaranteed Liapunov stability, using the control law of Eq. (13) and the reference rigid body torque given by Eqs. (8)-(12). From Figure 6, it is clear that sufficiently small  $u_{max}$  and large  $\alpha$  result in arbitrarily small tracking errors, but the (small  $\alpha$ , large  $u_{max}$ ) near-bang reference maneuvers cannot be tracked as accurately. It is easy to see how a family of candidate  $(\alpha, u_{max})$  designs can be found which satisfy specified inequalities on maneuver times, tracking errors, and residual vibration energy, by direct examination of the surfaces of Figures 5-7.

Our experiments with simulations (and in the actual hardware implementations presented below and in [1,

6, 7] support the conclusion that we can use these surfaces (together with disturbance rejection simulations to select the reference trajectory and tune the feedback gains) to establish a large family of feasible designs. Prior to discussing our experimental results, we present some further simulations to show state and control variables histories along typical trajectories of underlying the above surfaces. We include in these simulations the effects of disturbance torques, to illustrate the effectiveness of the controls in the presence of unmodeled effects. Table 1 summarizes the physical parameters and a detailed hardware description of the maneuver experiment is given in Ref. [1]. For simplicity, we consider here only the case of a  $40^\circ$  rest-to-rest maneuver, and set  $u_{max} = 400$  oz-in for all cases.

For our computational and experimental studies, we consider two control laws, namely the output feedback law (Control Law I) of Eq. (7), and the tracking-type feedback control law (Control Law II) of Eq. (13). While Control Law II could be used with an arbitrary reference trajectory, we elect to specifically investigate the torque-shaped rigid body trajectories of Eqs. (8)-(12). The torque-shaped open loop control history  $u_{ref}(t)$  is pre-computed (in a fraction of a second!) from Eqs. (8)-(12) and stored. Note that the boundary conditions of Eq. (10) are enforced by using Eq. (12) to compute the target trajectory maneuver time as a function of the maneuver angle, saturation torque, and torque-shape parameter.

We now discuss the simulation results using Control Law II, which obviously blends into to Control Law I in the end game (for  $t \geq T$ ). In the experimental results, we report maneuvers carried out by both control laws. Both open loop (all  $g_i \equiv 0$ ) and closed loop time histories of selected variables are shown in Figures 8a-8d. On the left of Figure 8, we show the hub angle and angular velocity for the case of an open loop control and in the presence of substantial impulsive and quasi-random (5 oz-in,  $1 \sigma$ ) disturbance torques. It is evident that the disturbance torque history is significant vis-a-vis exciting substantial rigid body and flexural motions. On the right, we show the closed loop behavior of the system excited by the same disturbance torque history. The random

component of this disturbance has been found to be typically pessimistic vis-a-vis our experimental hardware, however certain non-random, nonlinear effects associated with the bearing friction cause disturbances which are correlated in time and are not well represented by the present white noise model of the disturbance torques. In spite of the substantial disturbance torques (Figs. 8a-8b), it is evident that we obtain a near minimum time rigid body motion while effectively suppressing vibration (8c-8d). This fact was also confirmed by evaluation of the energy distribution in the first six modes.

### V. Experimental Results

In all of the experiments discussed below, we set the target final angle to  $40^\circ$  and  $\mu_{max} = 400$  oz-in. The values of the tracking gains ( $g_1, g_2, g_3$ ) and of the torque shape parameter ( $\alpha$ ) were assigned several feasible values to demonstrate the effects of these upon the closed loop behavior of the system. Moderate bearing friction and aerodynamic damping were present in our experiments.

Figure 9 shows the system response for a Control Law I (the constant gain control law of Eq. (11)) maneuver with ( $g_1 = 600$  oz-in/rad,  $g_2 = 800$  oz-in/rad/sec, and  $g_3 = 0$ ). Since this initial position error is large, the maneuver starts from zero with an initial discontinuity to a large torque. For this gain selection, we see a large overshoot ( $\sim 10^\circ$ ) and significant structural vibration which settled around 12 seconds; the control was terminated at 16 seconds.

Control Law II leads to very attractive near-minimum-time maneuvers. One good set of gain settings and torque shape parameters leads to the results in Figure 10. The effect of using a smooth, judiciously shaped reference torque history is evident if one compares the output and control variable histories in Figure 10 with those of Figure 9. Law II produced much smaller overshoot ( $\approx 1.5^\circ$  vs  $\sim 10^\circ$ ), shorter settling time (6 sec. vs 12 sec.) and greatly reduced the severity of peak vibration. These results, especially when considered in conjunction with numerous other cases are reported in [1, 7, 8] are convincing evidence of the truth that Control Law II

is a very versatile and highly effective way to incorporate open loop torque shape optimization with vibration suppression. The fact that a globally continuous control structure is implicit in this approach leads to minimal difficulties in realizing robust control laws; note the handoff from here. However, as previously reported in [1], we did encounter some practical difficulties in our experimental work. Firstly, the shear and bending moment measurements via strain gauges resulted in sufficiently noisy measurements that this feedback ( $g_3 \neq 0$ ) did not improve the controlled response over, for example the results in Figure 10. Also, deriving the angular velocity estimate from the noisy angle encoder readout was difficult to accomplish with high precision, and as a consequence, we constructed a digital noise filter to process our angle encoder data and eliminate all of the frequency content above 10 Hz; this was necessary to avoid erroneous, phase lagged feedback which would otherwise disturb the higher frequency modes. This problem can be eliminated by investing in a more precise sensor to measure angular displacement and/or angular velocity.

Finally, our bearing presented us with some practical difficulties. Based upon mechanical tests and analysis of our bearing hardware, it is evident that interaction of the structure with the bearing accounts for the overwhelming source of unmodeled disturbances. The bearing friction/stiction model developed from our analysis [1] has the form

$$\tau_{\text{bearing}} = -c_1 \text{sign}(\dot{\theta}) - c_2 \dot{\theta} + \text{HOT} \quad (19)$$

where we find  $c_1 \sim 20$  oz-in and  $c_2 \sim 0.001$  oz-in/rad/sec. Thus the first (stiction) term of Eq. (19) dominates the bearing torque for moderate  $\dot{\theta}$  and is about 5% of the peak commanded torque of 400 oz-in. While we believe Eq. (19) models the bearing friction well, it is difficult to use this model to compensate for bearing friction in real time, since our estimated value of  $\dot{\theta}$  is uncertain due to angle encoder measurement noise. Thus if we modify our control using Eq. (19), the commanded discontinuity (near the estimated time  $\dot{\theta}$  changes sign) will not coincide exactly with the actual discontinuity; mis-timed compensation torque discontinuities can actually worsen the disturbance! While we experimented with several bearing friction compensation schemes, we ultimately decided to

simply consider this an anticipated and well-modeled disturbance. Our simulations (such as the results shown in Figure 8) indicated our control approach could easily tolerate disturbances of this magnitude, and our successful experiments Figures 9, 10, and in [1], certainly confirm that our implemented control laws are robust in the presence of the actual disturbances.

## VI. Concluding Remarks

We have presented an approach to design of feedback control laws for large maneuvers of distributed parameter systems, and have conducted successful experiments. This approach establishes stable gain regions over which subsequent optimizations can be carried out with global stability guaranteed (to within model errors, of course). The formulation permits approximate imposition of actuator saturation constraints and a priori control shaping via user specification of a torque-shaped, optimized reference trajectory. The resulting tracking-type control law is shown to result in Liapunov stability in the sense that all trajectories are globally attracted to a small region near the reference trajectory. The tracking law automatically blends smoothly into a globally stable, constant gain, terminal output feedback controller. We believe this approach is much more attractive than gain scheduling, because the logical and implementation complications associated with discontinuous gain change ("handoff") logic can be avoided altogether. We have considered in detail the case of single axis maneuvers of a flexible body system and a particular family of torque-shaped, near-minimum-time rigid body reference trajectories. We demonstrated numerically the effects of torque shaping upon maneuver time and established a pre-computable bound on the size of region near the target trajectory in which Liapunov-stable tracking cannot be guaranteed. We described hardware experiments which successfully implemented these ideas.

We have demonstrated the feasibility of our analytical formulations and experimental approach. We are optimistic that these ideas extend to a significant family of multi-axis maneuvers of multiple flexible body systems and the maneuver control problems associated with multiple body re-configuration, pointing/tracking, and deployment dynamics.

## VII. Acknowledgments

The authors are pleased to acknowledge the work of H. Fujii, S. R. Vadali, A. Das; their earlier research provided inspiration for this work. The support of the Air Force Office of Scientific Research (Contract F49620-87-C-0078) and A. K. Amos is appreciated. We also received support from the Texas Advanced Technology Program (Project 70110). We thank the following individuals for their contributions: T. C. Pollock for his contributions to all aspects of the design and development of the experiment hardware, Steve Morgan for identifying the structural parameters and for his assistance with the angle encoder, Johnny Hurtado for his assistance in carrying out the experiments, and Becky Masters for excellent support in preparing this manuscript.

## VIII. References

1. Junkins, J. L., Rahman, Z., and Bang, H., "Near-Minimum-Time Maneuvers of Flexible Vehicles: A Liapunov Control Law Design Method," AIAA Aerospace Sciences Meeting, Reno, Nevada, January, 1990, submitted for publication, AIAA Journal of Guidance, Control, and Dynamics.
2. Junkins, J. L. and Turner, J. D., *Optimal Spacecraft Rotational Maneuvers*, Elsevier, 1986, Amsterdam.
3. Wie, B., Weiss, H., and Araposthathis, "Quaternion Feedback for Spacecraft Eigenaxis Rotations," AIAA Journal of Guidance, Control, and Dynamics, Vol 12, No. 3, Mar-Jun, 1989, pp 375-380.
4. Juang, J. N., Horta, L. G., and Robertshaw, H. H., "A Sewing Control Experiment for Flexible Structures", *Proc. of the 5th VPI & SU Symposium on Dynamics and Control of Large Structures*, pp 547-551, Virginia Polytechnic Institute, Blacksburg, VA, June 12-16, 1985.
5. Fujii, H., Ohtsuka, T., and Udou, S., "Mission Function Control for Slew Maneuver Experiment", a preprint, to appear in the AIAA Journal of Guidance, Control, and Dynamics.
6. Junkins, J., Rahman, Z., Bang, H., and Hecht, N., "Near-Minimum Time Feedback Control of Distributed Parameter Systems: A Liapunov Control Law Design Method," 7th VPI & SU Symp. on Dyn. & Ctrl. of Large Str., proc. to appear.
7. Rahman, Z., Junkins, J. L., Pollock, T. C., and Bang, H., "Large Angle Maneuvers with Vibration Suppression: Analytical and Experimental Results," 7th VPI & SU Symp. on Dyn. & Ctrl. of Large Str., proc. to appear.
8. Thompson, R. C., Junkins, J. L., and Vadali, S. R., "Near-Minimum-Time Open-Loop Slewing of Flexible Vehicles," AIAA Journal of Guidance, Control, and Dynamics, Vol 12, No. 1, Jan-Feb, 1989, pp 82-88.
9. Vadali, S. R., "Feedback Control of Flexible Spacecraft Large Angle Maneuvers Using Liapunov Theory", paper No. 1674, *Proceedings of the 1984 Amer. Ctrls. Conf.*, pp 1674-1678, IEEE, 1984.
10. Byers, R. M., Vadali, S. R., and Junkins, J. L., "Near-Minimum-Time Closed Loop Slewing of Flexible Spacecraft," to appear, AIAA Journal of Guidance, Control and Dynamics.
11. Meirovitch, L. and Quinn, R., "Maneuvering and Vibration Control of Flexible Spacecraft," *Journal of the Astronautical Sciences*, Vol, 35, No. 3, July-Sept., 1987, pp 301-328.

12. Singh, G., Kabamba, P., and McClamroch, N., "Planar Time Optimal Slewing Maneuvers of Flexible Spacecraft", to appear, *AIAA Journal of Guidance, Control, and Dynamics*.
13. Breakwell, J. A., "Optimal Feedback Control for Flexible Spacecraft", *AIAA Journal of Guidance, Control, and Dynamics*, Vol 4, No. 5, Sept-Oct 1981, pp 472-479.
14. VanderVelde W. and He, J., "Design of Space Structure Control Systems Using On-Off Thrusters," *AIAA Journal of Guidance, Control, and Dynamics*, Vol. 6, Jan-Feb., 1983, pp 759-775.

**Table 1. Hub/Appendage Configuration Parameters**

**Hub & Appendages**

Total System Inertia, I	2128 [oz-in-sec <sup>2</sup> -in]
Hub Center to Gage Center, $l_g$	5.5470 [in]
Hub Center to Tip Mass, $l$	51.07 [in]
Tip Mass, $m$	.15627 [oz-sec <sup>2</sup> /in]
Appendage Modules of Elasticity, E	161.6 [10 <sup>6</sup> oz/in <sup>2</sup> ]
Inertia of Bending Section, I	.000813 [in <sup>4</sup> ]
Density of Appendages $\rho$	.00307 [oz-sec <sup>2</sup> /in <sup>2</sup> ]
Distance between two gage set	1.365 [in]

**Motor (PMI, Servodisc DC Motor: JR16M 4 CH)**

Torque Constant, $K_t$	52.77 [oz-in/amp]
Back EMF Constant, $K_e$	39.77 [v/1000rpm]
Tachometer Constant	3 [v/1000rpm]

**Power Supply (KEPCO BOP 36-12M)**

Current Gain	1.2 [amp/volt]
--------------	----------------

**Figure 1. Texas A&M Hub-Appendage Configuration: Anti-Symmetric Deformation**

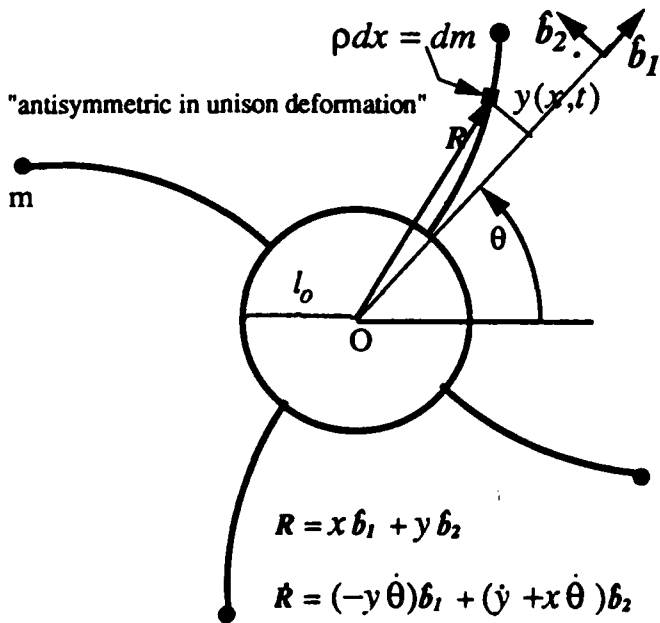


**Figure 2. Hub Assembly: Motor, Reaction Wheel, and Sensing Systems**

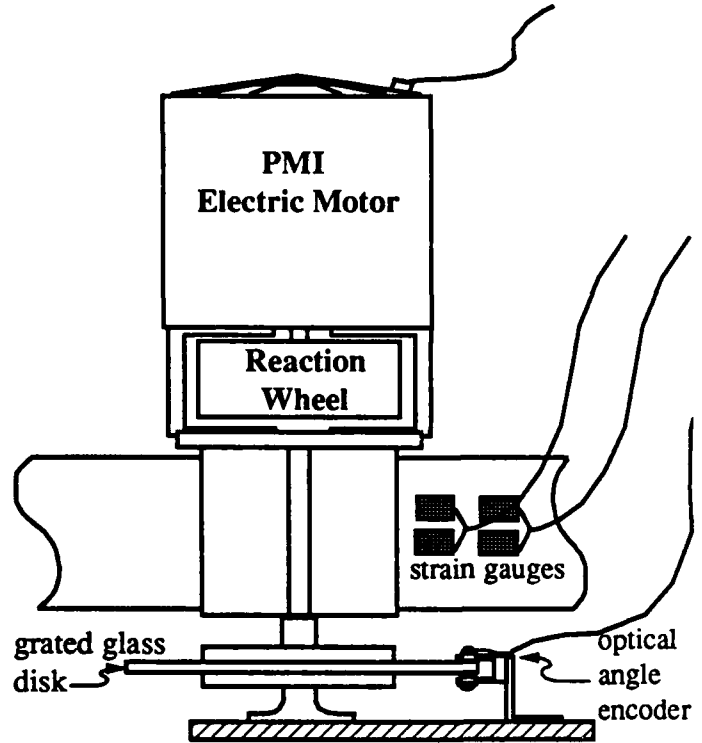


**Figure 3. System Functional Block Diagram**

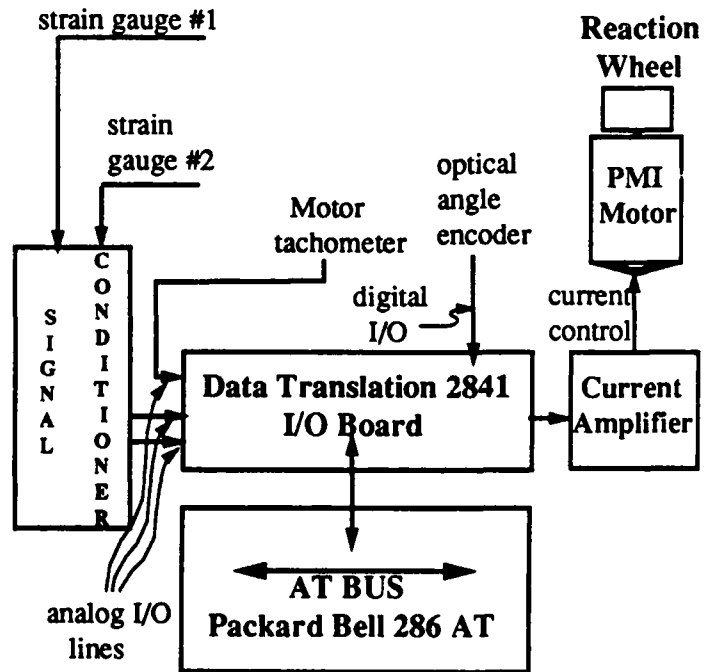


Figure 4. Torque Shaped Rigid Body Maneuver

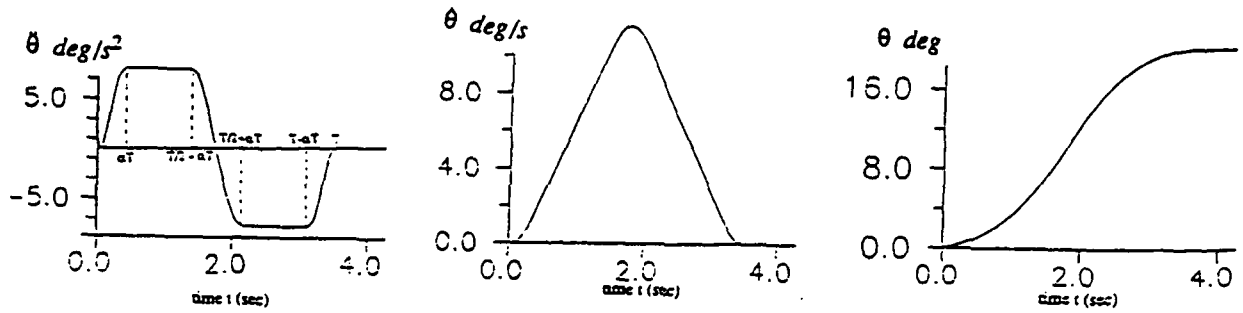


Figure 5. Rigid Body Maneuver vs. Saturation Torque and Shape Parameter

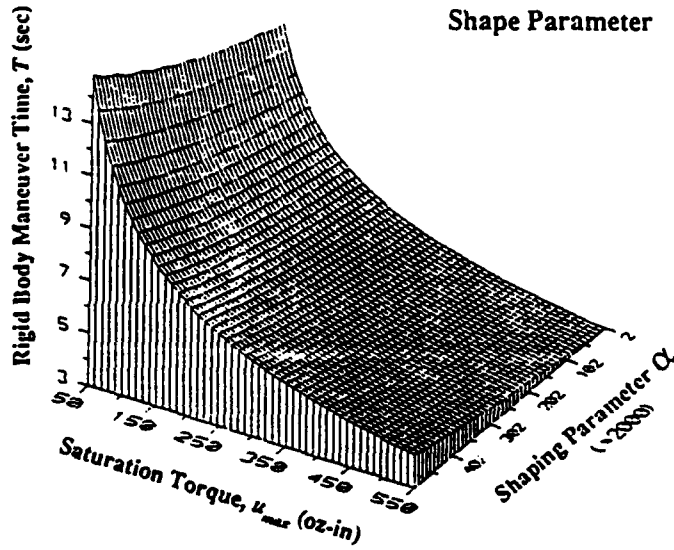


Figure 6. Flexible Body Residual Vibration Energy vs. Saturation Torque and Shape Parameter

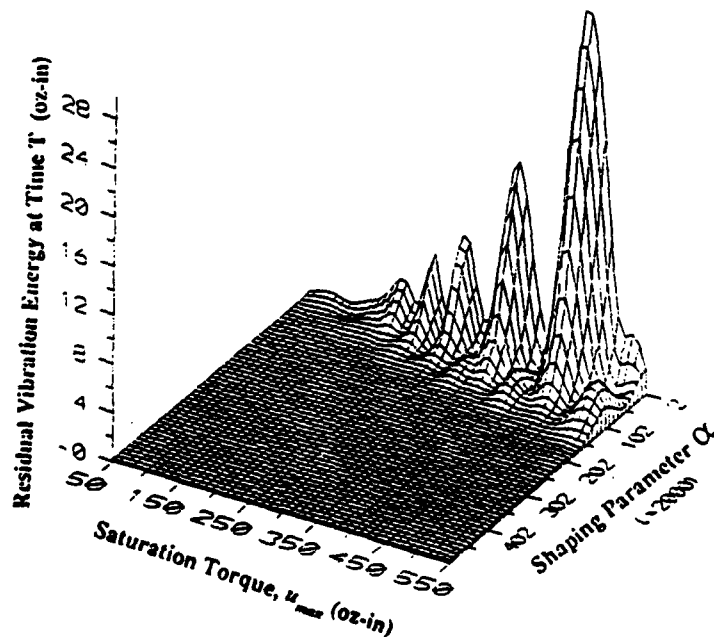


Figure 7. Boundary of the Liapunov-Stable Tracking Region vs. Saturation Torque and Shape Parameter

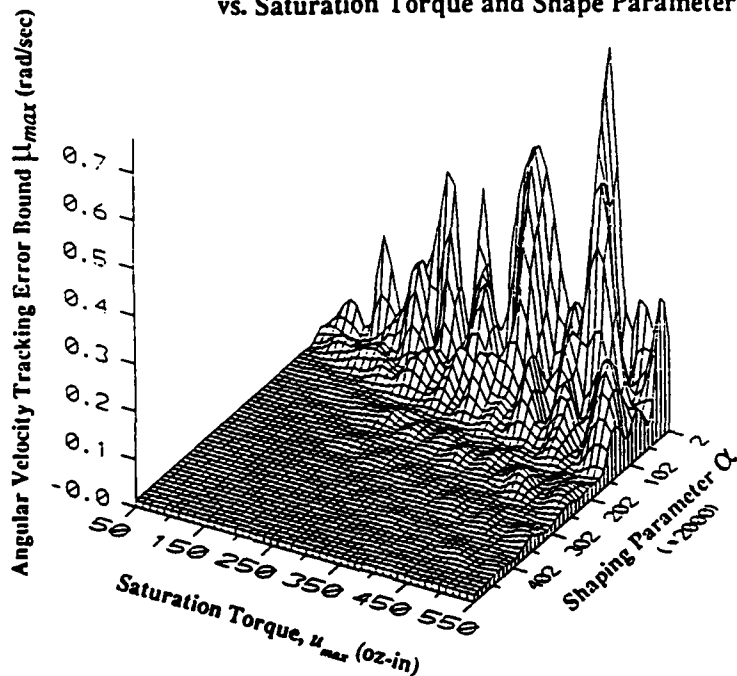


Figure 8. Simulated Open- and Closed-loop  $40^\circ$  Maneuver with Disturbances

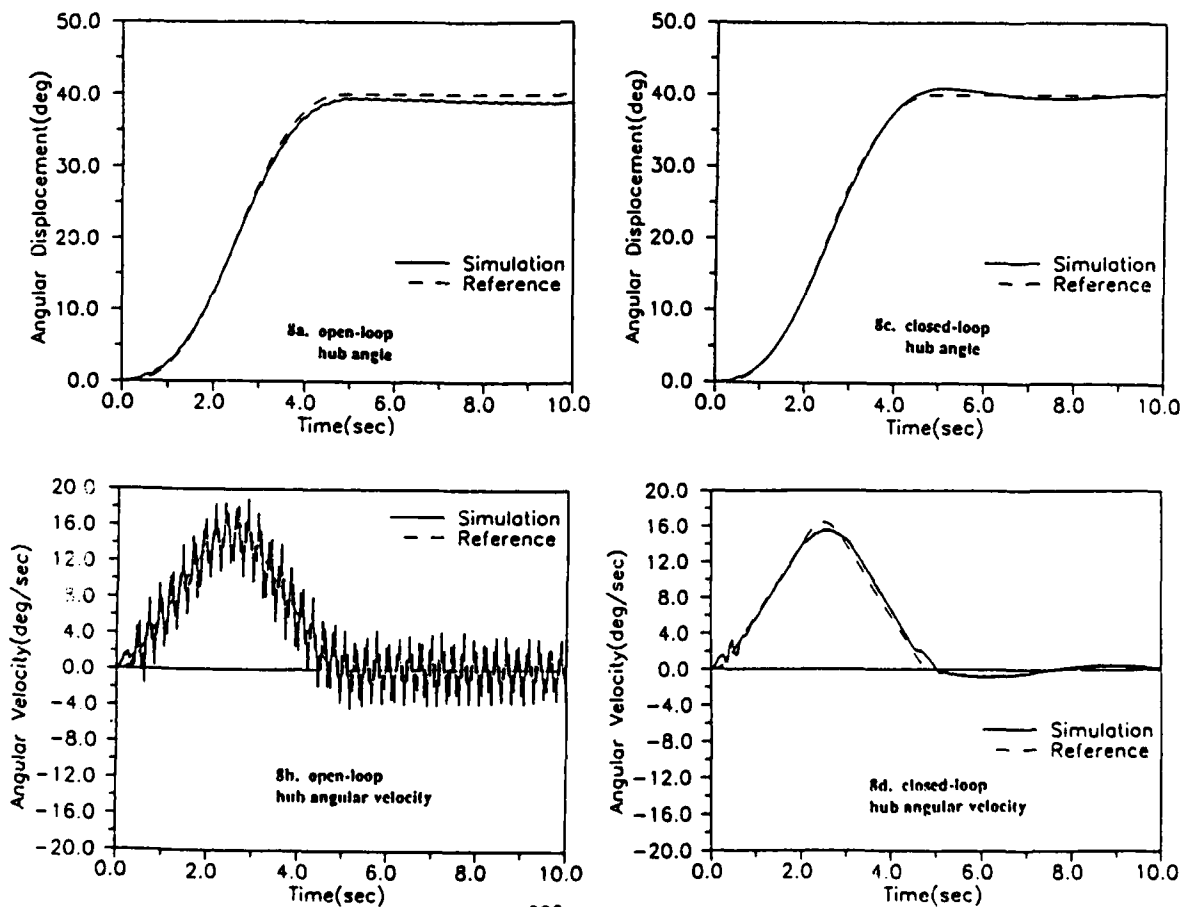


Figure 9. Experimental Results: Control Law I

control gains:  $g_1 = 600 \text{ oz-in/rad}$ ,  $g_2 = 800 \text{ oz-in/rad/s}$ ,  $g_3 = 0$

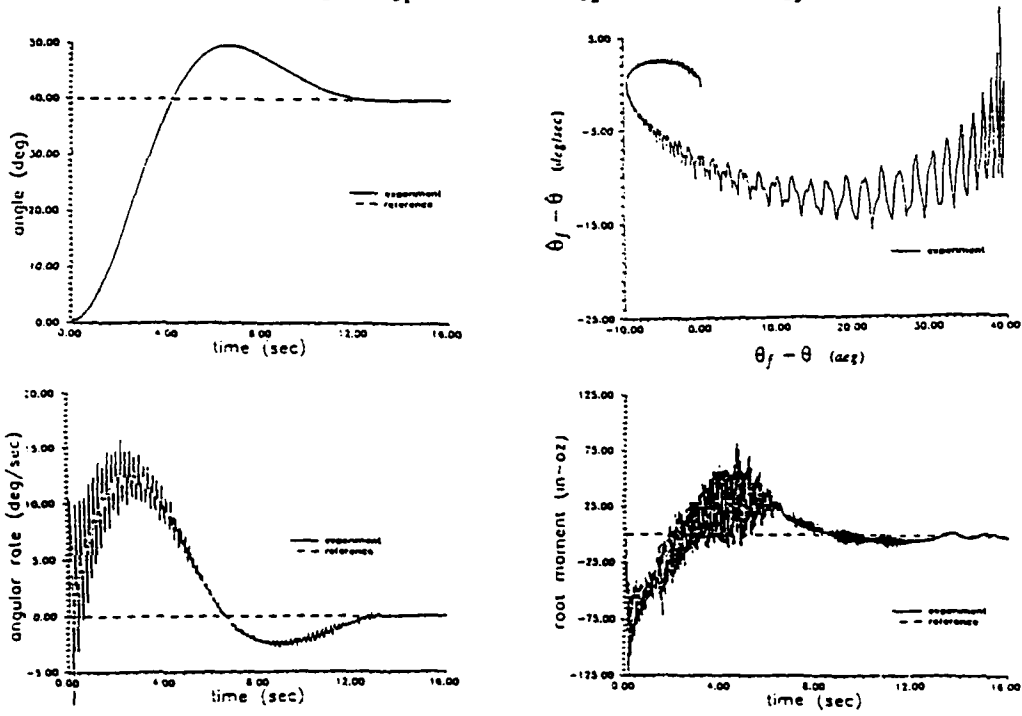
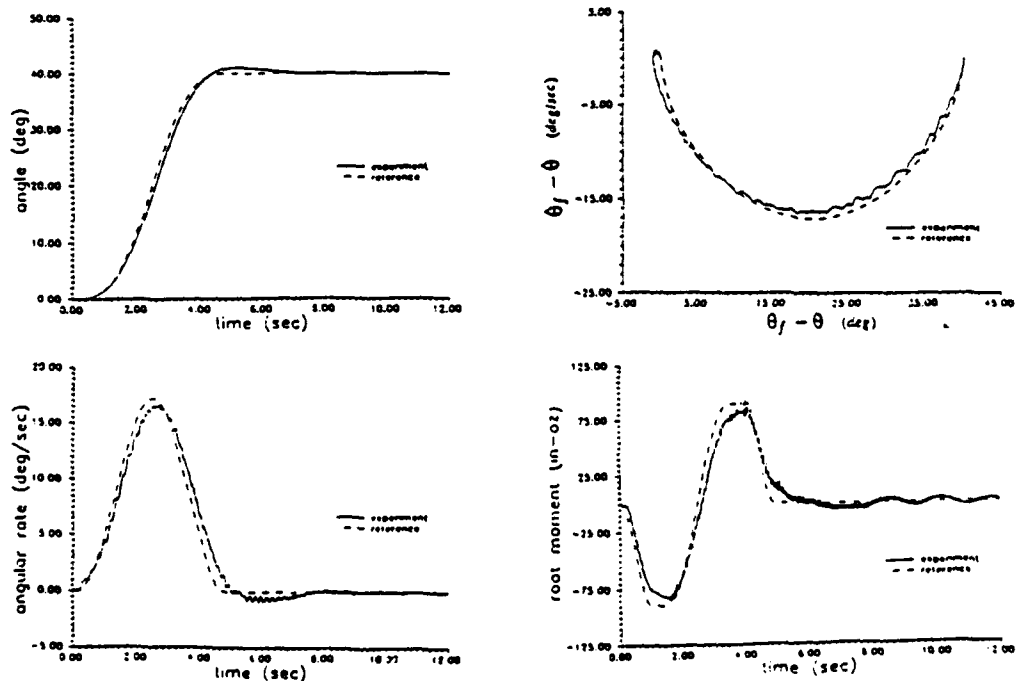


Figure 10. Experimental Results: Control Law II

torque shape parameter:  $\alpha = 0.2$ , control gains:  $g_1 = 600 \text{ oz-in/rad}$ ,  $g_2 = 800 \text{ oz-in/rad/s}$ ,  $g_3 = 0$



## ATTACHMENT 2

### Stable Maneuver Control Laws for Distributed Parameter Systems

*J. L. Junkins   Z. H. Rahman   H. Bang*

Department of Aerospace Engineering  
Texas A&M University  
College Station, Texas 77843

*a preprint of a paper presented to the*

*International Conference on Dynamics of Flexible Structures in Space*

*Cranfield Institute of Technology  
Cranfield, Bedford, UK  
May, 1990*

*to appear in the proceedings published by  
Computational Mechanics Publications*

## Stable Maneuver Control Laws for Distributed Parameter Systems

*J. L. Junkins   Z. H. Rahman   H. Bang*  
*Texas A&M University*  
*College Station, Texas 77843*

### Abstract

An approach for designing globally stable feedback control laws for maneuvers of distributed parameter structural systems is presented. Analytical and experimental results are discussed which support the practical merit of this approach. The method accommodates known nonlinearities and applies to systems described by hybrid coupled sets of ordinary and partial differential equations. Liapunov stability can be established for a large family of distributed parameter systems without relying upon spatial discretization. We develop tracking-type control laws to suppress the departure of the system state from an a priori determined smooth target trajectory. The target trajectory may be chosen as an exact or as an approximate solution of the system equations of motion. This approach is used to generate a family of near-minimum-time feedback controllers which accommodates general "torque-shaping". We show how to establish path-type stability-in-the-large during the maneuver, in the sense that the motion is globally attracted to a small region near the target trajectory. The flexibility of this approach permits one to achieve a judicious compromise between near-minimum-time and competing performance indices such as levels of vibration during the maneuver, sensitivity to model errors, disturbances, and control implementation errors. The experimental results provide significant evidence supporting the practical value of this approach.

### I. Introduction

Considerable recent research has been directed toward the problem of maneuvering a flexible spacecraft. The present paper grew out of our recent study [1]. In [2], we present a fairly comprehensive treatment of this family of problems up through 1985. Other analytical and experimental investigations<sup>3-13</sup> have been carried out to evaluate: (i) feedback control laws based upon minimizing quadratic indices, (ii) near-minimum time, switching-type controllers, and (iii) implementation issues. The main configuration of interest in the present discussion is a hub-appendage structure similar to the configuration of the Vander Velde and He study<sup>13</sup>, however, we address

the use of variable torque actuation via a reaction wheel instead of on-off thrusters, and utilize Lyapunov control design approaches and establish stable tracking-type control laws for distributed parameter systems.

## II. Maneuvers and Vibration Control for Distributed Parameter Systems

With reference to Figures 1 - 3, we consider single-axis maneuvers of a rigid hub with four cantilevered flexible appendages. In [1], we present an analogous control law for nonlinear three dimensional maneuvers. In [3], Wie, et al develop similar globally stable laws for rigid body maneuvers. For the present discussion, we consider in-plane vibration and the appendages are assumed to be identical uniform flexible beams. We further invoke the Euler-Bernoulli assumptions of negligible shear deformation and distributed rotary inertia. Each beam is cantilevered rigidly to the hub and has a finite tip mass. All motion is restricted to the horizontal plane, and a control torque  $u(t)$  acting on the hub is the only external effect considered at this stage of the developments. We subsequently address rejection of disturbances and discuss generalizations to accommodate other modeling assumptions.

We are interested in a class of rest-to-rest maneuvers and under the above assumptions, we can show that the beams will deform in the anti-symmetric fashion (Figure 1) with the configuration's instantaneous mass center remaining at the hub's geometrical center. Due to the anti-symmetric deformation of the beams, we need concern ourselves only with the deformation  $y(x,t)$  of a single beam. We adopt the continuum viewpoint and avoid introducing spatial approximations in the application of Liapunov concepts; the resulting control law and stability arguments will therefore apply rigorously to the distributed parameter system. The hybrid system of ordinary and partial differential equations governing the dynamics of this system are

$$\begin{aligned}
 I_{hub} \frac{d^2 \theta}{dt^2} &= u + 4(M_o - S_o l_o) \\
 - (M_o - S_o l_o) &= \int_0^l \rho x \left( \frac{\partial^2 y}{\partial t^2} + x \frac{d^2 \theta}{dt^2} \right) dx + ml \left( l \frac{d^2 \theta}{dt^2} + \frac{\partial^2 y}{\partial t^2} \Big|_l \right) + HOT \\
 \rho \left( \frac{\partial^2 y}{\partial t^2} + x \frac{d^2 \theta}{dt^2} \right) + EI \frac{\partial^4 y}{\partial x^4} &= 0 + HOT
 \end{aligned} \tag{1}$$

where

$\rho$  is the assumed constant mass/unit length of the beams,

$EI$  is the assumed constant beam bending stiffness ,

$(M_o, S_o)$  denote bending moment and shear force, at the root of the beams,

$\theta$  denotes hub inertial rotation,

$m$  denotes the mass of the tip mass, and

$(l, l_o)$  denote the distance from the hub center to the beam tip and the hub radius.

We denote higher order terms by *HOT* to indicate other known linear and nonlinear effects (such as rotational stiffening, shear deformation, etc.). The most fundamental of the developments given here do not consider these higher order effects, however.

we selectively discuss these generalizations as well. The boundary conditions on Eqs. (1) are

$$\begin{aligned} \text{at } x = l_0: y(t, l_0) = \frac{\partial y}{\partial x} \Big|_{l_0} = 0 \\ \text{at } x = l: \frac{\partial^2 y}{\partial x^2} \Big|_l = 0, \quad \frac{\partial^3 y}{\partial x^3} \Big|_l = \frac{m}{EI} \left( l \frac{d^2 \theta}{dt^2} + \frac{\partial^2 y}{\partial t^2} \Big|_l \right) \end{aligned} \quad (2)$$

The total energy of the system (constant in the absence of control or disturbances) is:

$$\begin{aligned} 2E = I_{hub} \left( \frac{d\theta}{dt} \right)^2 \\ + 4 \left[ \int_{l_0}^l \rho \left( \frac{\partial y}{\partial t} + x \frac{d\theta}{dt} \right)^2 dx + \int_{l_0}^l EI \left( \frac{\partial^2 y}{\partial x^2} \right)^2 dx + m \left( l \frac{d\theta}{dt} + \frac{\partial y}{\partial t} \Big|_l \right)^2 \right] \end{aligned} \quad (3)$$

Motivated by the recent work of Fujii<sup>5</sup> and Vadali<sup>9</sup>, and in view of the energy integral of the open loop system, we investigate the Liapunov function

$$\begin{aligned} 2U = a_1 I_{hub} \dot{\theta}^2 + a_2 (\theta - \theta_f)^2 \\ + 4a_3 \left[ \int_{l_0}^l \rho \left( \frac{\partial y}{\partial t} + x \dot{\theta} \right)^2 dx + \int_{l_0}^l EI \left( \frac{\partial^2 y}{\partial x^2} \right)^2 dx + m \left( l \dot{\theta} + \frac{\partial y}{\partial t} \Big|_l \right)^2 \right] \end{aligned} \quad (4)$$

where the positive weighting coefficients  $a_i$  are introduced to allow relative emphasis upon the three sets of contributors to the "error energy" of the system. We anticipate that only two of these weight parameters really matter, since we can scale Eq. (4) by an arbitrary constant without changing the location of the global minimum. Notice that the open loop system energy integral of Eq. (3) does not depend upon the rigid body displacement coordinate  $\theta$ . In addition to introducing weights on subsets of the system energy, to construct a meaningful Lyapunov function [Eq. (4)] for the closed loop system, we have modified the open loop energy integral by adding the second term  $a_2 (\theta - \theta_f)^2$  to make the desired final state

$$(\theta, \dot{\theta}, y(x,t), \frac{\partial y(x,t)}{\partial t})_{desired} = (\theta_f, 0, 0, 0)$$

be the global minimum of  $U$ . It is obvious by inspection that the logical requirement that  $a_i > 0$  guarantees that  $U \geq 0$ , and that indeed the global minimum of  $U=0$  occurs only at the desired state. Differentiation of Eq. (4), substitution of the equations of motion (Eqs. (1), (2)), and some calculus leads to

$$\dot{U} = \frac{dU}{dt} = \dot{\theta} \left[ a_1 u + a_2 (\theta - \theta_f) + 4(a_3 - a_1)(l_0 S_0 - M_0) \right] \quad (5)$$

Since we require that  $\dot{U} \leq 0$  to guarantee stability, we set the [ ] term to  $-a_4 \dot{\theta}$  and this leads to  $\dot{U} = -a_4 \dot{\theta}^2$  and the control law

$$u = -\frac{1}{a_1} \left[ a_2 (\theta - \theta_f) + a_4 \dot{\theta} + 4(a_3 - a_1)(l_0 S_0 - M_0) \right] \quad (6)$$

or, we see that the following *linear, spatially discrete* output feedback law globally stabilizes this distributed parameter system:

$$u = - [g_1 (\theta - \theta_f) + g_2 \dot{\theta} + g_3 (l_0 S_0 - M_0)]; \quad (7)$$

*with  $g_1 \geq 0$ ,  $g_2 \geq 0$ ,  $g_3 \geq -4$ , for global stability.*

This control law is elegant. Notice that controllers based upon this output feedback law are easy to implement since no state estimation is required. The root shear and bending moment can be measured by conventional strain gauges. The value and sign of the shear/moment feedback gain  $g_3 = 4(a_3 - a_1)/a_1$  depends upon whether we wish to emphasize dissipation of the beam energy (for  $a_3 > a_1$ ), or the motion of the hub (for  $a_3 < a_1$ ), as is evident from Eq. (4). Note  $\dot{U} = -a_4 \dot{\theta}^2$  is only negative semi-definite, since it is not an explicit function of the subset of state variables  $(\theta, y(x,t), \frac{\partial y(x,t)}{\partial t})$ ; the stability arguments therefore implicitly depend upon the truth that all infinity of modes of motion of this structure, under the assumption of anti-symmetric deflections, have generally non-zero hub angular velocity ( $\dot{\theta}$ ).

It is of significance that the linear feedback law of Eq. (7) maintains its globally stabilizing character even when the Euler/Bernoulli assumptions are relaxed to include additional linear and nonlinear effects; in particular, closed loop stability is maintained when we include the following effects neglected above: rotational stiffening, coriolis kinematic coupling terms, aerodynamic drag, shear deformation, beam rotary inertia, and finite rotational inertia of the tip mass. The verification of these truths requires appropriate modifications of the kinetic and potential energy functions, and of course, the differential equations of motion must be generalized consistently. *In short, global stability of the system using the simple linear control law of Eq. (7) has been found very forgiving of modeling assumptions and therefore modeling errors.*

On the other hand, the overall performance measures (time constants, required energy, rms output errors, etc.) of the system versus our simulations are generally not as forgiving as the most fundamental performance measure (stability). While we can guarantee stability for a large family of model errors, it should be apparent that *performance predictions are generally very sensitive to modeling errors.* With appropriate system modeling and selection of the feedback gains, however, we have found numerically and experimentally, that this feedback law works well over finite regions of the state and gain space, and in the presence of typical model errors.

While the constant gain linear feedback works well for terminal pointing and vibration suppression, we have found it to be a poor law for carrying out both large angle maneuvers and terminal pointing/vibration suppression. In fact, it is evident from both analytical and experimental studies that gain scheduling is needed to use the linear feedback law of Eq. (7) to efficiently control both the large maneuvering motions and the small terminal motions. This is because the large gains required for

effective vibration suppression and disturbance rejection near the target state typically differ by several orders of magnitude from the smaller ones needed far from the target state (i., e., large gains appropriate for terminal vibration suppression, when used during a large angle maneuver typically result in actuator saturation and significant  $\theta$  overshoots). To obtain a control law more appropriate for large angle maneuvers with vibration suppression, we can modify the above developments; a stable tracking-type feedback control law is presented in the following discussion.

### III. Near-Minimum-Time Maneuvers of Distributed Parameter Systems

Consider first the near-minimum-time maneuver of a rigid body. We know that the strict minimum time control is a bang-bang law<sup>2</sup>, which for the rest-to-rest maneuver-to-the-origin case, saturates negatively during the first half of the maneuver and positively during the last half of the maneuver. From an implementation point of view, the instantaneous switches of bang-bang control are often troublesome for several reasons:

- (i) no torque-generating device exists which can switch instantaneously,
- (ii) when generalized and applied to flexible structures, the discontinuous class of controls typically excite poorly modeled higher frequency modes, and
- (iii) the predicted (model-derived) switch times and the predicted response of the actual system are usually sensitive to modeling errors.

As a consequence, we find that bang-bang control of flexible body dynamics usually lacks robustness with respect to modeling errors, especially when one attempts to control several modes of vibration in addition to the large angle motion.

Recently, an attractive family of controllably smooth approximations of the sign (*sgn*) function which arises in time-optimal control has been introduced. The smoothed control approximations presented in Ref. [1, 8] has been studied in the context of near-minimum-time maneuvers of flexible bodies. These studies motivate the use of a smoothly switching family of controls for single axis maneuvers. The approach involves applying a judiciously shaped torque profile to a rigid body to provide a nearly achievable target trajectory for the flexible body maneuver. One such smooth family of rigid body maneuvers for near minimum time control is generated as follows:

$$I \ddot{\theta} = u = \pm u_{max} f(\Delta t, t_f, t) \quad (8)$$

where

$u_{max}$  is the saturation torque,

$t_f$  is the maneuver time, we choose the + sign if  $\theta_f > \theta_o$ ,

$$t_1 = \frac{t_f}{2} - \Delta t, \quad t_2 = \frac{t_f}{2} + \Delta t, \quad t_3 = t_f - \Delta t,$$

$\Delta t$  is the rise time, and the smooth torque shape function adopted is

$$f(\Delta t, t_f, t) \begin{cases} = \left(\frac{t}{\Delta t}\right)^2 [3 - 2\left(\frac{t}{\Delta t}\right)], & \text{for } 0 \leq t \leq \Delta t \\ = 1, & \text{for } \Delta t \leq t \leq t_1 \\ = 1 - 2\left(\frac{t-t_1}{2\Delta t}\right)^2 [3 - 2\left(\frac{t-t_1}{2\Delta t}\right)], & \text{for } t_1 \leq t \leq t_2 \\ = -1, & \text{for } t_2 \leq t \leq t_3 \\ = -1 + \left(\frac{t-t_3}{\Delta t}\right)^2 [3 - 2\left(\frac{t-t_3}{\Delta t}\right)] & \text{for } t_3 \leq t \leq t_f \end{cases}$$

Adopting the positive sign, Eq. (8) integrates to yield

$$\dot{\theta}(t) = \dot{\theta}_o + \frac{u_{max}}{I} \int_{t_o}^t f(t_1, t_f, \tau) d\tau \quad (9)$$

$$\theta(t) = \theta_o + \dot{\theta}_o(t-t_o) + \frac{u_{max}}{I} \int_{t_o}^t \int_{t_o}^{\tau_1} f(t_1, t_f, \tau_2) d\tau_2 d\tau_1$$

The integrations indicated in Eq. (9) can be carried out in terms of elementary functions which are not presented here for brevity. Figure 4 shows the maneuver resulting from these integrations for a typical selection of parameters. For rest-to-rest maneuvers, we can impose the boundary conditions

$$\begin{aligned} \text{at } t_o = 0: \quad & \theta(0) = \theta_o, \quad \dot{\theta}(0) = 0; \\ \text{at } t_f = T: \quad & \theta(T) = \theta_f, \quad \dot{\theta}(T) = 0 \end{aligned} \quad (10)$$

and upon carrying through the integrations of Eqs. (9), we find the useful relationship

$$\theta_f - \theta_o = \frac{u_{max}}{I} \left[ \frac{1}{4} - \frac{1}{2}\alpha + \frac{1}{10}\alpha^2 \right] T^2, \quad \text{with } t_1 = \Delta t = \alpha T, \quad 0 < \alpha < \frac{1}{4} \quad (11)$$

$$\text{or } T = \left[ \frac{I(\theta_f - \theta_o)}{u_{max} \left( \frac{1}{4} - \frac{1}{2}\alpha + \frac{1}{10}\alpha^2 \right)} \right]^{1/2} \quad (12)$$

In Eq. (12) we have the explicit rigid body tradeoff between torque shaping ( $\alpha$ ),

maneuver time ( $T$ ), maneuver angle ( $\theta_f - \theta_o$ ), and maximum angular acceleration ( $u_{max} / I$ ). Obviously, Eq. (11) can be inverted for any of these as a function of the remaining parameters. If we set  $\alpha = \Delta t / T = 0$ , of course, we obtain the special case result ( $T^2 = 4I(\theta_f - \theta_o) / u_{max}$ ) expressing the well-known square-root relationship between the minimum time, maneuver angle, inertia, and saturation torque for bang-bang control.

Figure 5 shows the rigid body maneuver time ( $T$ ) versus  $\alpha$  and  $u_{max}$ . Notice that the maneuver time is strongly dependent upon  $u_{max}$ , but varies much less as a function of  $\alpha$ . However, we find when the torque  $u_{ref}(t) = u_{max} f(\alpha T, T, t)$  of Eq. (8) is applied to a flexible body, the reverse is true vis-a-vis the residual vibration energy at time  $T$ . To illustrate this point, we approximated the solution of Eqs. (1) by introducing a Galerkin expansion (of the beam deflection in terms of the first ten clamped-free cantilever mode shapes times time varying generalized coordinates). The forced response of the resulting 20th order system was judged adequately converged. Using this solution, we applied the same family of torques used for the rigid body results of Figure 5 and computed the flexible body open loop response for each choice of  $\alpha$  and  $u_{max}$ . Figure 6 shows the total energy of the flexible body system at time  $T$  for this same family of maneuvers. As is evident, the vibration energy vanishes for sufficiently small  $u_{max}$  and is significantly reduced for any given  $u_{max}$  by increasing  $\alpha$ . Notice the triangular region (large  $\alpha$ , small  $u_{max}$ ) for which the vibration energy at time  $T$  is negligible. We will subsequently see that measures of the largest errors with which the closed-loop-controlled flexible body system can track the rigid body maneuvers of Figure 5 behave in a qualitatively similar way.

The above results and those of Ref. [1, 6, 7, 8] support the intuitively obvious truth that applying judiciously "smoothed bang-bang" open-loop controls such as Eq. (8) to generate maneuvers of a flexible body results in moderate structural vibration, for sufficiently slow and smooth maneuvers (small  $u_{max}$  and large  $\alpha$ ). Of course unmodeled disturbances, control implementation errors, and model errors negate some of these apparent gains, especially without feedback. For relatively small penalties in maneuver time<sup>1,7</sup>, actual torque-shaped maneuvers enjoy several orders of magnitude reduction in residual vibration, even without feedback, although some offset in rigid body position usually results. Thus overall maneuver time, including vibration arrest, can be reduced dramatically by modest torque shaping, as compared to simply using bang-bang control augmented by vibration suppression. Also of significance, we find that it is usually desirable to select the torque profile (e.g.,  $u_{max}$ ,  $\alpha$ , etc.) to consider the sensor and actuator dynamics and thereby make the commanded torque history more nearly physically achievable. More generally, however, we can use any reference maneuver (not necessarily a rigid body torque-shaped maneuver).

Suppose we adopt a reference open-loop rigid body maneuver denoted by the subscript *ref* as  $\{\theta_{ref}(t), \dot{\theta}_{ref}(t), \ddot{\theta}_{ref}(t) = u_{ref} / I\}$  and satisfying Eqs. (8-12). Note  $I$  is the undeformed moment of inertia, and we have implicitly selected the torque shaping parameters  $\alpha$ ,  $u_{max}$ , and thereby established the corresponding target

maneuver time  $T$  from Eq. (12) for specified initial and final angle. Motivated by the issues discussed above and the quadratic regulator perturbation feedback controllers in refs. [2,11,13], we hypothesize the following structure for the control law

$$u = u_{ref}(t) - [g_1 (\theta - \theta_{ref}) + g_2 (\dot{\theta} - \dot{\theta}_{ref}) + g_3 ((I_o S_o - M_o) - (I_o S_o - M_o)_{ref})] \quad (13)$$

where the root moment for the reference (rigid body) motion is proportional to the angular acceleration:  $(I_o S_o - M_o)_{ref} = [\rho(l^3 - l_o^3)/3 + m l^2] \ddot{\theta}_{ref}(t)$ .

We wish to gain insight on the stability characteristics of the flexible body's closed-loop departure dynamics [from the target (*ref*) rigid body motion (for  $t < T$ ), and from the fixed target state (for  $t \geq T$ )], and we will provide an analytical justification for the tracking control law of Eq. (13). Let us denote by the subscript  $r$  the state variables along the open-loop flexible body solution of Eqs. (1) when driven by the torque  $u_{ref}(t)$  of Eqs. (8-12). The instantaneous displacement of the open-loop flexible body solution from the open loop rigid body motion is denoted  $\Delta() = ()_r - ()_{ref}$ ; for example,  $\Delta\theta(t) = \theta_r(t) - \theta_{ref}(t)$ . Variables without subscripts represent the actual instantaneous closed-loop controlled solution variables. Consider the candidate error energy Liapunov function

$$\begin{aligned} 2U = & a_1 I_{hub} (\dot{\theta} - \dot{\theta}_r)^2 + a_2 (\theta - \theta_r)^2 \\ & + 4a_3 \left[ \int_{l_o}^l \rho \left[ \left( \frac{\partial y}{\partial t} - \frac{\partial y_r}{\partial t} \right) + x(\theta - \theta_r) \right]^2 \right. \\ & \left. + \int_{l_o}^l EI \left( \frac{\partial^2 y}{\partial x^2} - \frac{\partial^2 y_r}{\partial x^2} \right)^2 dx + m \left[ l(\theta - \theta_r) + \left( \frac{\partial y}{\partial t} \Big|_l - \frac{\partial y_r}{\partial t} \Big|_l \right) \right]^2 \right] \end{aligned} \quad (14)$$

Assuming the actual control is some general, to-be-determined  $u(t)$ , and that the actual motion satisfies Eqs. (1), we have investigated the time derivative of  $U$  of Eq. (14) and found that it is given by the following equation

$$\dot{U} = a_1 (\dot{\theta} - \dot{\theta}_r) \left[ u - u_{ref} + \frac{a_2}{a_1} (\theta - \theta_r) + 4 \frac{a_3 - a_1}{a_1} [(I_o S_o - M_o) - (I_o S_o - M_o)_r] \right] \quad (15)$$

Analogous to the logic leading to Eq. (5), we see that we could determine a globally stabilizing  $u(t)$  by setting the bracketed term to a positive quantity  $g_2$  times  $-(\dot{\theta} - \dot{\theta}_r)$  (i. e., this makes  $\dot{U}$  a negative definite function of the error in hub angular velocity), and gives the globally stabilizing control law

$$u = u_{ref}(t) - [g_1 (\theta - \theta_r) + g_2 (\dot{\theta} - \dot{\theta}_r) + g_3 ((I_o S_o - M_o) - (I_o S_o - M_o)_r)] \quad (16)$$

with  $\dot{U} = -a_1 g_2 (\theta - \theta_r)^2$  and we introduced the gain definitions as  $g_1 \equiv a_2/a_1$ , and  $g_3 \equiv 4(a_3 - a_1)/a_1$ . Notice, to guarantee global stability, that  $g_1$  and  $g_2$  must be positive, but as before  $g_3$  must be greater than  $-4$ . The only difficulty with this control law is that it requires pre-computing the flexible body solution, which is generally infeasible in an on-line implementation. Obviously, we'd prefer a tracking law which requires a much simpler (e., g., rigid body) maneuver to be pre-computed. Let us pursue this objective. Since Eq. (15) holds for an arbitrary  $u(t)$ , we introduce instead of Eq. (16) the control law of Eq. (13), and investigate its stability characteristics. Using the notation  $\Delta O = O_r - O_{ref}$ , Eq. (15) simplifies to

$$\dot{U} = -a_1 (\theta - \theta_r) \{ g_2 (\theta - \theta_r) + [g_1 \Delta \theta + g_2 \Delta \dot{\theta} + g_3 \Delta(l.S. - M.)] \} \quad (17)$$

A sufficient condition characterizing the region where  $\dot{U} \leq 0$  is the dominance of the first term in the  $\{ \}$  of Eq. (17), this gives the inequality

$$|\theta - \theta_r| > \frac{1}{g_2} |g_1 \Delta \theta + g_2 \Delta \dot{\theta} + g_3 \Delta(l.S. - M.)| \equiv \mu \quad (18)$$

It is further apparent that the  $\Delta$  quantities on the right hand side of Eq. (18) are finite and (pre-) computable differences between the open loop flexible and rigid body motions, thus an upper bound can be established directly by a one-time family of a priori simulations of the two open loop motions, and using a particular set of feedback gains. Equation (18) thus determines an angular velocity boundary region. Note that large motions are globally attracted to the region bounded by  $\mu$  of Eq. (18). Thus the control law of Eq. (13) is almost globally stabilizing, and the only region where asymptotic stability cannot be guaranteed is a boundary layer region near the target trajectory. Furthermore, note the right hand side of Eq. (18) is essentially a weighted measure of how nearly the target trajectory satisfies the flexible body equations of motion; further note that judicious choice of the torque shaping parameters defining the target trajectory can result in  $\mu$  being arbitrarily small.

A bounded-input/bounded-output viewpoint of stability can also be considered, based upon the departure motion differential equations obtain by differencing Eqs. (1) evaluated at each instant along the flexible body closed loop trajectory and along the flexible body open loop  $O_r$  motion. Upon formulating these equations, we find departure motion is governed by an otherwise asymptotically stable system of differential equations forced by the known  $\Delta( )$  terms which appear in Eqs. (18). Since these forcing terms can be bounded by direct calculation, the resulting departure motion can also be bounded. Since the actual numerical bounds on the  $\Delta$  quantities can be made arbitrarily small (depending upon how nearly the user defined reference trajectory is made to satisfy the open loop equations of motion), we have a very attractive theoretical and practical situation vis-a-vis stability of the closed loop tracking motion. *We see that the closed-loop motion is globally attracted to the controllably small region near the target trajectory which violates the inequality of Eq. (18), and considering the motions within this small region, we have bounded-input, bounded-output stability.*

The above discussion can probably be generalized for any smooth target trajectory, but we find that it is attractive to use a torque-shaped rigid body reference trajectory, such as Eqs. (8)-(12). Note that Eqs. (8)-(13) result in a  $C^1$  continuous transition:

$\{u_{ref}(t), \theta_{ref}(t), \dot{\theta}_{ref}(t), M_{o_{ref}}(t), S_{o_{ref}}(t)\} \Rightarrow \{0, \theta_f, 0, 0, 0\}$  as  $t \Rightarrow T$ ; so that for  $t > T$ , only the three feedback terms of Eq. (13) are contributing to the terminal fine-pointing/vibration arrest control. Thus the controls blend continuously from the large angle tracking law into a constant gain controller (for  $t > T$ ) identical to the globally stable fixed point output feedback case of Eq. (7).

#### IV. Simulated Results for the Large Angle Maneuvers Experiment

Returning to the family of  $40^\circ$  open loop maneuvers used to generate the energy surface of Figure 6, we computed the velocity tracking bound  $\mu$  for Liapunov stability [as given by Eq. (18)] and found the maximum value ( $\mu_{max}$ ) of  $\mu(t)$  along each trajectory. Figure 7 displays this worst case tracking bound (maximum value of  $\mu$ ) surface  $\mu_{max}(\alpha, u_{max})$  over the same  $(\alpha, u_{max})$  region used to generate Figures 5, 6. The closed-loop tracking error bound has a roughly analogous behavior to the open-loop residual vibration energy surface of Figure 6. Recall that outside the region bounded by the inequality of Eq. (18), we have guaranteed Liapunov stability, using the control law of Eq. (13) and the reference rigid body torque given by Eqs. (8)-(12). From Figure 6, it is clear that sufficiently small  $u_{max}$  and large  $\alpha$  result in arbitrarily small tracking errors, but the (small  $\alpha$ , large  $u_{max}$ ) near-bang reference maneuvers cannot be tracked as accurately. It is easy to see how a family of candidate  $(\alpha, u_{max})$  designs can be found which satisfy specified inequalities on maneuver times, tracking errors, and residual vibration energy, by direct examination of the surfaces of Figures 5-7.

Our experiments with simulations (and in the actual hardware implementations presented below and in [1, 6, 7] support the conclusion that we can use these surfaces (together with disturbance rejection simulations to select the reference trajectory and tune the feedback gains) to establish a large family of feasible designs. Prior to discussing our experimental results, we present some further simulations to show state and control variables histories along typical trajectories of underlying the above surfaces. We include in these simulations the effects of disturbance torques, to illustrate the effectiveness of the controls in the presence of unmodeled effects. Table 1 summarizes the physical parameters and a detailed hardware description of the maneuver experiment is given in Ref. [1]. For simplicity, we consider here only the case of a  $40^\circ$  rest-to-rest maneuver, and set  $u_{max} = 400$  oz-in for all cases.

For our computational and experimental studies, we consider two control laws, namely the output feedback law (Control Law I) of Eq. (7), and the tracking-type feedback control law (Control Law II) of Eq. (13). While Control Law II could be used with an arbitrary reference trajectory, we elect to specifically investigate the torque-shaped rigid body trajectories of Eqs. (8)-(12). The torque-shaped open loop control history  $u_{ref}(t)$  is pre-computed (in a fraction of a second!) from Eqs. (8)-(12) and stored. Note that the boundary conditions of Eq. (10) are enforced by using Eq. (12) to compute the target trajectory maneuver time as a function of the maneuver angle, saturation torque, and torque-shape parameter.

We now discuss the simulation results using Control Law II, which obviously blends

into to Control Law I in the end game (for  $t \geq T$ ). In the experimental results, we report maneuvers carried out by both control laws. Both open loop (all  $g_i \equiv 0$ ) and closed loop time histories of selected variables are shown in Figures 8a-8d. On the left of Figure 8, we show the hub angle and angular velocity for the case of an open loop control and in the presence of substantial impulsive and quasi-random (5 oz-in, 1  $\sigma$ ) disturbance torques. It is evident that the disturbance torque history is significant vis-a-vis exciting substantial rigid body and flexural motions. On the right, we show the closed loop behavior of the system excited by the same disturbance torque history. The random component of this disturbance has been found to be typically pessimistic vis-a-vis our experimental hardware, however certain non-random, nonlinear effects associated with the bearing friction cause disturbances which are correlated in time and are not well represented by the present white noise model of the disturbance torques. In spite of the substantial disturbance torques (Figs. 8a-8b), it is evident that we obtain a near minimum time rigid body motion while effectively suppressing vibration (8c-8d). This fact was also confirmed by evaluation of the energy distribution in the first six modes.

## V. Experimental Results

In all of the experiments discussed below, we set the target final angle to  $40^\circ$  and  $u_{max} = 400$  oz-in. The values of the tracking gains ( $g_1, g_2, g_3$ ) and of the torque shape parameter ( $\alpha$ ) were assigned several feasible values values to demonstrate the effects of these upon the closed loop behavior of the system. Moderate bearing friction and aerodynamic damping were present in our experiments.

Figure 9 shows the system response for a Control Law I (the constant gain control law of Eq. (11)) maneuver with ( $g_1 = 600$  oz-in/rad,  $g_2 = 800$  oz-in/rad/sec, and  $g_3 = 0$ ). Since this initial position error is large, the maneuver starts from zero with an initial discontinuity to a large torque. For this gain selection, we see a large overshoot ( $\sim 10^\circ$ ) and significant structural vibration which settled around 12 seconds; the control was terminated at 16 seconds.

Control Law II leads to very attractive near-minimum-time maneuvers. One good set of gain settings and torque shape parameters leads to the results in Figure 10. The effect of using a smooth, judiciously shaped reference torque history is evident if one compares the output and control variable histories in Figure 10 with those of Figure 9. Law II produced much smaller overshoot ( $\approx 1.5^\circ$  vs  $\sim 10^\circ$ ), shorter settling time (6 sec. vs 12 sec.) and greatly reduced the severity of peak vibration. These results, especially when considered in conjunction with numerous other cases are reported in [1, 7, 8] are convincing evidence of the truth that Control Law II is a very versatile and highly effective way to incorporate open loop torque shape optimization with vibration suppression. The fact that a globally continuous control structure is implicit in this approach leads to minimal difficulties in realizing robust control laws; note the handoff from lare However, as previously reported in [1], we did encounter some practical difficulties in our experimental work. Firstly, the shear and bending moment measurements via strain gauges resulted in sufficiently noisy measurements that this feedback ( $g_3 \neq 0$ ) did not improve the controlled response over, for example

the results in Figure 10. Also, deriving the angular velocity estimate from the noisy angle encoder readout was difficult to accomplish with high precision, and as a consequence, we constructed a digital noise filter to process our angle encoder data and eliminate all of the frequency content above 10 Hz; this was necessary to avoid erroneous, phase lagged feedback which would otherwise disturb the higher frequency modes. This problem can be eliminated by investing in a more precise sensor to measure angular displacement and/or angular velocity.

Finally, our bearing presented us with some practical difficulties. Based upon mechanical tests and analysis of our bearing hardware, it is evident that interaction of the structure with the bearing accounts for the overwhelming source of unmodeled disturbances. The bearing friction/stiction model developed from our analysis [1] has the form

$$\tau_{\text{bearing}} = -c_1 \text{sign}(\dot{\theta}) - c_2 \dot{\theta} + \text{HOT} \quad (19)$$

where we find  $c_1 \sim 20$  oz-in and  $c_2 \sim 0.001$  oz-in/rad/sec. Thus the first (stiction) term of Eq. (19) dominates the bearing torque for moderate  $\dot{\theta}$  and is about 5% of the peak commanded torque of 400 oz-in. While we believe Eq. (19) models the bearing friction well, it is difficult to use this model to compensate for bearing friction in real time, since our estimated value of  $\dot{\theta}$  is uncertain due to angle encoder measurement noise. Thus if we modify our control using Eq. (19), the commanded discontinuity (near the estimated time  $\dot{\theta}$  changes sign) will not coincide exactly with the actual discontinuity; mis-timed compensation torque discontinuities can actually worsen the disturbance! While we experimented with several bearing friction compensation schemes, we ultimately decided to simply consider this an anticipated and well-modeled disturbance. Our simulations (such as the results shown in Figure 8) indicated our control approach could easily tolerate disturbances of this magnitude, and our successful experiments Figures 9, 10, and in [1], certainly confirm that our implemented control laws are robust in the presence of the actual disturbances.

## VI. Concluding Remarks

We have presented an approach to design of feedback control laws for large maneuvers of distributed parameter systems, and have conducted successful experiments. This approach establishes stable gain regions over which subsequent optimizations can be carried out with global stability guaranteed (to within model errors, of course). The formulation permits approximate imposition of actuator saturation constraints and a priori control shaping via user specification of a torque-shaped, optimized reference trajectory. The resulting tracking-type control law is shown to result in Liapunov stability in the sense that all trajectories are globally attracted to a small region near the reference trajectory. The tracking law automatically blends smoothly into a globally stable, constant gain, terminal output feedback controller. We believe this approach is much more attractive than gain scheduling, because the logical and implementation complications associated with discontinuous gain change ("handoff") logic can be avoided altogether. We have considered in detail the case of single axis maneuvers of a flexible body system and a particular family of torque-shaped, near-minimum-time rigid body reference trajectories. We demonstrated numerically the effects of torque shaping upon maneuver time and established a pre-computable bound on the size of region near the target trajectory in

which Liapunov-stable tracking cannot be guaranteed. We described hardware experiments which successfully implemented these ideas.

We have demonstrated the feasibility of our analytical formulations and experimental approach. We are optimistic that these ideas extend to a significant family of multi-axis maneuvers of multiple flexible body systems and the maneuver control problems associated with multiple body re-configuration, pointing/tracking, and deployment dynamics.

### VII. Acknowledgments

The authors are pleased to acknowledge the work of H. Fujii, S. R. Vadali, A. Das; their earlier research provided inspiration for this work. The support of the Air Force Office of Scientific Research (Contract F49620-87-C-0078) and A. K. Amos is appreciated. We also received support from the Texas Advanced Technology Program (Project 70110). We thank the following individuals for their contributions: T. C. Pollock for his contributions to all aspects of the design and development of the experiment hardware, Steve Morgan for identifying the structural parameters and for his assistance with the angle encoder, Johnny Hurtado for his assistance in carrying out the experiments, and Becky Masters for excellent support in preparing this manuscript.

### VIII. References

1. Junkins, J. L., Rahman, Z., and Bang, H., "Near-Minimum-Time Maneuvers of Flexible Vehicles: A Liapunov Control Law Design Method," AIAA Aerospace Sciences Meeting, Reno, Nevada, January, 1990, submitted for publication, AIAA Journal of Guidance, Control, and Dynamics.
2. Junkins, J. L. and Turner, J. D., Optimal Spacecraft Rotational Maneuvers, Elsevier, 1986, Amsterdam.
3. Wie, B., Weiss, H., and Araposthathis, "Quaternion Feedback for Spacecraft Eigenaxis Rotations," AIAA Journal of Guidance, Control, and Dynamics, Vol 12, No. 3, Mar-Jun, 1989, pp 375-380.
4. Juang, J. N., Horta, L. G., and Robertshaw, H. H., "A Sewing Control Experiment for Flexible Structures", Proc. of the 5th VPI & SU Symposium on Dynamics and Control of Large Structures, pp 547-551, Virginia Polytechnic Institute, Blacksburg, VA, June 12-16, 1985.
5. Fujii, H., Ohtsuka, T. and Udou, S., "Mission Function Control for Slew Maneuver Experiment", a preprint, to appear in the AIAA Journal of Guidance, Control, and Dynamics.
6. Junkins, J., Rahman, Z., Bang, H., and Hecht, N., "Near-Minimum Time Feedback Control of Distributed Parameter Systems: A Liapunov Control Law Design Method," 7th VPI & SU Symp. on Dyn. & Ctrl. of Large Str., proc. to appear.
7. Rahman, Z., Junkins, J. L., Pollock, T. C., and Bang, H., "Large Angle Maneuvers with Vibration Suppression: Analytical and Experimental Results," 7th VPI & SU Symp. on Dyn. & Ctrl. of Large Str., proc. to appear.
8. Thompson, R. C., Junkins, J. L., and Vadali, S. R., "Near-Minimum-Time Open-Loop Slewing of Flexible Vehicles," AIAA Journal of Guidance, Control, and Dynamics, Vol 12, No. 1, Jan-Feb, 1989, pp 82-88.
9. Vadali, S. R., "Feedback Control of Flexible Spacecraft Large Angle Maneuvers Using Liapunov Theory", paper No. 1674, Proceedings of the 1984 Amer. Ctrls. Conf., pp 1674-1678, IEEE, 1984.
10. Byers, R. M., Vadali, S. R., and Junkins, J. L., "Near-Minimum-Time Closed Loop Slewing of Flexible Spacecraft," to appear, AIAA Journal of Guidance, Control and Dynamics.
11. Meirovitch, L. and Quim, R., "Maneuvering and Vibration Control of Flexible Spacecraft," Journal of the Astronautical Sciences, Vol 35, No. 3, July-Sept., 1987, pp 301-328.
12. Singh, G., Kabamba, P., and McClamroch, N., "Planar Time Optimal Slewing Maneuvers of Flexible Spacecraft", to appear, AIAA Journal of Guidance, Control, and Dynamics.
13. Breakwell, J. A., "Optimal Feedback Control for Flexible Spacecraft", AIAA Journal of Guidance, Control, and Dynamics, Vol 4, No. 5, Sept-Oct 1981, pp 472-479.
14. VanderVelde W. and He, J., "Design of Space Structure Control Systems Using On-Off Thrusters," AIAA Journal of Guidance, Control, and Dynamics, Vol. 6, Jan-Feb., 1983, pp 759-775.

**Table 1. Hub/Appendage Configuration Parameters**

**Hub & Appendages**

Total System Inertia, $I$	2128 [oz - sec <sup>2</sup> - in]
Hub Center to Gage Center, $l_o$	5.5470 [in]
Hub Center to Tip Mass, $l$	51.07 [in]
Tip Mass, $m$	0.15627 [oz - sec <sup>2</sup> /in]
Appendage Modules of Elasticity, $E$	161.6 [million oz/in <sup>2</sup> ]
Inertia of Bending Section, $I$	.000813 [in <sup>4</sup> ]
Density of Appendages $\rho$	.00307 [oz - sec <sup>2</sup> /in <sup>2</sup> ]
Distance between two gage set	1.365 [in]

**Motor** (PMI, Servodisc DC Motor: JR16M 4 CH)

Torque Constant, $K_t$	52.77 [oz-in/amp]
Back EMF Constant, $K_e$	39.77 [v/1000rpm]
Tachometer Constant	3 [v/1000rpm]

**Power Supply** (KEPCO BOP 36-12M)

Current Gain	1.2 [amp/volt]
--------------	----------------

Figure 1. Texas A&M Maneuverable Space Structure Experiment

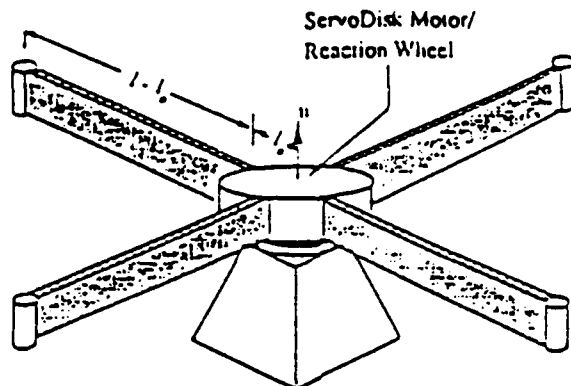


Figure 1a. Configuration Sketch

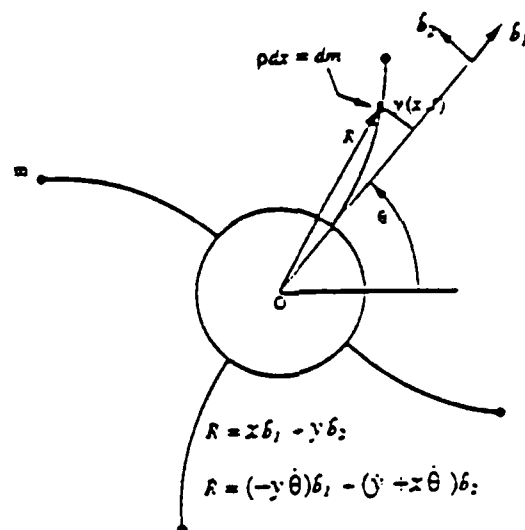


Figure 1b. Anti-Symmetric Deformation

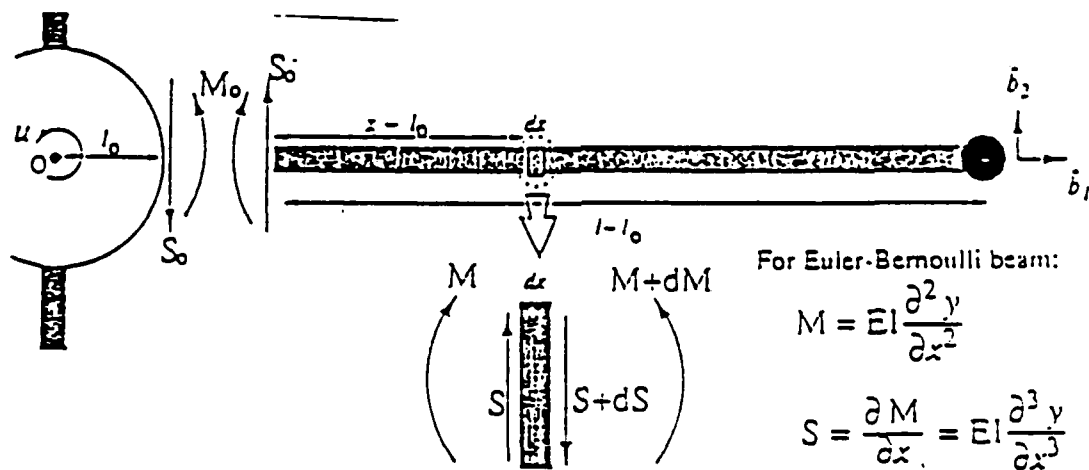


Figure 1c. Notation for Forces, Moments, and Euler-Bernoulli Constitutive Model

Figure 2. Hub Assembly

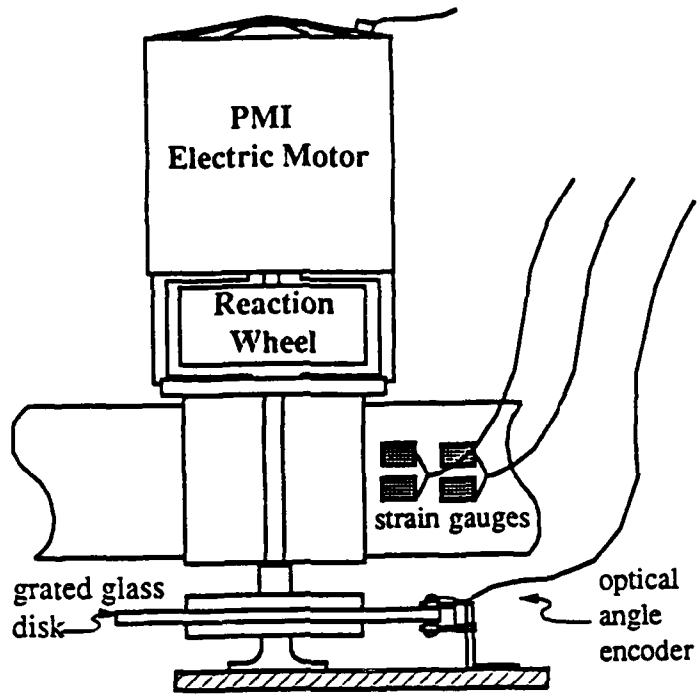


Figure 3. System Functional Block Diagram

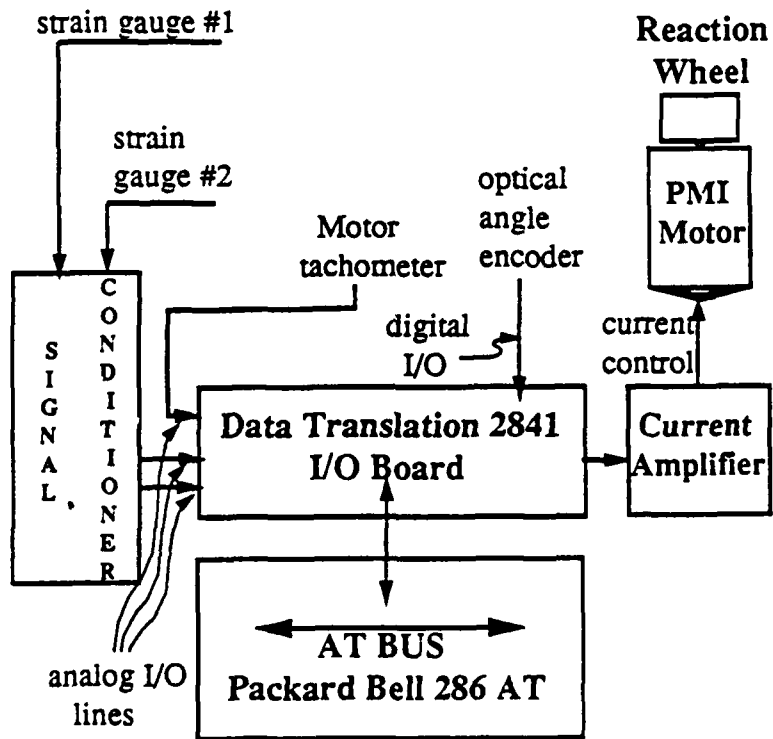


Figure 4. Torque Shaped Rigid Body Maneuver

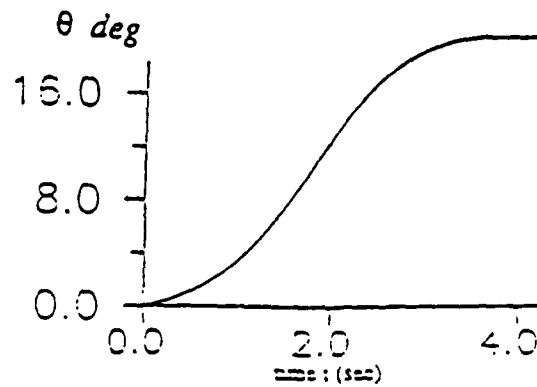
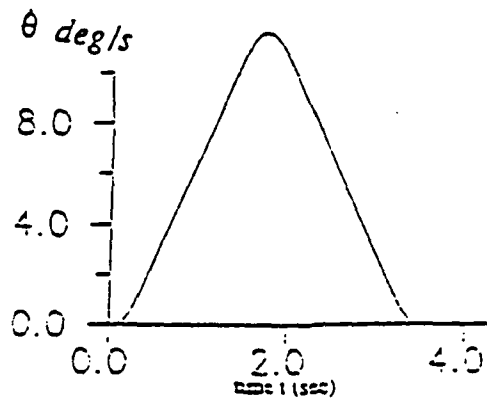
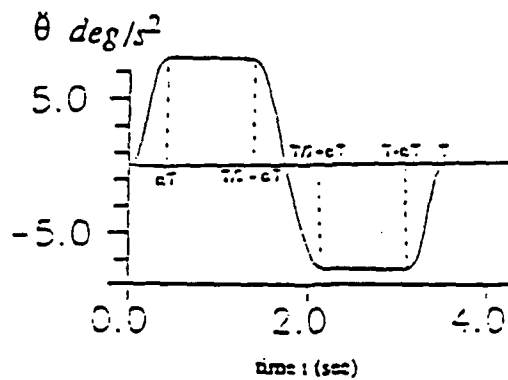


Figure 5. Rigid Body Maneuver vs. Saturation Torque and Shape Parameter

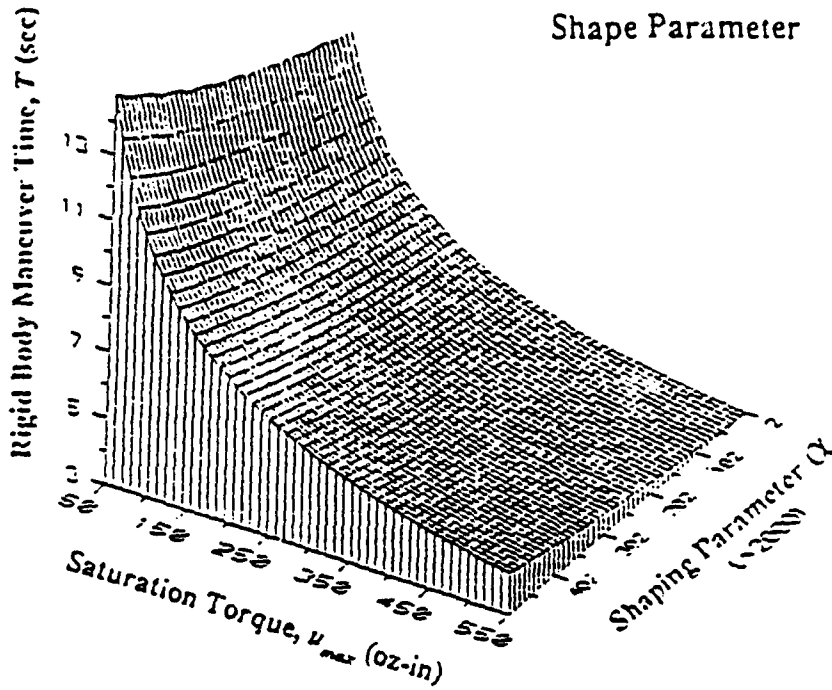


Figure 6. Flexible Body Residual Vibration Energy vs. Saturation Torque and Shape Parameter

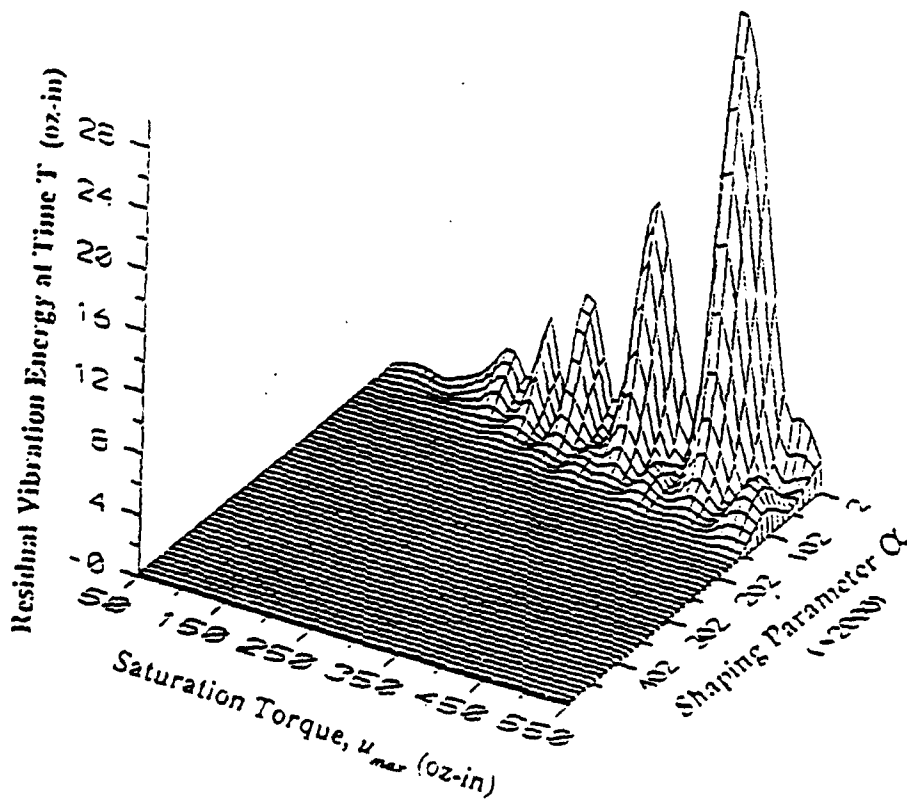


Figure 7. Boundary of the Liapunov-Stable Tracking Region vs. Saturation Torque and Shape Parameter

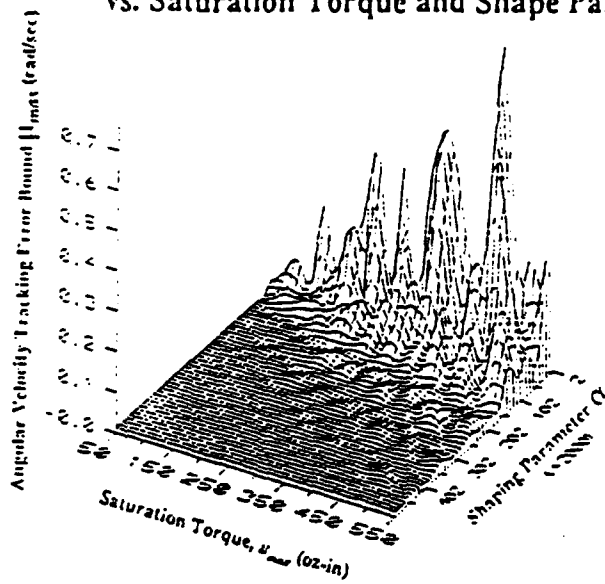
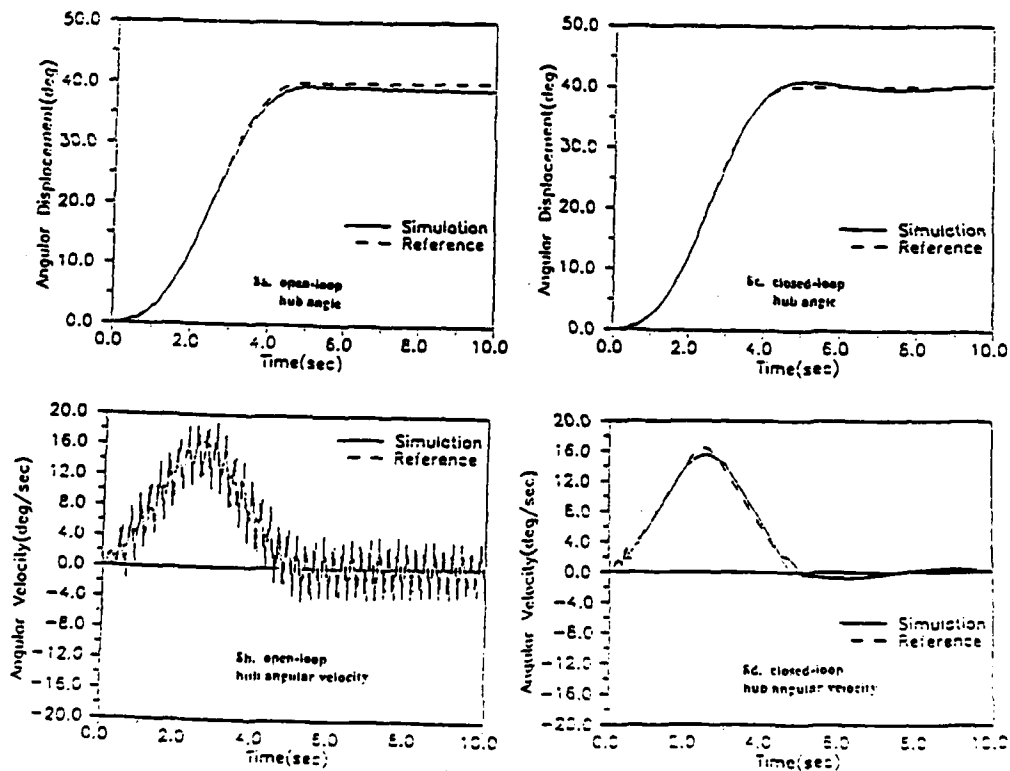
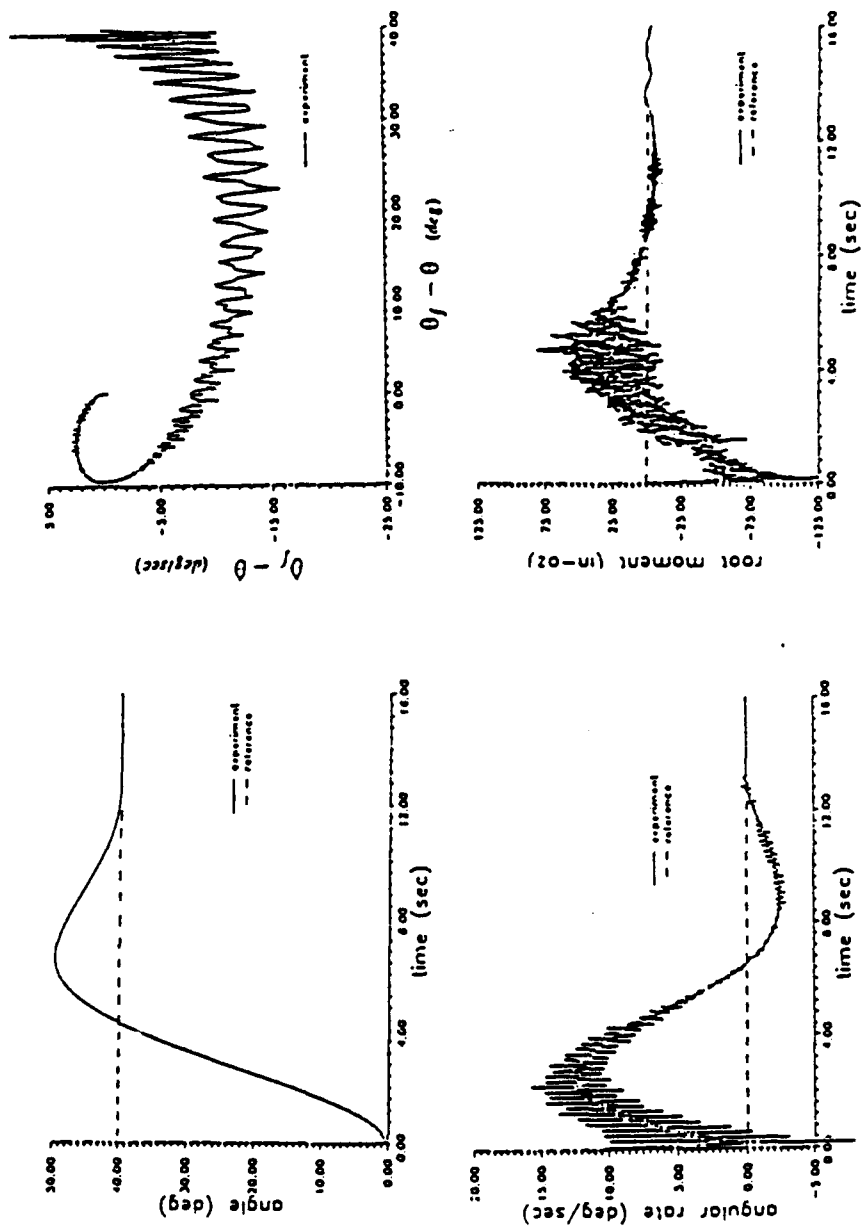


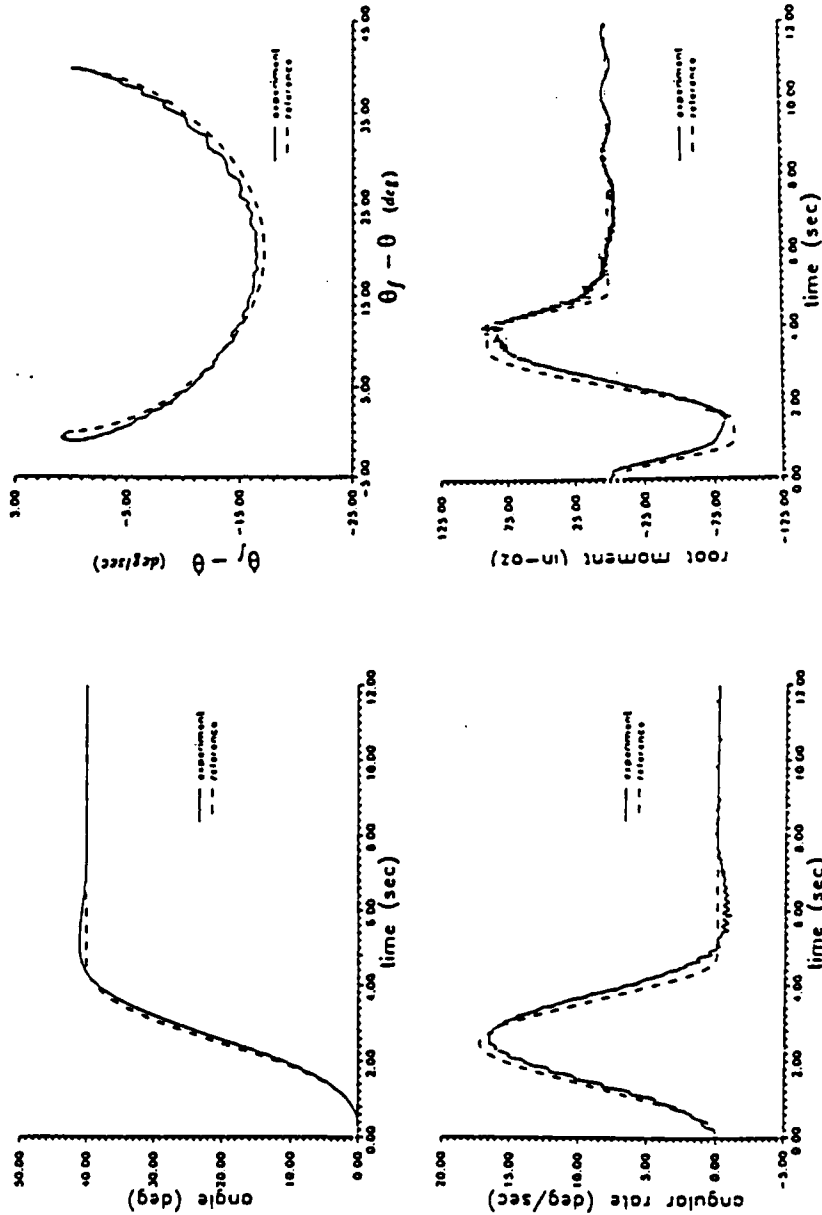
Figure 8. Simulated Open- and Closed-loop 40° Maneuver with Disturbances



**Figure 9. Experimental Results: Control Law I**  
 control gains:  $g_1 = 600$  oz-in/rad,  $g_2 = 800$  oz-in/rad/s,  $g_3 = 0$



**Figure 10. Experimental Results: Control Law II**  
 torque shape parameter:  $\alpha = 0.2$ , control gains:  $g_1 = 3000$  oz-in/rad,  $g_2 = 800$  oz-in/rad/s,  $g_3 = 0$



**Near-Minimum-Time Maneuvers of Flexible Vehicles:  
Analytical and Experimental Results**

*J. L. Junkins  
Z. H. Rahman  
H. Bang*

Department of Aerospace Engineering  
Texas A&M University  
College Station, Texas 77843

*a preprint of paper to be presented at*

*AIAA Aerospace Sciences Meeting  
Reno, Nevada  
January 1990*

*submitted for publication in  
AIAA Journal of Guidance, Control, and Dynamics  
September 1989*

# Near-Minimum-Time Maneuvers of Flexible Vehicles: Analytical and Experimental Results

*J. L. Junkins\**

*Z. H. Rahman\*\**

*H. Bang\*\*\**

Texas A&M University

## Abstract

A method for designing globally stable feedback control laws for maneuvers of flexible dynamical systems is presented. Both analytical and experimental results are discussed. The approach readily accommodates known nonlinearities and applies to systems described by hybrid coupled sets of ordinary and partial differential equations. Our proof of Liapunov stability does not rely upon spatially discretizing distributed parameter systems. The most fundamental developments lead to output feedback controls which drive the system to a target fixed point in the state space. More generally, we develop feedforward/feedback tracking-type control laws to null the departure of the system state from an a priori determined smooth target trajectory. The target trajectory may be an exact or an approximate solution of the system equations of motion. This approach can be used to generate, for example, near-minimum-time feedback controllers which accommodate general "torque-shaping" to achieve a judicious compromise between near-minimum-time and competing performance indices such as levels of sensitivity to model errors, disturbances, and control implementation errors. The method has a seamless continuous handoff from the large angle "approach pattern" control to the "end game" controls for fine pointing. Experimental results are presented for a variety of control gains and shaped torque reference maneuvers; the results are in excellent agreement with the analytical developments and simulated results. The analytical and experimental results jointly provide strong analytical justification and conclusive experimental evidence of the practical merit of this approach to design of controllers for distributed parameter systems.

---

\* George J. Eppright Chair Professor of Aerospace Engineering, Fellow AIAA

\*\* Research Engineer

\*\*\* Ph. D. Candidate

## I. Introduction

Considerable recent research has been directed toward the problem of maneuvering a flexible spacecraft. In Reference 1, we present a fairly comprehensive treatment of this family of problems up through 1985. Other analytical and experimental investigations<sup>2-12</sup> have been carried out to evaluate: (i) feedback control laws based upon minimizing quadratic indices, (ii) near-minimum time, switching-type controllers, and (iii) implementation issues. The main configuration of interest in the present discussion is similar to the structure of the Vander Velde and He study<sup>12</sup>, however, we address the use of variable torque actuation via a reaction wheel instead of on-off thrusters, and utilize Lyapunov control design approaches and establish stable tracking-type control laws for distributed parameter systems.

We present a method for generating globally stable feedback control laws for maneuvers of distributed parameter structural systems. The method can accommodate nonlinearity and our proof of stability does not rely upon spatially discretizing distributed parameter systems. The most fundamental developments are related to similar ideas presented in Refs. [3, 6], and lead to controls which drive the system to a target fixed point in the state space. However, we extend these ideas to achieve near-minimum-time control. We present novel tracking-type control laws to null the departure motion of the system state from an arbitrary smooth target trajectory, and develop the conditions for stability of the closed loop system. The control law structure is such that the large motion controller (a tracking law) blends continuously into a constant gain terminal controller. This "seamless" transition is qualitatively more attractive than, for example, gain scheduling approaches. The target trajectory (for the tracking law) may be any smooth path; i. e., the target trajectory can be selected as an exact or approximate solution of the system equations of motion. We show how this approach can be used to generate near-minimum-time feedback controllers which achieve global stability about a fixed terminal state. This approach accommodates general "torque-shaping" to achieve a compromise between near-minimum-time and competing performance indices such as levels of sensitivity to model errors, disturbances, and implementation errors.

While we subsequently develop methods for controlling distributed parameter systems governed by hybrid coupled sets of ordinary and partial differential equations, we first consider a system described by a sixth order set of nonlinear, ordinary differential equations.

## II. Motivation of the Approach Using Rigid Body Maneuvers

The ideas are easily introduced by considering general three dimensional nonlinear maneuvers of a single rigid body. The equations governing large motion can be written as<sup>1</sup>

$$\begin{aligned}
 I_1 \dot{\omega}_1 &= (I_2 - I_3) \omega_2 \omega_3 + u_1 & 2\dot{q}_1 &= \omega_1 - \omega_2 q_3 + \omega_3 q_2 + q_1 (q_1 \omega_1 + q_2 \omega_2 + q_3 \omega_3) \\
 I_2 \dot{\omega}_2 &= (I_3 - I_1) \omega_3 \omega_1 + u_2 & 2\dot{q}_2 &= \omega_2 - \omega_3 q_1 + \omega_1 q_3 + q_2 (q_1 \omega_1 + q_2 \omega_2 + q_3 \omega_3) \\
 I_3 \dot{\omega}_3 &= (I_1 - I_2) \omega_1 \omega_2 + u_3 & 2\dot{q}_3 &= \omega_3 - \omega_1 q_2 + \omega_2 q_1 + q_3 (q_1 \omega_1 + q_2 \omega_2 + q_3 \omega_3)
 \end{aligned} \quad (1)$$

where  $(\omega_1, \omega_2, \omega_3)$  and  $(q_1, q_2, q_3)$  are the principal axis components of angular velocity and the Euler-Rodriguez parameters, respectively. Also  $(I_1, I_2, I_3)$  and  $(u_1, u_2, u_3)$  are the principal moments of inertia and the principal axis components of the external control torque, respectively. For the case of zero control torque, it can be readily verified that total rotational kinetic energy is an exact integral of the motion, viz.  $2T = (I_1 \omega_1^2 + I_2 \omega_2^2 + I_3 \omega_3^2)$ .

Motivated by this total system energy integral, we investigate the trial Liapunov function

$$U = \frac{1}{2}(I_1 \omega_1^2 + I_2 \omega_2^2 + I_3 \omega_3^2) + A(q_1^2 + q_2^2 + q_3^2) \equiv \text{kinetic energy} + A \tan^2 \frac{\phi}{2} \quad (2)$$

where  $\phi$  is the instantaneous principal rotation angle (about the instantaneous Eulerian principal rotation axis, from the current angular position to the desired final angular position of the body<sup>1</sup>). It is apparent that the additive term  $A(q_1^2 + q_2^2 + q_3^2)$  can be viewed as the potential energy stored in a conservative spring. We can therefore anticipate that the system dynamics will evolve such that  $U$  is constant, if the only external torque is the associated conservative moment. Of course, we are not interested in preserving  $U$  as a constant, but rather we seek to drive it to zero. We therefore anticipate the necessity to determine an additional judicious control moment to guarantee that  $U$  is a decreasing function of time. It is obvious by inspection that  $U$  is positive definite and vanishes only at the desired state  $q_i =$

$\omega_i = 0$ . Differentiation of Eq. (2) and substitution of Eqs. (1) leads directly to the following expression for  $\dot{U}$

$$\dot{U} = \sum_{i=1}^3 \omega_i [u_i + Aq_i(1 + q_1^2 + q_2^2 + q_3^2)] \quad (3)$$

Of all of the infinity of possible control laws, we can see that any  $u_i(q_1, q_2, q_3, \omega_1, \omega_2, \omega_3)$  which reduces the bracketed terms to a negative definite function times  $\omega_i$  will guarantee that  $\dot{U}$  is globally negative semi-definite. The simplest choice: Select  $u_i$  so that the  $i^{\text{th}}$  bracketed term becomes  $-k_i \omega_i$ ; this gives  $\dot{U} = -(k_1 \omega_1^2 + k_2 \omega_2^2 + k_3 \omega_3^2)$  which is obviously a negative definite function of angular velocity, if we choose all  $k_i > 0$ . It is easy to verify from Eqs. (1) that  $(\omega_1, \omega_2, \omega_3)$  are generally non-zero, except at an equilibrium state, and the only equilibrium point {where  $(\omega_1, \omega_2, \omega_3) = (\dot{\omega}_1, \dot{\omega}_2, \dot{\omega}_3) = (0, 0, 0)$ } of the closed loop system is the origin of the state space:  $(q_1, q_2, q_3, \omega_1, \omega_2, \omega_3) = (0, 0, 0, 0, 0, 0)$ . Thus we obtain a globally stabilizing nonlinear feedback control law<sup>2-4</sup> for large angle attitude control:

$$u_i = -[k_i \omega_i + Aq_i(1 + q_1^2 + q_2^2 + q_3^2)], \quad i = 1, 2, 3 \quad (4)$$

Since  $U$  is a positive definite, decreasing function of time along all trajectories, and since it vanishes at the origin, then the necessary and sufficient conditions are satisfied for global Liapunov stability. We have implicitly excluded the geometric singularity ( $q_i \rightarrow \infty$ ), associated with this parameterization of rotational motion as  $\phi \rightarrow n\pi$ ; we can use the quaternion or Euler parameter description of motion and avoid all geometric singularities, as well. The nonlinear feedback control law of Eq. (4) guarantees stability of the nonlinear closed loop system, under the assumption of zero model errors. In practice, of course, guaranteed stability in the presence of zero model error is not a sufficient condition to guarantee stability of the actual plant having arbitrary model errors and disturbances. On the other hand, rigorously defining a region in gain space guaranteeing global stability for our best model of the nonlinear system is an important step; it is reasonable to restrict the optimization of gains to this stable family of designs.

The determination of the particular gain values, selected from the space of globally stabilizing gains, is usually based upon performance optimization criteria specified in consideration of the disturbance environment, sensitivity to model errors, desired system time constants, actuator saturation, and sensor/actuator bandwidth limitations. For the purpose of gain optimization, it is usually convenient to introduce spatial approximations and discretize partial differential equation systems to obtain a finite set of ordinary differential equations. It is also typically useful to linearize nonlinear differential equations about one or more points in the anticipated operation envelope. Using a generalization of the above example, we can rigorously determine a region of admissible gains which stabilize globally a generally nonlinear, partial differential equation description of the system. Note that approximations subsequently introduced in the gain design process cannot destabilize the zero model error system, if the gains are optimized over this known-to-be stable region. In the above rigid body discussion, so long as we restrict  $\{A, k_1, k_2, k_3\}$  to be positive, for example, approximations such as small angle linearizations used to select particular values cannot destabilize the system. Of course, approximations introduced to facilitate the gain design process can indeed lead to undesired and unanticipated performance variations of the actual nonlinear distributed parameter system, as compared to predictions based upon approximate models used to design the control gains.

Before generalizing the methodology to consider partial differential equation systems, it is important to reflect upon the selection of the above Liapunov function. Notice that if a system has no inherent stiffness with respect to rigid body displacements, it is necessary to augment the open loop energy integral by a pseudo potential energy term [such as  $A(q_1^2 + q_2^2 + q_3^2)$  in the above example]; generally speaking, the pseudo energy term should be defined such that the candidate Liapunov function ( $U$ ) is a positive-definite measure of motion which has its *global minimum at the desired target state*. Then, the controls are usually selected as simply as possible (from an implementation point of view) to force pervasive dissipation ( $\dot{U} \leq 0$ ) of the modified energy (Liapunov) function along all trajectories of the closed-loop system and thereby guarantee closed-loop stability.

While the above insights are useful, the Liapunov function is generally not unique. We'll see below that these ideas lead to an attractive strategy which define the Liapunov function with relative weights on the portions of the total energy associated with structural subsystems. To accommodate discussion of path-type stability of tracking motion control, we'll also introduce "error" energies measured from an a priori computed time varying trajectory. The lack of uniqueness of the Liapunov function is not necessarily a disadvantage in practice, because it is a source of user flexibility providing control design freedom qualitatively comparable to the freedom one has in selecting performance indices when applying optimal control theory.

### III. Maneuvers and Vibration Control for Distributed Parameter Systems

With reference to Figures 1 - 3, we consider control of a rigid hub with four cantilevered flexible appendages. We consider the appendages to be identical uniform flexible beams and make the Euler-Bernoulli assumptions of negligible shear deformation and distributed rotary inertia. Each beam is cantilevered rigidly to the hub and has a finite tip mass. Motion is restricted to the horizontal plane, and a control torque  $u(t)$  acting on the hub is the only external effect considered at this stage of the developments. We subsequently address rejection of disturbances.

We are interested in a class of rest-to-rest maneuvers and under the above assumptions, we can show that the beams will deform in the anti-symmetric fashion (Figure 1) with the configuration's instantaneous mass center remaining at the hub's geometrical center. Also, due to the anti-symmetric deformation of the beams, we need concern ourselves only with the deformation  $y(x,t)$  of a single beam. We adopt the continuum viewpoint and avoid introducing spatial approximations in the application of Liapunov concepts; the resulting control law and stability arguments will therefore apply rigorously to the distributed parameter system. The hybrid system of ordinary and partial differential equations governing the dynamics of this system are

$$I_{hub} \frac{d^2 \theta}{dt^2} = u + 4(M_o - S_o l_o)$$

$$-(M_o - S_o l_o) = \int_{l_o}^l \rho x \left( \frac{\partial^2 y}{\partial t^2} + x \frac{d^2 \theta}{dt^2} \right) dx + ml \left( l \frac{d^2 \theta}{dt^2} + \frac{\partial^2 y}{\partial t^2} \Big|_l \right) + HOT \quad (5)$$

$$\rho \left( \frac{\partial^2 y}{\partial t^2} + x \frac{d^2 \theta}{dt^2} \right) + EI \frac{\partial^4 y}{\partial x^4} = 0 \quad +HOT$$

where  $\rho$  is the assumed constant mass/unit length of the beams,  
 $EI$  is the assumed constant bending stiffness of the beams,  
 $(M_o, S_o)$  denote bending moment and shear force, at the root of the beam,  
 $\theta$  denotes hub inertial rotation,  
 $m$  denotes the mass of the tip mass, and  
 $(l, l_o)$  denote the distance from the hub center to the beam tip and the hub radius.

We denote higher order terms by *HOT* to indicate other known linear and nonlinear effects (such as rotational stiffening, shear deformation, etc.). The most fundamental developments do not consider these higher order effects, however, we selectively discuss these generalizations as well. The boundary conditions on Eqs. (5) are

$$\text{at } x = l_o: y(t, l_o) = \frac{\partial y}{\partial x} \Big|_{l_o} = 0$$

$$\text{at } x = l: \frac{\partial^2 y}{\partial x^2} \Big|_l = 0 \quad (\text{moment}), \quad \frac{\partial^3 y}{\partial x^3} \Big|_l = \frac{m}{EI} \left( l \frac{d^2 \theta}{dt^2} + \frac{\partial^2 y}{\partial t^2} \Big|_l \right) \quad (\text{shear}) \quad (6)$$

The total energy of the system (constant in the absence of control or disturbances) is:

$$2E = I_{hub} \left( \frac{d\theta}{dt} \right)^2 + 4 \left[ \int_{l_o}^l \rho \left( \frac{\partial y}{\partial t} + x \frac{d\theta}{dt} \right)^2 dx + \int_{l_o}^l EI \left( \frac{\partial^2 y}{\partial x^2} \right)^2 dx + m \left( l \frac{d\theta}{dt} + \frac{\partial y}{\partial t} \Big|_l \right)^2 \right] \quad (7)$$

Motivated by the recent work of Fujii<sup>3</sup> and Vadali<sup>6</sup>, we investigate the Liapunov function

$$2U = a_1 I_{hub} \hat{\theta}^2 + a_2 (\theta - \theta_f)^2$$

$$+ 4a_3 \left[ \int_{l_o}^l \rho \left( \frac{\partial y}{\partial t} + x \hat{\theta} \right)^2 dx + \int_{l_o}^l EI \left( \frac{\partial^2 y}{\partial x^2} \right)^2 dx + m \left( l \hat{\theta} + \frac{\partial y}{\partial t} \Big|_l \right)^2 \right] \quad (8)$$

where the weighting coefficients  $a_i$  are included to allow relative emphasis upon the three contributors to the "error energy" of the system. We have added the "torsional spring energy" term  $a_2 (\theta - \theta_f)^2$  to make the final state  $(\theta, \dot{\theta}, y(x,t), \frac{\partial y(x,t)}{\partial t})_{desired} = (\theta_f, 0, 0, 0)$

be the global minimum of  $U$ . It is obvious by inspection that imposing  $a_1 > 0$  guarantees that  $U \geq 0$ , and that indeed the global minimum of  $U=0$  occurs only at the desired state. Differentiation, substitution of the equations of motion (Eqs. (5), (6)), and some calculus lead to

$$\dot{U} = \frac{dU}{dt} = \dot{\theta} [ a_1 u + a_2 (\theta - \theta_f) + 4(a_3 - a_1)(l_0 S_0 - M_0) ] \quad (9)$$

Since we require that  $\dot{U} \leq 0$  to guarantee stability, we set the [ ] term to  $-a_4 \dot{\theta}$  and this leads to the control law

$$u = -\frac{1}{a_1} [ a_2 (\theta - \theta_f) + a_4 \dot{\theta} + 4(a_3 - a_1)(l_0 S_0 - M_0) ] \quad (10)$$

or, we see that the following *linear, spatially discrete* output feedback law globally stabilizes this distributed parameter system:

$$u = - [ g_1 (\theta - \theta_f) + g_2 \dot{\theta} + g_3 (l_0 S_0 - M_0) ]; \quad g_1 \geq 0, g_2 \geq 0, g_3 \geq -4, \text{ for stability} \quad (11)$$

This control law is elegant. Notice that controllers based upon this law are easy to implement since no state estimation is required. The root shear and bending moment can be measured by (albeit somewhat noisy) conventional strain gauges. The value and sign of the shear/moment feedback gain  $g_3 = 4(a_3 - a_1) / a_1$  depends upon whether we wish to emphasize dissipation of the beam energy (for  $a_3 > a_1$ ), or the motion of the hub (for  $a_3 < a_1$ ), as is evident from Eq. (8). Since  $\dot{U} = -a_4 \dot{\theta}^2$  is not an explicit, negative definite function of the subset of state variables  $(\theta, y(x,t), \frac{\partial y(x,t)}{\partial t})$ , the stability arguments implicitly depends upon the truth that all infinity of modes of motion of this structure, under the assumption of anti-symmetric deflections have generally non-zero hub angular velocity ( $\dot{\theta}$ ).

It is of significance that this same linear feedback law of Eq. (11) maintains it's globally stabilizing character even when the Euler/Bernoulli assumptions are relaxed to include additional linear and nonlinear effects; in particular, we have verified that closed loop

stability is maintained when we include the following: rotational stiffening, coriolis kinematic coupling terms, aerodynamic drag, shear deformation, beam rotary inertia, and finite inertia of the tip mass. The verification of these truths requires appropriate modifications of the kinetic and potential energy functions, and of course, the differential equations of motion must be generalized consistently. *In short, global stability of the system using the simple linear control law of Eq. (11) has been found very forgiving of modeling assumptions and therefore modeling errors.*

On the other hand, the overall performance measures (time constants, required energy, rms output errors, etc.) of the system versus our simulations are generally not as forgiving as the most fundamental performance measure (stability). While we are guaranteed stability for a large family of model errors, it should be apparent that *performance predictions are generally very sensitive to modeling errors.* With appropriate system modeling and selection of the feedback gains, however, it has been demonstrated experimentally<sup>3,5</sup> and in our results presented below, that this feedback law works well over finite regions of the state and gain space, and in the presence of typical model errors.

While the constant gain linear feedback works well for terminal pointing and vibration suppression, we have found it to be a poor law for carrying out both large angle maneuvers and terminal pointing/vibration suppression. In fact, it is evident from both analytical and experimental studies that gain scheduling is needed to use the linear feedback law of Eq. (11) to efficiently control both the large maneuvering motions and the small terminal motions. This is because the large gains required for effective vibration suppression and disturbance rejection near the target state are typically differ by several orders of magnitude from the smaller ones needed far from the target state (i., e., large gains appropriate for terminal vibration suppression, when used during a large angle maneuver typically result in actuator saturation and significant  $\theta$  overshoots). To obtain a control law more appropriate for large angle maneuvers with vibration suppression, we can modify the above developments; a stable tracking-type feedback control law is presented in the following discussion.

#### IV. Near-Minimum-Time Maneuvers of Distributed Parameter Systems

Consider first the near-minimum-time maneuver of a rigid body. We know that the strict minimum time control is a bang-bang law<sup>1</sup>, which for the rest-to-rest maneuver-to-the-origin case, saturates negatively during the first half of the maneuver and positively during the last half of the maneuver. From an implementation point of view, the instantaneous switches of bang-bang control are often troublesome for several reasons:

- (i) no torque-generating device exists which can in fact switch instantaneously,
- (ii) when generalized and applied to flexible structures, the discontinuous class of controls will typically excite poorly modeled higher frequency modes and
- (iii) the predicted (model-derived) switch times and the response of the actual system are usually very sensitive to modeling errors.

As a consequence of these sources of difficulty, our analytical and experimental work indicate that bang-bang control of flexible body dynamics usually lacks robustness with respect to modeling errors.

Recently, an intuitively attractive family of controllably smooth approximations of the sign (*sgn*) function which arises in time-optimal control has been introduced. The smoothed sign function approximations presented in Ref. [6] been studied in the context of optimization of near-minimum-time maneuvers considering multiple flexible body modes. However, this approach requires expensive pre-calculation of the solution to a two-point boundary-value problem (tpbvp) or interpolation from an a priori computed map of tpbvp solutions. Our recent analytical and experimental work<sup>4</sup> indicates that much simpler piecewise continuous spline approximations of the sign function used in conjunction with analytical approximations of the optimum maneuvers and associated optimum controls are more attractive from an implementation point of view. Using this approach, a typical near-minimum-time control law (for single axis, rest-to-rest maneuvers of a rigid body) has the form

$$I \ddot{\theta} = u = \pm u_{max} f(\Delta t, t_f, t) \quad (12)$$

where  $u_{max}$  is the saturation torque,

$t_f$  is the maneuver time, we choose the + sign if  $\theta_f > \theta_o$ ,

$\Delta t$  is the rise time, and the smooth sgn function approximation adopted is

$$f(\Delta t, t_f, t) \begin{cases} = \left(\frac{t}{\Delta t}\right)^2 [3 - 2\left(\frac{t}{\Delta t}\right)], & \text{for } 0 \leq t \leq \Delta t \\ = 1, & \text{for } \Delta t \leq t \leq \frac{t_f}{2} - \Delta t \equiv t_1 \\ = 1 - 2\left(\frac{t-t_1}{2\Delta t}\right)^2 [3 - 2\left(\frac{t-t_1}{2\Delta t}\right)], & \text{for } t_1 \leq t \leq \frac{t_f}{2} + \Delta t \equiv t_2 \\ = -1, & \text{for } t_2 \leq t \leq t_f - \Delta t \equiv t_3 \\ = -1 + \left(\frac{t-t_3}{\Delta t}\right)^2 [3 - 2\left(\frac{t-t_3}{\Delta t}\right)], & \text{for } t_3 \leq t \leq t_f \end{cases}$$

Adopting the positive sign, Eq. (12) integrates to yield

$$\theta(t) = \theta_o + \frac{u_{max}}{I} \int_{t_o}^t f(\Delta t, t_f, \tau) d\tau \quad (13)$$

$$\theta(t) = \theta_o + \dot{\theta}_o(t-t_o) + \frac{u_{max}}{I} \int_{t_o}^t \int_{t_o}^{\tau_1} f(\Delta t, t_f, \tau_2) d\tau_2 d\tau_1$$

The integrations can be carried out in terms of elementary functions which are not presented here for brevity. Figure 4 shows the maneuver resulting from these integrations for a typical selection of parameters. For rest-to-rest maneuvers, we can impose the boundary conditions

$$\text{at } t_o = 0: \theta(0) = \theta_o, \dot{\theta}(0) = 0; \quad \text{at } t_f = T: \theta(T) = \theta_f, \dot{\theta}(T) = 0 \quad (14)$$

and from carrying through the integrations of Eqs. (13), we obtain the useful relationship

$$\theta_f - \theta_o = \frac{u_{max}}{I} \left[ \frac{1}{4} - \frac{1}{2}\alpha + \frac{1}{10}\alpha^2 \right] T^2, \quad \Delta t = \alpha T, \quad 0 < \alpha < \frac{1}{4} \quad (15)$$

$$\text{or } T = \left[ \frac{I(\theta_f - \theta_o)}{u_{max} \left( \frac{1}{4} - \frac{1}{2}\alpha + \frac{1}{10}\alpha^2 \right)} \right]^{1/2} \quad (16)$$

In Eq. (16) we have the explicit rigid body tradeoff between torque shaping ( $\alpha$ ), maneuver time ( $T$ ), maneuver angle ( $\theta_f - \theta_o$ ), and maximum angular acceleration ( $u_{max}/I$ ). Obviously, Eq. (15) can be inverted for any of these as a function of the remaining parameters. If we set

$\alpha = \Delta t/T = 0$ , of course, we obtain the special case result  $\{ T^2 = 4I(\theta_f - \theta_o)/u_{max} \}$  expressing the well-known square-root relationship between the minimum time, maneuver angle, inertia, and saturation torque for bang-bang control.

Figure 5 shows the rigid body maneuver time ( $T$ ) versus  $\alpha$  and  $u_{max}$ . Notice that the maneuver time is strongly dependent upon  $u_{max}$ , but varies much less as a function of  $\alpha$ . However, we find when the torque  $u_{ref}(t) = u_{max} f(\alpha T, T, t)$  of Eq. (12) is applied to a flexible body, the reverse is true. To illustrate this point, we approximated the solution of Eqs. (5) by introducing a Galerkin expansion (of the beam deflection in terms of the first ten clamped-free cantilever mode shapes times time varying generalized coordinates). The forced response of the resulting 20th order system was judged adequately converged. Using this solution, we applied the same family of torques used in for the rigid body results of Figure 5 and computed the flexible body open loop response for each choice of  $\alpha$  and  $u_{max}$ . Figure 6 shows the total energy of the flexible body system at time  $T$  for this same family of maneuvers. As is evident, the vibration energy vanishes for sufficiently small  $u_{max}$  and is significantly reduced for any given  $u_{max}$  by increasing  $\alpha$ . Notice the triangular region (large  $\alpha$ , small  $u_{max}$ ) for which the vibration energy at time  $T$  is negligible. We will subsequently see that measures of the largest errors with which the closed-loop-controlled flexible body system can track the rigid body maneuvers of Figure 5 behave in a qualitatively similar way.

The above results and those of Ref. [4] support the intuitively obvious truth that applying judiciously "smoothed bang-bang" open-loop controls such as Eq. (12) to generate maneuvers of a flexible body results in moderate structural vibration, for sufficiently slow and smooth maneuvers (small  $u_{max}$  and large  $\alpha$ ). Of course unmodeled disturbances, control implementation errors, and model errors negate some of these apparent gains, especially without feedback. For relatively small penalties in maneuver time<sup>4,5</sup>, actual torque-shaped maneuvers enjoy several orders of magnitude reduction in residual vibration, even without feedback, although some offset in rigid body position usually results. Thus overall

maneuver time, including vibration arrest, can be reduced dramatically by modest torque shaping, as compared to simply using bang-bang control augmented by vibration suppression. Also of significance, we find that it is usually desirable to select the torque profile (e.g.,  $u_{max}$ ,  $\alpha$ , etc.) to consider the sensor and actuator dynamics and thereby make the commanded torque history more nearly physically achievable. More generally, however, we can use any reference maneuver (not necessarily a rigid body torque-shaped maneuver). We will find merit in considering a certain class of flexible body reference motions in our discussion below.

Suppose we adopt a reference open-loop rigid body maneuver denoted by the subscript *ref* as  $\{\theta_{ref}(t), \dot{\theta}_{ref}(t), \ddot{\theta}_{ref}(t) = u_{ref}/I\}$  and satisfying Eqs. (12-16). Note  $I$  is the undeformed moment of inertia, and we have implicitly selected the torque shaping parameters  $\alpha$ ,  $u_{max}$ , and thereby established the corresponding target maneuver time  $T$  from Eq. (16) for specified initial and final angle. Motivated by the issues discussed above and the quadratic regulator perturbation feedback controllers discussed in Refs. [1, 9, 11], we hypothesize the following structure for the control law

$$u = u_{ref}(t) - [g_1(\theta - \theta_{ref}) + g_2(\dot{\theta} - \dot{\theta}_{ref}) + g_3((I_o S_o - M_o) - (I_o S_o - M_o)_{ref})] \quad (17)$$

where it is easy to show that the root moment for the reference (rigid body) motion is proportional to the angular acceleration:  $(I_o S_o - M_o)_{ref} = + [\rho(l^3 - l_o^3)/3 + m l^2] \ddot{\theta}_{ref}(t)$ .

We wish to gain insight on the stability characteristics of the flexible body's closed-loop departure dynamics [from the target (*ref*) rigid body motion (for  $t < T$ ), and from the fixed target state (for  $t \geq T$ )], and we anticipate providing an analytical justification for the tracking control law of Eq. (17). Let us denote by the subscript *r* the state variables along the open-loop flexible body solution of Eqs. (5) when driven by the torque  $u_{ref}(t)$  of Eqs. (12-16). The instantaneous displacement of the open-loop flexible body solution from the open loop rigid body motion is denoted  $\Delta() = ()_r - ()_{ref}$ ; for example,  $\Delta\theta(t) = \theta_r(t) - \theta_{ref}(t)$ . Variables

without subscripts represent the "actual" instantaneous closed-loop controlled solution variables. Consider the candidate error energy Liapunov function

$$\begin{aligned}
 2U = & a_1 I_{hub} (\dot{\theta} - \dot{\theta}_r)^2 + a_2 (\theta - \theta_r)^2 \\
 & + 4a_3 \left[ \int_{l_0}^l \rho \left[ \left( \frac{\partial y}{\partial t} - \frac{\partial y_r}{\partial t} \right) + x(\dot{\theta} - \dot{\theta}_r) \right]^2 dx \right. \\
 & \left. + \int_{l_0}^l EI \left( \frac{\partial^2 y}{\partial x^2} - \frac{\partial^2 y_r}{\partial x^2} \right)^2 dx + m \left[ l(\dot{\theta} - \dot{\theta}_r) + \left( \frac{\partial y}{\partial t} \Big|_l - \frac{\partial y_r}{\partial t} \Big|_l \right) \right]^2 \right] \quad (18)
 \end{aligned}$$

Assuming the actual control is some general, to-be-determined  $u(t)$ , and that the actual motion satisfies Eqs. (5), we have investigated the time derivative of  $U$  of Eq. (18) and found that it is given by the following equation

$$\dot{U} = -a_1 (\dot{\theta} - \dot{\theta}_r) \left[ u - u_{ref} + \frac{a_2}{a_1} (\theta - \theta_r) + 4 \frac{a_3 - a_1}{a_1} [(l_0 S_0 - M_0) - (l_0 S_0 - M_0)_r] \right] \quad (19)$$

Analogous to the logic leading to Eq. (9), we see that we could determine a stabilizing  $u(t)$  by setting the bracketed term to a positive quantity ( $g_2$ ) times  $(\dot{\theta} - \dot{\theta}_r)$  (i. e., this makes  $\dot{U}$  a negative definite function of the error in hub angular velocity). This gives the control law

$$u = u_{ref}(t) - \left[ g_1 (\theta - \theta_r) + g_2 (\dot{\theta} - \dot{\theta}_r) + g_3 [(l_0 S_0 - M_0) - (l_0 S_0 - M_0)_r] \right] \quad (20)$$

with  $\dot{U} = -a_1 g_2 (\dot{\theta} - \dot{\theta}_r)^2$  and we introduced the definitions  $g_1 \equiv a_2/a_1$ ,  $g_3 \equiv \frac{a_3 - a_1}{4}$ .

Notice, to guarantee stability, that  $g_1$  and  $g_2$  must be positive, but as before  $g_3$  must be greater than -4. The main difficulty with this control law is that it requires pre-computing the flexible body solution, we'd prefer a tracking law which requires a much simpler rigid body maneuver to be pre-computed. Let us pursue this objective. Since Eq. (19) holds for an arbitrary  $u(t)$ , we introduce the control law of Eq. (17) and investigate it's stability characteristics. Making use of the notation  $\Delta O = O_r - O_{ref}$ , we are led to

$$\dot{U} = -a_1 (\dot{\theta} - \dot{\theta}_r) \{ g_2 (\dot{\theta} - \dot{\theta}_r) + [g_1 \Delta \theta + g_2 \Delta \dot{\theta} + g_3 \Delta (l_0 S_0 - M_0)] \} \quad (21)$$

Obviously, a sufficient condition characterizing the region where  $\dot{U} \leq 0$  is the dominance of the first term in the  $\{ \}$  of Eq. (21), this gives the inequality

$$|\dot{\theta} - \dot{\theta}_r| > \frac{1}{g_2} |g_1 \Delta\theta + g_2 \Delta\dot{\theta} + g_3 \Delta(l.S. - M_s)| \equiv \mu \quad (22)$$

It is apparent that the  $\Delta$  quantities on the right hand side of Eq. (22) are finite and (pre-) computable differences between the open loop flexible and rigid body motions, thus an upper bound can be established directly by a priori simulation of the two open loop motions, and using a particular set of feedback gains. Note the right hand side of Eq. (22) is essentially a weighted measure of how nearly the target trajectory satisfies the flexible body equations of motion.

A bounded-input/bounded-output viewpoint of stability can also be considered, based upon the departure motion differential equations obtain by differencing Eqs. (5) evaluated at each instant along the actual closed loop trajectory and along the flexible body open loop ( ), motion. Upon formulating these equations, we find departure motion motion is governed by an otherwise asymptotically stable system of differential equations forced by the known  $\Delta( )$  terms which appear in Eqs. (22). Since these forcing terms can be bounded by direct calculation, the resulting departure motion can also be bounded. Since the actual numerical bounds on the  $\Delta$  quantities can be made arbitrarily small (depending upon how nearly the user defined reference trajectory is made to satisfy the open loop equations of motion), we have a very attractive theoretical and practical situation vis-a-vis stability of the closed loop tracking motion. *We see that the closed-loop motion is globally attracted to the controllably small region near the target trajectory which violates the inequality of Eq. (22), and considering the motions within this small region, we have bounded-input, bounded-output stability.*

The above discussion can probably be generalized for any smooth target trajectory, but we find that it is attractive to use a torque-shaped rigid body reference trajectory, such as Eqs. (12)-(16). An attractive and significant feature of Eqs. (12)-(17) is that we have a  $C^1$  continuous transition:  $\{u_{ref}(t), \theta_{ref}(t), \dot{\theta}_{ref}(t), M_{oref}(t), S_{oref}(t)\} \Rightarrow \{0, \theta_f, 0, 0, 0\}$  as  $t \Rightarrow T$ ; so that for  $t > T$ , only the three feedback terms of Eq. (17) are contributing to the terminal fine-pointing/vibration arrest control. Thus the controls blend continuously from the large

angle tracking law into a constant gain controller identical to the globally stable fixed point output feedback case.

## V. Simulated Results for the AFOSR/TAMU Large Angle Maneuvers Experiment

Returning to the family of  $40^\circ$  open loop maneuvers used to generate the energy surface of Figure 6, we computed the velocity tracking bound  $\mu$  for Liapunov stability [as given by Eq. (22)] and found the maximum value ( $\mu_{max}$ ) of  $\mu(t)$  along each trajectory. Figure 7 displays this worst case tracking bound surface  $\mu_{max}(\alpha, u_{max})$  over the same  $(\alpha, u_{max})$  region as Figures 5, 6. As evident the closed-loop tracking error bound has a roughly analogous behavior to the open-loop residual vibration energy surface of Figure 6. Recall that outside the region bounded by the inequality of Eq. (22), we have guaranteed Liapunov stability, when using the control law of Eq. (17) and the reference rigid body torque given by Eqs. (12)-(16). From Figure 6, it is clear that sufficiently small  $u_{max}$  and sufficiently large  $\alpha$  result in arbitrarily small tracking errors, but the (small  $\alpha$ ) near-bang reference maneuvers cannot be tracked as accurately. It is easy to see how a family of candidate  $(\alpha, u_{max})$  designs could be selected which satisfy specified inequalities on maneuver times, tracking errors, and residual vibration energy, by direct examination of the surfaces of Figures 5-7.

Our experiments with simulations (and in the actual hardware implementations presented in Reference [5] and below) support the conclusion that it is easy to use the above surfaces (together with disturbance rejection simulations to select the reference trajectory and the feedback gains to obtain well-behaved closed loop control) to establish a large family of feasible designs. Prior to discussing our experimental results, we present some further simulations to show typical state and control variables histories along some of the trajectories of underlying the above surfaces. We include in these simulations the effects of disturbance torques, to illustrate the effectiveness of the controls in the presence of unmodeled effects. The Appendix summarizes the physical parameters and hardware descrip-

tion of the maneuver experiment, sketched in Fig. 1. For simplicity, we consider only the case of a  $40^\circ$  rest-to-rest maneuver, and set  $u_{max} = 400$  oz-in for all cases.

For our computational and experimental studies, we consider two control laws, namely the output feedback law (Control Law I)<sup>3-5</sup> of Eq. (11), and the tracking-type feedback control law (Control Law II) of Eq. (17). While Control Law II could be used with an arbitrary reference trajectory, we elect to specifically investigate the torque-shaped rigid body trajectories of Eqs. (12)-(16). The torque-shaped open loop control history  $u_{ref}(t)$  is pre-computed (in a fraction of a second!) from Eqs. (12)-(16) and stored. Note that the boundary conditions of Eq. (14) are enforced by using Eq. (16) to compute the target trajectory maneuver time as a function of the maneuver angle, saturation torque, and torque-shape parameter.

We now discuss the simulation results using Control Law II, which obviously blends into to Control Law I in the end game (for  $t \geq T$ ). In the experimental results, we report maneuvers carried out by both control laws. Both open loop (all  $g_i = 0$ ) and closed loop time histories of selected variables are shown in Figures 8a-8d. On the left of Figure 8, we show the hub angle and angular velocity for the case of an open loop control and in the presence of substantial impulsive and quasi-random (5 oz-in,  $1\sigma$ ) disturbance torques. It is evident that the disturbance torque history is significant vis-a-vis exciting substantial rigid body and flexural motions. On the right, we show the closed loop behavior of the system excited by the same disturbance torque history. The random component of this disturbance has been found to be typically pessimistic vis-a-vis our experimental hardware, however certain non-random, nonlinear effects associated with the bearing friction cause disturbances which are highly correlated in time and are not well represented by the present white noise representation of the disturbance torques. In spite of the substantial disturbance torques (Figs. 8a-8b), it is evident that we obtain a near minimum time rigid body motion while effectively suppressing vibration (8c-8d). This fact was also confirmed by evaluation of the energy distribution in the first six modes.

## VI. Description of Experimental Results

In all of the experiments discussed below, we set the target final angle to  $40^\circ$  and  $u_{max} = 400$  oz-in. The values of the tracking gains ( $g_1, g_2, g_3$ ) and of the torque shape parameter ( $\alpha$ ) were assigned several feasible values to demonstrate the effects of these upon the closed loop behavior of the system. Moderate bearing friction and aerodynamic damping were present in our experiments.

Figure 9 shows the system response for a Control Law I (the constant gain control law of Eq. (11)) maneuver with ( $g_1 = 600$  oz-in/rad,  $g_2 = 0$  oz-in/rad/sec, and  $g_3 = 0$ ). Since this initial position error is large, the maneuver starts from zero with an initial discontinuity to a large torque. For this gain selection, we see a large overshoot ( $-34^\circ$ ) which has not settled when the control was terminated at 30 seconds. Figure 10 shows a similar experiment but with  $g_2 = 800$  oz-in/rad/sec, to illustrate the constructive effects of active damping during the maneuver. This is representative set of "good" gains for Law I, but we will see that the maneuver time can be reduced by more than a factor of 2 by using Law II, whereas only about a 15% reduction can be achieved by optimizing gains for Law I (subject to a 400 oz-in saturation constraint). Notice the large transient (induced by instantaneously applying the gain  $g_1$  to the  $40^\circ$  initial angle error) decays after about 5 seconds, and the target rigid body position is acquired with small residual vibrations in about 12 seconds.

A family of results of using Control Law II, Eq. (17), (with  $\alpha = 0.1$  and  $0.2$ ,  $g_1 = 3000$ ,  $g_2 = 0, 200$ , and  $800$ , and  $g_3 = 0, 0.8$ , and  $-0.8$ ) are shown in Figure 11-16. These results demonstrate the effectiveness of Law II in comparison to Law I (e. g., compare Figures 10,14), and show the effects of varying the torque shape parameter ( $\alpha$ ) and the feedback gains ( $g_1, g_2, g_3$ ). Due to the tracking type of control, the initial errors operated upon by these gains are not as large for Law II as in the case of Law I, as a consequence of using a reference trajectory which departs smoothly from the initial state. Moreover, the smoothly increasing

torque profile of Law II does not "ring" the structure with an initial jump discontinuity at time  $t = 0$  to a large torque as in Law I. The effect of using a smooth, judiciously shaped reference torque history is evident if one compares the results in Figure 14 with those of Figure 10. Law II produced much smaller overshoot ( $\approx 1.5^\circ$  vs  $>10^\circ$ ), shorter settling time (6 seconds vs over 12 seconds) and greatly reduced the severity of peak vibration. Notice in Figures 9, 11, 12, that significant passive energy dissipation exists due to the combined effects of bearing friction, aerodynamics, and structural mechanisms, because the velocity feedback gain is zero in these three experiments. On the other hand the rate of passive energy dissipation is sufficiently low that active vibration control is required to satisfactorily arrest the structure. In comparing Figures 11 and 12, notice that increasing  $\alpha$  results in significantly reducing the amplitude of the structural vibration (which is primarily the first cantilever mode). As is evident in Figures 13 and 14, a judicious selection of the velocity feedback gain ( $g_2$ ) and the torque shaping parameter ( $\alpha$ ) suppresses the structural vibration during the maneuver as well as in the end game.

Figures 15, 16 provide some additional experimental results to contrast with the best design studied (Figure 14). Notice that including feedback ( $g_3$ ) on the root bending moment was not found to be effective in further refining our results. We did a number of experiments with other  $g_3$  values without improving over the results of Figure 14. The reason has been traced to the noisy derived angular rate from the angle encoder, and the fact that the accelerometer acts as a noisy angular accelerometer. Our simulations indicated that noise-free root bending moment feedback would be effective, over and above the hub angle and angular rate feedback, in suppressing the vibrations of all modes above 12 Hz. However, the effective bandwidth of our derived angular velocity was only 0-10 Hz and therefore we were unable to control the higher frequencies without injecting substantial noise-induced disturbance accelerations. We anticipate that enough attention to optimizing the design of analog and/or digital filters will lead to marginal improvements over the excellent results of Figure 14, however, we feel that it would be more productive to invest in an accurate angular rate measuring device and eliminate the source of this paradox.

Based upon mechanical tests and analysis of our bearing hardware, it is evident that interaction of the structure with the bearing accounts for the overwhelming source of unmodeled disturbances. The bearing friction/stiction model developed from our analysis has the form

$$\tau_{\text{bearing}} = -c_1 \text{sign}(\dot{\theta}) - c_2 \dot{\theta} + \text{HOT} \quad (23)$$

where we find  $c_1 \sim 20$  oz-in and  $c_2 \sim 0.001$  oz-in/rad/sec. Thus the first (stiction) term of Eq. (23) dominates the bearing torque for moderate  $\dot{\theta}$  and is about 5% of the peak commanded torque of 400 oz-in. While we believe Eq. (23) models the bearing friction well, it is difficult to use this model to compensate for bearing friction in real time, since our estimated value of  $\dot{\theta}$  is uncertain due to angle encoder measurement noise. Thus if we modify our control using Eq. (23), the commanded discontinuity (near the estimated time  $\dot{\theta}$  changes sign) will not coincide exactly with the actual discontinuity; mis-timed compensation torque discontinuities can actually worsen the disturbance! While we experimented with bearing friction compensation schemes, we ultimately decided to simply consider this an anticipated and well-modeled disturbance. Our simulations (such as the results shown in Figure 8) indicated our control approach could easily tolerate disturbances of this magnitude, and our successful experiments (Figures 9-16) certainly confirm that our implemented control laws are robust in the presence of the actual disturbances.

## VII. Concluding Remarks

We have presented a novel approach to design of feedback control laws for large maneuvers of distributed parameter systems, and have conducted successful experiments. The approach permits approximate imposition of actuator saturation constraints and a priori control shaping via user specification of a torque-shaped, optimized reference trajectory. The tracking-type control law is shown to result in Liapunov stability in the sense that all trajectories are globally attracted to a controllably small region near the reference trajectory. The

tracking law automatically blends smoothly into a globally stable, constant gain, terminal output feedback controller. We believe this approach is much more attractive than, for example, gain scheduling, because the logical and implementation complications associated with discontinuous gain change ("handoff") logic can be avoided altogether. We have considered in detail the case of single axis maneuvers of a flexible body system and a particular family of torque-shaped, near-minimum-time rigid body reference trajectories. We demonstrated numerically the effects of torque shaping upon maneuver time and established a bound on the usually small region near the target trajectory in which Liapunov-stable tracking cannot be guaranteed.

We described hardware experiments which successfully implemented near-minimum-time feedback control of single axis maneuvers of a flexible structure, using a family of torque-shaped rigid body reference trajectories. We presented new analytical developments, numerical simulations, and experimental results all of which support the conclusion that robust, near-minimum time control can be achieved by this approach. The simplicity of implementation makes this approach attractive, notice that no state estimator is required, and no truncation or spillover effects degrade our stability arguments. Our relatively low-budget experimental work afforded an excellent opportunity to demonstrate the validity and robustness of this feedback control approach: We were blessed (cursed?!) by difficulties associated with nonlinear friction/stiction phenomena in our hub bearing system, and significant angle encoder sensor noise. In particular, most of our implementation difficulties arose from relatively crude ( $-0.5$  deg/sec) angular velocity estimates derived from the prediction/smoothing of the moderately precise ( $-0.01$  deg) angle encoder measurements of hub rotation angle. The particular choice of the angle encoder filtering/smoothing/differentiation algorithms and the sample interval were found to impact the behavior of the control law, although we had no difficulty finding a large family of stable designs. Use of an accurate gyro to directly measure the hub angular velocity should eliminate this source of difficulty. It is also significant that more accurate angular rate measurements would permit correspondingly more accurate compensation for the bearing friction/stiction effects.

Of course, roughly analogous problems are associated with the support mechanism (in our case, bearing friction) in any ground maneuver experiment, but obviously disappear in actual zero-g on-orbit implementations. The non-ideal sensor and actuator problems we encountered are judged to be typical of those associated with on-orbit implementations, although hindsight suggests we should have invested in a sensor to directly measure hub angular velocity to eliminate the primary source of difficulty. While the effect of departures from ideal sensor, actuator and support system behavior are present in our experiments, especially near zero angular velocity, the control law nevertheless achieved excellent qualitative agreement with our simulated closed loop response, and routinely isolated the terminal state to within our sensor precision. Furthermore, our experiments were repeatable to within sensor precision. Our simulations and hardware experiments clearly establish that the unmodeled effects are well within the stability robustness margins of our control law.

We feel we have conclusively demonstrated the feasibility of our analytical formulations and experimental approach. We are optimistic that these ideas can be extended to a significant family of multiple flexible body systems and the maneuver control problems associated with multiple body re-configuration, pointing/tracking, and deployment dynamics.

### VIII. Acknowledgments

The authors are pleased to acknowledge the work of H. Fujii, S. R. Vadali, A. Das; their earlier research provided inspiration for this work. The support of the Air Force Office of Scientific Research (Contract F49620-87-C-0078) and A. K. Amos is appreciated. We also received support from the Texas Advanced Technology Program (Project 70110). We thank the following individuals for their contributions: T. C. Pollock for his contributions to all aspects of the design and development of the experiment hardware, Steve Morgan for identifying the structural parameters and for his assistance with the angle encoder, Johnny Hurtado for his assistance in carrying out the experiments, and Becky Masters for excellent support in preparing this manuscript.

## IX. References

1. Junkins, J. L. and Turner, J. D., *Optimal Spacecraft Rotational Maneuvers*, Elsevier, 1986, Amsterdam.
2. Juang, J. N., Horta, L. G., and Robertshaw, H. H., "A Sewing Control Experiment for Flexible Structures", *Proc. of the 5th VPI & SU Symposium on Dynamics and Control of Large Structures*, pp 547-551, Virginia Polytechnic Institute, Blacksburg, VA, June 12-16, 1985.
3. Fujii, H., Ohtsuka, T, and Udou, S., "Mission Function Control for Slew Maneuver Experiment", a preprint, to appear in the *AIAA Journal of Guidance, Control, and Dynamics*.
4. Junkins, J., Rahman, Z., Bang, H., and Hecht, N., "Near-Minimum Time Feedback Control of Distributed Parameter Systems: A Liapunov Control Law Design Method," 7th VPI & SU Symp. on Dyn. & Ctrl. of Large Str., proc. to appear.
5. Rahman, Z., Junkins, J. L., Pollock, T. C., and Bang, H., "Large Angle Maneuvers with Vibration Suppression: Analytical and Experimental Results," 7th VPI & SU Symp. on Dyn. & Ctrl. of Large Str., proc. to appear.
6. Thompson, R. C., Junkins, J. L., and Vadali, S. R., "Near-Minimum-Time Open-Loop Slewing of Flexible Vehicles," *AIAA Journal of Guidance, Control, and Dynamics*, Vol 12, No. 1, Jan-Feb, 1989, pp 82-88.
7. Vadali, S. R., "Feedback Control of Flexible Spacecraft Large Angle Maneuvers Using Liapunov Theory", paper No. 1674, *Proceedings of the 1984 Amer. Ctrls. Conf.*, pp 1674-1678, IEEE, 1984.

8. Byers, R. M., Vadali, S. R., and Junkins, J. L., "Near-Minimum-Time Closed Loop Slewing of Flexible Spacecraft," to appear, *AIAA Journal of Guidance, Control and Dynamics*.
9. Meirovitch, L. and Quinn, R., "Maneuvering and Vibration Control of Flexible Spacecraft," *Journal of the Astronautical Sciences*, Vol, 35, No. 3, July-Sept., 1987, pp 301-328.
10. Singh, G., Kabamba, P., and McClamroch, N., "Planar Time Optimal Slewing Maneuvers of Flexible Spacecraft", to appear, *AIAA Journal of Guidance, Control, and Dynamics*.
11. Breakwell, J. A., " Optimal Feedback Control for Flexible Spacecraft", *AIAA Journal of Guidance, Control, and Dynamics*, Vol 4, No. 5, Sept-Oct 1981, pp 472-479.
12. VanderVelde W. and He, J., "Design of Space Structure Control Systems Using On-Off Thrusters," *AIAA Journal of Guidance, Control, and Dynamics.*, Vol. 6, Jan-Feb., 1983, pp 759-775.

## Appendix: TAMU/AFOSR Maneuver Experiment Hardware Description

Figures 1 - 2 shows sketches of our experimental structure. The structure is comprised of four identical cantilevered flexible appendages, each having a finite tip mass. The actuator is a DC motor with a reaction wheel. The stator of the motor is rigidly connected to the top of the hub keeping the axis of rotation aligned. The whole assembly is pivoted on a ceramic bearing such that it can rotate freely in the horizontal plane. Tipping motion is restrained by an adjustable slip bearing. An angle encoder, two full-bridge strain gauges near the root of an appendage and a motor tachometer are employed to respectively measure the hub angular position, the appendage bending moment and shear forces, and the reaction wheel speed as functions of time. Based on these measurements, and an appropriate control law, a control signal is provided to a current amplifier which drives the DC motor to produce the necessary torque.

Figure 3 shows a block diagram of the overall system. The central unit for the system is a Packard Bell 286 (PB286) computer and Data Translation DT2841 I/O board. The DT2841 performs digital input/output (I/O), analog to digital (A/D) conversion, digital to analog (D/A) conversion and timing operations. Packard Bell 286 reads in data from the I/O board, and does the necessary computations in its own CPU and then sends out the resulting control signal to the amplifier through the I/O board.

The angle encoder (Teledyne Gurley: 8708) output is decoded and converted into a 16 bit digital number in hundredths of a degree by a logic converter (Teledyne Gurley: SCA CC) and counter (C-Tek: Lin-101-50-21-41-BE) combination. The angle encoder is accurate to  $0.01^{\circ}$ . This angle information is read into PB286 through the 16 bit digital port of DT2841. We utilize a sequential least squares filter to extract smoothed angle and angular velocity estimates from the angle encoder measurements. Least square filters are also used to smooth the shear and moment measurements.

The motor used to apply the torque is a PMI Servodisc DC motor equipped with a tachometer. The motor produces a torque proportional to the current in the armature as sent by the current amplifier. The commanded current is sent out to the amplifier by PB286 through digital to analog line (DAC0) of DT2841. The tachometer output is read by the computer through one analog to digital line (ADC2) and used in our control laws to compensate for the motor friction torque. A separate study has been carried out to characterize the motor bearing friction. Except near zero wheel speed, the friction is well-modeled as a quadratic function of the wheel speed. A discontinuity characterizes the nonlinear stiction region at zero wheel speed.

The two full bridge strain gauges are employed near the root of one of the appendages at a finite distance apart from each other to determine the instantaneous bending moment and shear force. The strain gauge signals are read with the PB286 through 2 additional analog to digital channels (ADC0, ADC1). Least square filters are also used to smooth the shear and moment measurements. The bandwidth of the closed loop system was found to be about 10Hz, the limitation to low frequencies is a direct consequence of the errors introduced by deriving the angular rate approximation from the angle encoder measurements.

Four KEPCO Bipolar-operational power supply (BOP's) in series are used to supply current to the motor. They can supply up to 12 Amperes of current for up to a compliance voltage of 150volts. The BOP's are remotely programmed by PB286 through one of the D/A channels (DAC0) of DT2841.

DT2841 from Data Translation Inc. performs all the I/O (Digital, A/D, D/A) operations for PB286. The board has two programmable clocks (DACLK and ADCLK). DACLK and ADCLK are programmed to run at 75Hz and 4000Hz respectively; DACLK runs continuously during a whole control operation and ADCLK runs in a burst mode (i.e.,intermittently).

Every DACLK timing signal initiates the following:

- a.) Converts a digital data into an analog signal to be used by the BOP to push the corresponding current through the motor.
- b) Generates a hardware interrupt to initiate a new control cycle.

The new control cycle proceeds as follows:

- i) read angle encoder (through digital port)
- ii) start ADCLK, complete reading the two strain gauges and the tachometer values (through A/D channels 0, 1, & 2) during the next three ADCLK cycles and then disable ADCLK.
- iii) filter the data digitally
- iv) predict the current required at the beginning of the next cycle
- v) store the data in RAM for time history and make the predicted data available to the D/A converter to be converted at the beginning of the next cycle.
- vii) wait till next DACLK signal which converts the digital data into an analog signal and generates a hardware interrupt to initiate the next control cycle.

The control software is written in FORTRAN except the PB286's interrupt controller setting, the I/O board functions, and I/O routines which are all written in assembly code.

The control cycle is updated at the rate of 75Hz (DACLK rate).

**Table 1. Hub/Appendage Experiment Configuration Parameters**

**Hub & Appendages**

Total System Inertia, $I$	2128 [oz - sec <sup>2</sup> - in]
Hub Center to Gage Center, $l_g$	5.5470 [in]
Hub Center to Tip Mass, $l$	51.07 [in]
Tip Mass, $m$	0.15627 [oz - sec <sup>2</sup> /in]
Appendage Modules of Elasticity, $E$	161.6 [million oz/in <sup>2</sup> ]
Inertia of Bending Section, $I$	0.000813 [in <sup>4</sup> ]
Mass Density of Appendage/Length, $\rho$	0.003007 [oz - sec <sup>2</sup> /in <sup>2</sup> ]
Distance between two gage set	1.365 [in]

**Motor (PML, Servodisc DC Motor: JR16M 4 CH)**

Torque Constant, $K_t$	52.77 [oz-in/amp]
Back EMF Constant, $K_b$	39.77 [v/1000rpm]
Tachometer Constant	3 [v/1000rpm]

**Power Supply (KEPCO BOP 36-12M)**

Current Gain	1.2 [amp/commanded volt]
--------------	--------------------------

Figure 1. Texas A&M Maneuverable Space Structure Experiment

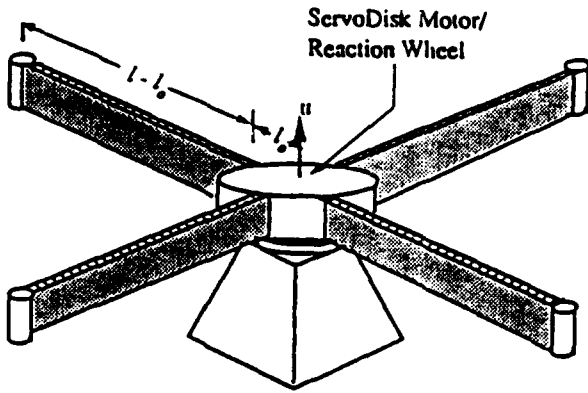


Figure 1a. Configuration Sketch

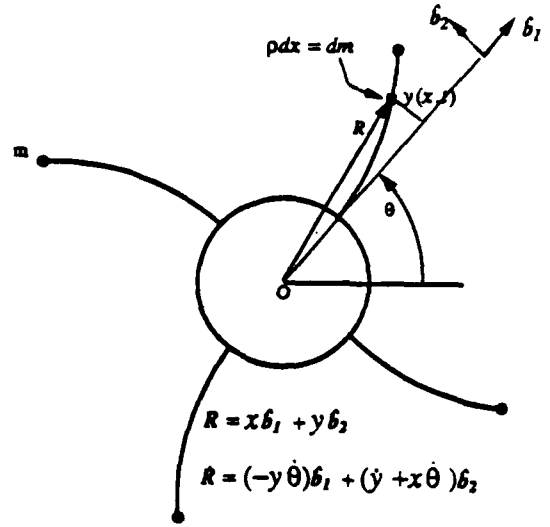


Figure 1b. Anti-Symmetric Deformation

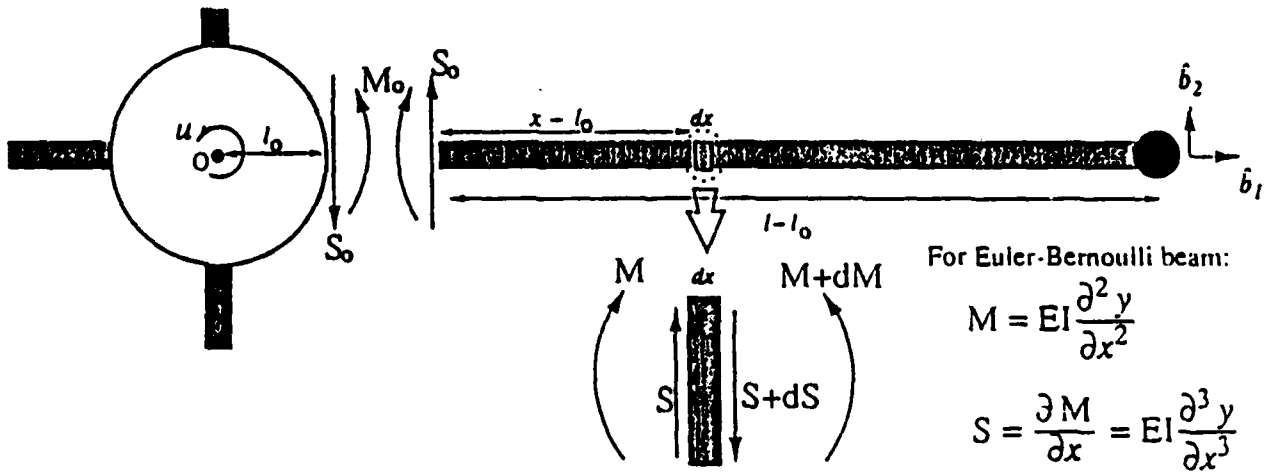


Figure 1c. Notation for Forces, Moments, and Euler-Bernoulli Constitutive Model

Figure 2. Hub Assembly

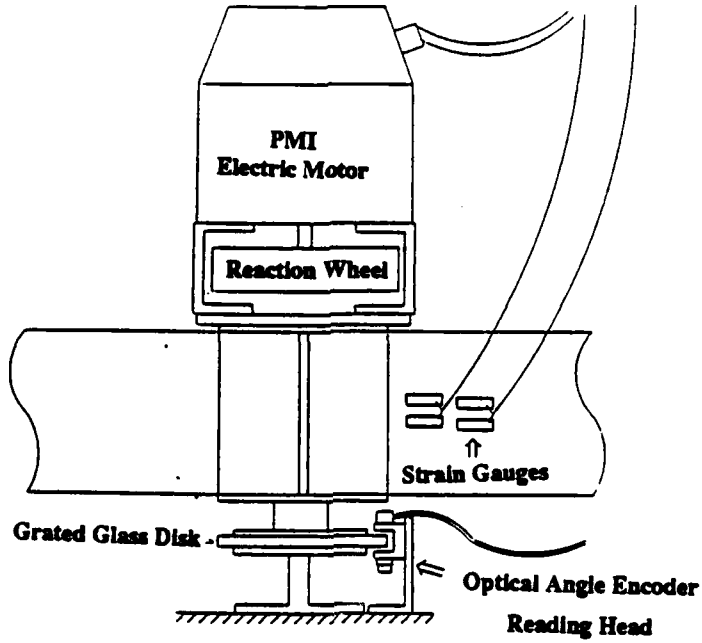


Figure 3. System Functional Block Diagram

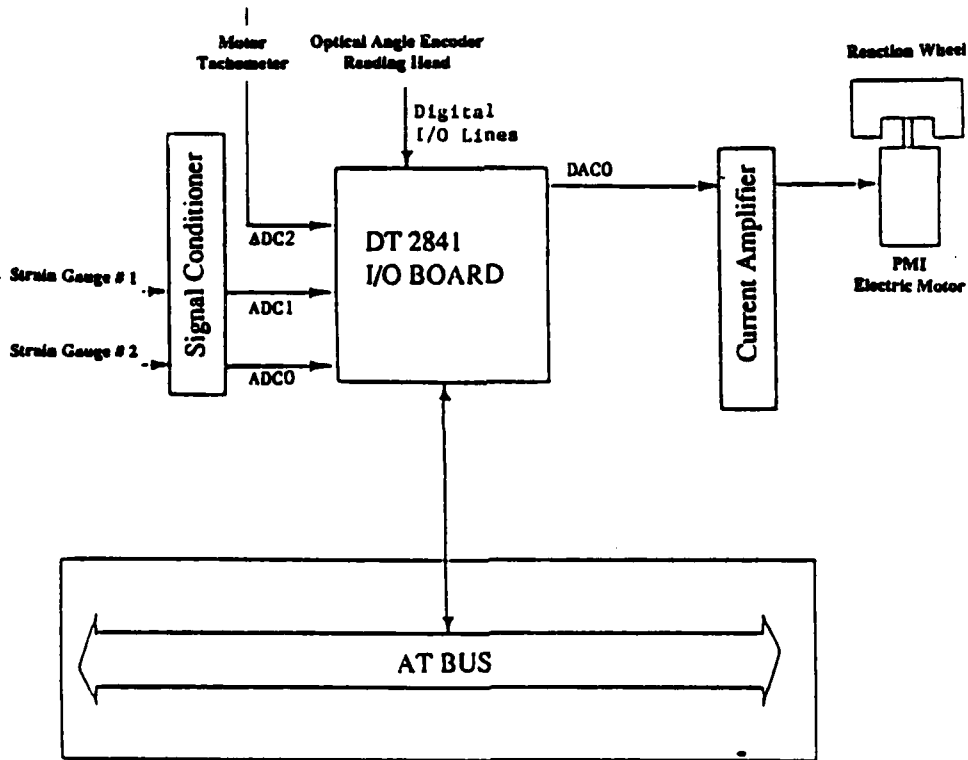


Figure 4. Torque Shaped Rigid Body Maneuver

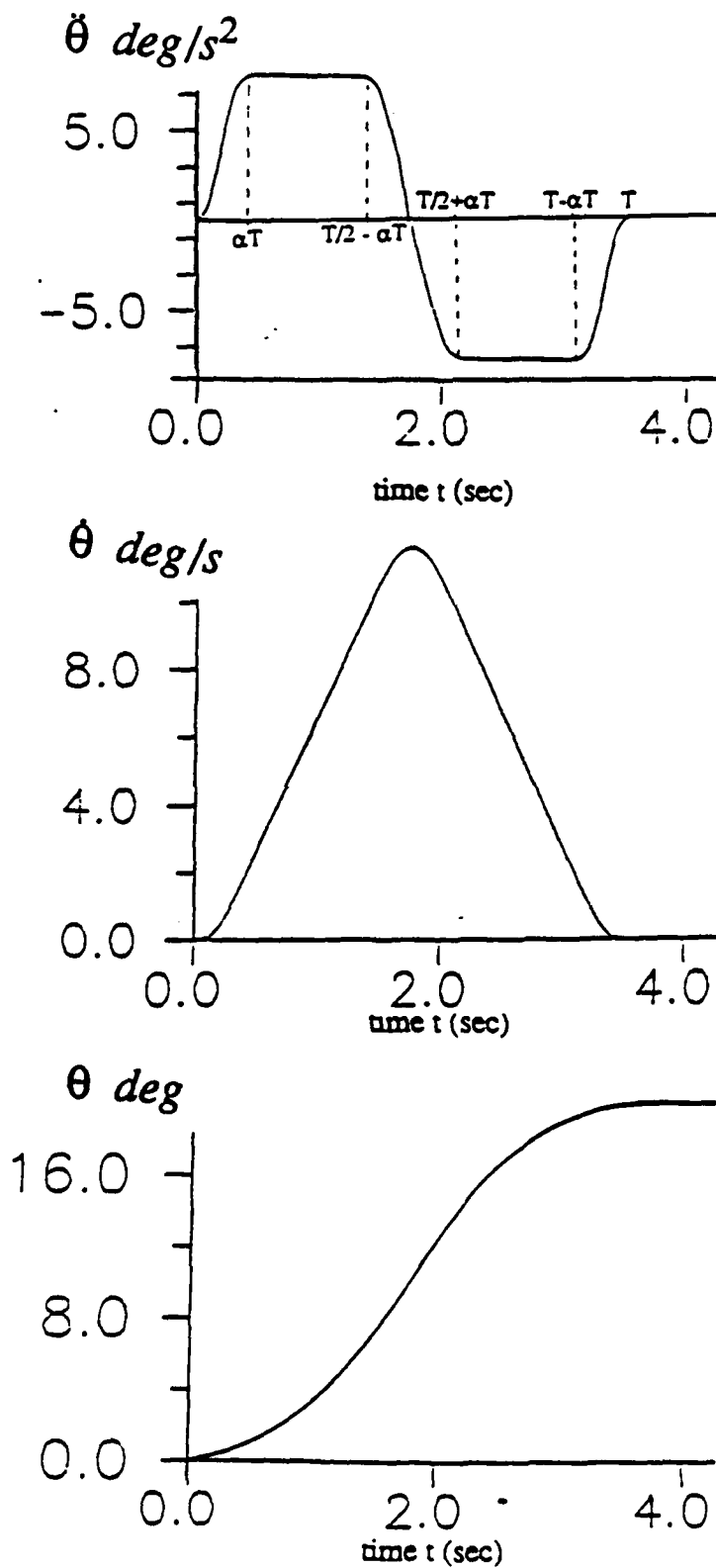


Figure 5. Rigid Body Maneuver vs. Saturation Torque and Shape Parameter

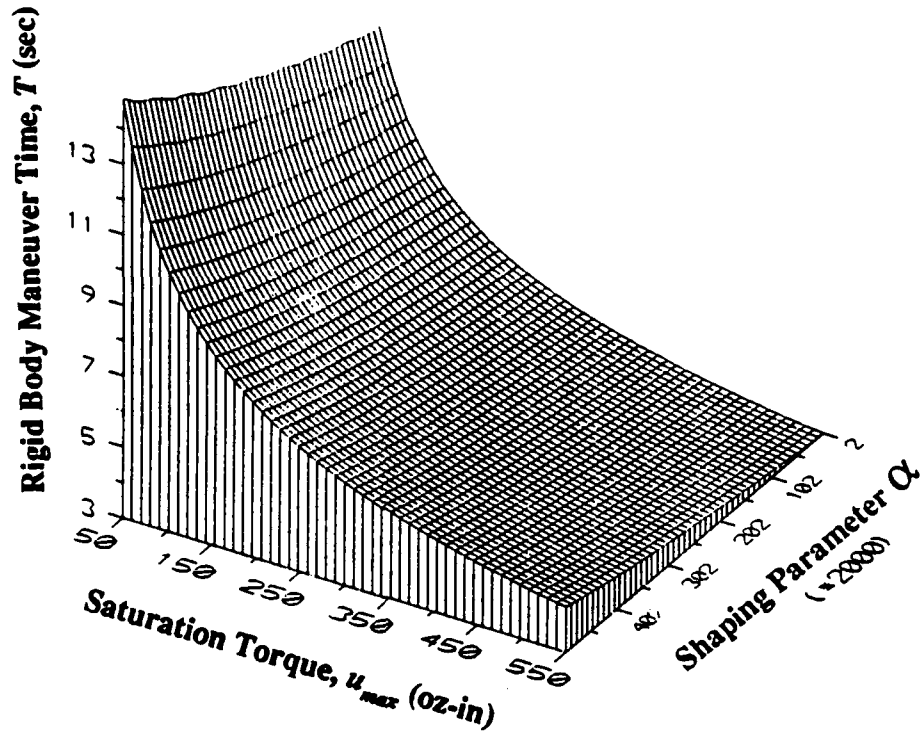
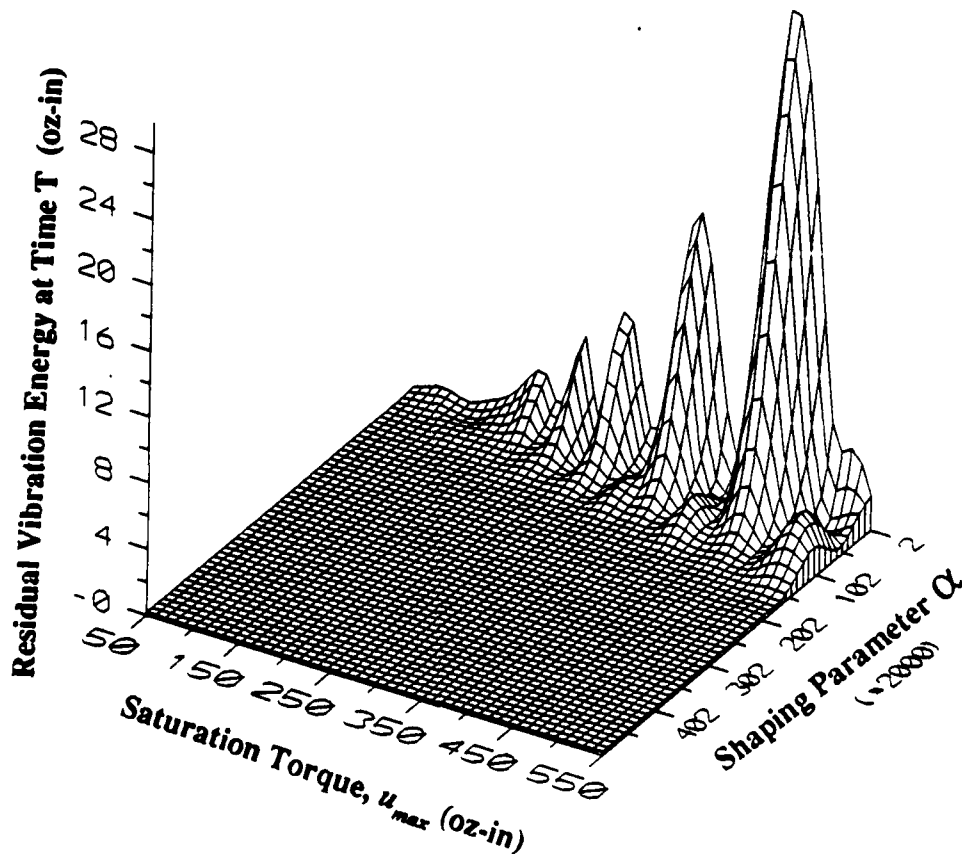


Figure 6. Flexible Body Residual Vibration Energy vs. Saturation Torque and Shape Parameter



**Figure 7. Boundary of the Liapunov-Stable Tracking Region vs. Saturation Torque and Shape Parameter**

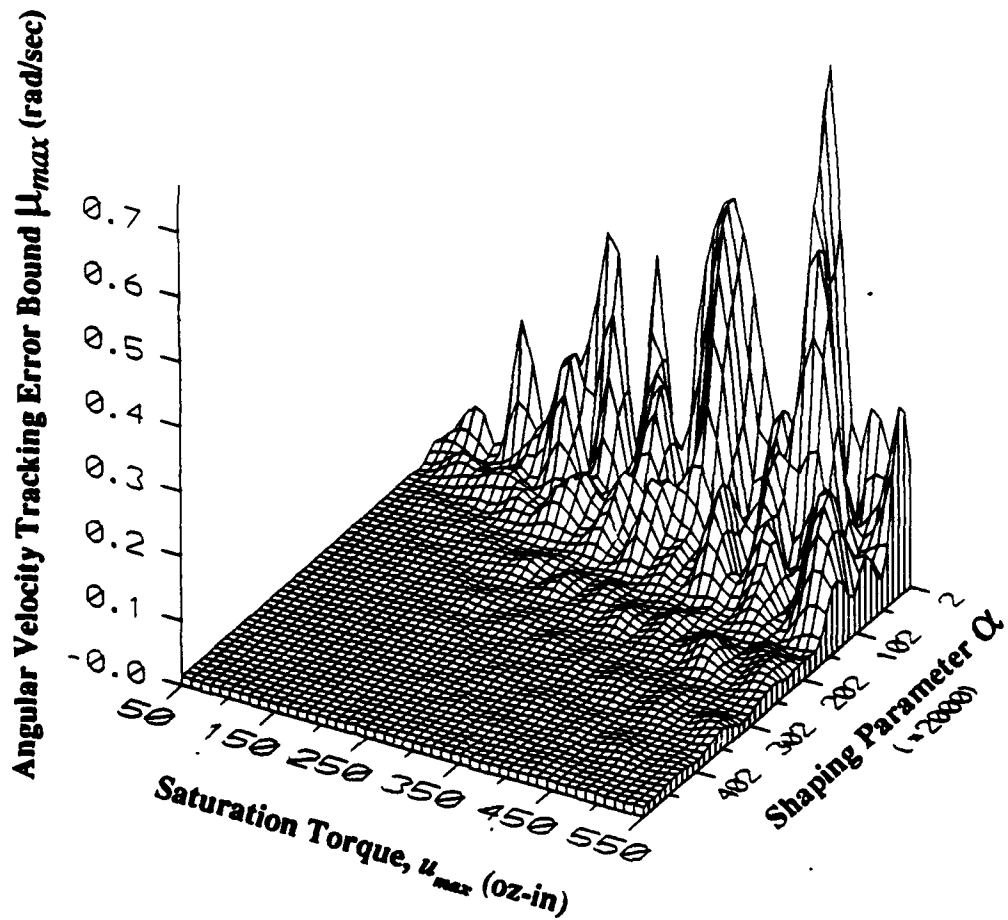


Figure 8. Simulated Open- and Closed-loop 40° Maneuver with Disturbances

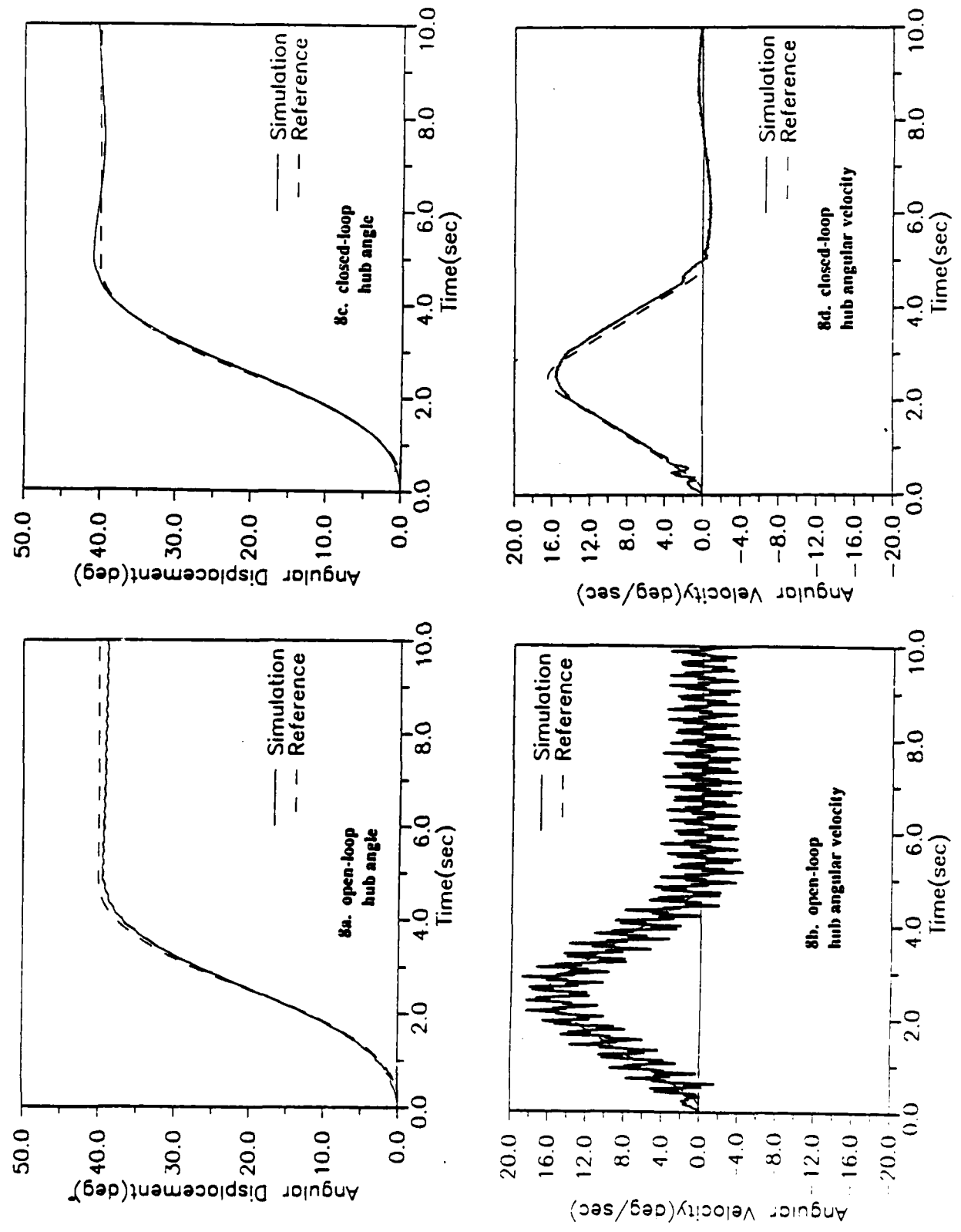


Figure 9. Experimental Results: Control Law I  
 control gains:  $g_1 = 600$  oz-in/rad,  $g_2 = 0$  oz-in/rad/s,  $g_3 = 0$

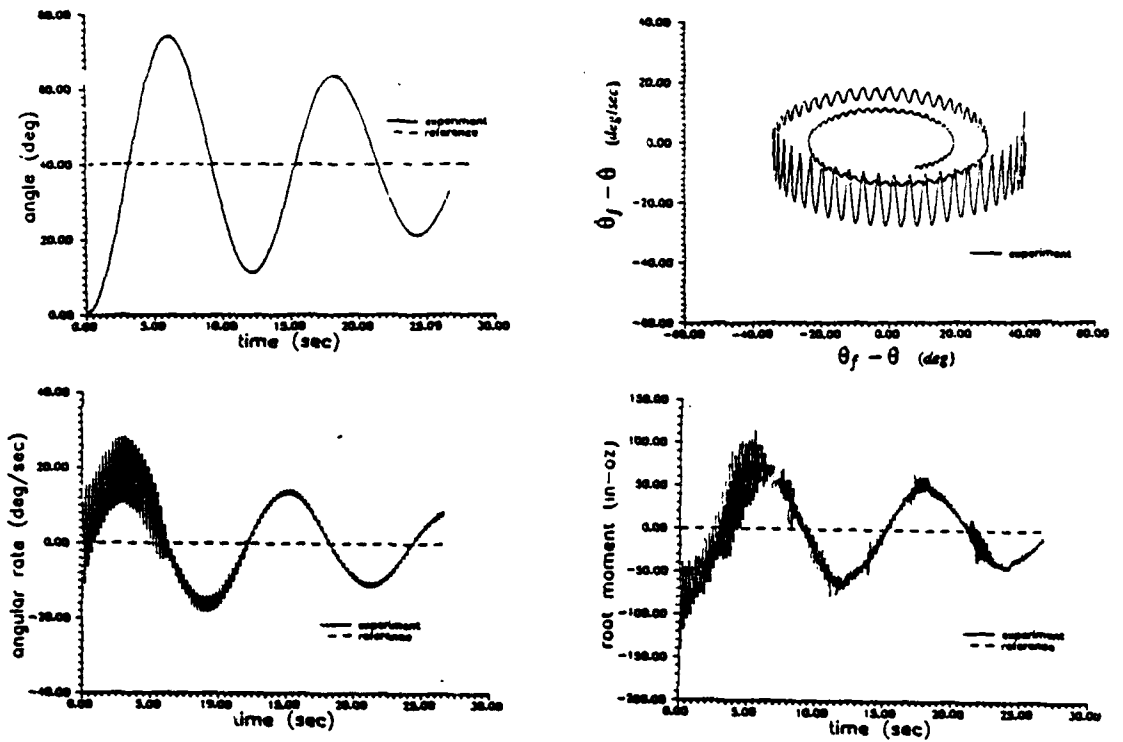
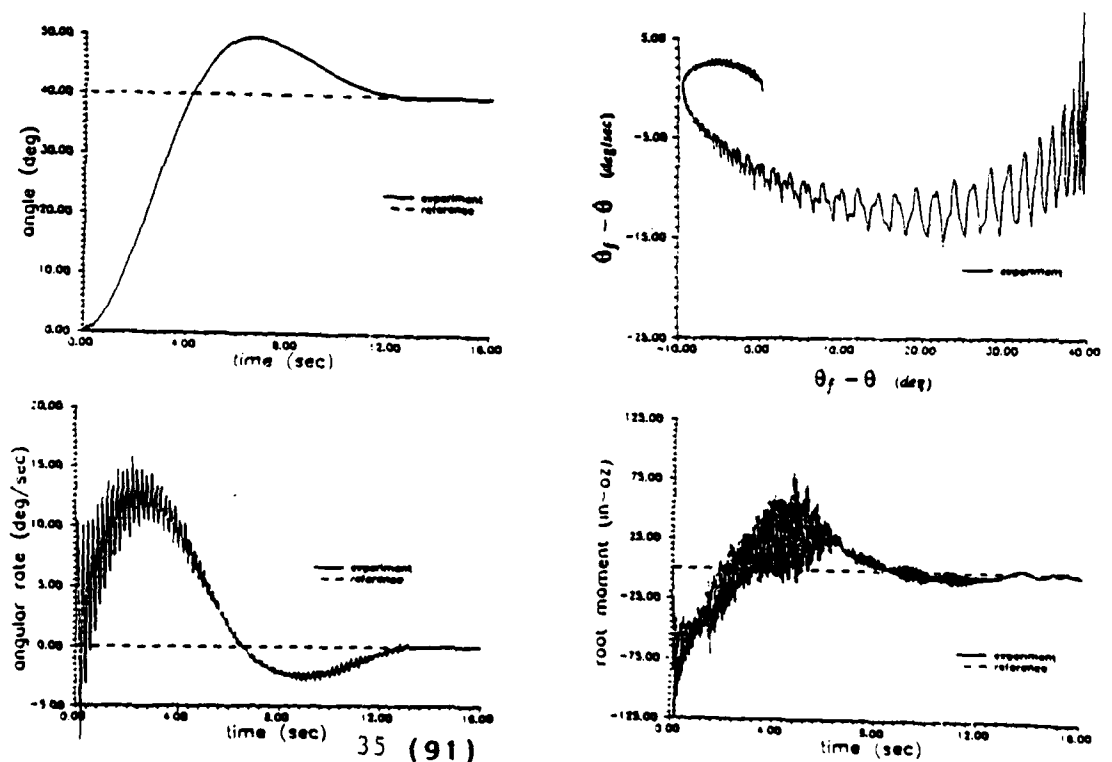
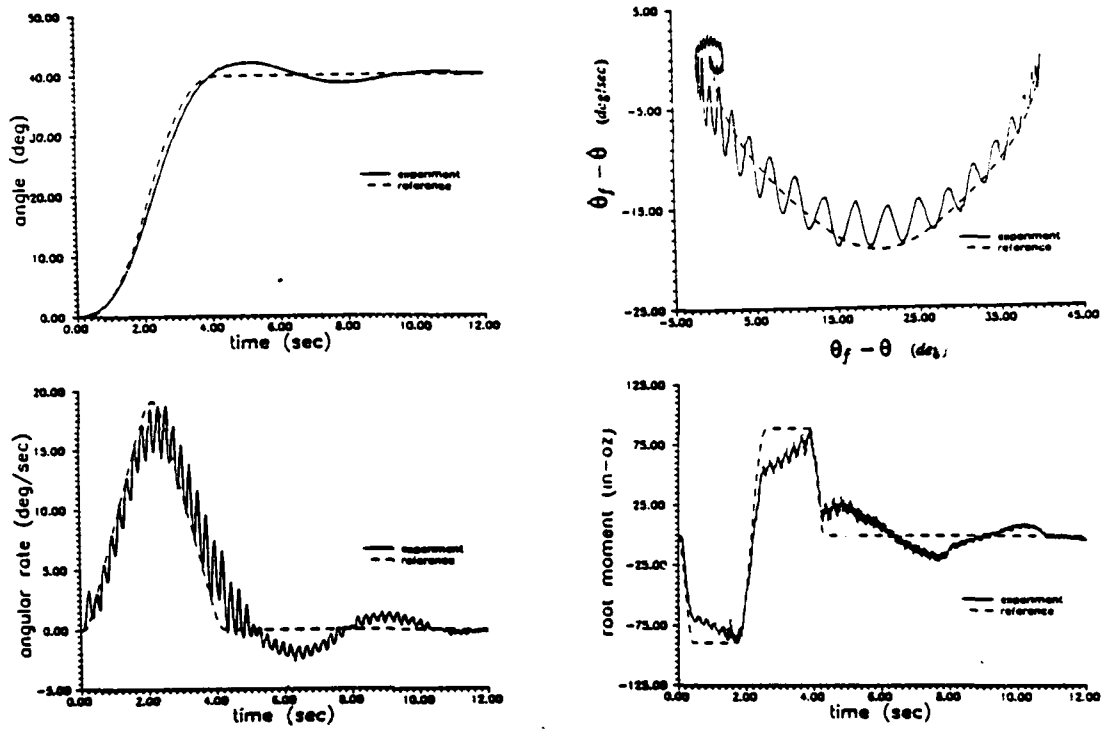


Figure 10. Experimental Results: Control Law I  
 control gains:  $g_1 = 600$  oz-in/rad,  $g_2 = 300$  oz-in/rad/s,  $g_3 = 0$



**Figure 11. Experimental Results: Control Law II**

torque shape parameter:  $\alpha = 0.1$ , control gains:  $g_1 = 3000$  oz-in/rad,  $g_2 = 0$  oz-in/rad/s,  $g_3 = 0$



**Figure 12. Experimental Results: Control Law II**

torque shape parameter:  $\alpha = 0.2$ , control gains:  $g_1 = 3000$  oz-in/rad,  $g_2 = 0$  oz-in/rad/s,  $g_3 = 0$

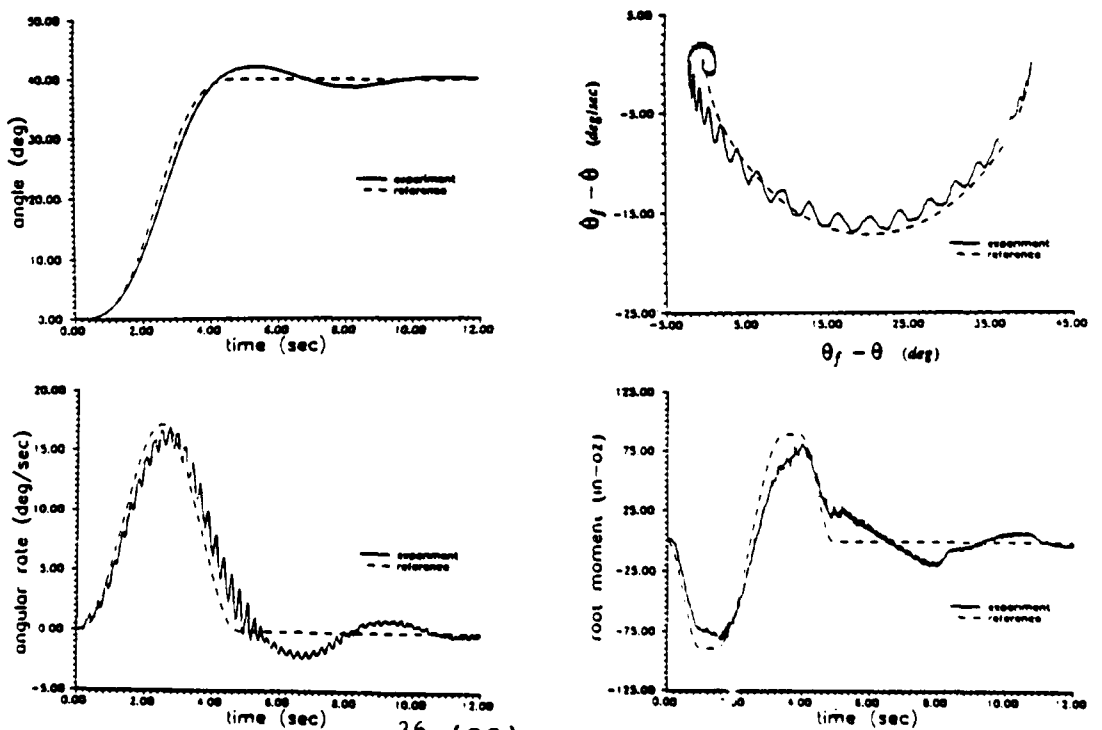


**Figure 13. Experimental Results: Control Law II**

torque shape parameter:  $\alpha = 0.1$ , control gains:  $g_1 = 3000$  oz-in/rad,  $g_2 = 800$  oz-in/rad/s,  $g_3 = 0$

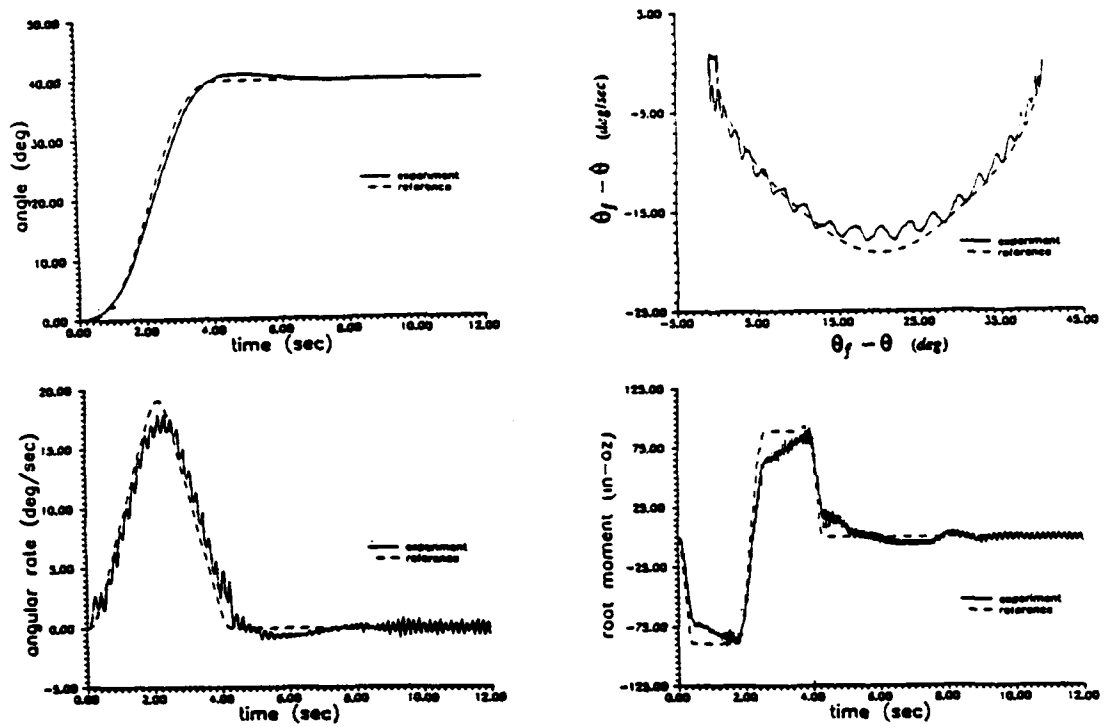


**Figure 14. Experimental Results: Control Law II**

torque shape parameter:  $\alpha = 0.2$ , control gains:  $g_1 = 3000$  oz-in/rad,  $g_2 = 800$  oz-in/rad/s,  $g_3 = 0$

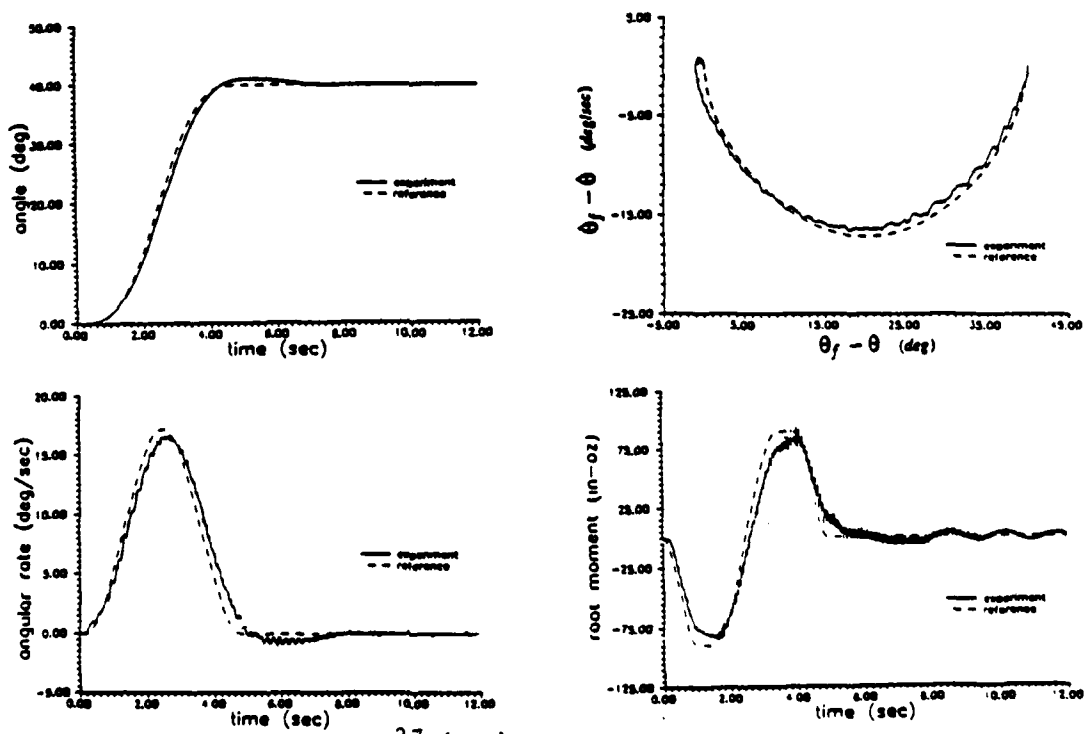


Figure 15. Experimental Results: Control Law II

torque shape parameter:  $\alpha = 0.1$ , control gains:  $g_1 = 3000$  oz-in/rad,  $g_2 = 200$  oz-in/rad/s,  $g_3 = 0.8$

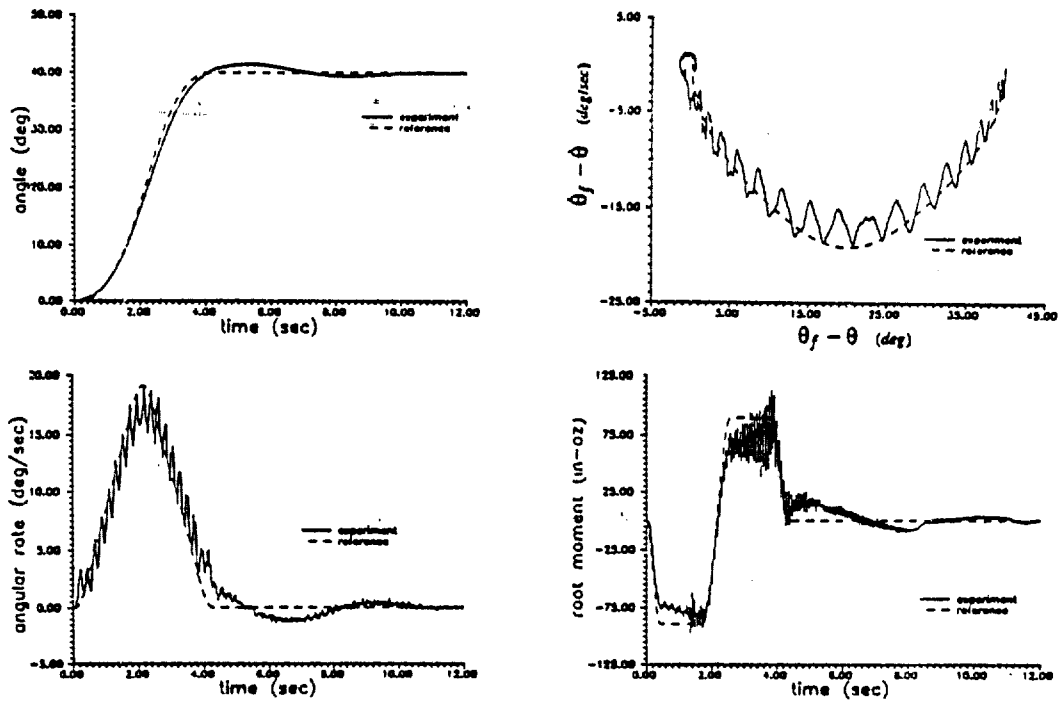
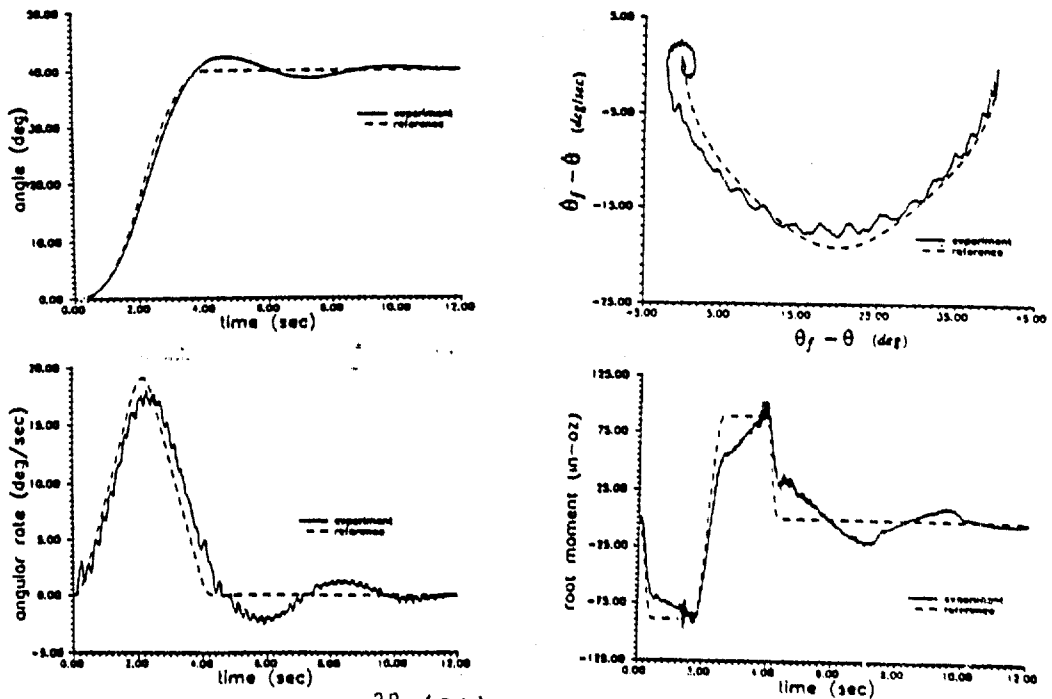


Figure 16. Experimental Results: Control Law II

torque shape parameter:  $\alpha = 0.1$ , control gains:  $g_1 = 3000$  oz-in/rad,  $g_2 = 200$  oz-in/rad/s,  $g_3 = -0.8$



A Measure of Controllability for Actuator Placement

*Youdan Kim      John L. Junkins*

Department of Aerospace Engineering  
Texas A&M University  
College Station, Texas 77843

submitted for publication

AIAA Journal of Guidance, Control, and Dynamics  
December, 1989

and submitted for presentation

AIAA Guidance, Navigation, and Control Conference  
Portland, Oregon  
August, 1990

## A Measure of Controllability for Actuator Placement

Youdan Kim\* and John L. Junkins†  
Texas A&M University, College Station, Texas

### Abstract

*A new measure of controllability for linear time invariant dynamical systems is introduced. The controllability measure is designed especially to guide the placement of actuators to control vibrating structures. An example is presented and the design of optimal feedback control laws for each of several actuator configurations supports the practical value of the new controllability measure.*

### I. Introduction

The problem of choosing actuator locations for the control of large flexible space structures is an important area of current research. By recognizing the fundamental role played by the actuator locations, it is natural that the problem of placing actuators be considered simultaneously with the quest to define meaningful measures of controllability (MOC).

---

\* Ph.D. Candidate, Department of Aerospace Engineering, Member AIAA

† George J. Eppright Chair Professor, Department of Aerospace Engineering, Fellow AIAA

Longman<sup>1,2</sup> presents a definition of a degree of controllability and applies it to optimize actuator placement. For the purpose of model reduction, Moore<sup>3</sup> introduces an internally balanced system by using the singular values to define measures of nearness to rank deficiency of the controllability and observability gramians. The smallest singular value of the controllability gramian (of Moore's balanced system) can be taken as the MOC. Hamdan and Nayfeh<sup>4</sup> proposed a new measure of modal controllability by using the generalized angles between the left eigenvectors of the system matrix  $A$  and the columns of the input influence matrix  $B$  for the system described by the triple  $(A,B,C)$ . They also showed that their measure has interesting connections with Longman's degree of controllability, and is also related to the singular values of Moore's balancing method<sup>5</sup>. Hamdan and Nayfeh's measure provides us useful information on each mode's controllability.

In this paper, we extend Hamdan and Nayfeh's measure by introducing a new controllability index which combines their controllability ideas with modal cost analysis<sup>6,7</sup>. Our index addresses simultaneously the physical importance of each mode and its degree of controllability. In order to evaluate the usefulness of the proposed new index, we design two sets of controllers - one set using symmetric output feedback<sup>8</sup> and another set using the linear quadratic regulator approach: each set includes controllers for ten different configurations (that is, ten different actuator locations for the same structure), and compare the results of the ten pairs

of controllers with the new indices.

## II. Measure of Modal Controllability

Consider the linear dynamical system in the state-space form

$$\dot{x} = Ax - Bu \quad (1)$$

where  $x \in R^n$ ,  $u \in R^m$ ,  $A$  and  $B$  real matrices with appropriate dimensions.

It is well known that the Popov, Belevitch, and Hautus (PBH) eigenvector test<sup>9</sup> is useful to test the modal controllability of the system (1). The PBH eigenvector test specifies that any column vector  $b_j$  of input matrix  $B$  cannot be orthogonal to the  $i$ -th left eigenvector  $q_i$  of  $A$ , if the  $i$ -th mode of the system is controllable. Unfortunately, the information from the PBH eigenvector test is a binary Yes/No type. By introducing an idea based upon a geometrical interpretation of the PBH eigenvector test, Hamdan and Nayfeh<sup>4</sup> proposed the following two measures of controllability:

**Proposition** (Hamdan and Nayfeh)

1) A measure of controllability of the  $i$ -th mode from the  $j$ -th actuator input of the given system is  $\cos \theta_{ij}$ , where  $\theta_{ij}$  is the angle between  $b_j$  and  $q_i$ .

$$\cos \theta_{ij} = \frac{|q_i^T b_j|}{\|q_i\| \|b_j\|} \quad (2)$$

2) The Euclidian (root sum square) norm of the vector  $f_i$ , where  $f_i^T = q_i^T B / \|q_i\|$  is a gross measure of controllability  $\rho_i$  of the  $i$ -th mode from all inputs.

Note that the different power levels in the different inputs on modal controllability is considered in the gross measure of controllability. The gross measure of controllability  $\rho_i$  is related with the measure of controllability as follows:

$$\rho_i = \|f_i\| \tag{3}$$

$$F = (\cos \Theta) \text{diag}[\|b_1\|, \|b_2\|, \dots, \|b_m\|]$$

where  $f_i^T$  is the  $i$ -th row of  $F$ , and  $\cos \Theta$  is the  $m \times n$  matrix of modal controllability measures.

Since a gross measure of controllability of a given mode considering all input is important, we will adopt the second measure of the above proposition as each mode's measure of controllability. When we compute the measure of controllability, we should be careful dealing with the coordinate transformation. Since these measures are not invariant under any coordinate transformation that is not orthogonal, the measures should be used consistently only after all transformations, including scaling have been carried out.

The least controllable mode is often considered to be critical for the controllability of the system, therefore we could conjecture the following rule. *"The smallest value of the gross measures of controllability  $\rho_j$  is the controllability index for the given*

system." This rule is definitely "false" for most practical applications. Consider a system for which the  $k$ -th mode of the system is the least controllable, then the  $k$ -th mode's gross measure of controllability  $\rho_k$  (i.e., the minimum  $\rho_k$ ) would be taken as the system's controllability index if we use the above rule. However, if the  $k$ -th mode does not participate significantly in the important physical outputs of the system, then using only the controllability of the  $k$ -th mode to characterize the system controllability is clearly not suitable. Therefore we need an index which incorporates more information in order to properly measure the controllability of the system. Using some measure of the "relative importance of each mode" to the system performance is recommended to weight the modal controllability measures. The most appealing approach is to combine the modal cost ideas of Skelton *et al.*<sup>6,7</sup> with the modal controllability ideas of Hamdan and Nayfeh<sup>4</sup>. We develop this approach in the following sections and define a new measure of controllability.

### III. Modal Cost Analysis

The scalar function

$$\int_0^{\infty} \mathbf{y}^T(t) \mathbf{Q} \mathbf{y}(t) dt$$

is widely used as a measure of system performance where the vector  $\mathbf{y}(t)$  is composed of those output error variables that are of importance to the designer. The unit

impulse response with zero initial condition is also commonly used to discuss the transient response of the system. By considering the above two observations, we can take the cost function which represents the system performance as follows:

$$V = \int_0^{\infty} y_d^T(t) Q_v y_d(t) dt \quad (4)$$

$$y_d(t) = C_d x(t)$$

where  $x(t)$  is the response due to the unit impulse input applied at  $t = 0$  with zero initial conditions,  $Q_v$  is a weighting matrix, and  $C_d$  is taken such that  $y_d(t)$  be an important variable for the design objectives.

The developments leading to a modal decomposition of this cost function have been derived by Skelton<sup>6</sup>. We may use the contribution of each modal state variable to the cost function as a measure of that mode's relative importance in the system performance. The cost function  $V$  and the contribution  $V_{x_i}$  of the state variable  $x_i$  in the cost function  $V$  can be computed as follows<sup>6</sup>:

$$V = \text{trace}\{Q_v C_d X C_d^T\} \quad (5)$$

$$V_{x_i} = [X C_d^T Q_v C_d]_{ii} \quad (6)$$

where  $X$  is the controllability gramian which satisfies the following Lyapunov equation

$$X A^T - A X - B B^T = 0 \quad (7)$$

What we really need is each modes's contribution to the cost function, which is called the "modal cost". When the "modal" coordinates are used as the state vector, it is obvious that each state's contribution becomes the modal cost. For a formulation of the system dynamics which uses "physical" or "configuration" coordinates in the state vector, on the other hand, the modal cost can be obtained via a modal coordinate transformation.

For a system having a given actuator placement configuration, we can determine each mode's gross measure of controllability and modal cost by using the results presented above and in the current section. In the following section, we address the issue of how to combine the modal cost with the gross measure of modal controllability, to define a new measure of controllability, for the purpose of deciding where to place the actuators.

#### IV. Output Measure of Controllability for the Second Order System

In the study of vibrating mechanical systems we usually encounter the system of  $n$  second order equations

$$M\ddot{x} - C\dot{x} - Kx = Du \quad (8)$$

where  $x \in R^n$  and  $u \in R^m$  are configuration and control vectors, respectively,  $M$  is an  $n \times n$  positive definite symmetric mass matrix,  $C$  is an  $n \times n$  positive semi-definite

symmetric structural damping matrix,  $K$  is an  $n \times n$  positive semi-definite stiffness matrix,  $D$  is an  $n \times m$  control influence matrix, and  $(\dot{\phantom{x}})$  represents differentiation with respect to time.

In Section II, we mentioned that the MOC is generally variant under any coordinate transformation that is not orthogonal. We need to choose the coordinate system in order to discuss controllability. When modal coordinates are used, two well-known benefits are realized: (i) the computational processes become simplified, and (ii) each state's contribution to the cost function corresponds to the modal cost. We will use the modal coordinates for all subsequent discussions.

To perform the modal coordinate transformation, the following open-loop eigenvalue problem should be solved first<sup>10</sup>.

$$K\underline{\phi}_i = \lambda_i M\underline{\phi}_i, \quad i = 1, 2, \dots, n \quad (9)$$

with the normalization equation

$$\underline{\phi}_i^T M \underline{\phi}_i = 1, \quad i, j = 1, 2, \dots, n \quad (10)$$

Introduce the modal matrix

$$\Phi = [\underline{\phi}_1, \underline{\phi}_2, \dots, \underline{\phi}_n] \quad (11)$$

The general modal coordinate transformation is

$$\mathbf{x}(t) = \Phi \underline{\eta}(t) \quad (12)$$

where  $\underline{\eta}(t)$  is the  $n \times 1$  vector of modal coordinates.

The transformed equation of motion becomes

$$\bar{M}\ddot{\underline{\eta}} - \bar{C}\dot{\underline{\eta}} - \bar{K}\underline{\eta} = \bar{D}u \quad (13)$$

where

$$\bar{M} = \Phi^T M \Phi = I$$

$$\bar{C} = \Phi^T C \Phi = \text{diag}(2\zeta_1\omega_1, 2\zeta_2\omega_2, \dots, 2\zeta_n\omega_n)$$

$$\bar{K} = \Phi^T K \Phi = \text{diag}(\omega_1^2, \omega_2^2, \dots, \omega_n^2)$$

$$\bar{D} = \Phi^T D$$

The diagonal structure of  $\bar{C}$  requires that  $C$  be a linear combination of  $M$  and  $K$ , we make this restriction for the sake of convenience. The results developed for computing Hamdan and Nayfeh's controllability measures are directly applicable to the second-order representation (13), these are reported in Ref. 4.

For control applications, the system dynamics are usually modeled in first order differential equations. Let us introduce the "2n" dimensional modal state vector

$$z = \begin{pmatrix} \eta \\ \dot{\eta} \end{pmatrix} \quad (14)$$

Equation (13) can be written as the first order system

$$\dot{z} = Az - Bu \quad (15)$$

where

$$A = \begin{bmatrix} 0 & I \\ -\tilde{K} & -\tilde{C} \end{bmatrix}, \quad B = \begin{bmatrix} 0 \\ \tilde{D} \end{bmatrix} \quad (16)$$

The right and left eigenvalue problems [associated with  $z = pe^{\lambda t}$  solutions of the open loop system in Eq. (15)] are

$$\begin{aligned} \text{right:} \quad \lambda_i p_i &= A p_i & i &= 1, 2, \dots, 2n \\ \text{left:} \quad \lambda_i q_i &= A^T q_i & i &= 1, 2, \dots, 2n \end{aligned} \quad (17)$$

where the conventional normalization<sup>11</sup> of the biorthogonality conditions for the eigenvectors are adopted as

$$\begin{aligned} p_i^T p_i &= 1, & i &= 1, 2, \dots, 2n \\ q_j^T p_i &= \delta_{ij}, & i, j &= 1, 2, \dots, 2n \end{aligned} \quad (18)$$

so that

$$q_j^T A p_i = \lambda_i \delta_{ij}, \quad i, j = 1, 2, \dots, 2n \quad (19)$$

The gross measure of modal controllability can be obtained by using the proposition in Section II with the above left eigenvectors and B matrix in Eq. (15).

In order to evaluate the modal cost for the system, we take the following system performance (Eq. (4)) as the cost function

$$V = \int_0^{\infty} y_d^T(t) Q_v y_d(t) dt \quad (20)$$

$$y_d(t) = \begin{bmatrix} C_{dx} & 0 \\ 0 & C_{d\dot{x}} \end{bmatrix} \begin{pmatrix} x(t) \\ \dot{x}(t) \end{pmatrix} \equiv C_d \begin{pmatrix} x(t) \\ \dot{x}(t) \end{pmatrix} \quad (21)$$

where  $Q_v$  is a weighting matrix,  $y_d(t)$  is a vector of physically important variables and  $x(t)$  is a physical (configuration) coordinate vector.

We adopted the weighting matrix as follows:

$$Q_v = \begin{bmatrix} Q_x & 0 \\ 0 & Q_{\dot{x}} \end{bmatrix} \quad (22)$$

By introducing the modal coordinate transformation, the vector  $y_d(t)$  becomes

$$y_d(t) = C_d \begin{pmatrix} \Phi \eta(t) \\ \Phi \dot{\eta}(t) \end{pmatrix} = \begin{bmatrix} C_{dx} \Phi & 0 \\ 0 & C_{d\dot{x}} \Phi \end{bmatrix} \begin{pmatrix} \eta(t) \\ \dot{\eta}(t) \end{pmatrix} \equiv C_{d\eta} \begin{pmatrix} \eta(t) \\ \dot{\eta}(t) \end{pmatrix} \quad (23)$$

Therefore matrix  $C_d$  in Eqs. (5)-(6) must be replaced by  $C_{d\eta}$  to evaluate the total cost and modal cost in the modal coordinate system. Since modal coordinates are used, we can take advantage of the analytical solution of the  $2n \times 2n$  Lyapunov equation (7), available in Ref. 7:

$$X = \begin{pmatrix} X_{\eta\eta} & X_{\eta\dot{\eta}} \\ X_{\eta\dot{\eta}}^T & X_{\dot{\eta}\dot{\eta}} \end{pmatrix} \quad (24)$$

where the elements of  $n \times n$  block matrices are

$$\begin{aligned} [X_{\eta\eta}]_{ij} &= \frac{2(\zeta_i \omega_i - \zeta_j \omega_j)}{\Delta} [\bar{D} \bar{D}^T]_{ij} & i, j = 1, 2, \dots, n \\ [X_{\eta\dot{\eta}}]_{ij} &= \frac{\omega_i^2 - \omega_j^2}{\Delta} [\bar{D} \bar{D}^T]_{ij} & i, j = 1, 2, \dots, n \\ [X_{\dot{\eta}\dot{\eta}}]_{ij} &= \frac{2\omega_i \omega_j (\zeta_i \omega_j - \zeta_j \omega_i)}{\Delta} [\bar{D} \bar{D}^T]_{ij} & i, j = 1, 2, \dots, n \end{aligned} \quad (25)$$

with

$$\Delta = (\omega_i^2 - \omega_j^2)^2 - 4\omega_i \omega_j (\zeta_i \omega_i - \zeta_j \omega_j)(\zeta_i \omega_j - \zeta_j \omega_i)$$

Note that the  $i$ -th mode's modal cost consists of two parts: the modal cost of the  $i$ -th mode's displacement and the modal cost of the corresponding mode's velocity, that is,

$$V_i = V_{\eta_i} + V_{\dot{\eta}_i} \quad (26)$$

where  $V_i$  is the  $i$ -th mode's cost and  $\eta_i$  is the modal coordinate.

The above  $V_{\eta_i}$  and  $V_{\dot{\eta}_i}$  can be obtained by substituting Eqs. (22)-(24) into Eq. (6) as follows:

$$V_{\eta_i} = [X_{\eta\eta} \Phi^T C_{dx}^T Q_x C_{dx} \Phi]_{ii} \quad (27)$$

$$V_{\dot{\eta}_i} = [X_{\dot{\eta}\dot{\eta}} \Phi^T C_{dx}^T Q_{\dot{x}} C_{dx} \Phi]_{ii}$$

By judicious selection (problem dependent, obviously) of the physically important variable vector  $y_d(t)$ , the modal cost  $V_i$  in the cost function  $V$  represents the contribution of the  $i$ -th mode. Thus the normalized modal cost ( $V_i/V$ ) provides a measure of each mode's relative importance in the system performance. We conjecture that the normalized modal cost ( $V_i/V$ ) is precisely the "measure of importance" needed to weight the modal controllability measure of Hamdan and Nayfeh.

In view of the above considerations, we introduce the following new index as a measure of controllability.

$$\alpha = \sum_{i=1}^n \frac{V_i}{V} \rho_i^2 \quad (28)$$

where

$\alpha$  : New controllability index

$V_i$  :  $i$ -th mode's component cost in the cost function  $V$

$\rho_i$  :  $i$ -th mode's gross measure of modal controllability from all inputs

(Eq. (3)).

Qualitatively, this new index represents a measure of "output controllability" which reflects both modal controllability and the modal participation of all modes in the physically important cost function.

In the following section, we design two controllers (with several actuator configurations) for an example flexible structure, and use the results to evaluate the utility of the new index.

## V. Numerical Examples

To study the utility of the new index proposed in the previous section, two controllers: (i) a robust output feedback controller<sup>8,12</sup> and (ii) a linear quadratic regulator, will be designed for the example flexible structure; we will compare the results of these controllers (for several actuator configurations) with the new controllability index.

We adopt as an example, a sixty degree-of-freedom model of a grid structure<sup>12</sup>. A finite element analysis of the grid was performed. Nodes were placed at each of the twenty joints on the grid. Each substructure of the grid were modeled using beam elements. Three degrees of freedom (one normal displacement and two, transverse and vertical rotations) appropriate for motion normal to the nominal plane of the grid were considered for each node. Figure 1 shows the flexible grid experimental configuration. The material properties for this model are listed in Table 1.

Angular velocity feedback torques are provided by three reaction wheel actuators. The actuator axes (about which control torques are applied) lie in the plane of the grid as indicated by the arrows in Fig. 1. The actuators (Clifton Precision Motors) have approximately a 60 Hz bandwidth and  $\pm 20$  oz-in ( $\pm 0.1412$  N-m) saturation. The grid angular displacement and velocity are measured about the same axes with Watson solid state sensors. These sensors have a DC to 100 Hz bandwidth accurate to  $\pm 0.001^\circ$  and  $\pm 10^{-5}$  rad/sec. The particular position and orientation of the sensors and actuators shown in Figure 1 represent one (Configuration 6) of the ten configurations which will be discussed. In order to avoid disruption of the symmetrical property of the grid structure, only symmetrical locations and the direction of the actuators are considered in the present discussion, and the admissible actuator locations considered are the 20 grid locations and the direction of the actuators are permitted to be either vertical or horizontal. The locations

Table 1. Material Properties of Grid Model

EI	3255.2 lb · in <sup>2</sup>	9.34982 N · m <sup>2</sup>
GJ	4943.0 lb · in <sup>2</sup>	14.18550 N · m <sup>2</sup>
$\rho A$	0.0000648 lb · sec <sup>2</sup> · in <sup>2</sup>	0.44678 kg/m
$\rho J$	0.0000217 lb · sec <sup>2</sup>	0.0000965 kg · m

and the direction of the actuators of ten configurations are displayed in Figure 2. In all cases the actuator torque axis and the active sensor axis are co-located as accurately as possible. We present only numerical studies in the present paper. A future paper will address experimental issues and results.

For high order systems such as a flexible structure, it is usually desirable and often necessary to develop a reduced-order model to save on computational time when designing control laws. A high order model is generally retained to verify the resulting design. The most common order reduction method is the modal truncation method in which a partition is introduced into the modal matrix to select a subset of low frequency modes (determined to be of most importance in the particular application). The criteria for mode selection can be based upon modal cost, for example. The general modal coordinate transformation is partitioned as

$$\mathbf{x}(t) = \Phi \underline{\eta}(t) = [\Phi_1 \quad \Phi_2] \begin{pmatrix} \eta_1(t) \\ \eta_2(t) \end{pmatrix} \quad (29)$$

where  $\Phi$  is the modal matrix solved from the eigenvalue problem (Eq. (9)),  $\eta_1$  is

the retained subset of  $n_r$  modal coordinates which we are interested in including in the reduced order model, and  $\underline{\eta}_2$  is the residual modal coordinates.

The reduced-order equation of motion becomes

$$\tilde{M}\ddot{\underline{\eta}}_1 + \tilde{C}\dot{\underline{\eta}}_1 - \tilde{K}\underline{\eta}_1 = \tilde{D}u \quad (30)$$

where

$$\tilde{M} = \Phi_1^T M \Phi_1 = I$$

$$\tilde{C} = \Phi_1^T C \Phi_1 = \text{diag}(2\zeta_1\omega_1, \dots, 2\zeta_{n_r}\omega_{n_r})$$

$$\tilde{K} = \Phi_1^T K \Phi_1 = \text{diag}(\omega_1^2, \dots, \omega_{n_r}^2)$$

$$\tilde{D} = \Phi_1^T D$$

A reduced order model is used for the current design process. In this example, we simply adopted the first ten lowest frequency modes. The order reduction process is not central to this discussion, although it is important that a "good" reduced order model be used to obtain practical results efficiently. Since the controllers are designed by using the reduced-order model, there is no additional problems introduced by using a reduced-order model to evaluate the new index. Some physically important variable vector is selected to construct the cost function. For this simple illustration, the normal displacement (perpendicular to the grid plane) of the lower-left corner is taken to be  $y_d$ .

## Control Design 1 : Symmetric Output Feedback Design

For the above model, we apply a symmetric output feedback controller<sup>8,12</sup> design method to move the system's first three modes to a desired region and, subject to this condition, minimize a robustness measure (e.g., the sensitivity of the eigenvalues with respect to variation of uncertain parameters). For the measure of sensitivity, we use the condition number of the closed loop eigenvector matrix.

The symmetric or "structural" output feedback form of the control law (collocated sensors and actuators) is given by

$$\mathbf{u} = -(\mathbf{G}_1 \bar{\mathbf{D}}^T \underline{\eta}_1 + \mathbf{G}_2 \bar{\mathbf{D}}^T \underline{\dot{\eta}}_1) \quad (31)$$

where  $\mathbf{G}_1$  and  $\mathbf{G}_2$  are  $m \times m$  positive definite symmetric gain matrices.

For any/all choices for the gain matrices from this stable family (i.e., the set of all positive definite  $\mathbf{G}_i$  matrices), asymptotic stability of the closed-loop system is guaranteed in the Lyapunov sense. Of course, we do not choose the  $\mathbf{G}_i$  at random. Positive definite gain matrices are parameterized by introducing the Cholesky decomposition, and the gain parameter vector is defined as  $\mathbf{p}_{\text{gain}}$ , the distinct elements of the Cholesky factors of  $\mathbf{G}_1$  and  $\mathbf{G}_2$ <sup>8,13</sup>. With the above formulation, our gain design problem becomes a nonlinear optimization problem as follows:

$$\text{Minimize } \mathcal{K}(\Phi^c(\mathbf{p}_{\text{gain}})) \quad (32)$$

subject to closed-loop eigenvalue placement constraints, for example, we adopt the frequency constraints

$$\omega_i^o - \Delta\omega_i \leq \omega_i^c \leq \omega_i^o + \Delta\omega_i, \quad \Delta\omega_i = 1 \text{ percent of } \omega_i^o, \quad i = 1, \dots, 3$$

and the time constant constraints

$$\omega_i^c \zeta_i^c \geq T_i, \quad i = 1, \dots, 3$$

where

$$\omega_i^c(\mathbf{p}_{\text{gain}}) = \text{Im}(\lambda_i)$$

$$\zeta_i^c(\mathbf{p}_{\text{gain}}) = -\frac{\text{Re}(\lambda_i)}{|\lambda_i|}$$

$\mathcal{K}(\Phi^c(\mathbf{p}_{\text{gain}}))$  is the condition number of the closed loop eigenvector matrix, and the superscripts c and o denote the closed-loop and the open loop.

For this example we take the time constants as  $T_1=0.2$ ,  $T_2=0.2$ , and  $T_3=0.25$ . The above nonlinear constrained optimization problem can be solved by homotopic nonlinear programming<sup>13,14</sup> in conjunction with a minimum norm gain correction strategy.

The computed output measures ( $\alpha$  of Eq. (28)) of the system controllability for the ten different configurations and the results of the controllers designed for the corresponding configurations are summarized in Table 2. The configuration number is an arbitrary reference number we assigned a priori for each configuration.

Table 2. The Measure of Controllability (Output Feedback Controller)

Configuration	New Index( $\alpha$ )	$\ \bar{G}_1\ _F$	$\ \bar{G}_2\ _F$	Cond. No.
9	0.00333	0.306	6.514	129.864
8	0.00234	0.142	7.434	131.611
10	0.00208	0.444	7.691	161.167
4	0.00158	1.600	7.732	128.707
5	0.00153	6.804	9.827	130.363
6	0.00130	1.595	31.143	147.774
3	0.00123	6.745	19.920	159.009
2	0.00102	13.379	16.483	140.672
7	0.00084	21.576	16.411	140.715
1	0.00078	22.160	25.379	141.402

In the Section IV, the output measure of controllability is conjectured to properly weigh both modal controllability and participation in the output cost function. That means, we expect the configuration possessing the large index to be more output controllable than one having the small index. We further expect that more controllable configurations should require less energy to control the system, and therefore, we anticipate the associated optimal controller to have smaller gain matrices. Based upon these heuristic observations, for example, if Eq. (28) is an appropriate measure, we should anticipate the large  $\alpha$  designs will correspond to the smaller control gains. As we can see in Table 2, the magnitudes of the total gain

norms of the first four configurations (configuration number 9,8,10, and 4) are indeed significantly smaller than those of the remaining six configurations. In fact, designs 9,8,10, and 4 appear to be correctly ranked based upon the fact that decreasing  $\alpha$  corresponds to an increasing control gain norm. All of the above designs have closed loop modal matrices with small condition numbers, but it is also significant that the small condition numbers appear to be negatively well-correlated with large  $\alpha$  values. These results imply that the new index proposed is highly correlated to the actual controllability and robustness of the system and can apparently serve as an excellent indication of the desirability of a given actuator configuration.

### ***Control Design 2 : Linear Quadratic Regulator Design***

The symmetric output feedback controller used in Controller Design 1 (and implicit in Table 2) is perhaps unfamiliar to many readers. Since this is true and in order to confirm the usefulness of the new index, we also designed control laws for each of the ten actuator configurations using the well-known linear quadratic regulator (LQR) and we compare the results with the new indices as well as the symmetric output feedback designs of Table 2. We adopted the following performance index for LQR:

$$J = \int_0^{\infty} (z^T Q z - u^T R u) dt \quad (33)$$

where

$$Q = \begin{bmatrix} \Omega & 0 \\ 0 & I \end{bmatrix} \quad R = rI$$

$$z = \begin{pmatrix} \eta_1 \\ \underline{\eta}_1 \end{pmatrix}$$

$$\Omega = \text{diag}[\omega_1^2, \omega_2^2, \dots, \omega_{n_r}^2]$$

the scalar  $r$  is chosen in order to satisfy the conditions  $\omega_i^c \zeta_i^c \geq T_i$ ,

$$i = 1, \dots, 3 \text{ with } T_1 = 0.2, T_2 = 0.2, \text{ and } T_3 = 0.25.$$

The above performance index is an energy type, since the first term and the second term in the performance index correspond to the state energy and the control energy respectively. Note  $r$  is a tuning factor used to place the first three closed-loop eigenvalues to achieve the desired time constant. Without judiciously assigning the tuning factor  $r$  we cannot control the position of the closed-loop eigenvalues, and the closed-loop performances for the different configurations become dispersed. The results of the LQR controller designs for the ten configurations and the corresponding configuration's new index are summarized in Table 3. Note in Table 3 that the magnitude of the gain norm of the first four configurations is again smaller than that of the remaining six configurations.

Note in Table 3 that after the first four designs (9,8,10,4), the descending order of the new index is different from that of the magnitude of the output feedback controller, and is also different from that of LQR. It is obvious that the two

Table 3. The Measure of Controllability (LQR : Full State Feedback))

Configuration	New Index( $\alpha$ )	$G_{\alpha}$	Cond. No.
9	0.00333	11.2704	128.3908
8	0.00234	10.5103	127.8386
10	0.00208	22.1138	131.9951
4	0.00158	15.1570	129.2909
5	0.00153	45.3070	140.6412
6	0.00130	96.3776	144.0756
3	0.00123	48.9767	135.9563
2	0.00102	48.8298	135.6727
7	0.00084	47.4010	135.7873
1	0.00078	47.0973	135.7440

gain optimization problems should not be expected to produce the same results, especially since the design of Table 2 are output feedback whereas those of Table 3 are full-state feedback. Therefore we can not expect that the new index is one-to-one mapped with the results of the two design methods studied (or any other!) In view of this, the proposed new index appears to be a remarkably good measure of controllability for the given configuration, since the results in Tables 2 and 3 are well correlated. Notice that the first four configurations (9.8.10.4) have smallest gains in both Table 2 and 3 as compared to the other six designs.

Two of the ten configurations - to illustrate the consequences of using relatively

"good" and "bad" configurations, we adopted for further study. Specially configurations No. 9 and 6 were taken to study the closed-loop performance of both the symmetric output feedback control (design 1) and the LQR full-state feedback control (design 2). The closed loop response histories of the normal displacement to the grid plane (at three nodes of the bottom of the grid structure) of two configurations due to a typical set of initial conditions are shown in Figures 3 and 5, and the control input histories are displayed in Figures 4 and 6. The typical set of initial conditions are constructed by using static loading such that the displacement of the lower-left corner be 1 inch (2.54 cm). The static load is removed at the initial time. We have imposed control saturation bounds (20 oz-in; 0.1412 N-m) to keep the reaction wheel speeds to modest levels. First, consider the symmetric output feedback design (control design 1). Note in the figures (a) and (b) of Fig. 3 that the closed-loop performance of configuration No. 6 and No. 9 are almost identical. When you study the figures (a) and (b) in Fig. 5, however, it is evident by inspection that configuration No. 9 needs more control input energy. That is consistent with our expectation based upon the computed output measures of controllability. We reach the same conclusion when we compare the closed-loop responses (Fig. 4) and the control torque histories (Fig. 6) of the LQR (control design 2.) Thus we are again encouraged that the controllability measure predicts the correct trend for the controlled response with two distinct underlying controller design optimizations.

## VI. Discussion

The present paper introduces a new measure of controllability and considers its implications for actuator placement. The proposed new index  $\alpha$  of Eq. (28) is a combination of the squares of Hamdan and Nayfeh's modal controllability measures weighted by the respective modes' contributions to a quadratic output cost function. The usefulness of this new index has been verified by comparing the results of two control design methods for a grid structure with ten different actuator configurations.

## Acknowledgements

The authors are pleased to acknowledge that our initial interest in this research topic <sup>arose</sup> ~~was~~ following discussions with R.W. Longman. We also benefited from studying the research contribution of A.H. Nayfeh, A.M.A. Hamdan, R.E. Skelton, and B.C. Moore. This research was supported by the Air Force Office of Scientific Research under Contract F49620-87-C-0078, and the Texas Advanced Technology Program, Project No. 70110.

## References

1. Viswanathan, C.N., Longman, R.W., and Likins, P.W., "A Degree of Controllability Definition: Fundamental Concepts and Application to Modal Systems," *AIAA Journal of Guidance, Control, and Dynamics*, Vol.7, No.2, 1984, pp.222-230.
2. Lindberg, R.E. and Longman, R.W., "Optimization of Actuator Placement via Degree of Controllability Criteria Including Spillover Considerations," *AIAA/AAS Paper 82-1435*, San Diego, Calif., August 1982.
3. Moore, B.C., "Principal Component Analysis in Linear Systems: Controllability, Observability, and Model Reduction," *IEEE Transactions on Automatic Control*, Vol. AC-26, No.1, 1981, pp.17-32.
4. Hamdan, A.M.A. and Nayfeh, A.H., "Measure of Modal Controllability and Observability for First- and Second-Order Linear Systems," *AIAA Journal of Guidance, Control, and Dynamics*, Vol.12, No.3, 1989, pp.421-428.  
Same authors and title: Erratum, *AIAA JGCD*, Vol.12, No.5, 1989.
5. Lindner, D.L., Babendreier, J., and Hamdan, A.M.A., "Measures of Controllability and Observability and Residues," *IEEE Transactions of Automatic Control*, Vol. AC-34, No.6, 1989, pp.648-650.

6. Skelton, R.E., "Dynamic System Control - Linear System Analysis and Synthesis." John. Wiley, 1988.
7. Skelton, R.E., Singh, R., and Ramakrishnan, J., "Component Model Reduction by Component Cost Analysis," AIAA Guidance, Navigation, and Control Conference, Minneapolis, Minnesota, August, 1988.
8. Junkins, J.L. and Kim, Y., "A Minimum Sensitivity Design Method for Output Feedback Controllers," AIAA "Progress in Aeronautics and Astronautics Series" 1990, Mechanics and Control of Large Space Structures, Chapter 17, to be published.
9. Kailath, T., Linear Systems, Prentice-Hall, Englewood Cliffs, NJ, 1980.
10. Meirovitch, L.. Computational Methods in Structural Dynamics. Sijthoff & Moordhoff, The Netherlands, Rockville, Maryland, 1980
11. Lim, K.B., Junkins, J.L., and Wang, B.P., "Re-examination of Eigenvector Derivatives," AIAA Journal of Guidance, Control, and Dynamics, Vol.10, No.6, 1987, pp.581-587.
12. Creamer, N.G. and Junkins, J.L., "A Pole Placement Technique for Vibration Suppression of Flexible Structures," AIAA/AAS Astrodynamics Conference, Minn., MN, Aug. 15-17, 1988.

13. Junkins, J.L. and Kim, Y., "First and Second Order Sensitivity of the Singular Value Decomposition," Preprint, To appear, *Journal of the Astronautical Sciences*, 1989.
14. Donyak, J.P., Junkins, J.L., and Watson, L.T., "Robust Nonlinear Least Square Estimation Using the Chow-Yorke Homotopy Method," *AIAA Journal of Guidance, Control, and Dynamics*, Vol.7, No.6, 1984, pp.752-755.

**Figure 1. Texas A&M Structural Control Test Article**

The grid is a 5' x 5' aluminum grid cut from a single piece of aluminum. It is clamped and mounted in a vertical plane. The first natural frequency is .8 Hz, 10 modes have natural frequencies below 30 Hz.

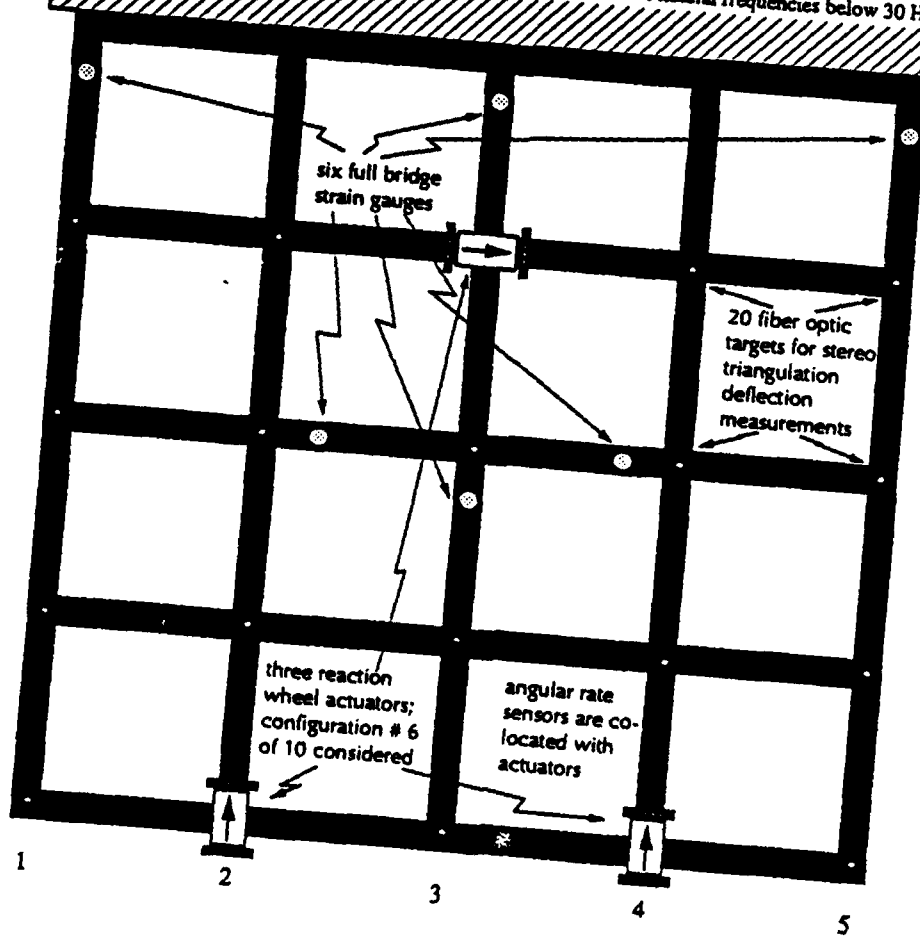
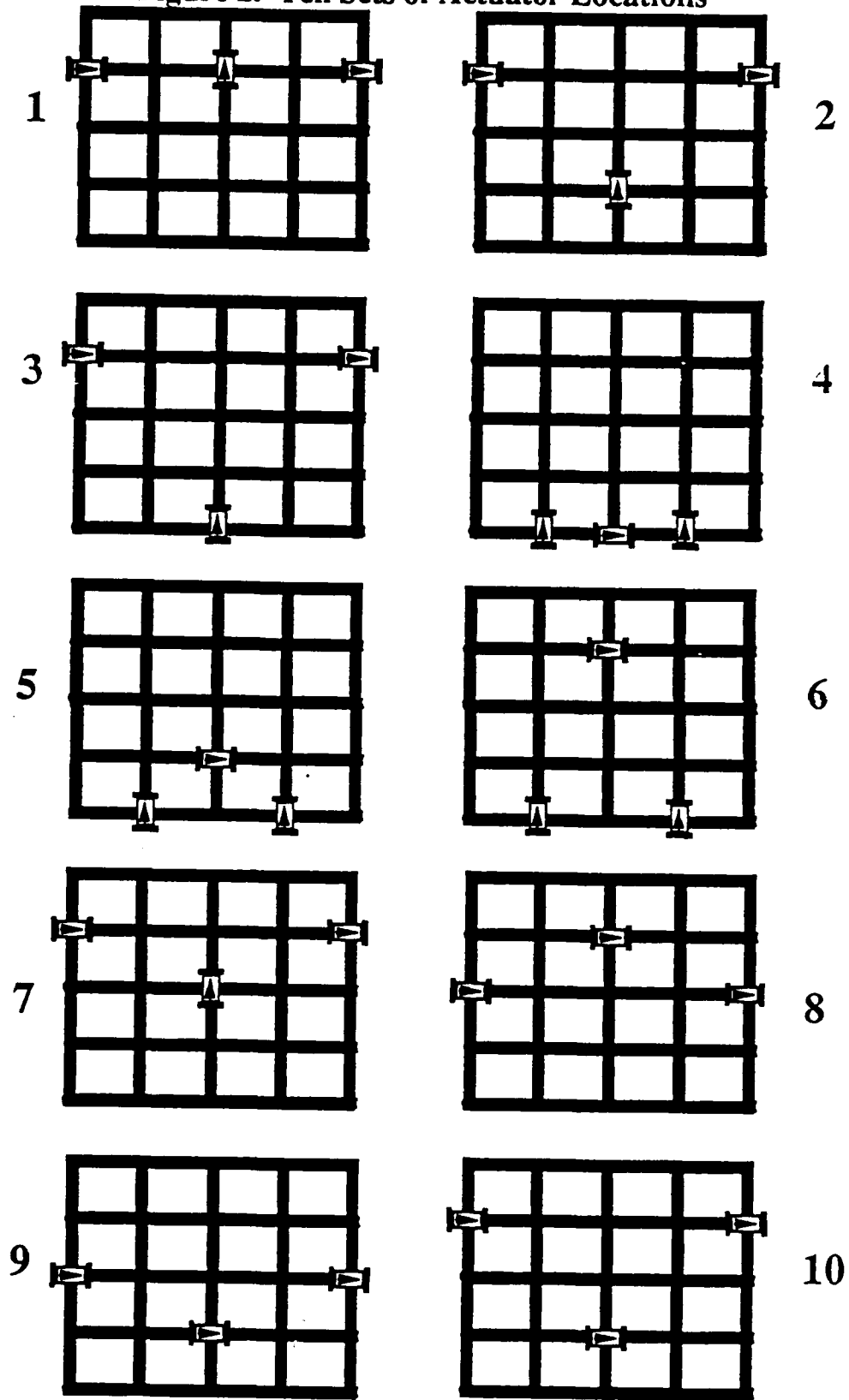
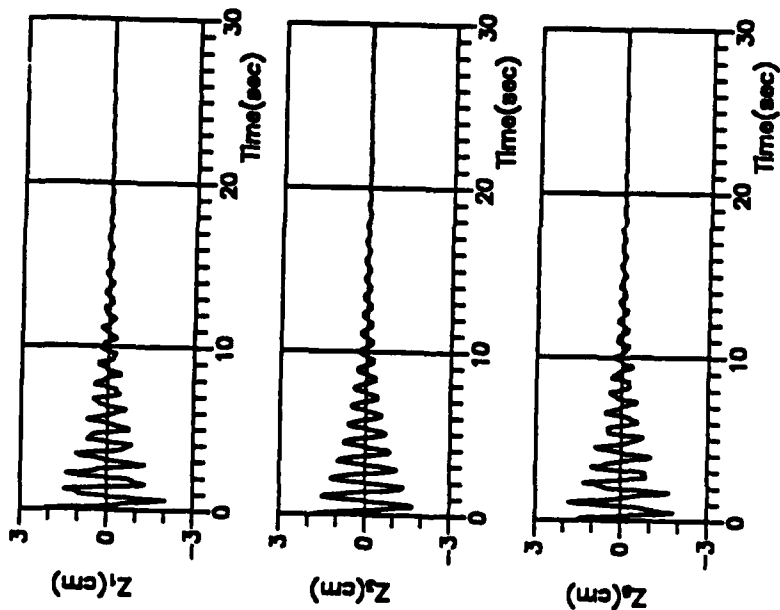
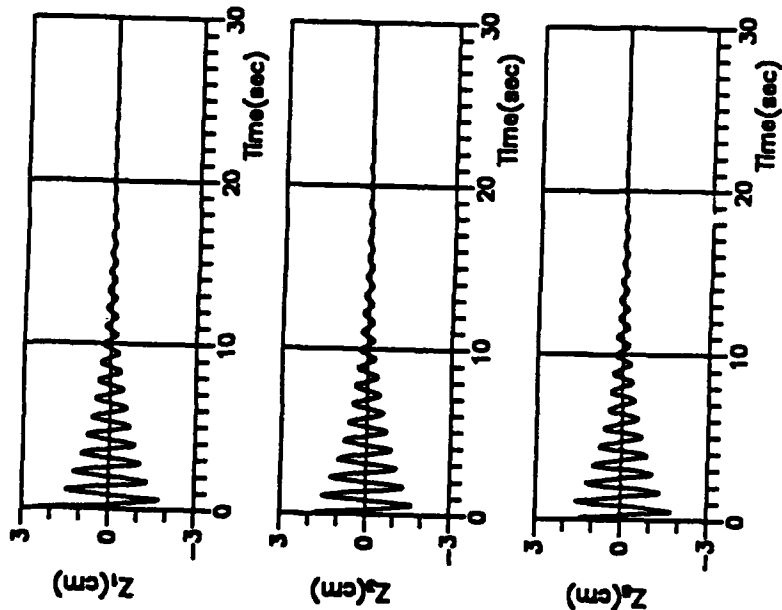


Figure 2. Ten Sets of Actuator Locations



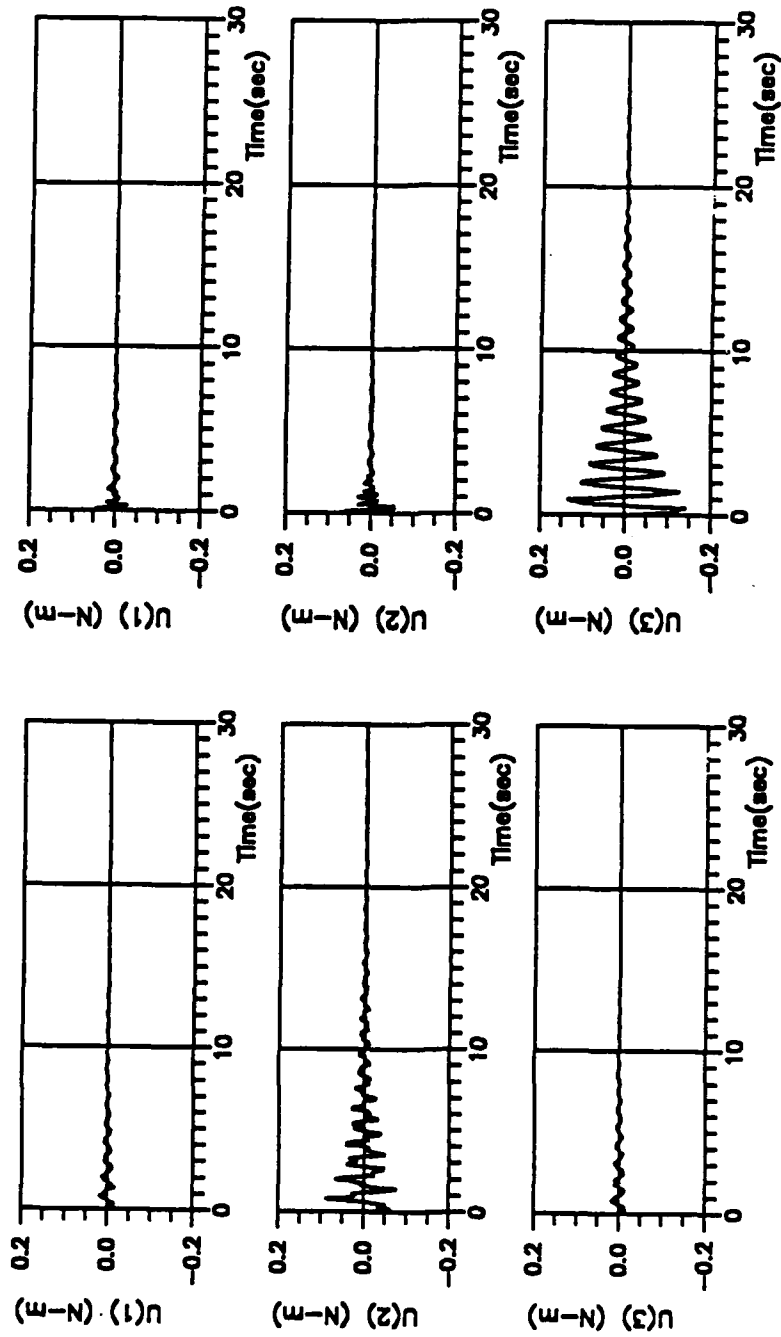


(a) Configuration No. 9



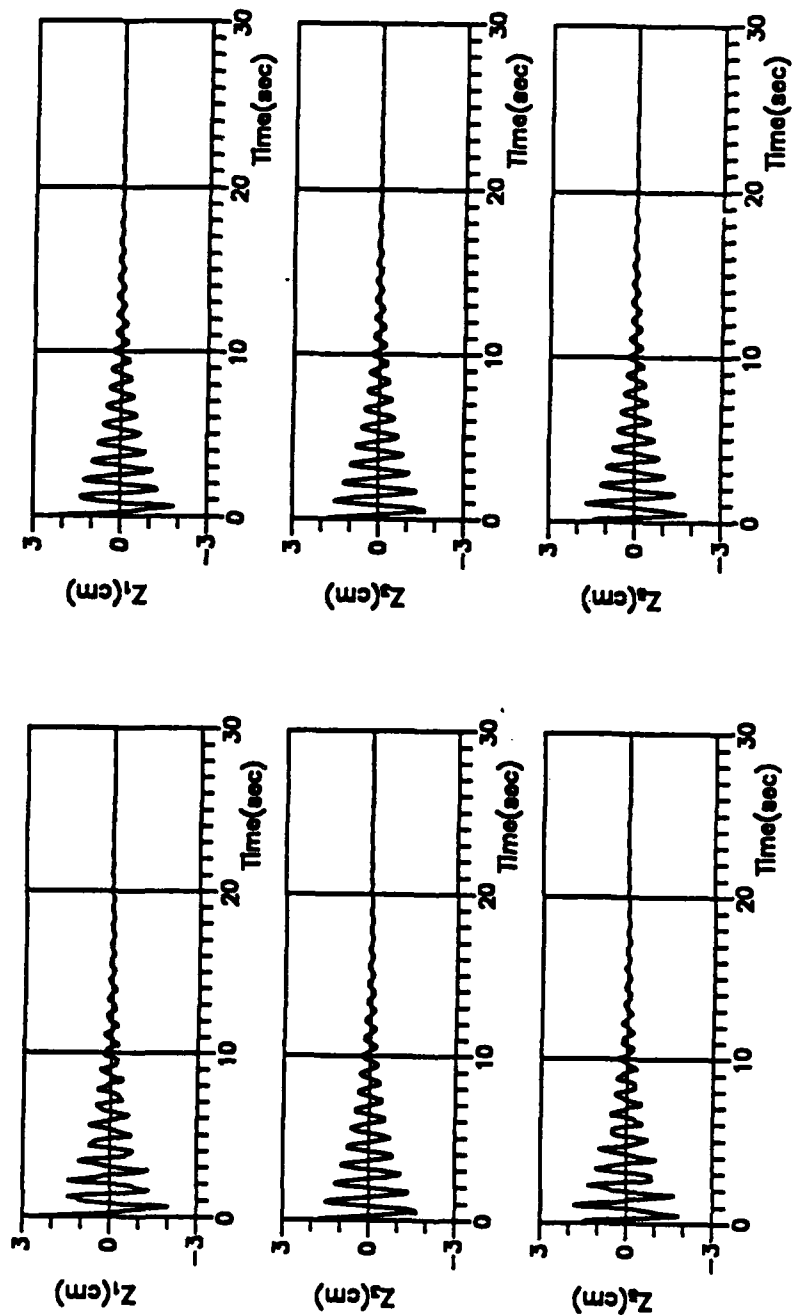
(b) Configuration No. 6

Figure 3. Closed Loop Response of the Flexible Grid (Control Design 1)



(a) Configuration No. 9 (b) Configuration No. 6

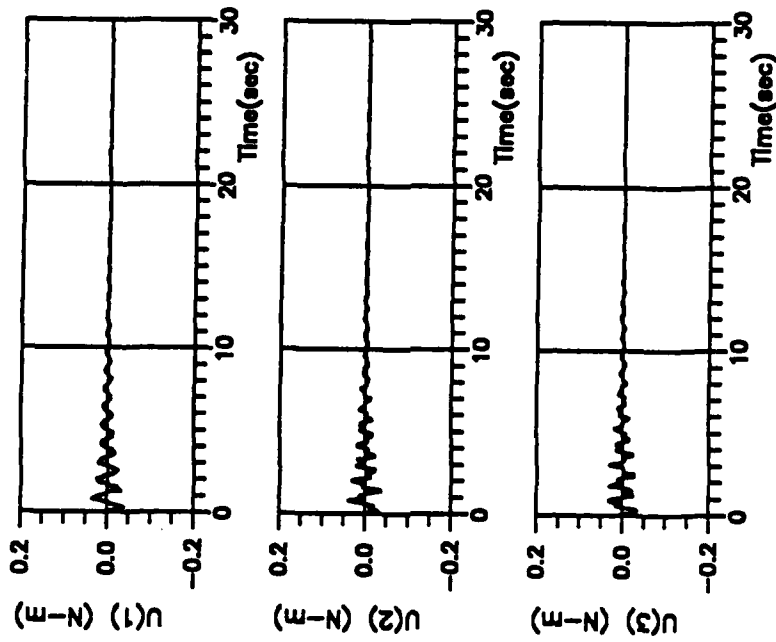
Figure 4. Control Torque Input History (Control Design 1)



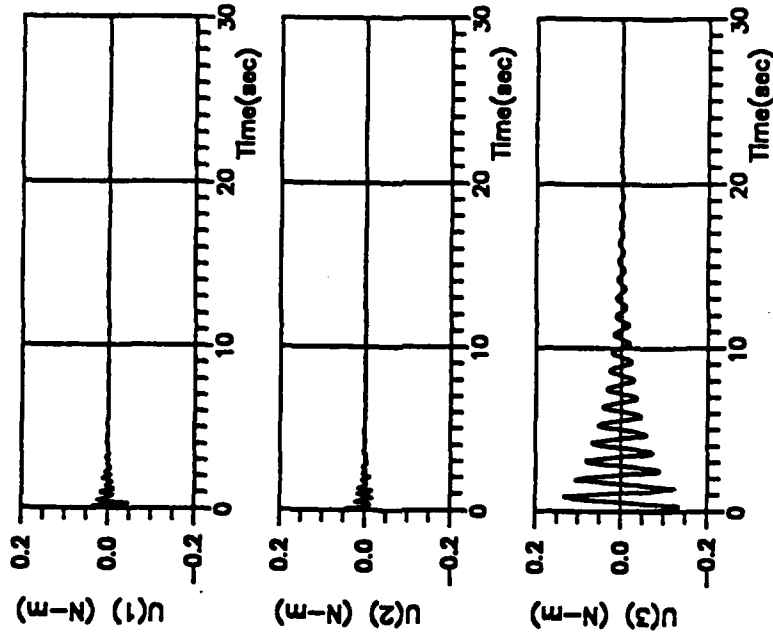
(a) Configuration No. 9

(b) Configuration No. 6

Figure 5. Closed Loop Response of the Flexible Grid (Control Design 2)



(a) Configuration No. 9



(b) Configuration No. 6

Figure 6. Control Torque Input History (Control Design 2)

ATTACHMENT 5

**First and Second Order Sensitivity of  
the Singular Value Decomposition**

*John L. Junkins  
Youdan Kim*

Texas A&M University  
Dept. of Aerospace Engineering  
College Station, Texas 77843

*a reprint from  
The Journal of the Astronautical Sciences  
Vol. 38, No. 1  
Jan-Mar 1990*

# First and Second Order Sensitivity of the Singular Value Decomposition

John L. Junkins<sup>1</sup> and Youdan Kim<sup>1</sup>

## Abstract

We develop algebraic expressions for the first- and second-order sensitivities of the singular value decomposition of a general complex matrix. These algebraic results have been verified by numerical methods. Owing to the increasing analytical and computational applications of singular value analysis of dynamical systems, these results have many potential applications. To illustrate a typical family of applications in design of robust controllers, we consider a stabilizing class of output feedback controllers, and set up an approach to minimize the condition number of the matrix of closed-loop eigenvectors. As specific numerical illustrations, we use the formulation as an integral part of a control design algorithm to design controls for a low dimensioned example (6th order, 4 outputs, 2 inputs) and a moderately high dimensioned example (40th order, 6 outputs, 3 inputs). In the latter case we also illustrate the use of the methodology in a problem where order reduction is an issue. In both cases, we optimize the feedback gains to maximize a robustness measure for the closed loop system, subject to inequality constraints on the system time constants.

## Introduction

Singular value decomposition (SVD) analysis has emerged during the past decade as a very important aspect of many diverse sub-disciplines of dynamical system analysis, and numerous researchers are rapidly expanding the applications of the SVD. In [1], the usefulness of SVD to measure the robustness of feedback-controlled linear systems is discussed. Matrix singular value methods are given in [2] for evaluating gain and phase margins of multiloop control systems. In [3], singular value gradients and parameter optimization techniques are used to design robust controllers for multiloop control systems. In [4, 5], SVD methods are developed for system identification, model truncation, and error analysis.

In this paper, we develop algebraic expressions for the first and second partial derivatives of singular values of a general complex matrix, with respect to a parameter vector (upon which the matrix depends in a twice differentiable fashion). These developments provide important gradients in applying first and second order numerical optimization algorithms to singular value measures of system performance. The

<sup>1</sup>Department of Aerospace Engineering, Texas A&M University, College Station, TX 77843.

analytical developments have been carefully verified by first and second order finite differences.

We also address an illustrative numerical controller design example wherein the condition number (ratio of maximum and minimum singular values) of the closed-loop matrix of eigenvectors is minimized (over a family of stable output feedback gains, subject to eigenvalue placement and system time constant constraints). The minimization of this condition number, for fixed eigenvalue placement, is equivalent to maximizing the robustness with respect to plant uncertainty (as measured by the Patel-Toda [6] measure).

### Singular Value Decomposition

We restrict the initial discussion to the partial derivatives of a square  $(2n) \times (2n)$  complex-valued matrix  $\Phi$ , the *singular value decomposition*, that is the matrix factorization

$$\Phi = U \Sigma V^H \quad (1)$$

where  $U$  and  $V$  are  $(2n) \times (2n)$  unitary matrices normalized so that

$$U^H U = I \quad (2)$$

$$V^H V = I \quad (3)$$

The matrix  $\Sigma = \text{diag}(\sigma_1, \sigma_2, \dots, \sigma_{2n})$ , contains as its elements the real *singular values* of  $\Phi$  ordered as  $\sigma_1 \geq \sigma_2 \geq \dots \geq \sigma_{2n} \geq 0$ . The superscript  $H$  denotes the conjugate transpose.

Since  $U$  and  $V$  are unitary, we can use equations (2) and (3) to rearrange equation (1) as

$$\Sigma = U^H \Phi V \quad (4)$$

The above four equations can be expressed as conditions upon the  $(2n) \times 1$  complex column vectors of  $U = [U_1 \ U_2 \ \dots \ U_{2n}]$  and  $V = [V_1 \ V_2 \ \dots \ V_{2n}]$  as

$$\Phi V_i = U_i \sigma_i, \quad i = 1, 2, \dots, 2n \quad (5)$$

$$\Phi^H U_i = V_i \sigma_i, \quad i = 1, 2, \dots, 2n \quad (6)$$

$$U_i^H U_j = \delta_{ij} \quad (7)$$

$$V_i^H V_j = \delta_{ij} \quad (8)$$

$$\sigma_i \delta_{ij} = U_i^H \Phi V_j \quad (9)$$

Using equations (7) through (9) in equations (5) and (6), it is easy to verify that  $\sigma_i^2$ ,  $V_i$  are eigenvalue, eigenvector pairs of the symmetric matrix  $\Phi^H \Phi$ , whereas  $\sigma_i^2$ ,  $U_i$  are eigenvalue, eigenvector pairs of the symmetric matrix  $\Phi \Phi^H$ . This interpretation of the singular values is of theoretical significance, but does not lead to good algorithms. (It is not necessary or advisable to square the matrix; the decomposition of equation (1) can be generated directly from Householder reductions of  $\Phi$ , using the methods of [7, 8].) It has been our experience that the SVD can be computed more routinely and more accurately than usual matrix operations such as Cholesky decompositions or inversion. Since the SVD also applies to rectangular, complex, rank-deficient matrices as well, the range of applications is large indeed. While we are concerned with the

case of a general  $\Phi$ , certain of the details presented herein apply only to the case of distinct singular values. The generalizations for the repeated singular value cases can likely be pursued in a fashion analogous to the developments in [9], for the sensitivity of eigenvectors for repeated eigenvalues.

### Partial Derivatives of the Singular Values

We define the  $N \times 1$  parameter vector  $\mathbf{p}$  as

$$\mathbf{p} = [p_1, p_2, \dots, p_N]^T \quad (10)$$

and we assume that the matrix  $\Phi$  is a twice differentiable function of  $\mathbf{p}$ , namely,

$$\Phi = \Phi(\mathbf{p}) \quad (11)$$

Differentiating equations (5) and (6) with respect to a typical element  $p_k$  of  $\mathbf{p}$ , upon premultiplying the resulting two equations by  $U_i^H$  and  $V_i^H$ , gives

$$U_i^H \frac{\partial \Phi}{\partial p_k} V_i + U_i^H \Phi \frac{\partial V_i}{\partial p_k} = U_i^H \frac{\partial U_i}{\partial p_k} \sigma_i + U_i^H U_i \frac{\partial \sigma_i}{\partial p_k} \quad (12)$$

$$V_i^H \frac{\partial \Phi^H}{\partial p_k} U_i + V_i^H \Phi^H \frac{\partial U_i}{\partial p_k} = V_i^H \frac{\partial V_i}{\partial p_k} \sigma_i + V_i^H V_i \frac{\partial \sigma_i}{\partial p_k} \quad (13)$$

Adding equations (12) and (13) gives

$$\begin{aligned} U_i^H \frac{\partial \Phi}{\partial p_k} V_i + V_i^H \frac{\partial \Phi^H}{\partial p_k} U_i + (U_i^H \Phi - V_i^H \sigma_i) \frac{\partial V_i}{\partial p_k} \\ + (V_i^H \Phi^H - U_i^H \sigma_i) \frac{\partial U_i}{\partial p_k} = \frac{\partial \sigma_i}{\partial p_k} (U_i^H U_i + V_i^H V_i) \end{aligned} \quad (14)$$

Using equations (5) to (9) in equation (12), we obtain the following result (identical to that in [2]) for the gradient of the singular values

$$\frac{\partial \sigma_i}{\partial p_k} = \frac{1}{2} \left( U_i^H \frac{\partial \Phi}{\partial p_k} V_i + V_i^H \frac{\partial \Phi^H}{\partial p_k} U_i \right) = \text{Re} \left( U_i^H \frac{\partial \Phi}{\partial p_k} V_i \right) \quad (15)$$

Upon differentiating equation (15) with respect to  $p_l$ , we obtain the following expression for the second partial derivatives of the singular values

$$\frac{\partial^2 \sigma_i}{\partial p_k \partial p_l} = \text{Re} \left( \frac{\partial U_i^H}{\partial p_l} \frac{\partial \Phi}{\partial p_k} V_i + U_i^H \frac{\partial^2 \Phi}{\partial p_k \partial p_l} V_i + U_i^H \frac{\partial \Phi}{\partial p_k} \frac{\partial V_i}{\partial p_l} \right) \quad (16)$$

Since equation (16) involves the singular vector gradients  $\partial U_i / \partial p_l$  and  $\partial V_i / \partial p_l$ , we must either evaluate them or eliminate them, we choose the latter approach.

Notice that either set of unitary vectors (the columns of  $U$  or  $V$ ) form a complete set of basis vectors spanning the  $2n \times 1$  complex vector space, so any other vector can be formed as a linear combination of one of these two sets of basis vectors. We choose to project  $\partial U_i / \partial p_l$  and  $\partial V_i / \partial p_l$  onto the corresponding sets of unitary vectors as

$$\begin{aligned} \frac{\partial U_i}{\partial p_l} &= \sum_{j=1}^{2n} a_{ji}^l U_j \\ \frac{\partial V_i}{\partial p_l} &= \sum_{j=1}^{2n} b_{ji}^l V_j \end{aligned} \quad (17)$$

where  $a_{ii}^i$  and  $b_{ii}^i$  are scalar complex constant "components" of the singular vector gradients.

Differentiating equation (5) with respect to the typical parameter  $p_i$ , upon premultiplying the result by  $U_r^H$  and making use of equations (17), gives

$$U_r^H \frac{\partial \Phi}{\partial p_i} V_i + \sum_{j=1}^{2n} b_{ij}^i U_r^H \Phi V_j = \sigma_i \sum_{j=1}^{2n} a_{ij}^i U_r^H U_j + U_r^H U_i \frac{\partial \sigma_i}{\partial p_i} \quad (18)$$

Using equations (7) and (9) in equation (18), we obtain the following equation

$$\sigma_i a_{ii}^i - \sigma_r b_{ii}^i = U_r^H \frac{\partial \Phi}{\partial p_i} V_i - \frac{\partial \sigma_i}{\partial p_i} \delta_n \quad (19)$$

Similarly, differentiating equation (6) with respect to  $p_i$ , upon premultiplying the resulting equation by  $V_r^H$  and making use of equations (5), (7), (8), and (17), gives

$$\sigma_r a_{ii}^i - \sigma_i b_{ii}^i = -V_r^H \frac{\partial \Phi^H}{\partial p_i} U_i + \frac{\partial \sigma_i}{\partial p_i} \delta_n \quad (20)$$

In the case of the "diagonal" terms for which  $r = i$ , equations (19) and (20) become

$$\begin{aligned} a_{ii}^i - b_{ii}^i &= \frac{1}{\sigma_i} \left( U_i^H \frac{\partial \Phi}{\partial p_i} V_i - \frac{\partial \sigma_i}{\partial p_i} \right) \\ a_{ii}^i - b_{ii}^i &= \frac{1}{\sigma_i} \left( -V_i^H \frac{\partial \Phi^H}{\partial p_i} U_i + \frac{\partial \sigma_i}{\partial p_i} \right) \end{aligned} \quad (21)$$

It is evident that subtraction of the first of equations (21) from the second provides another verification of equation (15), but we have another use for equations (21) in evaluating the second partials of equation (16).

In the case of  $r \neq i$ , we have the following result from equations (19) and (20)

$$\begin{aligned} \sigma_i a_{ii}^i - \sigma_r b_{ii}^i &= U_r^H \frac{\partial \Phi}{\partial p_i} V_i \\ \sigma_r a_{ii}^i - \sigma_i b_{ii}^i &= -V_r^H \frac{\partial \Phi^H}{\partial p_i} U_i = - \left( U_i^H \frac{\partial \Phi}{\partial p_i} V_r \right)^H \end{aligned} \quad (22)$$

Except for the  $r = i$  case, and the case of repeated singular values, we can solve equations (22) for the singular vector gradient projection coefficients as

$$\begin{aligned} a_{ii}^i &= \frac{1}{\sigma_i^2 - \sigma_r^2} \left[ \sigma_i \left( U_r^H \frac{\partial \Phi}{\partial p_i} V_i \right) + \sigma_r \left( U_i^H \frac{\partial \Phi}{\partial p_i} V_r \right)^H \right] \\ b_{ii}^i &= \frac{1}{\sigma_i^2 - \sigma_r^2} \left[ \sigma_r \left( U_r^H \frac{\partial \Phi}{\partial p_i} V_i \right) + \sigma_i \left( U_i^H \frac{\partial \Phi}{\partial p_i} V_r \right)^H \right] \end{aligned} \quad (23)$$

The singular vector sensitivities must be consistent with the normalization of equations (7) and (8). Upon setting  $j = i$  and differentiating with respect to  $p_i$ , then substituting equations (17) and making use of equations (7) and (8), we find the diagonal projection coefficients are purely imaginary

$$\begin{aligned} (a_{ii}^i)^H + a_{ii}^i &= \text{Re}(a_{ii}^i) = 0 \\ (b_{ii}^i)^H + b_{ii}^i &= \text{Re}(b_{ii}^i) = 0 \end{aligned} \quad (24)$$

Using equations (21) in (24), and substitution of equations (15) into the result gives

$$(a'_{ii})^H + b'_{ii} = \frac{-1}{\sigma_i} \left( U_i^H \frac{\partial \Phi}{\partial p_i} V_i - \frac{\partial \sigma_i}{\partial p_i} \right) = \frac{-i}{\sigma_i} \operatorname{Im} \left( U_i^H \frac{\partial \Phi}{\partial p_i} V_i \right), \quad i = \sqrt{-1} \quad (25)$$

Substitution of equations (17) into equation (16) gives

$$\frac{\partial^2 \sigma_i}{\partial p_k \partial p_l} = \operatorname{Re} \left[ \sum_{j=1}^{2n} \left( (a'_{ji})^H U_j^H \frac{\partial \Phi}{\partial p_k} V_j + (b'_{ji}) U_j^H \frac{\partial \Phi}{\partial p_k} V_j \right) + U_i^H \frac{\partial^2 \Phi}{\partial p_k \partial p_l} V_i \right]$$

or

$$\frac{\partial^2 \sigma_i}{\partial p_k \partial p_l} = \operatorname{Re} \left[ \sum_{\substack{j=1 \\ j \neq i}}^{2n} \left( (a'_{ji})^H U_j^H \frac{\partial \Phi}{\partial p_k} V_j + (b'_{ji}) U_j^H \frac{\partial \Phi}{\partial p_k} V_j \right) + U_i^H \frac{\partial^2 \Phi}{\partial p_k \partial p_l} V_i + [(a'_{ii})^H + (b'_{ii})] U_i^H \frac{\partial \Phi}{\partial p_k} V_i \right] \quad (26)$$

Finally, eliminating  $(a'_{ii})^H + (b'_{ii})$  using equation (25) and  $a'_{ji}, b'_{ji}$  for  $j \neq i$  using equation (23) and after straightforward algebraic operations, we obtain the final expression for the second partial derivatives of the singular values

$$\begin{aligned} \frac{\partial^2 \sigma_i}{\partial p_k \partial p_l} = \operatorname{Re} \left[ \sum_{\substack{j=1 \\ j \neq i}}^{2n} \frac{1}{\sigma_i^2 - \sigma_j^2} \left\{ \sigma_i \left[ \left( U_j^H \frac{\partial \Phi}{\partial p_l} V_j \right)^H \left( U_j^H \frac{\partial \Phi}{\partial p_k} V_j \right) + \left( U_i^H \frac{\partial \Phi}{\partial p_l} V_i \right)^H \right. \right. \right. \\ \left. \left. \left. \cdot \left( U_i^H \frac{\partial \Phi}{\partial p_k} V_i \right) \right] + \sigma_j \left[ \left( U_i^H \frac{\partial \Phi}{\partial p_l} V_i \right) \left( U_j^H \frac{\partial \Phi}{\partial p_k} V_j \right) + \left( U_j^H \frac{\partial \Phi}{\partial p_l} V_j \right) \left( U_i^H \frac{\partial \Phi}{\partial p_k} V_i \right) \right] \right\} \right. \\ \left. + U_i^H \frac{\partial^2 \Phi}{\partial p_k \partial p_l} V_i \right] + \frac{1}{\sigma_i} \operatorname{Im} \left( U_i^H \frac{\partial \Phi}{\partial p_l} V_i \right) \operatorname{Im} \left( U_i^H \frac{\partial \Phi}{\partial p_k} V_i \right) \quad (27) \end{aligned}$$

This expression has been carefully validated by second finite difference studies, analogous to those reported in [10] for validating analytical partial derivatives for eigenvalue and eigenvector derivatives.

### Example: Minimum Sensitivity Symmetric Output Feedback Gain Design

Suppose that a mechanical system is defined by the equation of motion

$$M\ddot{x} + C\dot{x} + Kx = Du \quad (28)$$

where  $x \in R^n$  and  $u \in R^m$  are the configuration and control vectors, respectively.  $M$  is the  $n \times n$  positive-definite symmetric mass matrix,  $C$  is the  $n \times n$  positive semi-definite symmetric damping matrix,  $K$  is the  $n \times n$  positive semi-definite symmetric stiffness matrix,  $D$  is the  $n \times m$  control influence matrix, and  $(\dot{\cdot}) \equiv d(\cdot)/dt$ .

Motivated by the developments in [5, 11, 12], we introduce the symmetric or "structural" output feedback form of the control law

$$u = -(G_1 D^T x + G_2 D^T \dot{x}) \quad (29)$$

where  $G_1$  and  $G_2$  are  $m \times m$  positive definite symmetric gain matrices. For all members of this special class of output feedback controllers, we can verify that asymptotic

stability is guaranteed. The most familiar member of the family is the so-called "direct feedback" case of diagonal  $G_1$  and  $G_2$ . More generally, fully populated gains allow every actuator to linearly operate on all sensor measurements and thereby provides more controller design freedom. This class of controllers is attractive because a stable family of controllers is guaranteed even in the presence of model errors, and it is not necessary to implement a state observer. However, it is necessary to have all sensors located at actuator stations; and this requirement presents a stumbling block in some applications. For this reason, generalizations and modifications of this approach have recently been proposed [11] to circumvent these difficulties.

We admit the most general family of positive definite gain matrices by introducing the Cholesky decomposition gain parameterizations

$$G_1 = L_1 L_1^T \quad \text{and} \quad G_2 = L_2 L_2^T \quad (30)$$

$G_1$  and  $G_2$  are guaranteed to be positive semi-definite for any real elements ( $q_{ij}, r_{ij}$ ) assigned to the lower triangular matrices

$$L_1 = \begin{bmatrix} q_{11}^2 & 0 & 0 & \cdots & 0 \\ q_{21} & q_{22}^2 & 0 & \cdots & 0 \\ q_{31} & q_{32} & q_{33}^2 & \cdots & 0 \\ \vdots & \vdots & \vdots & \vdots & \vdots \\ q_{m1} & q_{m2} & q_{m3} & \cdots & q_{mm}^2 \end{bmatrix} \quad \text{and} \quad L_2 = \begin{bmatrix} r_{11}^2 & 0 & \cdots & 0 \\ r_{21} & r_{22}^2 & \cdots & 0 \\ r_{31} & r_{32} & \cdots & 0 \\ \vdots & \vdots & \vdots & \vdots \\ r_{m1} & r_{m2} & \cdots & r_{mm}^2 \end{bmatrix} \quad (31)$$

The corresponding global gain parameter vector then becomes

$$\mathbf{p} = [q_{11} \ q_{21} \ \cdots \ q_{m1} \ q_{22} \ \cdots \ q_{mm} \ r_{11} \ r_{21} \ \cdots \ r_{m1} \ r_{22} \ \cdots \ r_{mm}]^T \quad (32)$$

We consider  $G_1$  and  $G_2$  to be functions of  $\mathbf{p}$ ; through equations (30) and (31), it is clear that

$$G_1 = G_1(\mathbf{p}) \quad \text{and} \quad G_2 = G_2(\mathbf{p}) \quad (33)$$

and that, for example, the partial derivatives of the gain matrices with respect to the elements of the parameter vector  $\mathbf{p}$  can be constructed easily.

Substitution of equation (29) into equation (28) gives the closed-loop system

$$M\ddot{\mathbf{x}} + \bar{\mathbf{C}}\dot{\mathbf{x}} + \bar{\mathbf{K}}\mathbf{x} = 0 \quad (34)$$

where the closed-loop system matrices are

$$\bar{\mathbf{C}} = \mathbf{C} + \mathbf{D}G_2\mathbf{D}^T \quad \text{and} \quad \bar{\mathbf{K}} = \mathbf{K} + \mathbf{D}G_1\mathbf{D}^T \quad (35)$$

It is apparent from equations (33) and (35) that the closed-loop damping and stiffness matrices are simple algebraic functions of the gain vector  $\mathbf{p}$ , i.e.,

$$\bar{\mathbf{C}} = \bar{\mathbf{C}}(\mathbf{p}) \quad \text{and} \quad \bar{\mathbf{K}} = \bar{\mathbf{K}}(\mathbf{p}) \quad (36)$$

Considering a first-order state-space form of the system differential equations which is equivalent to the second-order closed-loop system of equation (34), we write

$$\mathbf{B}\dot{\mathbf{z}} = \mathbf{A}\mathbf{z} \quad (37)$$

where

$$\mathbf{z} = \begin{Bmatrix} \mathbf{x} \\ \dot{\mathbf{x}} \end{Bmatrix}, \quad \mathbf{A} = \begin{bmatrix} [0] & \mathbf{M} \\ -\bar{\mathbf{K}} & -\bar{\mathbf{C}} \end{bmatrix}, \quad \mathbf{B} = \begin{bmatrix} \mathbf{M} & [0] \\ [0] & \mathbf{M} \end{bmatrix} \quad (38)$$

It is evident that

$$A = A(p) \quad (39)$$

The right and left eigenvalue problems associated with  $z = \phi e^{\lambda t}$  solutions of equation (37) are

$$\begin{aligned} \text{right: } \lambda_i B \phi_i &= A \phi_i, & i &= 1, 2, \dots, 2n \\ \text{left: } \lambda_i B^T \psi_i &= A^T \psi_i, & i &= 1, 2, \dots, 2n \end{aligned} \quad (40)$$

where we adopt the usual normalizations [10] of the biorthogonality conditions

$$\begin{aligned} \phi_i^T B \phi_i &= 1, & i &= 1, 2, \dots, 2n \\ \psi_j^T B \phi_i &= \delta_{ij}, & i, j &= 1, 2, \dots, 2n \\ \psi_j^T A \phi_i &= \lambda_j \delta_{ij}, & i, j &= 1, 2, \dots, 2n \end{aligned} \quad (41)$$

Since  $A = A(p)$ , it is natural that we consider the eigenvalues and eigenvectors to be functions of  $p$ . Except for isolated events of multiple eigenvalues and root bifurcations, we can consider the eigenvalues and eigenvectors to be smooth differentiable functions of  $p$ .

In order to apply gradient-based optimization algorithms, it is useful to compute analytical partial derivatives of the eigenvalues and eigenvectors. Differentiating equations (40) and using equations (41), we can obtain the following results [10]

$$\begin{aligned} \frac{\partial \lambda_i}{\partial p_k} &= \psi_i^T \left( \frac{\partial A}{\partial p_k} - \lambda_i \frac{\partial B}{\partial p_k} \right) \phi_i, & i &= 1, 2, \dots, 2n \\ \frac{\partial \phi_i}{\partial p_k} &= \sum_{j=1}^{2n} c_{ji}^k \phi_j = \Phi C^k \\ \frac{\partial \psi_i}{\partial p_k} &= \sum_{j=1}^{2n} d_{ji}^k \psi_j = \Psi D^k \end{aligned} \quad (42)$$

with  $\Phi = [\phi_1 \phi_2 \dots \phi_{2n}]$ ,  $\Psi = [\psi_1 \psi_2 \dots \psi_{2n}]$ ,  $C^k = [c_{ij}^k]$ ,  $D^k = [d_{ij}^k]$

where

$$\begin{aligned} c_{ji}^k &= \frac{1}{\lambda_i - \lambda_j} \psi_j^T \left( \frac{\partial A}{\partial p_k} - \lambda_i \frac{\partial B}{\partial p_k} \right) \phi_i, & j &\neq i \\ &= -\frac{1}{2} \left[ \phi_i^T \frac{\partial B}{\partial p_k} \phi_i + \sum_{l=1}^{2n} c_{li}^k \phi_l^T (B + B^T) \phi_i \right], & j &= i \\ d_{ji}^k &= \frac{1}{\lambda_i - \lambda_j} \psi_i^T \left( \frac{\partial A}{\partial p_k} - \lambda_i \frac{\partial B}{\partial p_k} \right) \phi_j, & j &\neq i \\ &= -\psi_i^T \frac{\partial B}{\partial p_k} \phi_i - c_{ii}^k, & j &= i \end{aligned} \quad (43)$$

It is apparent that we can also obtain expressions for the second partial derivatives of the right (or left) eigenvectors by differentiating equation (42) with respect to  $p_l$  as

$$\frac{\partial^2 \Phi}{\partial p_k \partial p_l} = \frac{\partial \Phi}{\partial p_l} C^k + \Phi \frac{\partial C^k}{\partial p_l} \quad (44)$$

where

$$C^k = [c_{ij}^k] \quad \text{and} \quad \frac{\partial C^k}{\partial p_i} = \left[ \frac{\partial c_{ij}^k}{\partial p_i} \right].$$

We can obtain expressions for  $\partial c_{ij}^k / \partial p_i$  by differentiating  $c_{ij}^k$  in equation (43), using the chain rule as is developed in [10].

### Numerical Demonstrations

We consider two specific physical systems to illustrate the above ideas. The first system is a transparent low order example of 6th order. The second example is a flexible structure which provides an occasion to indicate how the issues of order reduction approximations enter the developments.

First we consider the low order system which has three degrees of freedom and two actuators. The mass, stiffness, and control influence matrices are

$$M = \begin{bmatrix} 1 & 0 & 0 \\ 0 & 1 & 0 \\ 0 & 0 & 1 \end{bmatrix}, \quad K = \begin{bmatrix} 20 & -10 & 0 \\ -10 & 30 & -20 \\ 0 & -20 & 20 \end{bmatrix}, \quad D = \begin{bmatrix} 1 & 0 \\ 0 & 0 \\ 0 & 1 \end{bmatrix} \quad (45)$$

Conditioning of the eigenvectors is a direct measure of the sensitivity of the corresponding eigenvalue to perturbations in the elements of the closed loop system matrices [13]. The condition number of the *modal matrix* of closed loop eigenvectors can be used to establish finite bounds on the system matrices within which stability can be guaranteed [6]. We therefore adopt the condition number  $\mathcal{N}(\Phi^c)$  of the closed loop modal matrix  $\Phi^c$  as our performance measure. This performance measure is related to the singular values as

$$J(\mathbf{p}) = \mathcal{N}(\Phi^c(\mathbf{p})) = \frac{\sigma_1(\Phi^c(\mathbf{p}))}{\sigma_{2n}(\Phi^c(\mathbf{p}))} \quad (46)$$

where  $\sigma_1$  and  $\sigma_{2n}$  denote the maximum and minimum singular values of the right modal matrix  $\Phi^c$ .

We also adopt the two equality and two inequality constraints on eigenvalue placement

$$\begin{aligned} f_i(\mathbf{p}) &= \omega_{i0} - \omega_i(\mathbf{p}) = 0, & i &= 1, 2 \\ g_i(\mathbf{p}) &= \omega_i(\mathbf{p})\zeta_i(\mathbf{p}) \geq T_i, & i &= 1, 2 \end{aligned} \quad (47)$$

where

$$\begin{aligned} \omega_i(\mathbf{p}) &= \text{Im}(\lambda_i) \\ \zeta_i(\mathbf{p}) &= -\frac{\text{Re}(\lambda_i)}{|\lambda_i|} \end{aligned} \quad (48)$$

The eigenvalues are ordered according to increasing frequencies

$$|\text{Im } \lambda_1(\mathbf{p})| \leq |\text{Im } \lambda_2(\mathbf{p})| \leq |\text{Im } \lambda_3(\mathbf{p})| \leq \dots \leq |\text{Im } \lambda_{2n}(\mathbf{p})| \quad (49)$$

Thus, we impose constraints on the first two closed-loop frequencies and time constants.

The objective values for the frequencies,  $\omega_{\omega}$ , are simply taken as their corresponding zero gain values. The inequality constraints are introduced to bound the slowest system time constant, and we adopted  $T_i = 0.3$ ,  $i = 1, 2$ .

Utilizing the minimum norm differential correction algorithm and the homotopy technique of [14], we successfully solved the above nonlinear programming problem.

The characteristics of the open-loop and closed-loop systems are summarized in Tables 1 and 2. The final converged position and velocity gain matrices are

$$G_1 = \begin{bmatrix} 1.1591 & 0.0253 \\ 0.0253 & 1.0557 \end{bmatrix}, \quad \|G_1\|_F = 1.5682,$$

$$G_2 = \begin{bmatrix} 2.2539 & 0.2834 \\ 0.2834 & 2.6918 \end{bmatrix}, \quad \|G_2\|_F = 3.5336$$

where  $\|G\|_F$  is the Frobenius norm of the gain matrix  $G$ .

As is evident, we successfully imposed the system time constant constraints and also improved the conditioning of the closed-loop eigenvectors as compared to the open loop system. For fixed eigenvalue constraints, minimization of the condition number maximizes the Patel-Toda measure [6] of robustness with respect to plant uncertainty.

The optimization process was initiated by simply adopting identity matrices for the  $G_i$  starting iteratives. Ten homotopy steps were required with three to four minimum norm differential gain corrections on each step. The singular value gradients were computed using equation (15). The minimum norm correction process did not require the second partials, but these were computed as well and verified by finite differences.

TABLE 1. Characteristics of the Open Loop System

Eigenvalues	$\omega_i$	$\zeta_i \omega_i$	Cond. No. $\lambda(\Phi^0)$
$\pm 1.4447i$	1.4447	0	9.4903
$\pm 4.4721i$	4.4721	0	
$\pm 6.9219i$	6.9219	0	

TABLE 2. Characteristics of the Closed Loop System

Eigenvalues	$\omega_i$	$\zeta_i \omega_i$	Cond. No. $\lambda(\Phi^c)$
$-0.8833 \pm 1.4447i$	1.4447	0.7532	8.1291
$-1.0574 \pm 4.4721i$	4.4721	1.0189	
$-0.5322 \pm 6.7872i$	6.7872	0.5306	

As a second example, consider the planar rotational/vibrational dynamics of the flexible structure consisting of a rigid hub with four cantilevered flexible appendages (Fig. 1). Table 3 summarizes the Draper/RPL configuration parameters [14]. The model is restricted such that the opposing beams deflect antisymmetrically. The equations can be derived by using a Lagrangian approach:

$$\frac{d}{dt} \left( \frac{\partial T}{\partial \dot{x}_i} \right) - \frac{\partial T}{\partial x_i} + \frac{\partial V}{\partial x_i} = F_i \quad i = 1, \dots, n \quad (50)$$

where  $T$  is the system kinetic energy,  $V$  is the system potential energy,  $F_i$  is the  $i$ th generalized force, and  $x_i$  is the  $i$ th element of the configuration vector,  $x$ :

$$x = \{\theta \ q_{11} \ q_{21} \ \dots \ q_{N1} \ q_{12} \ q_{22} \ \dots \ q_{N2}\}^T \quad (51)$$

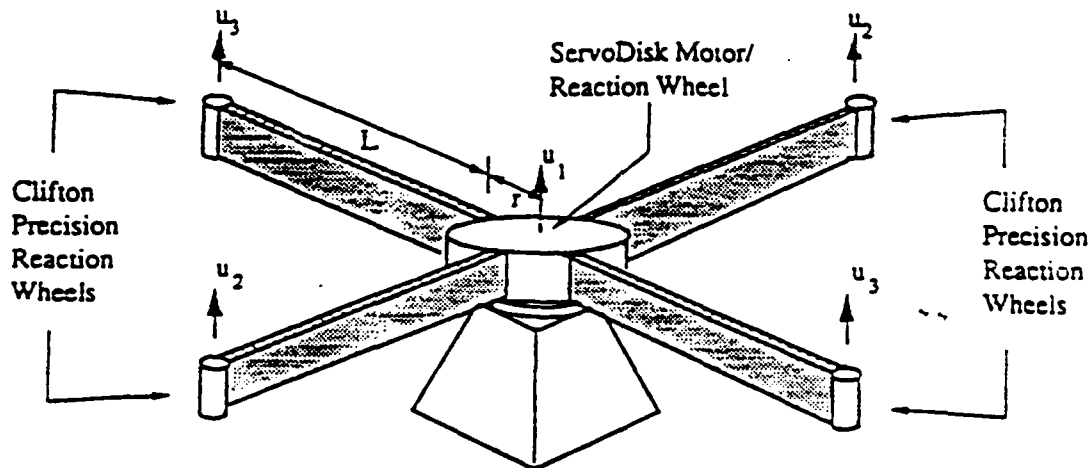


FIG. 1. Maneuverable Flexible Structure: Experimental Configuration.

TABLE 3. Draper/RPL Configuration Parameters

Parameter	Symbol	Value
Hub radius	$r$	1 ft
Rotary inertia of hub	$J_h$	8 slug-ft <sup>2</sup>
Mass density of beams	$\rho$	0.0271875 slug/ft
Elastic modulus of the arms	$E$	$0.1584E + 10$ lb/ft <sup>2</sup>
Arm thickness	$t$	0.125 in
Arm height	$h$	6.0 in
Arm length	$L$	4.0 ft
Tip mass	$m$	0.156941 slug
Rotary inertia of tip masses	$J_i$	0.0018 slug-ft <sup>2</sup>

The  $q_{ij}$  are generalized beam coordinates which result from using a Ritz approach to approximate the local beam deflections,  $y_i$ , as the truncated series

$$y_i(t, z) = \sum_{j=1}^N q_{ji}(t) \phi_j(z), \quad i = 1, 2, \quad 0 \leq z \leq L \quad (52)$$

The comparison functions  $\phi_j(z)$  in equation (52) are chosen as [15]

$$\phi_j(z) = 1 - \cos\left(\frac{j\pi z}{L}\right) + \frac{1}{2}(-1)^{j+1}\left(\frac{j\pi z}{L}\right)^2 \quad (53)$$

which satisfy the geometric and physical boundary conditions of a clamped-free beam (clamped to the hub).

We apply a torque  $u_1$  to the hub, a torque  $u_2$  to the end of appendages 1 and 3, and a torque  $u_3$  to the end of the appendages 2 and 4.

Lagrange's equations then lead to the following matrix form for the system equations of motion

$$\begin{bmatrix} J & M_{\theta q_1}^T & M_{\theta q_2}^T \\ M_{\theta q_1} & M_{q_1 q_1} & 0 \\ M_{\theta q_2} & 0 & M_{q_2 q_2} \end{bmatrix} \ddot{\mathbf{x}} + \begin{bmatrix} 0 & 0 & 0 \\ 0 & K_{q_1 q_1} & 0 \\ 0 & 0 & K_{q_2 q_2} \end{bmatrix} \mathbf{x} = \begin{bmatrix} 1 & 2 & 2 \\ 0 & 2\phi'(L) & 0 \\ 0 & 0 & 2\phi'(L) \end{bmatrix} \mathbf{u} \quad (54)$$

where

$$J = J_h + 4 \int_0^L \rho(x+r)^2 dx + 4[J_t + m(r+L)^2]$$

$$[M_{\theta q_1}]_{,i} = [M_{\theta q_2}]_{,i} = 2 \left[ \int_0^L \rho(x+r) \phi_i(x) dx + m(r+L) \phi_i(L) + J_t \phi_i'(L) \right]$$

$$[M_{q_1 q_1}]_{,ij} = [M_{q_2 q_2}]_{,ij} = 2 \left[ \int_0^L \rho \phi_i(x) \phi_j(x) dx + m \phi_i(L) \phi_j(L) + J_t \phi_i'(L) \phi_j'(L) \right]$$

$$[K_{q_1 q_1}]_{,ij} = [K_{q_2 q_2}]_{,ij} = 2 \int_0^L EI \phi_i''(x) \phi_j''(x) dx$$

Note that  $J_h$  is the rotary inertia of the hub,  $J_t$  is the rotary inertia of the tip mass,  $\rho$  is the mass density of the beam,  $m$  is the mass of the tip mass,  $L$  is the arm length,  $r$  is the hub radius, and  $\phi_i(x)$  is the comparison function (equation (53)). More simply,

$$M\ddot{\mathbf{x}} + K\mathbf{x} = D\mathbf{u} \quad (55)$$

The eigenvalues (natural frequencies) and eigenvectors (mode shapes) of the free vibration problem associated with equation (55) satisfy the orthogonality conditions

$$\begin{aligned} \Phi^T M \Phi &= I \\ \Phi^T K \Phi &= \text{diag}(\omega_1^2, \omega_2^2, \dots, \omega_n^2) \end{aligned} \quad (56)$$

where  $\Phi$  is the ( $n \times n$ ) modal matrix of eigenvectors.

For high order systems such as a flexible structure, it is usually desirable and often necessary to develop a reduced-order model to save on computational time when designing control laws. The high order model is generally retained to verify the resulting design. We elect to make use of truncation to construct the reduced order model, for illustration purposes.

The modal coordinate transformation is introduced as

$$\mathbf{x}(t) = \Phi \boldsymbol{\eta}(t) = [\Phi_1 \Phi_2] \begin{Bmatrix} \eta_1 \\ \eta_2 \end{Bmatrix} \quad (57)$$

where  $\eta_1$  is the first  $n_r$  modal coordinates which we are interested in retaining in the reduced order model. Then the reduced-order equation of motion becomes

$$\bar{M} \ddot{\boldsymbol{\eta}}_1 + \bar{K} \boldsymbol{\eta}_1 = \bar{D} \mathbf{u} \quad (58)$$

where

$$\bar{M} = \Phi_1^T M \Phi_1, \quad \bar{K} = \Phi_1^T K \Phi_1, \quad \bar{D} = \Phi_1^T D$$

For "structural feedback" control, the control force vector takes the following form

$$\mathbf{u} = (\bar{G}_1 \bar{D}^T \boldsymbol{\eta}_1 + \bar{G}_2 \bar{D}^T \dot{\boldsymbol{\eta}}_1) \quad (59)$$

In the present example, we take  $N = 20$ , and  $n_r = 9$ . Therefore we design the control gain matrices  $\bar{G}_1$  and  $\bar{G}_2$  by using the reduced (18th) order model and use the full (42nd) order system to verify the controller design.

We adopt the condition number of the closed-loop modal matrix as our performance measure, and impose constraints on the first three closed-loop frequencies and time constants. The objective value for the closed-loop frequency of the rigid body mode is taken as 0.3, and the objective values for the first two flexible mode closed-loop frequencies are taken as their corresponding zero gain values. We adopt the following time constants for lower bounds on the first three closed-loop eigenvalues:  $T_1 = 0.2$ ,  $T_2 = 0.2$ , and  $T_3 = 0.25$ .

The optimization process was initiated by simply adopting identity matrices for the  $G_i$  starting iteratives. The characteristics of the open loop and closed loop systems are summarized in Table 4. The final converged position and velocity gain matrices are

$$G_1 = \begin{bmatrix} 1.8342 & 0.2592 & 0.2601 \\ 0.2592 & 0.0409 & 0.0405 \\ 0.2601 & 0.0405 & 0.0403 \end{bmatrix} \quad \|G_1\|_F = 1.9080$$

$$G_2 = \begin{bmatrix} 7.4284 & 0.4579 & 0.8335 \\ 0.4579 & 0.2411 & 0.0211 \\ 0.8335 & 0.0211 & 0.3509 \end{bmatrix} \quad \|G_2\|_F = 7.5612$$

The small differences of the first two flexible mode frequencies stem from the fact that we designed the controller by using a reduced-order model and used it for the full order system. It is obvious that our reduced-order model was sufficiently accurate for control design purposes. Due to the positive definite symmetry of the gain matrices, all modes of the full order model are stabilized. It is important that the symmetric feedback form of the control *guarantees stability*, even though we may not have

TABLE 4. The Characteristics of the Open-loop and Closed-loop System (First Nine Modes of the Full Order System)

OPEN LOOP		CLOSED LOOP	
$\omega_i$	$\zeta_i \omega_i$	$\omega_i$	$\zeta_i \omega_i$
0	0	0.3000	0.2000
4.3724	0	4.3726	0.2061
7.9070	0	7.9071	0.2539
51.4510	0	52.0041	5.3354
52.8058	0	53.0653	8.0875
157.5566	0	158.0285	14.0467
158.3659	0	158.5273	21.4808
313.7099	0	308.8039	34.8815
314.3402	0	311.7689	22.6602
Condition No.	$\infty$	Condition No.	37210.8

chosen a good reduced-order model. In this case it is obvious that we have successfully imposed the specified constraints on the closed-loop eigenvalues and improved conditioning of the closed-loop eigenvectors.

These examples are illustrations of the utility of singular value derivatives in the optimization of feedback control laws; while we have adopted a particular stable family of output feedback control gains, any parameterization of the feedback law can in principle be employed.

### Concluding Remarks

Algebraic expressions for the sensitivity of the singular value decomposition has been derived and verified numerically. We also summarize a simple numerical demonstration of the utility of these derivatives to optimize feedback control gains to minimize the closed-loop eigenvector condition number subject to eigenvalue placement constraints. The main contribution of this paper is a concise derivation of the singular value first and second order partial derivatives; these will find wide applications in singular value analysis of dynamical systems. A significant secondary contribution is the presentation and demonstration of an algorithm utilizing these singular value sensitivities to design robust output feedback controllers.

### Acknowledgment

We are pleased to acknowledge the support of the Air Force Office of Scientific Research (Contract F49620-87-C-0078), and the Texas Advanced Technology Program (Project 70110).

### Appendix: Homotopic Nonlinear Programming Based Upon Minimizing Successive Design Modifications

Figure A1 provides a logical flow chart showing (the macroscopic details of) a homotopic nonlinear programming algorithm which achieves convergence reliability by defining a sequence of neighboring constraint specifications and minimizing the sequence of design modifications required to satisfy the constraint sequence.

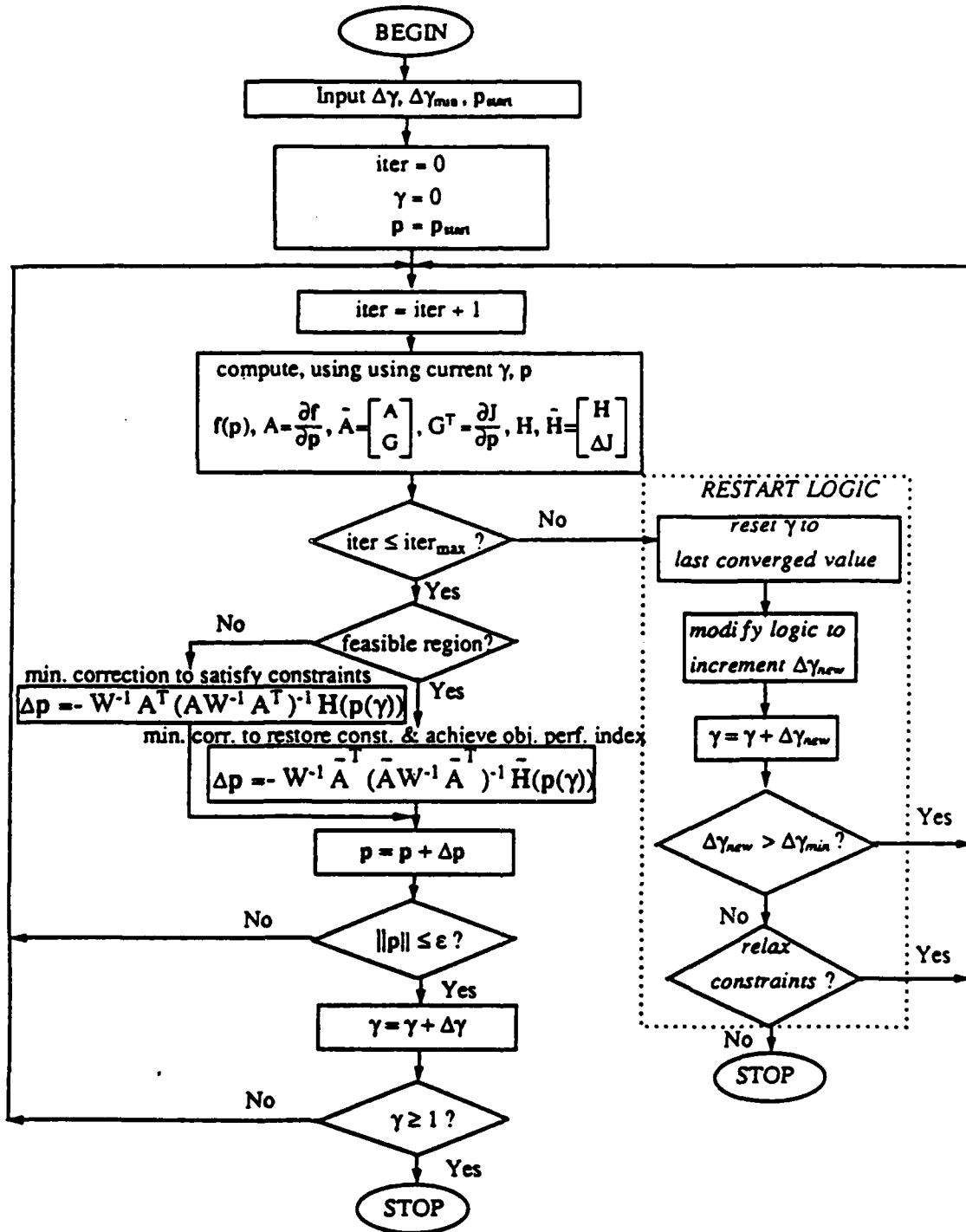


FIG. A1. Logic Flow of the Minimum Correction Homotopy Algorithm for Nonlinear Programming.

The central feature of our nonlinear programming algorithm is the use of the minimum norm differential correction of the design variables. This is a generalized Newton process for solving a system of underdetermined nonlinear equations; on each iteration, we seek to minimize the norm (sum square) of the correction vector to satisfy the specified constraints. The constraint functions are locally linearized to pro-

vide a system of linear algebraic equations to solve for the correction vector; the process is iterated with the derivatives (the Jacobian matrix) locally evaluated. We discuss below the procedure used to deal with inequality as well as equality constraints. Of course the key requirements underlying successful convergence of any Newton-like algorithm are: (i) the existence of a feasible solution and (ii) the availability of a sufficiently close starting iterative. As we show below, the homotopic continuation method effectively guarantees that we can deform the constraints by controllable, arbitrarily small amounts and thereby remain controllably close to a neighboring converged solution; this effectively guarantees "arbitrarily good" starting iteratives for each local iteration. An embedding method is used to define a continuous family of problems which contain two important members: (i) a trivial problem (one for which the solution is available) and (ii) the problem of interest.

The continuous one-parameter family of problems is constructed in such a way that an imbedding parameter ( $0 \leq \gamma \leq 1$ ) may be set to define any member of the family with  $\gamma = 0$  generating the trivial problem and  $\gamma = 1$  generating the problem of interest. By sweeping  $\gamma$  and controlling the  $\gamma$  increments, we control how closely spaced the neighboring solutions lie (in the space of the constraint functions), and the  $\gamma$  increments can be assigned adaptively based upon convergence progress. Thus we can remain as near to neighboring converged solutions as is necessary to maintain sufficiently good starting iteratives. Therefore, if a local convergence cannot be achieved (for some  $\gamma$  value), we have eliminated the most common problem (of having a poor starting iterative), and we can focus on other, more interesting convergence issues, such as the non-existence of feasible solutions, local linear dependence of the linearized constraint equations, turning points, and other issues. For example, comparing the active constraint sets and the corresponding Jacobian rows between the apparently un-reachable set (the one for which convergence cannot be achieved) and the previous converged solution, will usually reveal which constraints are in competition and will usually suggest avenues for revision of the problem and/or provide insights as to why the convergence failure occurred.

We now discuss the algorithm, beginning with the statement of the parameter optimization problem we are addressing: We seek to find  $\mathbf{p}^*$  which minimizes a function

$$J = J(\mathbf{p}) \quad (\text{A1})$$

subject to the constraints

$$\begin{aligned} f_i(\mathbf{p}) &= f_{oi}, & i &= 1, 2, \dots, m \\ g_j(\mathbf{p}) &\geq T_j, & j &= 1, 2, \dots \end{aligned} \quad (\text{A2})$$

where  $f_{oi}$  is the "objective" value of the  $i$ th equality constraint, and  $T_j$  represents boundaries on the feasible region.

Converging from an approximate starting solution  $\mathbf{p}_{start}$ , to a feasible solution satisfying the constraints of equations (A2) may be approached by locally considering all of the equality constraints and only the active (locally violated) subset of inequality constraints. The locally violated subset of inequality constraints are simply considered as additional equality constraints of the form

$$f_j(\mathbf{p}) = T_j, \quad j = m + 1, m + 2, \dots, r \quad (\text{A3})$$

The subset of inequality constraints  $g_i(\mathbf{p}) \geq T_i$  included in equations (A3), as local equality constraints, obviously depends upon which constraints are locally violated and thus will typically change during the differential correction process. So long as  $r$  (the number of locally violated constraints plus the  $m$  equality constraints) does not exceed  $N$  (the number of elements in  $\mathbf{p}$ ), then we can proceed with the discussion below, otherwise, only the  $N - m$  "most important" inequality constraints will be locally imposed, assuming the original ordering represents the "importance hierarchy" of the inequality constraints. Adopting this approach permits the specification of greater than  $N - m$  inequality constraints, although not more than  $N - m$  can be active on any iteration, especially the last one. Note that it is often the case that final convergence to a feasible solution satisfying equations (A2) is achieved even when local iterations encounter more than  $N - m$  locally active constraints (i.e., it is typical that only a small subset of the specified inequality constraints are active when convergence to a feasible solution is achieved, and only under special circumstances will this finally active subset of constraints be invariant during the local iterations). These ideas must also be viewed in the context of the homotopy procedure which we discuss below.

Thus our re-stated optimization problem is to minimize  $J$  of equation (A1) subject to

$$\mathbf{f}(\mathbf{p}) = \mathbf{f}_o \quad (\text{A4})$$

where  $\mathbf{f}(\mathbf{p})$  is the  $r \times 1$  vector of  $m$  equality constraints and the  $r - m$  active inequality constraints.

We initially address the problem of achieving a feasible solution near our starting solution, and delay considering minimization of  $J$  until a feasible design has been achieved. To enhance coverage, we introduce a "portable objective" vector  $\mathbf{f}_p(\gamma)$  as the one parameter family of objective constraint values

$$\mathbf{f}_p(\gamma) = \gamma \mathbf{f}_o + (1 - \gamma) \mathbf{f}(\mathbf{p}_{start}), \quad 0 \leq \gamma \leq 1 \quad (\text{A5})$$

where  $\gamma$  is the homotopy parameter. The linear homotopy map  $\mathbf{H}(\mathbf{p}(\gamma), \gamma)$  is generated by replacing  $\mathbf{f}_o$  in equation (A4) by  $\mathbf{f}_p$  from equation (A5) to obtain

$$\mathbf{H}(\mathbf{p}(\gamma), \gamma) = \gamma \mathbf{f}_o + (1 - \gamma) \mathbf{f}(\mathbf{p}_{start}) - \mathbf{f}(\mathbf{p}(\gamma)) = \mathbf{0} \quad (\text{A6})$$

Notice the  $\gamma$  boundary conditions satisfied by  $\mathbf{H}(\mathbf{p}(\gamma), \gamma)$  in equation (A6):

at  $\gamma = 0$ , trivial problem:

$$\mathbf{H}(\mathbf{p}(0), 0) = \mathbf{f}(\mathbf{p}_{start}) - \mathbf{f}(\mathbf{p}(0)) = \mathbf{0} \Leftrightarrow \mathbf{p}(0) = \mathbf{p}_{start}$$

at  $\gamma = 1$ , problem of interest:

$$\mathbf{H}(\mathbf{p}(1), 1) = \mathbf{f}_o - \mathbf{f}(\mathbf{p}(1)) = \mathbf{0} \Leftrightarrow \mathbf{p}(1) = \mathbf{p}_{feasible} \quad (\text{A7})$$

It is apparent that an arbitrary guess  $\mathbf{p}_{start}$  satisfies the homotopy map of equation (A6) for  $\gamma = 0$ , and if we can obtain a solution for  $\gamma = 1$ , then we have a feasible solution  $\mathbf{p}_{feasible}$ . It is apparent that sweeping  $\gamma$  at a suitably small increment generates a sequence of neighboring problems. We solve this sequence of problems, using the neighboring converged solutions to generate starting iteratives for each subsequent problem.

The local corrections (for each  $\gamma$  specification) are done by linearizing equation (A6) about the local  $\mathbf{p}$  iterative and computing the differential correction which will satisfy

the linearized constraint equation with the minimum correction norm. So we minimize  $\Delta \mathbf{p}^T W \Delta \mathbf{p}$ , subject to  $\mathbf{H}(\mathbf{p}(\gamma), \gamma) + A \Delta \mathbf{p} = \mathbf{0}$ , where  $A \equiv \partial \mathbf{H} / \partial \mathbf{p} = -\partial \mathbf{f}(\mathbf{p}(\gamma)) / \partial \mathbf{p}$ , and  $W$  is a suitable positive definite weight matrix. The solution provides the minimum norm differential correction result [16]

$$\Delta \mathbf{p} = -W^{-1} A^T (A W^{-1} A^T)^{-1} \mathbf{H}(\mathbf{p}(\gamma)) \quad (\text{A8})$$

and we use the recursion  $\mathbf{p}_{\text{new}} = \mathbf{p}_{\text{old}} + \Delta \mathbf{p}$  iterate until equation (A6) is satisfied for each local  $\gamma$  value. Upon achieving a local convergence,  $\gamma$  is incremented by a prescribed amount. If local convergence is not achieved, the  $\gamma$  increment is reduced and  $\gamma$  is assigned nearer the largest  $\gamma$  value for which convergence was previously achieved. The process is halted if (i) convergence to a feasible solution is achieved (at  $\gamma = 1$ ), or (ii) local convergence cannot be achieved when we increment  $\gamma$  by some small tolerance  $\Delta \gamma \leq \epsilon$ . In the latter case the user should re-evaluate the problem statement in view of the active constraint set and other considerations from evaluation of the largest  $\gamma$  solution achieved.

Having achieved convergence to a feasible solution, we now consider minimization of the performance index  $J$  subject to the local equality constraint of equation (A6). Assuming there are  $r < N$  active constraints, this can readily be accomplished [16] by simply introducing an objective value for the performance index  $J_o$  and treating it as the  $(r + 1)$ th equality constraint. The corresponding minimum norm differential correction, in lieu of equation (A8) is

$$\Delta \mathbf{p} = -W^{-1} \bar{A}^T (\bar{A} W^{-1} \bar{A}^T)^{-1} \bar{\mathbf{H}}(\mathbf{p}(\gamma)) \quad (\text{A9})$$

where

$$\bar{A} = \begin{bmatrix} A \\ \dots \dots \dots \\ \frac{\partial J}{\partial p_1} \quad \frac{\partial J}{\partial p_2} \quad \dots \quad \frac{\partial J}{\partial p_N} \end{bmatrix}, \quad \bar{\mathbf{H}}(\mathbf{p}(\gamma)) = \begin{Bmatrix} \mathbf{H}(\mathbf{p}(\gamma)) \\ \dots \dots \dots \\ J(\mathbf{p}(\gamma)) - J_o \end{Bmatrix} \quad (\text{A10})$$

Upon achieving convergence to the feasible region, we reset  $\gamma = 0$  and subsequently use equation (A9) to compute the differential corrections. For the iterations subsequent to the first feasible solution, a new homotopy process is established to drive the objective function to its minimum value, or alternatively, drive it to a "goal" value  $J_{\text{goal}}$ . The objective value  $J_o(\gamma)$  is assigned the one parameter family of values

$$J_o(\gamma) = \gamma J_{\text{goal}} + (1 - \gamma) J(\mathbf{p}_{\text{feasible}}) \quad (\text{A11})$$

where  $\mathbf{p}_{\text{feasible}}$  is the first feasible solution (satisfies equation (A6) with  $\gamma = 1$ ).

The value for  $J_{\text{goal}}$  may be an actual goal, but is more typically interpreted as "the best one could possibly hope for"; it is often taken as zero for a minimization problem. We increment  $\gamma$  from zero toward unity, with the size of the increments dictated by convergence progress of the differential corrections for each  $\gamma$  value. When convergence can not be achieved for a small tolerance increase in  $\gamma$ , we adopt the solution corresponding to the largest  $\gamma$  for which convergence was achieved as the constrained minimum. We have rigorously proven [16] that this process is mathematically equivalent to a gradient projection with appropriate strategies for correction step size control. However this algorithm is superior to the gradient projection method because (i) the correction formulas are more easily programmed, and (ii) the one parameter homo-

topic continuation process has been found much more attractive than step size control, in that it is inherently self-starting. Of course, if the problem under consideration has multiple constrained minima, one will find that the above problem formulation does not save you from the local versus global convergence difficulties.

## References

- [1] FREUDENBERG, J. S., LOOZE, D. P. and CRUZ, J. B. "Robustness Analysis Using Singular Value Sensitivities," *International Journal of Control*, Vol. 35, No. 1, 1982, pp. 95-116.
- [2] MUKHOPADHYAY, V. and NEWSOM, J. R. "Application of Matrix Singular Value Properties for Evaluating Gain and Phase Margins of Multiloop Systems," NASA TM-84524, July 1982.
- [3] NEWSOM, J. R. and MUKHOPADHYAY, V. "The Use of Singular Value Gradients and Optimization Techniques to Design Robust Controllers for Multiloop Systems," NASA TM-85720, November 1983.
- [4] LONGMAN, R. W., BERGMAN, M., and JUANG, J. N. "Variance and Bias Confidence Criterion for ERA Model Parameter Identification," AIAA Paper No. 88-4312-CP, *Proceedings of the AIAA/AAS Astrodynamics Conference*, Minneapolis, Minnesota, August 1988.
- [5] REW, D. W. and JUNKINS, J. L. "Multi-criterion Approaches to Optimization of Linear Regulators," AIAA Paper No. 86-2198-CP, *Proceedings of the AIAA Guidance, Navigation, and Control Conference*, Williamsburg, Virginia, August 1986; also, *Journal of the Astronautical Sciences* (to appear).
- [6] PATEL, R. V. and TODA, M. "Quantitative Measures of Robustness for Multivariable Systems," *Proceedings of Joint Automatic Control Conference*, TP8-A, Vol. I, San Francisco, California, 1980.
- [7] KLEMA, V. C. and LAUB, A. J. "The Singular Value Decomposition: Its Computation and Some Applications," *IEEE Transactions on Automatic Control*, Vol. AC-25, No. 2, April 1980, pp. 164-176.
- [8] CHAN, T. F. "An Improved Algorithm for Computing the Singular Value Decomposition," *ACM Transactions on Mathematical Software*, Vol. 8, No. 1, March 1982, pp. 72-83.
- [9] JUANG, J. N. and LIM, K. B. "On the Eigenvalue and Eigenvector Derivatives of a Non-Defective Matrix," AIAA Paper No. 88-2352.
- [10] LIM, K. B., JUNKINS, J. L., and WANG, B. P. "Re-examination of Eigenvector Derivatives," *Journal of Guidance, Control, and Dynamics*, Vol. 10, No. 6, November-December 1987, pp. 581-587.
- [11] CREAMER, N. G. and JUNKINS, J. L. "A Pole Placement Technique for Vibration Suppression of Flexible Structures," AIAA Paper No. 88-4254-CP, *Proceedings of the AIAA/AAS Astrodynamics Conference*, Minneapolis, Minnesota, August 15-17, 1988.
- [12] JUANG, J. N. and PAPPAS, R. S. "An Eigensystem Realization Algorithm (ERA) for Model Parameter Identification," *Journal of Guidance, Control, and Dynamics*, Vol. 8, No. 5, September-October, 1985.
- [13] WILKINSON, J. H. *The Algebraic Eigenvalue Problems*, Oxford University Press, Oxford, 1965.
- [14] BODDEN, D. S. and JUNKINS, J. L. "Eigenvalue Optimization Algorithms for Structure/Controller Design Iterations," *Journal of Guidance, Control, and Dynamics*, Vol. 8, No. 6, November-December 1985, pp. 697-706.
- [15] TURNER, J. D., and CHUN, H. M. "Optimal Feedback Control of a Flexible Spacecraft During a Large Angle Rotational Maneuver," *Journal of Guidance, Control, and Dynamics*, Vol. 7, No. 3, May-June 1984, pp. 257-264.
- [16] JUNKINS, J. L. "Equivalence of the Minimum Norm and Gradient Projection Constrained Optimization Techniques," *AIAA Journal*, Vol. 10, No. 7, July 1972, pp. 927-929.

ATTACHMENT 6

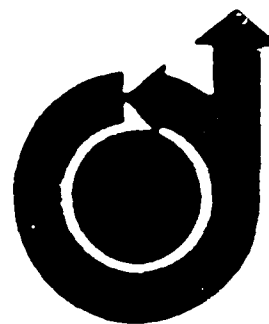
**Novel Sensing and Structural Identification Methods:  
Preliminary Analytical and Experimental Results**

*G. H. James*

*J. L. Junkins*

Texas A&M University  
Dept. of Aerospace Engineering  
College Station, Texas 77843

*AAS/AIAA Astrodynamics Specialist Conference*  
*Paper No. 89-425*  
*Stowe, Vermont*  
*August 7-10, 1989*



NOVEL SENSING AND STRUCTURAL IDENTIFICATION METHODS:  
PRELIMINARY ANALYTICAL AND EXPERIMENTAL RESULTS

G. H. James and J. L. Junkins  
Department of Aerospace Engineering  
Texas A & M University  
College Station, Texas 77843

**AAS/AIAA Astrodynamics  
Specialist Conference**

STOWE, VERMONT, AUGUST 7-10, 1989  
AAS Publications Office, P.O. Box 28130, San Diego, CA 92128

# NOVEL SENSING AND STRUCTURAL IDENTIFICATION METHODS: PRELIMINARY ANALYTICAL AND EXPERIMENTAL RESULTS

G. H. James and J. L. Junkins  
Department of Aerospace Engineering  
Texas A & M University  
College Station, Texas 77843

We present results of recent structural identification research in the Dynamics and Control Laboratory at Texas A & M University. Analytical developments, sensor/actuator systems and experimental results are described. The general framework of our identification method is presented. The method is an extension of the Creamer/Junkins<sup>1,2</sup> approach which scales user-defined substructures' contributions to the model matrices to fit the system's experimentally determined free and forced response in a least squares sense.

The test article is a 5' X 5' aluminum grid cantilevered in the vertical plane. The grid was cut from a single sheet of metal and is thus free of joints. A stereo-triangulation optical imaging system operating at 200 fields per second is used to measure inertial deflections of twenty active targets mounted on the structure. Conventional strain gauges are also mounted on the structure, both for identification measurement and for eventual real time control. Three reaction wheels are mounted on the structure for actuation. An instrumented impulse hammer is also available to excite the structure. The Eigensystem Realization Algorithm and software developed at Texas A&M are used for data reduction and modal identification.

## INTRODUCTION

The anticipated exploitation of the space environment for habitation, large scale scientific experiments, increased communication services, ballistic missile defense, surveillance, and energy production will require large structures on-orbit. Launch costs are extremely high and will force these structures to be very lightweight and therefore very flexible. The increased flexibility will cause the lower natural frequencies to be easily excited by control forces or other input forces. Mathematical models which reliably predict the dynamical response of these structures will be necessary to implement control systems or for analysis. These models are usually generated from a finite element process and give theoretical estimates of the natural frequencies, mode shapes, damping ratios, and frequency response functions.

A subset of these theoretical results can be experimentally determined on the actual structure or a representative test article. However the theoretical and experimental results will almost never agree. The sources of discrepancy are many, but the most important are: (i) model errors, (ii) measurement errors, and (iii) algorithm-induced errors. A process called structural identification is used to upgrade the mathematical model to obtain best estimated results in close agreement with experiment.

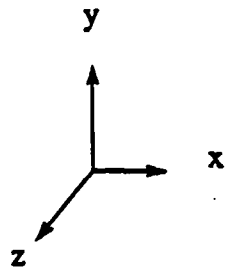
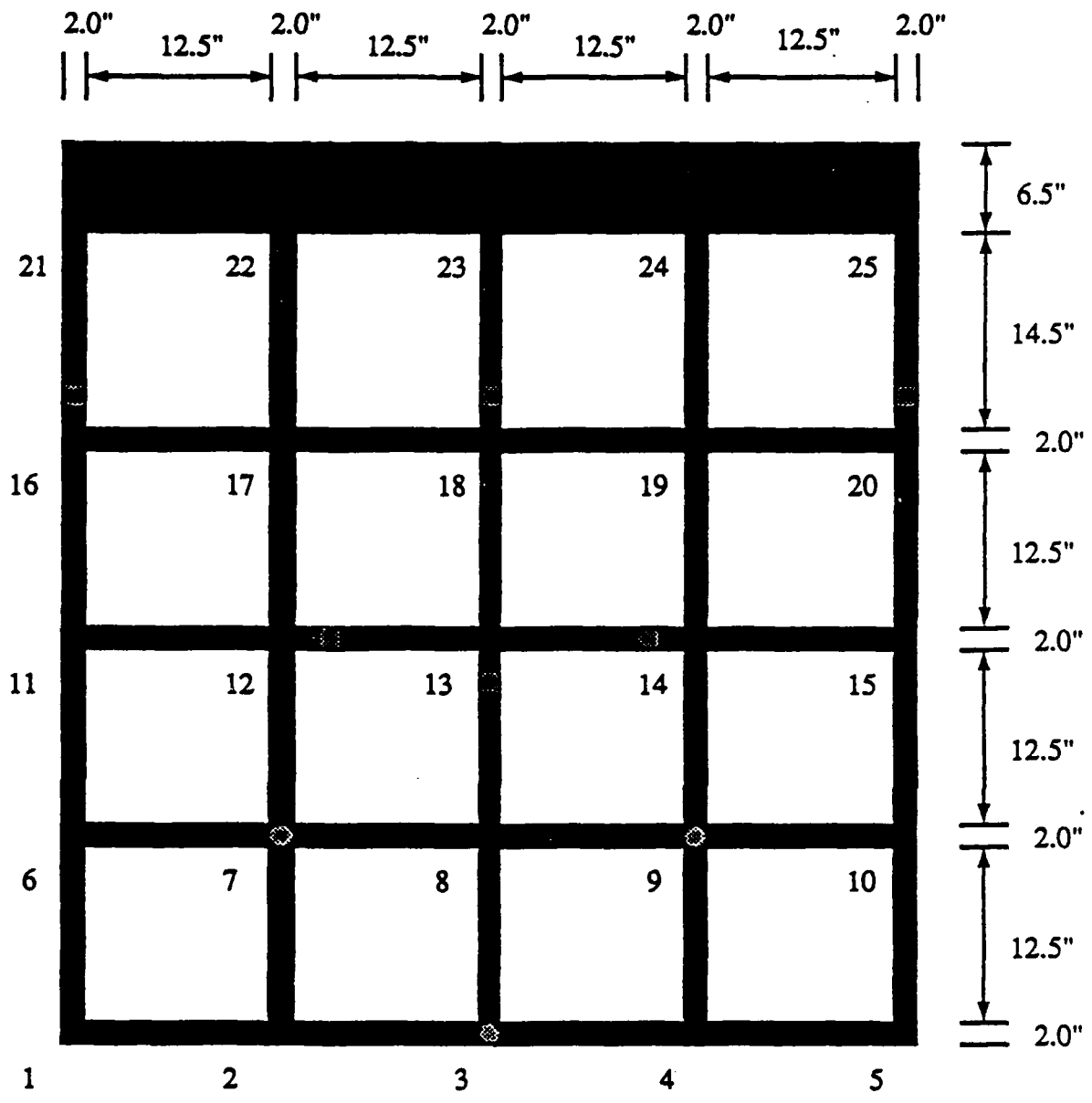
## HARDWARE DESCRIPTION

The test article used in this work is a 3003 H14 aluminum grid. The dimensions are shown in Fig. 1. The grid was cut from a single 5 foot wide sheet and is therefore monolithic. This unique feature eliminates nonlinear effects which arise in bolted or riveted structures. The test article is cantilevered in the vertical plane by a 6.5 inch tab. The tab is sandwiched between a 5 by 7 inch rectangular steel tube and a 5/8 inch thick aluminum plate. Ten bolts are used in the attachment.

Six full bridge strain gauge packets were mounted on the grid. The Micromeritics CEA-13-250UW-350 strain gauges were placed in pairs on opposite sides of the grid. The locations of the strain gauges are shown in Fig. 1. Three dual channel Micromeritics 2120-A conditioners are used to drive the strain gauges and amplify the signal. A Packard-Bell 280 P.C. and a Data Translation DT 281-G-16SE A to D board are used for data acquisition of strain gauge response. Edmund Scientific D-2536 jacketed light guides of outer diameter .087" are used to illuminate the 20 node points marked on the grid. The light guides are illuminated with a Kodak Carousel 850 projector with 500 watt bulb.

Three Clifton Precision AS-780D-100 electric motors with reaction wheels are mounted on the negative side of the grid at the locations marked in Fig. 1. The motor at node 3 is mounted with the shaft (torque axis) parallel to the y axis. The motors at nodes 7 and 9 are mounted with shafts parallel to the x axis. The motors can produce approximately 8 oz.-in of torque continuously or up to 16 oz.-in for short periods. The electrical time constant is approximately .35 milliseconds and the friction torque is approximately .6 oz.-in. The motors are powered by Kepco BOP-36-13M four quadrant power supplies. A Wavetek Model 188 Function Generator is used to provide sinusoidal input signals to drive the power supplies. A Hewlett Packard 5315A Universal Counter is used to read the frequency input to the motors. A reaction wheel is placed at each end of each motor shaft. These reaction wheels are brass disks 1.25" in diameter and .25" thick. A Kistler 9722A50 calibrated hammer is used for impulse testing.

Two NAC V-14B 200/60 field per second video cameras are being used in this research. These cameras contain 2/3 inch MOS focal plane charged coupled device detector arrays with 320 pixels in the horizontal direction and 244 pixels in the vertical direction. Two NAC model VTR V-32 video recorders are used to record the camera images at 200 f/s on 1/2" VHS video cassettes. A NAC V-61 viewfinder is available to monitor images at 200 f/s. A motion analysis SG-20 signal generator is used to externally synchronize both cameras and dub audio tones (used for timing) on the tapes. The 200 f/s recorded images are read at 60 f/s with a Panasonic AG-6300 video recorder and a Panasonic TR-124MA black and white monitor. A Motion Analysis VP-110 video processor is used to perform threshold-based edge detection, hardware editing, filtering, image boundary digitization, and data transfer of recorded images. A Sun 2/120 computer and Motion Analysis Corporation Expertvision 2D software are used to centroid image boundaries and produce focal plane trajectories of each centroid time history.



- 1 - 25 denote structure nodes
- - denotes strain gauge location
- - denotes motor location

Fig. 1 Grid Structure Dimensions

## MATHEMATICAL MODELLING

The grid structure is modelled using the following linear differential equation:

$$[M]\{\ddot{q}\} + [C]\{\dot{q}\} + [K]\{q\} = [B]\{u\} \quad (1)$$

$$\{\epsilon\} = [H]\{q\} \quad (2)$$

where

- [M] is the  $n \times n$  mass matrix;
- [C] is the  $n \times n$  damping matrix;
- [K] is the  $n \times n$  stiffness matrix;
- [B] is the  $n \times m$  input matrix;
- [H] is the  $s \times n$  strain transformation matrix;
- {q} is the  $n \times 1$  state vector;
- {u} is the  $m \times 1$  control vector;
- {ε} is the  $s \times 1$  strain vector;
- $n$  is the order of the system;
- $m$  is the number of inputs; and
- $s$  is the number of strain inputs.

## STRUCTURAL IDENTIFICATION

Cremer and Junkins<sup>1,2</sup> have developed a structural identification method which parameterizes the system matrices as follows:

$$M = M_0 + \sum_{i=1}^p \alpha_i M_i \quad (3)$$

$$C = C_0 + \sum_{j=1}^q \beta_j C_j \quad (4)$$

$$K = K_0 + \sum_{k=1}^r \gamma_k K_k \quad (5)$$

$$H = H_0 + \sum_{l=1}^s \mu_l H_l \quad (6)$$

$$B = B_0 + \sum_{m=1}^t \nu_m B_m \quad (7)$$

$M$ ,  $C$ ,  $K$ ,  $H$ , and  $B$  are the identified matrices.  $M_0$ ,  $C_0$ ,  $K_0$ ,  $H_0$  and  $B_0$  are the initial estimates.  $M_i$ ,  $C_j$ ,  $K_k$ ,  $H_l$ , and  $B_m$  are user defined submatrices which model contributions due to physical parameters, single elements, groups of elements, or partial derivative matrices.  $\alpha_i$ ,  $\beta_j$ ,  $\gamma_k$ ,  $\mu_l$ , and  $\nu_m$  are submatrix scale factors which are scaled to match experimentally determined subsets of the natural frequencies, mode shapes, damping ratios, and frequency

response functions in a least squares sense. The relationship between the model matrix scale factors and the system response is generally non-linear and an iterative solution is usually necessary.

Least squares differential correction<sup>3</sup> will be used to solve the above identification problem. The following parameter vector is defined:

$$P^T = \{ \alpha_1, \dots, \alpha_p, \beta_1, \dots, \beta_q, \gamma_1, \dots, \gamma_r, \mu_1, \dots, \mu_s, \nu_1, \dots, \nu_t \} \quad (8)$$

The parameter vector is then upgraded iteratively in the following fashion:

$$P_{i+1} = P_i + \Delta P_i \quad (9)$$

$$\Delta P_i = (A_i^T W A_i)^{-1} A_i^T W \Delta Q_i \quad (10)$$

$$\Delta Q_i = Q_{\text{measured}} - Q_{\text{calculated}} \quad (11)$$

$$Q^T = \{ \lambda, \psi, \zeta, h^r, h^i, R^r, R^i, 0_m, 0_k, 0_n, 0_p \}; \text{ and} \quad (12)$$

$$A_{uv} = \frac{\partial Q_u}{\partial P_v} \quad (13)$$

$\lambda$  is a subset of the undamped natural frequencies.  $\psi$  is a subset of the undamped mode shapes.  $\zeta$  is a subset of the damping ratios.  $h^r$  is real part of a subset of the frequency response functions away from resonance.  $h^i$  is the imaginary part of a subset of the frequency response functions near resonance.  $R^r$  is the real part of a subset of the frequency response functions near resonance.  $R^i$  is the imaginary part of a subset of the frequency response functions near resonance.  $0_m$  are zero entries in the Q vector which minimize changes in the orthogonality of the undamped eigenvectors with respect to the mass matrix.  $0_k$  are zero entries in the Q vector which minimize changes in the orthogonality of the undamped eigenvectors with respect to the stiffness matrix.  $0_n$  are zero entries in the Q vector which minimize changes in the normalization of the undamped eigenvectors.  $0_p$  are zero entries in the Q vector which minimize sizes of the submatrix scale factors.  $W$  is a weighting matrix for the Q vector.

The weights for  $\lambda$ ,  $\psi$ ,  $\zeta$ ,  $h^r$ ,  $h^i$ ,  $R^r$ , and  $R^i$  can be obtained from the uncertainty in the experiments. The weights on  $0_m$ ,  $0_k$ ,  $0_n$ , and  $0_p$  are user supplied and serve to constrain the problem to assure a solution. It may be necessary to utilize a structural identification preprocessor to assure that the starting estimates are close to the final estimates. Methods such as Creamer's<sup>1,2</sup> original method, Smith and Beatties' method<sup>4</sup> or Wei and Zhang's<sup>5</sup> method would be possible candidates.

## INITIAL MODEL

### Mass and Stiffness Matrices

The mass and stiffness properties of the structure are modelled using the approach of Paz<sup>6</sup>. Paz models simple grid structures as having three global degrees of freedom (d.o.f.) per node. The coordinate system given in Fig. 1 can be used to visualize the global d.o.f. as a rotation about the x-axis, a rotation about the y axis, and a displacement in the z direction. Paz therefore derives his grid element from an Euler-Bernoulli beam undergoing transverse displacement and an uncoupled torsional rotation. For our case, a total of 36 beam elements which connect the 25 nodes in Fig. 1 are used. All d.o.f. at nodes 21-25 are assumed fixed. This creates a global model of order 60.

The mass matrix is corrected to account for the effects of motor inertias at the appropriate modal locations using lumped masses and rotary inertias. A stiffness matrix correction for gravity was also calculated. The gravity correction is calculated by approximately the mass distribution as being lumped at the nodes and that the lumped masses act like multiple pendulum connected only in the vertical direction. The potential energy of this approximate representation assuming small angles is given as:

$$V \cong \sum_{i=1}^{20} gM_i L_i \{1 - (1/2) [(z_i - z_{i+5})/L_i]^2\} \quad (14)$$

where,  $g$  is acceleration due to gravity;

$M_i$  is the pendulum mass acting at each node;

$L_i$  is the length of the element connecting each node to the node above;

$z_i$  is the  $z$  displacement at node  $i$ ; and

$z_{i+5}$  is the  $z$  displacement at the node directly above node  $i$ .

A correction matrix for stiffness is calculated from  $\frac{\partial V}{\partial z_i}$  and added to the original stiffness matrix. Since the stiffness induced by gravity is a perturbation, the above approximations were found to give acceptable accuracy.

### Initial Damping Matrix

A proportional damping matrix is calculated as described by Craig<sup>7</sup> for an initial estimate. The initial damping matrix was calculated as:

$$C = 2\zeta_1 \omega_1 M \quad (15)$$

where  $\zeta_1$  is the expected damping ratio of the first mode, and  $\omega_1$  is the first theoretical

natural frequency.

### Input and Strain Transformation Matrix

The initial input matrix B is calculated by filling the appropriate entries in a 60x3 matrix of zeros with the current to torque constants for each motor. The strain transformation matrix is calculated from the following formula for a beam element undergoing a positive moment<sup>8</sup>:

$$\epsilon_i = \frac{-t}{2} \frac{d^2 z_e}{d x_e^2} \quad (16)$$

where,  $\epsilon_i$  is the  $i$ th strain gauge output;  
 $t$  is the beam element thickness;  
 $x_e$  is the length along the beam element; and  
 $z_e$  is the transverse displacement of the beam element.

$z_e$  is approximated as:

$$z_e = \psi_1 \delta_1 + \psi_2 \delta_2 + \psi_3 \delta_3 + \psi_4 \delta_4 \quad (17)$$

where  $\delta_1$  and  $\delta_3$  are  $z$  displacements at the nodes of the beam elements;  
 $\delta_2$  and  $\delta_4$  are  $x$  rotation or  $y$  rotation (depending on beam element orientation) at the element nodes; and  
 $\psi_i$  are shape functions.

The cubic shape functions are those which are commonly used for beam elements<sup>7</sup>:

$$\psi_1 = 1 - 3 \left( \frac{x_e}{L} \right)^2 + 2 \left( \frac{x_e}{L} \right)^3 \quad (18)$$

$$\psi_2 = x_e - 2L \left( \frac{x_e}{L} \right)^2 + L \left( \frac{x_e}{L} \right)^3 \quad (19)$$

$$\psi_3 = 3 \left( \frac{x_e}{L} \right)^2 - 2 \left( \frac{x_e}{L} \right)^3 \quad (20)$$

$$\psi_4 = -L \left( \frac{x_e}{L} \right)^2 + L \left( \frac{x_e}{L} \right)^3 \quad (21)$$

The 6x60 H matrix is filled by equations (16) - (21) for each beam element containing a strain gauge.

## OPTICAL SENSOR SYSTEM

The relationship between real world 3-dimensional ("object space") coordinates and 2-dimensional camera ("image space") coordinates is given by the following colinearity equations<sup>9</sup>:

$$u = u_0 + \Delta u + f_u \left[ \frac{c_{11} (x_p - x_c) + c_{12} (y_p - y_c) + c_{13} (z_p - z_c)}{c_{31} (x_p - x_c) + c_{32} (y_p - y_c) + c_{33} (z_p - z_c)} \right] \quad (22)$$

$$v = v_0 + \Delta v + f_v \left[ \frac{c_{21} (x_p - x_c) + c_{22} (y_p - y_c) + c_{23} (z_p - z_c)}{c_{31} (x_p - x_c) + c_{32} (y_p - y_c) + c_{33} (z_p - z_c)} \right] \quad (23)$$

$$C = C (\theta_1, \theta_2, \theta_3) \quad (24)$$

where,  $u$  and  $v$  are image plane coordinates;

$u_0$  and  $v_0$  are principle point offsets;

$f_u$  and  $f_v$  are focal lengths;

$x_c, y_c, z_c$  are the coordinates of the camera focal point in 3-D space.

$x_p, y_p, z_p$  are the 3-D coordinates of point being imaged;

$C_{ij}$  are elements of (1, 2, 3) Euler rotation matrix;

$\theta_1, \theta_2,$  and  $\theta_3$  are (1, 2, 3) Euler angles; and  $\Delta u$  and  $\Delta v$  model lens distortion.

First order expressions for  $\Delta u$  and  $\Delta v$  are given as:

$$\Delta u = \bar{u} K_1 r^2 + P_1 (r^2 + 2\bar{u}^2 \bar{v}) \quad (25)$$

$$\Delta v = \bar{v} K_1 r^2 + P_1 (2\bar{u}^2 \bar{v}) + P_2 (r^2 + 2\bar{v}^2) \quad (26)$$

$$r = [\bar{u}^2 + \bar{v}^2]^{\frac{1}{2}} \quad (27)$$

$$\bar{u} = u - u_0 \quad (28)$$

$$\bar{v} = v - v_0 \quad (29)$$

where,  $K_1$  is a parameter correcting radial distortion; and  $P_1$  and  $P_2$  correct for decentering distortion.

### Resection

The first step in using the optical sensor system is a static calibration (or resection) of the camera parameters given in equations (22) - (26). The twenty illuminated node points are viewed from two cameras while the structure is not in motion. This allows  $u$  and  $v$  focal plane coordinates and the associated statistics to be calculated for each point using both cameras. The static position of the grid nodal points and estimated uncertainties are also calculated. Initial estimates of the camera parameters and associated uncertainties could also be used as inputs to

the problem. The following vector of known quantities can then be collected:

$$Q^T = \{u^1_{p1}, v^1_{p1}, u^1_{p2}, \dots, v^1_{p20}, u^2_{p1}, \dots, v^2_{p20}, x_{p1}, y_{p1}, z_{p1}, \dots, z_{p20}, x^1_c, y^1_c, z^1_c, \theta^1_1, \theta^1_2, \theta^1_3, fu^1_1, fv^1_1, u^1_0, k^1_1, p^1_1, p^1_2, x^2_c, \dots, p^2_2\} \quad (30)$$

The exact positions of the static nodal points can be considered as unknowns as well as the camera parameters. The following 86x1 parameter vector then results:

$$P^T = \{x_{p1}, y_{p1}, z_{p1}, \dots, z_{p20}, x^1_c, y^1_c, z^1_c, \theta^1_1, \theta^1_2, \theta^1_3, fu^1_1, fv^1_1, u^1_0, k^1_1, p^1_1, p^1_2, x^2_c, \dots, p^2_2\} \quad (31)$$

The numerical subscripts in equations (30) and (31) denote the node number. The superscripts represent the first camera or second camera. The final parameter vector  $p$  is calculated iteratively using least squares differential correction<sup>3</sup>:

$$P_{i+1} = P_i + \Delta P_i \quad (32)$$

$$\Delta P_i = (A_i^T W A_i)^{-1} A_i^T W \Delta Q_i \quad (33)$$

where,  $\Delta P_i$  is the  $i$ th upgrade of the  $p$  vector;

$\Delta Q_i$  is the  $i$ th change in the  $Q$  vector;

$W$  is the 166 by 166 diagonal covariance matrix with the inverses of the variances of the  $Q$  vector on the diagonal; and

$A$  is the sensitivity matrix containing the partial derivatives of the  $Q$  vector with respect to the  $p$  vector.

The output of this problem includes the final parameter vector  $P_f$  and its approximate covariance matrix<sup>3</sup>  $W_p = (A_f^T W A_f)^{-1}$ . These are input to the next step which includes dynamic triangulation of the moving structure.

### Triangulation

This step allows the structure to move under the influence of free vibration or forced inputs. The position of each illuminated node is then calculated for each field of video data. The uncertainties of the final results are calculated by retaining the camera parameters as non-updated parameters and as measurements. The 30 by 1 vector of knowns is given as:

$$Q^T = \{u^1, v^1, u^2, v^2, x^1_c, y^1_c, z^1_c, \theta^1_1, \theta^1_2, \theta^1_3, fu^1_1, fv^1_1, u^1_o, k^1_1, p^1_1, p^1_2, x^2_c, \dots, p^2_2\} \quad (34)$$

and the 29x1 parameter vector is given as:

$$P^T = \{x_p, y_p, z_p, x^1_c, y^1_c, z^1_c, \theta^1_1, \theta^1_2, \theta^1_3, fu^1_1, fv^1_1, u^1_o, k^1_1, p^1_1, p^1_2, x^2_c, \dots, p^2_2\} \quad (35)$$

The final values of  $x_p$ ,  $y_p$ , and  $z_p$  are given by:

$$P_{i+1} = P_i + \Delta P_i \quad (36)$$

$$\Delta P_i = (A_i^T W A_i)^{-1} A_i^T W \Delta Q_i \quad (37)$$

This problem is solved iteratively as above. The final uncertainties are given in  $(A_i^T W A_i)^{-1}$ . This procedure allows the z displacement entries in the state vector to be measured directly, in non-contact fashion, and over a large area.

## DATA SET

### Natural Frequencies

The experimental natural frequencies will be determined from steady state, forced input tests with strain gauge output, from free vibration tests with strain gauge output, and from free vibration tests with video output. Fig. 2 shows a 14 second free vibration test with strain gauge output and its Fourier transform. Fig. 3 shows a 4.5 second free vibration test with video output. The Eigensystem Realization Algorithm (ERA) is currently being used to estimate damping ratios and natural frequencies from free vibration tests. Table 1 contains the modelled values of the first five natural frequencies in column one. Column two contains the current expected values of these frequencies. Standard errors for these frequencies will be estimated when the data base is large enough.

### Mode Shapes

The z displacement mode shapes are measurable with the video system from free or forced vibration tests. The free vibration data will be analyzed using ERA and time domain curve fits. The forced response data will be analyzed with sine-cosine curve fits. The curve fit method of data reduction has the advantage of providing estimates of the standard errors of the results. Table 2 contains the modelled values for the first mode z displacement mode shape in column one. Column two provides the experimentally determined values for the first mode. These results were obtained using a curve fit in the time domain on video data. The estimated standard

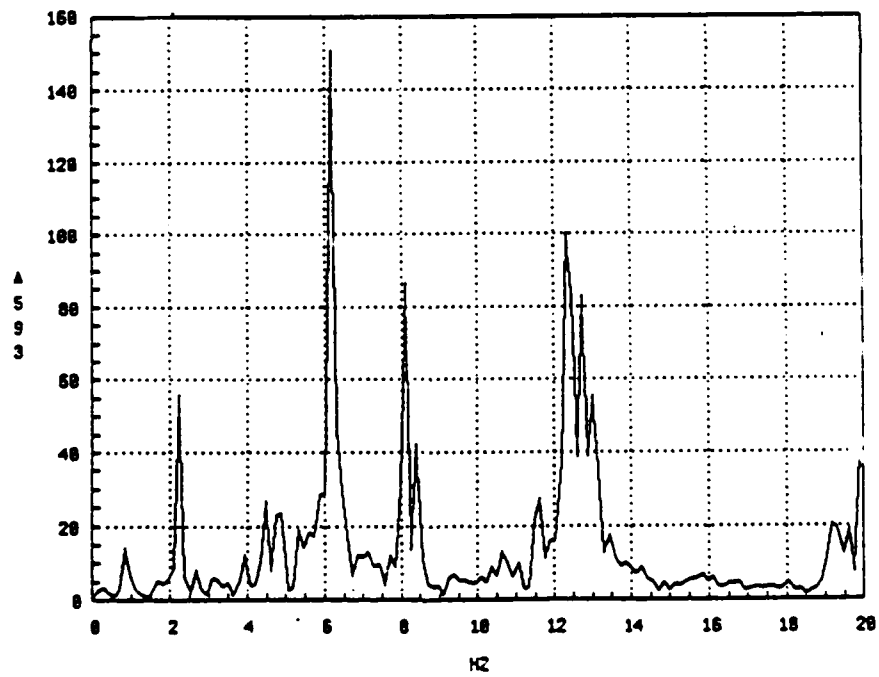
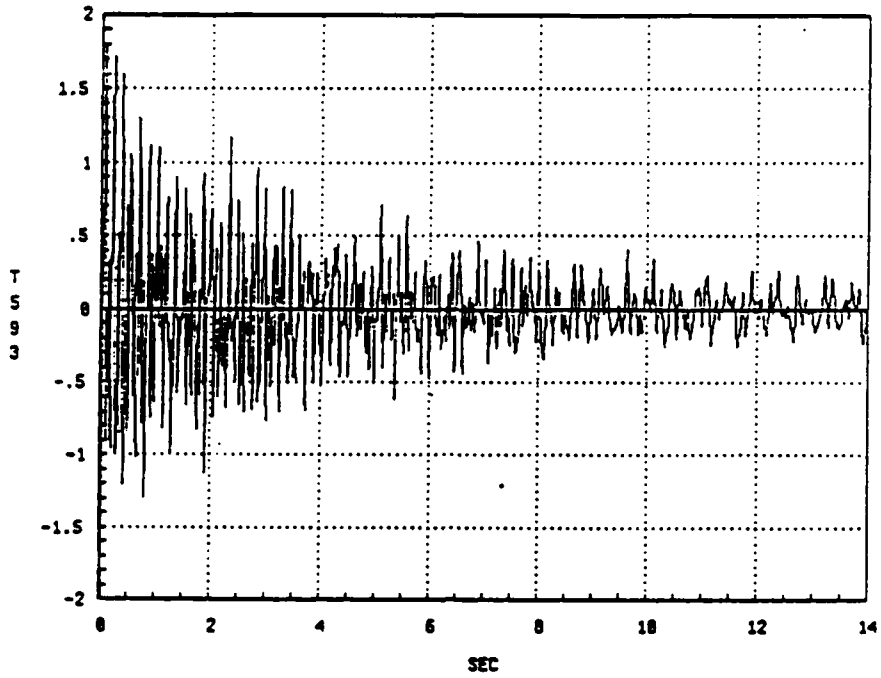


Fig. 2 Strain Gauge Free Vibration Test

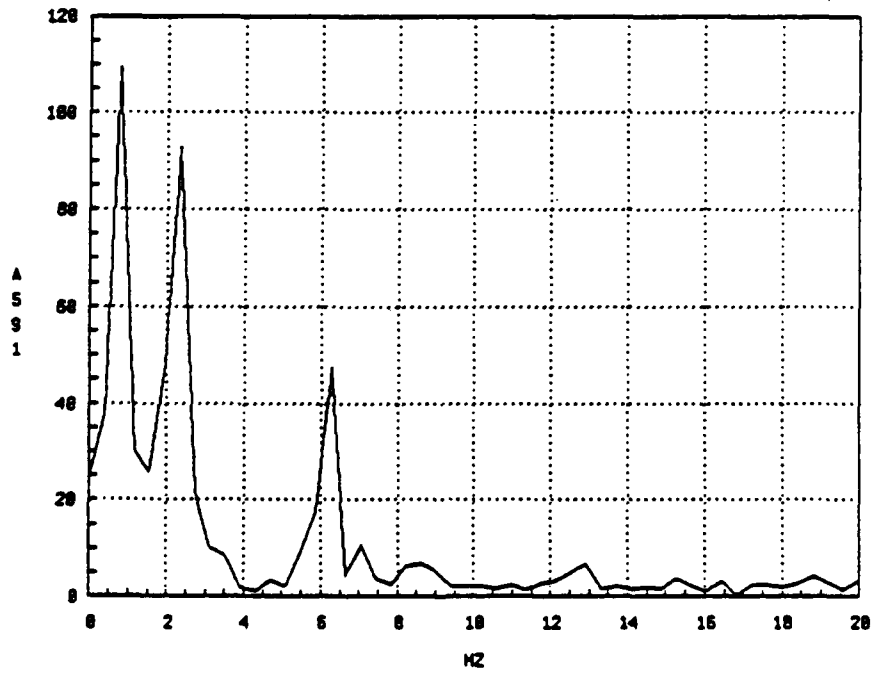
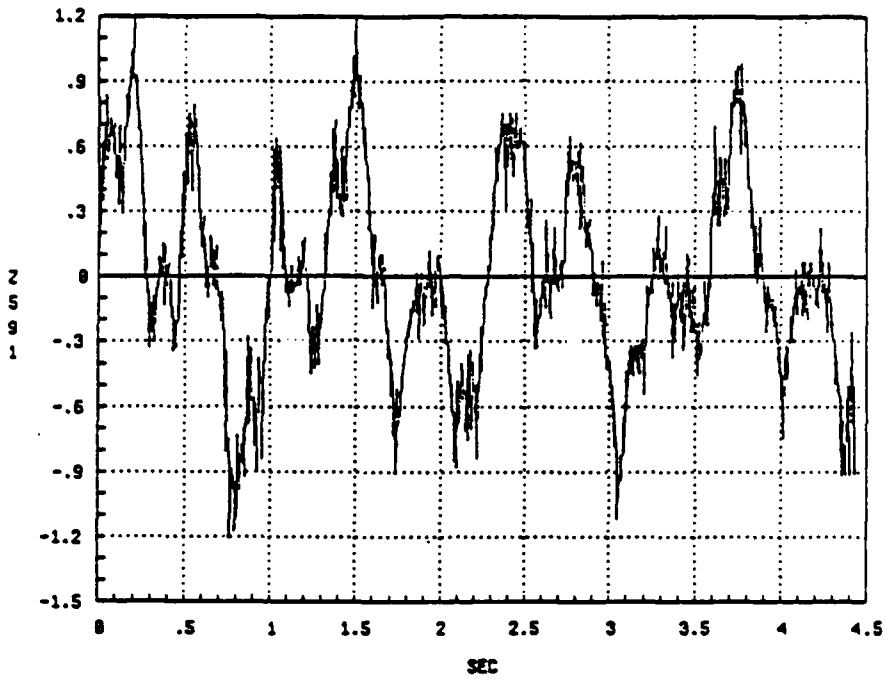


Fig. 3 Video Data Free Vibration Test

deviations are provided in column three. It should be noted that these results have been scaled with the analytical mass matrix.

Table 1

NATURAL FREQUENCY DATA

#	<u>Modelled (Hz)</u>	<u>Experiment (Hz)</u>	<u>Damping Ratio</u>	<u>D. R. Uncertainty</u>
1	.809	.877	.00603	.00043
2	2.21	2.19	.00489	.00033
3	4.48	4.81	.01105	.00208
4	5.65	6.17	.00596	.00045
5	7.76	8.18	.01293	.00116

Damping Ratios

The damping ratios will be estimated using ERA on free vibration tests and with time domain curve fits. Column three of Table 1 contains the current best estimates and column four contains the associated standard deviations. The standard deviations are most likely optimistic. Future analysis with a larger data base will probably refine these values. The first mode estimates were ERA results from long term strain gauge data. The estimates for modes 2, 3, 4, and 5 were obtained from short term video data.

Frequency Response Functions

The frequency response functions between all three motor inputs and all six strain gauge outputs were measured between .4Hz and 10.0Hz in increments of .2Hz. Additional data was taken at each of the first five frequencies simultaneously with video data. A linear sine and cosine curve fit to the data using the known forcing frequency was used to estimate real and imaginary parts of the response and the associated uncertainties. Fig. 4 provides a typical frequency response between the motor at mode 9 and the strain gauge near mode 14.

FUTURE WORK

The future analysis of free vibration video data will strengthen the estimation of the natural frequencies, mode shapes, and damping ratios as well as the associated statistics. The use of forced video data at resonance will also be used to strengthen the estimation of mode shapes, damping ratios, and aid in the identification of the strain transformation matrix.

The structural identification framework mentioned earlier will be used to upgrade the initial model to better fit the experimental data base. The use of the identified model for closed loop control is the real objective. This will be performed in subsequent work.

Table 2

## FIRST FREQUENCY MODE SHAPE

<u>Node #</u>	<u>Modelled</u>	<u>Experiment</u>	<u>Uncertainty</u>
1	8.25	7.66	.069
2	8.35	7.83	.060
3	8.40	8.18	.070
4	8.35	7.97	.074
5	8.25	8.54	.079
6	5.44	4.99	.071
7	5.52	5.10	.058
8	5.55	4.94	.085
9	5.52	6.17	.073
10	5.44	6.23	.072
11	2.85	2.12	.053
12	2.90	2.78	.052
13	2.92	3.57	.059
14	2.90	3.33	.069
15	2.85	3.95	.078
16	.871	1.14	.105
17	.897	.763	.096
18	.906	1.26	.079
19	.897	1.59	.092
20	.871	1.43	.080

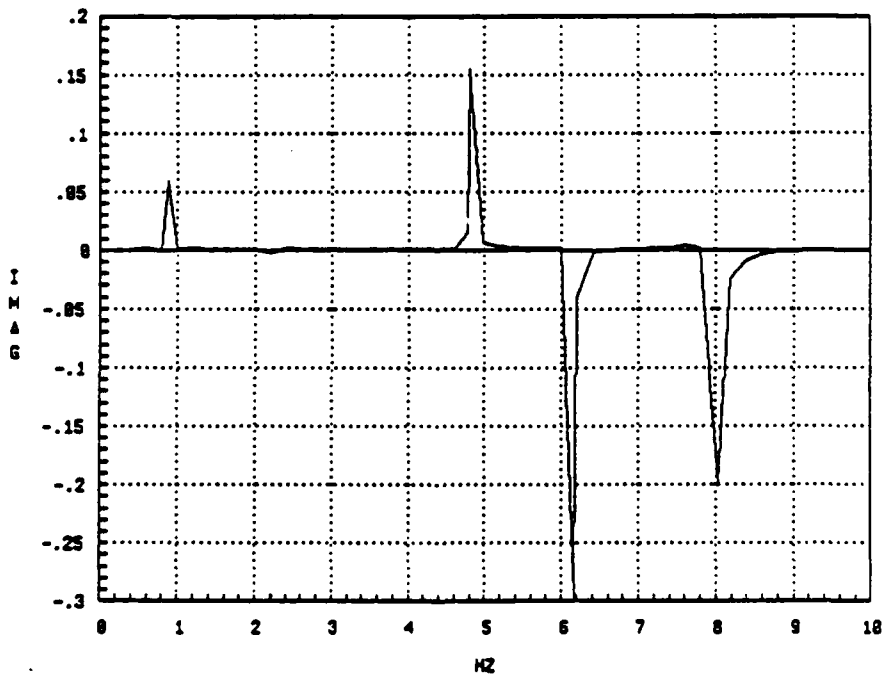
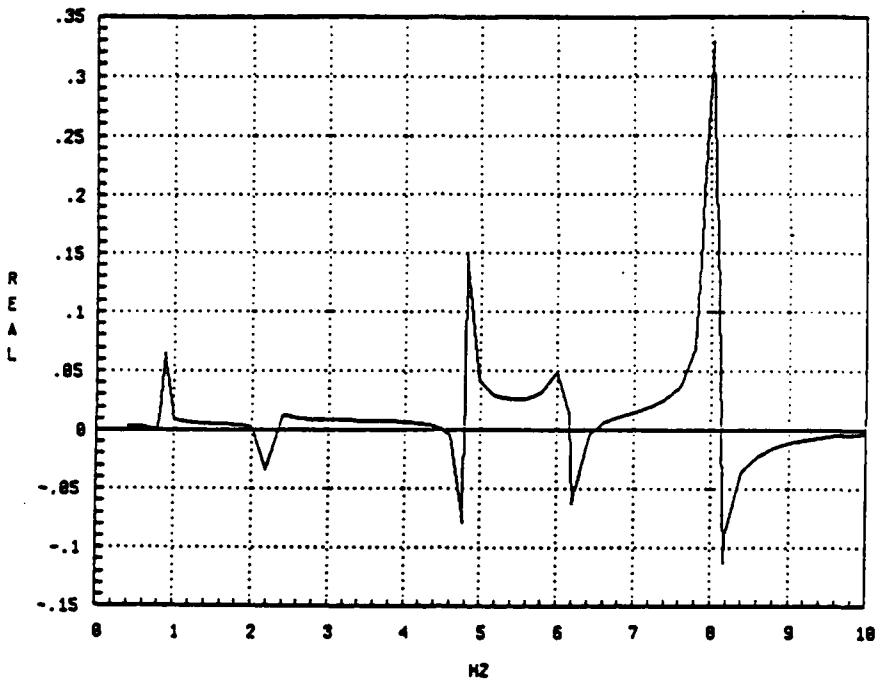


Fig. 4 Typical Frequency Response Function

## References

1. Creamer, N.G., *Identification of Flexible Structures*, Ph.D. Dissertation, Engineering Mechanics Department, Virginia Polytechnic and State University, 1987.
2. Creamer, N.G. and Junkins, J.L., "An Identification Method for Flexible Structures", *Journal of Guidance, Controls and Dynamics*, American Institute of Aeronautics and Astronautics, New York, New York.
3. Junkins, J. L., *Optimal Estimation of Dynamical Systems*, Sijthoff-Noordoff, Leyden, the Netherlands, 1978.
4. Beattie, C. S., and Smith, S. W., "Multiple Simultaneous Least - Change Secant Updates with Application to Structural Identification," Interdisciplinary Center for Applied Mathematics Report 88-09-01, VPI&SU, Blacksburg, Va., September 1988.
5. Wei, F., and Zhang, D., "Mass Matrix Modification Using Element Correction Method," *AIAA Journal*, Vol. 27, No. 1, January 1989.
6. Paz, M., *Structural Dynamics Theory and Computation*, 2nd Edition, Van Nostrand Reinhold Co., New York, New York, 1985.
7. Craig, R. R., *Structural Dynamics*, John Wiley and Sons, Inc., New York, New York, 1981.
8. Beer, F. P., and Johnston, E. R., *Mechanics of Materials*, McGraw Hill, Inc., New York, New York, 1981.
9. Brown, D. C., "Application of Close-Range Photogrammetry to Measurements of Structures in Orbit", Vol. 1, Geodetic Services Incorporated, Technical Report GSI 80-012, September 1980.

ATTACHMENT 7

Identification Method for Lightly Damped Structures

N. G. Creamer  
General Research Corporation  
Arlington, Virginia

J. L. Junkins  
Texas A&M University  
College Station, Texas

*a reprint from*  
*AIAA Journal of Guidance, Control and Dynamics*  
*Vol. 11, No. 6*  
*Nov-Dec 1988*

# Identification Method for Lightly Damped Structures

N. G. Creamer and J. L. Junkins

Reprinted from



## Journal of Guidance, Control, and Dynamics

Volume 11, Number 6, November-December 1988, Pages 571-576  
AMERICAN INSTITUTE OF AERONAUTICS AND ASTRONAUTICS, INC.  
370 L'ENFANT PROMENADE, SW • WASHINGTON, DC 20024

(167)

# Identification Method for Lightly Damped Structures

Nelson G. Creamer\*

General Research Corporation, Arlington, Virginia

and

John L. Junkins†

Texas A&M University, College Station, Texas

A structural model identification method is developed for determination of the mass and stiffness matrices of an undamped structure along with the damping matrix of a lightly damped structure. Using measurements of natural frequencies, damping factors, and frequency response elements, a unique identification of the model is established through incorporation of the spectral decomposition of the frequency response function and the modal orthonormality conditions. Numerical simulations demonstrate the flexibility and potential of the proposed method.

## Introduction

ACCURATE knowledge of the mass, damping, and stiffness associated with a dynamical system is a key ingredient for correlating theoretical and experimental results and for designing active control schemes for vibration suppression and attitude maneuvering. Discretization of a linear continuous structure by means of finite-element analysis (or other similar methods) yields the well-known mass and stiffness matrices. Although this discretization process may be well defined, the resulting structural model will be only as accurate as the parameters and modeling assumptions used to characterize the structural behavior. Also, determination of the damping matrix requires knowledge of parameters which may be difficult, if not impossible, to measure in the laboratory.

Methods for refining a priori structural models are readily available in the literature. References 1-6 address the identification of a set of physical/geometrical parameters using nonlinear least-squares and Bayesian estimation methods. The disadvantages of these methods are the following:

1) Use of natural frequencies and/or mode shapes, exclusively, results in nonunique identification of the initial parameterized model (in the sense that an infinity of linear models can produce the same set of eigenvalues and eigenvectors), unless some parameters are "fixed" at their initial values.

2) Convergence of the nonlinear estimation algorithms requires initial parameter estimates to be "close" to their true values.

References 7-11 determine mass and stiffness matrix improvements to enforce exact agreement between theory and experiment. Again, use of modal information alone results in both nonunique solutions and physically unrealistic coupling. Reference 12 utilizes submatrix scale factors to improve the initial mass and stiffness matrices using modal information, with the uniqueness problem once again surfacing. In Refs. 13-15, a linear algorithm is used to identify the mass, damping, and stiffness matrices from forced time-domain response. Although there is no initial estimate required for the model and the uniqueness problem is, in principle, eliminated, the disadvantages are now that the order of the resulting model is dependent on the number of sensors used on the structure and that the parameter vector consists of every element of the highly redundant mass, damping, and stiffness matrices.

dent on the number of sensors used on the structure and that the parameter vector consists of every element of the highly redundant mass, damping, and stiffness matrices.

A method for identifying the mass, damping, and stiffness matrices of an undamped or lightly damped structure using measured modal information and frequency response elements is developed in this paper. This method is designed to eliminate the problems described above and is simple to implement.

## Identification of Undamped Structures

Consider the classical second-order equations governing the motion of an undamped structural system

$$M\ddot{u} + Ku = f \quad (1)$$

where  $M$  and  $K$  are the  $n \times n$  mass and stiffness matrices,  $u$  is the  $n \times 1$  generalized coordinate vector, and  $f$  is the  $n \times 1$  generalized force vector. The initial estimates of the mass and stiffness matrices,  $\hat{M}$  and  $\hat{K}$ , are obtained from a standard discretization process, i.e., the finite-element method. It is assumed that the following measurements, extracted from response of the actual structure, are available: 1) a set of  $m$  ( $< n$ ) natural frequencies  $\hat{\omega}_n$ , 2) a set of corresponding  $n \times 1$  mode shapes  $\hat{\psi}_i$  (or approximations from the initial structural model), and 3) a small set of frequency response elements  $\hat{h}_{kr}(\omega)$  measured throughout the frequency range of interest for the structure. (A complete row/column of the frequency response matrix is not required.) Ewins<sup>16</sup> provides a review of many frequency- and time-domain approaches for generating these measurements. Ewins and Gleeson<sup>17</sup> developed a technique for obtaining modal measurements for lightly damped structures. Juang<sup>18</sup> provides a review of frequency- and time-domain modal identification techniques using system realization theory. The goal of the structural model identification method is to improve the initial mass and stiffness matrices such that the theoretical and experimental results are in agreement.

To begin, it is desirable to introduce the well-known spectral decomposition of the frequency response function

$$h_{kr}(\omega) = \sum_{j=1}^n \left( \frac{\phi_{kj} \phi_{jr}}{\omega_j^2 - \omega^2} \right) \quad (2)$$

Received May 1, 1987; revision received Sept. 3, 1987. Copyright © 1987 by J. L. Junkins. Published by the American Institute of Aeronautics and Astronautics, Inc., with permission.

\*Technical Staff, Member AIAA.

†TEES Chair Professor, Aerospace Engineering, Fellow AIAA.

where  $\phi_r$  is the  $j$ th element of the  $r$ th mass-normalized mode shape that, in matrix form, satisfies

$$\phi^T M \phi = I \tag{3}$$

Since the true mass matrix is not known, an approximation to Eq. (2) must be utilized. Introducing the relation

$$\phi_{jr} = \sqrt{\alpha_r} \bar{\psi}_{jr}, \quad r = 1, 2, \dots, m \tag{4}$$

into Eq. (2), and motivated by Ewins,<sup>16</sup> an approximation of the spectral decomposition can be written as

$$\bar{h}_{jk}(\omega) = \frac{a_1}{\omega^2} + \sum_{r=1}^m \left( \frac{\bar{\psi}_{jr} \bar{\psi}_{kr}}{\bar{\omega}_r^2 - \omega^2} \alpha_r \right) + a_2 \tag{5}$$

In Eq. (5), the first term represents the contribution from any rigid-body modes ( $\bar{\omega}_r = 0$ ), the last term represents an approximate residual contribution from high-frequency modes (outside the measured frequency range), and the  $\alpha$  are to-be-determined modal normalization factors. By "sampling" throughout the frequency range of interest ( $N$  represents the number of samples), Eq. (5) can be rearranged into the following standard linear format to identify the modal normalization factors by the method of least squares

$$\begin{Bmatrix} \bar{h}_{jk}(\omega_1) \\ \vdots \\ \bar{h}_{jk}(\omega_N) \end{Bmatrix} = \begin{bmatrix} \frac{1}{\omega_1^2} & L_{11} L_{12} \dots L_{1m} & 1 \\ \vdots & \ddots & \vdots \\ \frac{1}{\omega_N^2} & L_{N1} L_{N2} \dots L_{Nm} & 1 \end{bmatrix} \begin{Bmatrix} a_1 \\ \alpha_1 \\ \vdots \\ \alpha_m \\ a_2 \end{Bmatrix} \tag{6a}$$

where

$$L_{nr} = \frac{\bar{\psi}_{nr} \bar{\psi}_{kj}}{\bar{\omega}_r^2 - \omega_n^2} \tag{6b}$$

To include measurements from more than one frequency response element, if available, a simple augmentation (or "stacking") of Eqs. (6) is required.

Once the modal normalization factors have been determined, the orthonormality conditions that the mode shapes must satisfy can be written as

$$\bar{\psi}_i^T M \bar{\psi}_j = \delta_{ij} / \alpha_j \tag{7a}$$

$$\bar{\psi}_i^T K \bar{\psi}_j = \delta_{ij} \bar{\omega}_j^2 / \alpha_j \tag{7b}$$

To identify the true mass and stiffness matrices, the following expansions are used<sup>12</sup>

$$M = \bar{M} + \sum_{r=1}^P \gamma_r M_r \tag{8a}$$

$$K = \bar{K} + \sum_{r=1}^Q \beta_r K_r \tag{8b}$$

where  $\bar{M}$ , and  $\bar{K}$ , are the  $r$ th predetermined mass and stiffness submatrices,  $\gamma_r$  and  $\beta_r$ , the to-be-determined  $r$ th mass and stiffness submatrix scale factors, and  $P$  and  $Q$  the total number of mass and stiffness submatrices. The mass and stiffness submatrices can represent single finite elements or (more commonly) groups of common finite elements assembled into their corresponding global locations. The flexibility (and responsibility) in defining  $\bar{M}$ , and  $\bar{K}$ , in Eqs. (8) is an important feature that can be used to exploit an engineer's insight explicitly. Substitut-

ing Eqs. (8) into Eqs. (7) and re-arranging terms yields

$$\begin{Bmatrix} -\bar{\psi}_i^T \bar{M} \bar{\psi}_j + \frac{1}{\alpha_i} \\ -\bar{\psi}_i^T \bar{M} \bar{\psi}_j \end{Bmatrix} = \begin{bmatrix} \bar{\psi}_i^T M_1 \bar{\psi}_i & \dots & \bar{\psi}_i^T M_P \bar{\psi}_i \\ \bar{\psi}_i^T M_1 \bar{\psi}_j & \dots & \bar{\psi}_i^T M_P \bar{\psi}_j \end{bmatrix} \begin{Bmatrix} \gamma_1 \\ \vdots \\ \gamma_P \end{Bmatrix} \tag{9a}$$

$$\begin{Bmatrix} -\bar{\psi}_i^T \bar{K} \bar{\psi}_j + \frac{\bar{\omega}_i^2}{\alpha_i} \\ -\bar{\psi}_i^T \bar{K} \bar{\psi}_j \end{Bmatrix} = \begin{bmatrix} \bar{\psi}_i^T K_1 \bar{\psi}_i & \dots & \bar{\psi}_i^T K_Q \bar{\psi}_i \\ \bar{\psi}_i^T K_1 \bar{\psi}_j & \dots & \bar{\psi}_i^T K_Q \bar{\psi}_j \end{bmatrix} \begin{Bmatrix} \beta_1 \\ \vdots \\ \beta_Q \end{Bmatrix} \tag{9b}$$

where the second set of equations in Eqs. (9a) and (9b) are valid when  $i \neq j$ . Collecting Eqs. (9) for each measured natural frequency yields a set of equations (linear in the unknown submatrix scale factors), which can be solved by a least-squares method, provided that  $m(m+1)/2$  is greater than  $\max(P, Q)$ . Since Eq. (5) represents an approximation to the frequency response function, an iterative procedure can be used whereby the unmeasured natural frequencies and mode shapes are predicted from the present best estimate of the structural model and used in Eq. (5) in lieu of measurements.

### Identification of Lightly Damped Structures

If a small amount of damping is present in a structure, the structural identification method developed in the previous section can be used, in conjunction with matrix perturbation theory, to identify the mass, damping, and stiffness matrices. Consider the symmetrical state-space representation of Eq. (1) in the form

$$A \begin{Bmatrix} \dot{u} \\ \ddot{u} \end{Bmatrix} + B \begin{Bmatrix} u \\ \dot{u} \end{Bmatrix} = \begin{Bmatrix} 0 \\ f \end{Bmatrix} \tag{10a}$$

where

$$A = \begin{bmatrix} -K & 0 \\ 0 & M \end{bmatrix}, \quad B = \begin{bmatrix} 0 & K \\ K & 0 \end{bmatrix} \tag{10b}$$

If light viscous damping is introduced into the equations of motion in the form of the symmetric damping matrix  $C$ , the state-space representation is perturbed by the relation

$$B = \begin{bmatrix} 0 & K \\ K & 0 \end{bmatrix} + \begin{bmatrix} 0 & 0 \\ 0 & C \end{bmatrix} = B_0 + B_1 \tag{11}$$

where  $B_1$  represents the perturbation matrix due to the presence of the light damping. A first-order perturbation solution to the free-response eigenvalue problem of Eqs. (10) can be obtained to approximate the change in the eigenvalues due to the inclusion of the damping matrix.<sup>19</sup>

Consider the eigenvalue problem

$$-\lambda_{or} A_0 \Phi_{or} = B_0 \Phi_{or} \tag{12}$$

where  $A_0$  and  $B_0$  are  $2n \times 2n$  symmetric matrices and  $\lambda_{or}$  and  $\Phi_{or}$  ( $r = 1, 2, \dots, 2n$ ) are the eigenvalues and eigenvectors. It is assumed that the eigenvectors are normalized such that

$$\Phi_{or}^T A_0 \Phi_{or} = \delta_{jk} \tag{13a}$$

$$\Phi_{or}^T B_0 \Phi_{or} = -\lambda_{or} \delta_{jk} \tag{13b}$$

If small perturbations  $A_1$  and  $B_1$  are added to each matrix, the resulting eigenvalue problem becomes

$$-\lambda_r A \Phi_r = B \Phi_r \tag{14a}$$

where

$$A = A_0 + A_1 \tag{14b}$$

$$B = B_0 + B_1 \tag{14c}$$

$$\lambda_r = \lambda_{0r} + \lambda_{1r} \tag{14d}$$

$$\Phi_r = \Phi_{0r} + \Phi_{1r} \tag{14e}$$

The eigenvalues  $\lambda_{1r}$  and eigenvectors  $\Phi_{1r}$  represent small perturbations from their original values. Expanding Eq. (14a), using Eq. (12), and neglecting second-order terms yields the equation

$$B_1 \Phi_{0r} + B_0 \Phi_{1r} = -\lambda_{0r} A_1 \Phi_{0r} - \lambda_{0r} A_0 \Phi_{1r} - \lambda_{1r} A_0 \Phi_{0r} \tag{15}$$

Multiplying Eq. (15) by  $\Phi_{0s}^T$  and utilizing Eqs. (13) yields the relation

$$\Phi_{0s}^T B_1 \Phi_{0r} + \Phi_{0s}^T B_0 \Phi_{1r} = -\lambda_{0s} \Phi_{0s}^T A_1 \Phi_{0r} - \lambda_{0s} \Phi_{0s}^T A_0 \Phi_{1r} - \lambda_{1r} \delta_{rs} \tag{16}$$

It can be observed from Eqs. (14) that if  $A_1$  and  $B_1$  are zero, then  $\lambda_{1r} = 0$  ( $r = 1, 2, \dots, 2n$ ) and  $\Phi_{1r}$  become scalar multiples of  $\Phi_{0r}$ . In general,  $\Phi_{1r}$  can be written as a linear combination of the vectors  $\Phi_{01}, \Phi_{02}, \dots, \Phi_{02n}$ . To guarantee that  $\Phi_{1r} = 0$ , when  $A_1$  and  $B_1$  are zero, it is assumed that the perturbation eigenvector has the form<sup>19</sup>

$$\Phi_{1r} = \sum_{k=1}^{2n} \varepsilon_{rk} \Phi_{0k}, \quad \varepsilon_{rs} = 0, \quad s = 1, 2, \dots, 2n \tag{17}$$

Using Eq. (17) in Eq. (16) and letting  $s = r$  result in an expression for the perturbed eigenvalues

$$\lambda_{1r} = -\Phi_{0r}^T [\lambda_{0r} A_1 + B_1] \Phi_{0r}, \quad r = 1, 2, \dots, 2n \tag{18}$$

In the sequel, it will be shown that Eq. (18) can be used as the central equation for identification of the damping matrix.

For a lightly damped structure, the frequency response function closely resembles that of the corresponding undamped structure, except near the resonant peaks. Therefore, given a set of complex frequency response measurements from a lightly damped structure, identification of the mass and stiffness matrices can be performed, as described in the previous section, by using the real components of the frequency response measurements and the imaginary components of the eigenvalue measurements. Again, this method will only be accurate for frequency response measurements away from the resonant peaks. Once the mass and stiffness matrices have been identified, the damping matrix can be determined as follows. First, the perturbed eigenvalues  $\lambda_{1r}$  are obtained by simply subtracting the undamped modeled eigenvalues  $\lambda_{0r}$  from the measured eigenvalues  $\tilde{\lambda}_r$ ,

$$\lambda_{1r} = \tilde{\lambda}_r - \lambda_{0r} = (\bar{\sigma}_r + i\bar{\omega}_r) - (i\omega_{0r}) \tag{19a}$$

$$\lambda_{1r} = \bar{\sigma}_r + i(\bar{\omega}_r - \omega_{0r}) \tag{19b}$$

where  $\bar{\sigma}_r$  and  $\bar{\omega}_r$  are the  $r$ th measured damping term and damped natural frequency. To utilize Eq. (18), the eigenvectors  $\Phi_{0r}$  must be normalized according to Eqs. (13). In general, the form of the eigenvectors becomes

$$\Phi_{0r} = \begin{Bmatrix} \phi_{0r} \\ i\omega_{0r} \phi_{0r} \end{Bmatrix} \tag{20}$$

where  $\phi_{0r}$  are the mode shapes from the identified undamped model, normalized with respect to the identified mass matrix. Therefore, using Eq. (20) in Eq. (13a) determines scale factors

$\alpha_r$ , necessary to normalize  $\Phi_{0r}$ , such that Eq. (13) is satisfied

$$\alpha_r \{ \phi_{0r}^T \ i\omega_{0r} \phi_{0r}^T \} \begin{bmatrix} -K & 0 \\ 0 & M \end{bmatrix} \begin{Bmatrix} \phi_{0r} \\ i\omega_{0r} \phi_{0r} \end{Bmatrix} = 1 \tag{21a}$$

or

$$\alpha_r (-\phi_{0r}^T K \phi_{0r} - \omega_{0r}^2 \phi_{0r}^T M \phi_{0r}) = 1 \tag{21b}$$

or

$$\alpha_r = -\frac{1}{2\omega_{0r}^2} \tag{21c}$$

The normalized eigenvectors  $\Phi_{0r}$  can now be written as

$$\Phi_{0r} = \frac{i}{\sqrt{2\omega_{0r}}} \begin{Bmatrix} \phi_{0r} \\ i\omega_{0r} \phi_{0r} \end{Bmatrix} \tag{22}$$

Expanding the damping matrix in a similar fashion to Eqs. (8), and using Eqs. (22) and (19b) in Eq. (18) with  $A_1 = 0$  and  $B_1$  defined in Eq. (11), yields the relation

$$\bar{\sigma}_r + i(\bar{\omega}_r - \omega_{0r}) = -\frac{1}{2} \phi_{0r}^T \left[ \hat{C} + \sum_{q=1}^R \xi_q C_q \right] \phi_{0r} \tag{23}$$

where  $\hat{C}$  is the initial damping matrix,  $C_q$  the  $q$ th damping submatrix,  $\xi_q$  the  $q$ th damping submatrix scale factor, and  $R$  the total number of damping submatrices. Because the right side of Eq. (23) is real, the first-order perturbation solution does not predict a change in the undamped natural frequencies due to the addition of the light damping and, therefore, only the measured damping terms  $\bar{\sigma}_r$  are used to identify the damping matrix. Rearranging Eq. (23) to solve for the submatrix scale factors yields the linear least-squares problem

$$\begin{Bmatrix} -2\bar{\sigma}_1 - \phi_{01}^T \hat{C} \phi_{01} \\ \vdots \\ -2\bar{\sigma}_m - \phi_{0m}^T \hat{C} \phi_{0m} \end{Bmatrix} = \begin{bmatrix} \phi_{01}^T C_1 \phi_{01} & \dots & \phi_{01}^T C_R \phi_{01} \\ \vdots & & \vdots \\ \phi_{0m}^T C_1 \phi_{0m} & \dots & \phi_{0m}^T C_R \phi_{0m} \end{bmatrix} \begin{Bmatrix} \xi_1 \\ \vdots \\ \xi_R \end{Bmatrix} \tag{24}$$

where it is assumed that there are  $m$  ( $> R$ ) measured damping terms. Solving Eq. (24) for the submatrix scale factors leads to the desired damping matrix. The advantages of this perturbation approach are twofold: Identification of the damped equations of motion can be performed in configuration space without the need to solve the state-space eigenvalue problem, and the original damping matrix  $\hat{C}$  need only represent the true damping matrix in the coupling of the elements. (Due to the linearity of the equations, the original numerical values can be off by orders of magnitude.) In most practical applications, the form of the initial damping matrix  $\hat{C}$  will not be known. However, if an assumed form is prescribed (from a Rayleigh dissipation function, for example) Eq. (24) can still be used to provide a best fit (in a least-squares sense) to the measured damping terms  $\bar{\sigma}_r$ .

**Example 1**

The mass and stiffness matrices are identified for the simple manipulator arm, shown in Fig. 1. The structure consists of two flexible appendages, rotational springs at the base and at the connecting joint, and a grip with mass and inertia.

The estimation process is initiated using approximate mass and stiffness matrices obtained by increasing the true mass properties by 10% and decreasing the true stiffness properties by 10%. The first five natural frequencies of the true model and the frequency response function representing the ratio of transverse displacement at the connecting joint to torque at the base

Table 1 Group modal energy distributions for the simple manipulator arm

Mode	Kinetic energy (%) of mass groups				Potential energy (%) of stiffness groups			
	I	II	III	IV	I	II	III	IV
1	0.0	0.5	0.0	99.5	0.2	0.1	66.5	33.2
2	58.8	39.1	1.9	0.2	0.1	0.1	33.3	66.5
3	27.5	47.3	25.2	0.0	19.5	80.5	0.0	0.0
4	64.0	22.1	13.9	0.0	75.7	24.1	0.1	0.1
5	16.5	38.8	44.7	0.0	7.4	92.6	0.0	0.0

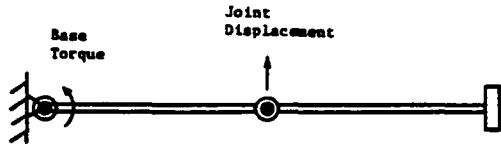


Fig. 1 Simple manipulator arm.

Table 2 Free-response identification results for the simple manipulator arm

Mode	$\omega_n$	$\omega_{ns}$	$\omega_{nr}$
1	0.0230 rad/s	0.0209 rad/s	0.0230 rad/s
2	1.062	0.9617	1.066
3	55.44	50.15	55.55
4	91.12	82.42	91.19
5	156.75	141.78	156.98

are treated as measurements. The mode shapes from the approximate initial model are used for "measured" mode shapes. To cast the model in terms of mass and stiffness submatrices, the following mass and stiffness element groups are chosen:

Mass:

- Group I Mass matrix contribution of appendage 1
- Group II Mass matrix contribution of appendage 2
- Group III Tip mass moment of inertia
- Group IV Tip mass

Stiffness:

- Group I Stiffness matrix contribution of appendage 1
- Group II Stiffness matrix contribution of appendage 2
- Group III Base rotational stiffness
- Group IV Joint rotational stiffness

The initial fractional modal energy contributions from each element group (obtained from  $\phi_0^T M \phi_0$  and  $\phi_0^T K \phi_0 / \omega^2$ ) are given in Table 1. It is apparent from examination of the potential energy distribution that the first two modes approximate those that would be obtained for a two degree-of-freedom model with rigid appendages and that the higher modes represent the flexibility of the appendages. As a consequence of this observation, a two-step process was used to identify the structure. First, the three highest modes were used to identify mass element groups I, II, and III and stiffness element groups I and II. Then, the two lowest modes were used to identify mass element group IV and stiffness element groups III and IV. The free- and forced-response identification results (after two iterations) are provided in Table 2 and Fig. 2, respectively.

Example 2

The mass, damping, and stiffness matrices are identified for the planar truss structure shown in Fig. 3. Both internal (mate-

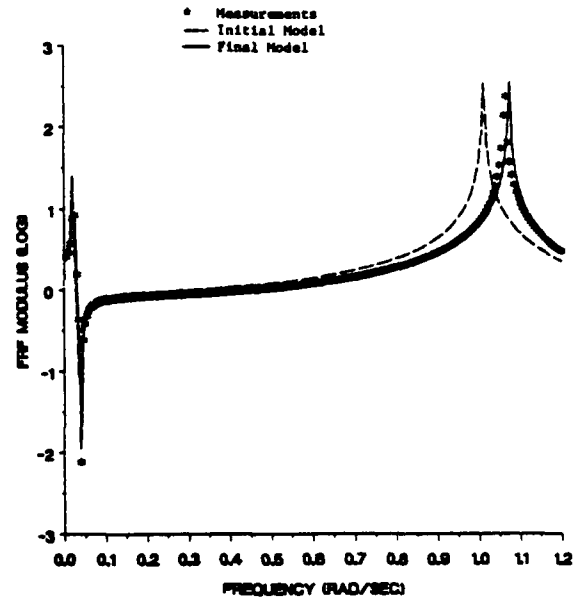


Fig. 2a Low-range frequency response results for the simple manipulator arm.

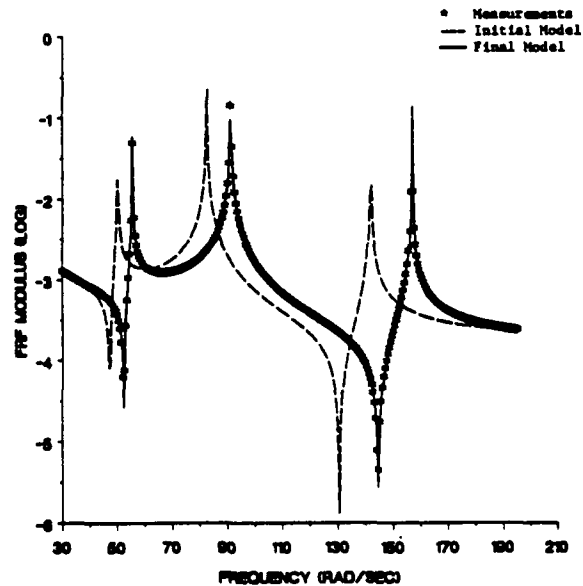


Fig. 2b High-range frequency response results for the simple manipulator arm.

Fig. 3 Planar truss structure.

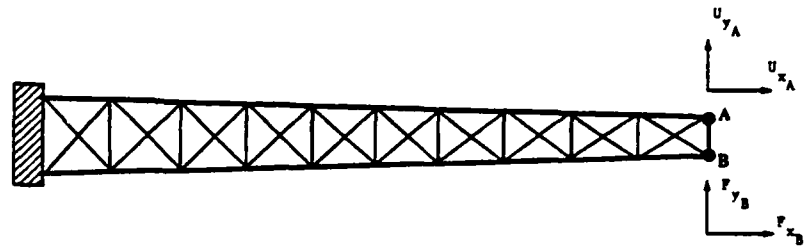


Table 3 Free-response identification results for the planar truss structure

Mode	$\bar{\lambda}$	$\lambda_0$	$\lambda_f$
1	$-0.0872 + 6.73i$	$6.11i$	$-0.0872 + 6.93i$
2	$-0.0890 + 34.59i$	$31.45i$	$-0.0888 + 35.46i$
3	$-0.0891 + 87.58i$	$78.89i$	$-0.0898 + 88.29i$
4	$-0.1042 + 117.11i$	$106.67i$	$-0.1039 + 119.39i$
5	$-0.0907 + 156.49i$	$142.12i$	$-0.0906 + 157.86i$
6	$-0.0914 + 240.33i$	$217.54i$	$-0.0915 + 240.05i$
7	$-0.0929 + 332.09i$	$302.00i$	$-0.0925 + 331.39i$
8	$-0.1039 + 359.29i$	$325.25i$	$-0.1042 + 363.28i$

rial) and external (atmospheric) light viscous damping is present, although the magnitude of damping is unknown.

The measurement set consists of the first eight complex eigenvalues and transverse and longitudinal frequency response functions between points A and B. To simulate measurement errors, the eigenvalue and frequency response measurements are corrupted with random Gaussian noise (zero mean,  $SD_{\lambda} = 0.01|\lambda_r|$ ,  $SD_h = 0.11|h_{\mu}|$ ). As in Example 1, the mode shapes from the initial model are chosen for "measured" mode shapes. To cast the model in terms of submatrices, the following element groups are chosen:

Mass and stiffness:

- Group I 20 upper and lower bending elements
- Group II 20 diagonal bending/shear elements

Damping:

- Group I External viscous damping matrix
- Group II Internal viscous damping matrix

Preliminary examination of the modal kinetic and potential energy distributions indicates that the vertical truss members contribute no energy to the first eight modes and are, therefore, not used for model improvement.

The mass and stiffness matrices are approximated initially by increasing the true mass properties by 10% and decreasing the true stiffness properties by 10%. The initial approximations of the external and internal passive damping matrices are only accurate in the coupling of the elements (the numerical values are off by orders of magnitude). The identification process requires two steps: 1) identification of the mass and stiffness matrices from the real components of the measured frequency response functions and the imaginary components of the measured eigenvalues, and 2) identification of the damping matrix from the real components of the measured eigenvalues. The free- and forced-response identification results for the structure are presented in Table 3 and Fig. 4, respectively.

Conclusions

A method for updating initial mathematical models of undamped and lightly damped linear structures has been presented and successfully tested in two simulated examples. The advantages of the method are the following:

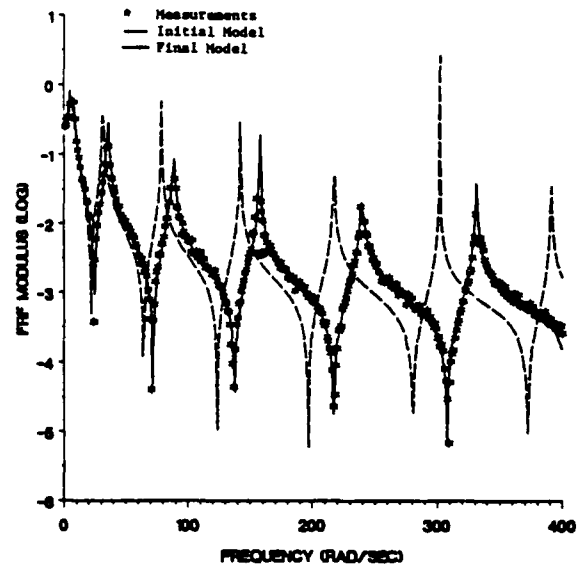


Fig. 4a Transverse frequency response results for the planar truss structure.

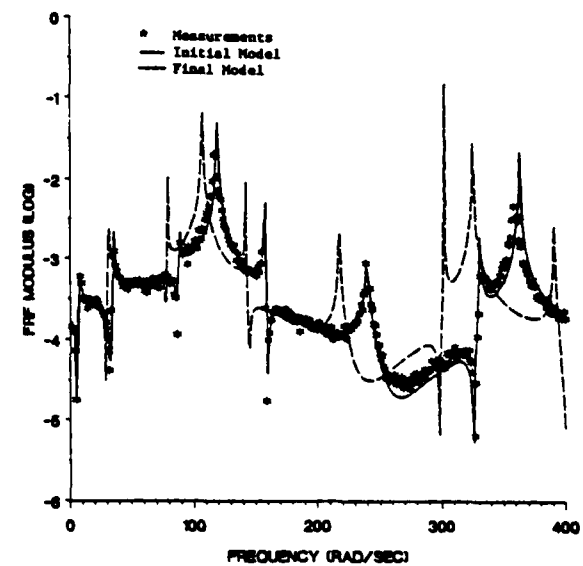


Fig. 4b Longitudinal frequency response results for the planar truss structure.

- 1) Incorporation of measured frequency response functions provides a unique scaling of prescribed submatrices of an initial mathematical model of the structure.
- 2) All least-squares formulations are linear.
- 3) The consistency of the original model is maintained. (No unmodeled coupling occurs as a consequence of the identification process.)

4) Use of submatrix scale factors can potentially limit the identification process to a relatively small set of parameters.

5) For lightly damped structures, the identification can be performed in the  $n$  configuration space without the need to solve the  $2n$  state-space eigenproblem.

6) For lightly damped structures, the original estimate of the damping matrix need only be accurate in the coupling of the elements. (The numerical values can be off by orders of magnitude.) However, if the original form of the damping matrix is unknown, the method will still provide a unique scaling of an assumed initial (symmetric) damping matrix and its submatrices to best fit measured damping terms.

It should be noted that the examples presented in this paper considered only those structures with widely spaced, well-defined modes. Further research is needed to address the applicability of the method to actual structures containing dense modal spectra and in the presence of real measurement and modeling errors.

### References

- <sup>1</sup>Hendricks, S. L., Hayes, S. M., and Junkins, J. L., "Structural Parameter Identification for Flexible Spacecraft," AIAA Paper 84-0060, Jan. 1984.
- <sup>2</sup>Creamer, N. G. and Hendricks, S. L., "Structural Parameter Identification Using Modal Response Data," *Proceedings of the Fifth VPI&SU/AIAA Symposium on Dynamics and Control of Large Flexible Spacecraft*, edited by L. Meirovitch, AIAA, New York, 1985.
- <sup>3</sup>Collins, J. D., Hart, G. C., Hasselman, T. K., and Kennedy, B., "Statistical Identification of Structures," *AIAA Journal*, Vol. 12, Feb. 1974, pp. 185-190.
- <sup>4</sup>Dobbs, M. W. and Nelson, R. B., "Parameter Identification of Large Structural Models—Concept and Reality," ASME Winter Annual Meeting, Boston, MA, Nov. 1983.
- <sup>5</sup>Hasselman, T. K., "A Perspective on Dynamics Model Verification," ASME Winter Annual Meeting, Boston, MA, Nov. 1983.
- <sup>6</sup>Martinez, D. R., "Estimation Theory Applied to Improving Dynamic Structural Models," Sandia National Lab., Albuquerque, NM, Sandia Rept. SAND82-0572, 1984.
- <sup>7</sup>Berman, A. and Flannelly, W. G., "Theory of Incomplete Models of Dynamic Structures," *AIAA Journal*, Vol. 9, Aug. 1971, pp. 1481-1487.
- <sup>8</sup>Berman, A. and Nagy, E. J., "Improvement of Large Analytical Model Using Test Data," *AIAA Journal*, Vol. 21, Aug. 1983, pp. 1168-1173.
- <sup>9</sup>Berman, A., "Mass Matrix Correction Using an Incomplete Set of Measured Modes," *AIAA Journal*, Vol. 17, Oct. 1979, pp. 1147-1148.
- <sup>10</sup>Wei, F. S., "Stiffness Matrix Corrections from Incomplete Test Data," *AIAA Journal*, Vol. 18, Oct. 1980, p. 1274.
- <sup>11</sup>Chen, J. C., Kuo, C. P., and Garba, J. A., "Direct Structural Parameter Identification by Modal Test Results," *Proceedings of the AIAA/ASME/ASCE/AHS 24th Structures, Structural Dynamics, and Materials Conference*, Part 2, AIAA, New York, 1983.
- <sup>12</sup>White, C. W. and Maytum, B. D., "Eigensolution Sensitivity to Parametric Model Perturbations," *Shock and Vibration Bulletin*, Bulletin 46, Part 5, Aug. 1976, pp. 123-133.
- <sup>13</sup>Rajaram, S., "Identification of Vibration Parameters of Flexible Structures," Ph.D. Dissertation, Virginia Polytechnic Institute and State University, Blacksburg, VA, May 1984.
- <sup>14</sup>Rajaram, S. and Junkins, J. L., "Identification of Vibrating Flexible Structures," *Journal of Guidance, Control, and Dynamics*, Vol. 8, July-Aug. 1985, pp. 463-470.
- <sup>15</sup>Hendricks, S. L., Rajaram, S., Kamat, M. P., and Junkins, J. L., "Identification of Large Flexible Structures Mass/Stiffness and Damping From On-Orbit Experiments," *Journal of Guidance, Control, and Dynamics*, Vol. 7, March-April 1984, pp. 244-245.
- <sup>16</sup>Ewins, D. J., *Modal Testing: Theory and Practice*, Research Studies Press, England, 1984.
- <sup>17</sup>Ewins, D. J. and Gleeson, P. T., "A Method for Modal Identification of Lightly Damped Structures," *Journal of Sound and Vibration*, Vol. 84, 1982, pp. 57-79.
- <sup>18</sup>Juang, J. N., "Mathematical Correlation of Modal Parameter Identification Methods Via System Realization Theory," NASA 87720, April 1986.
- <sup>19</sup>Meirovitch, L., *Computational Methods in Structural Dynamics*, Sijthoff & Noordhoff, Rockville, MD, 1980.

ATTACHMENT 8

**A Stereo-Triangulation Approach to Sensing  
for Structural Identification**

*John L. Junkins  
George H. James, III*

Texas A&M University  
Dept. of Aerospace Engineering  
College Station, Texas 77843

*AAS 11th Annual Guidance and Control Conference  
Paper No. 88-015  
Keystone, Colorado  
Jan 30-Feb 3, 1988*

AAS 88-015



# A Stereo-Triangulation Approach to Sensing for Structural Identification

*John L. Junkins and George H. James III*  
Texas A&M University

---

11th ANNUAL AAS GUIDANCE AND CONTROL CONFERENCE

---

January 30-February 3, 1988  
Keystone, Colorado



 PUBLICATIONS OFFICE, P. O. BOX 28130 - SAN DIEGO, CALIFORNIA 92128

(175)

# A Stereo-Triangulation Approach to Sensing for Structural Identification

*John L. Junkins and George H. James III*

Department of Aerospace Engineering  
Texas A&M University  
College Station, Texas, USA 77843

## 1.0 INTRODUCTION

Identification of large space structures' distributed mass, stiffness, and energy dissipation characteristics poses formidable analytical, numerical, and implementation difficulties. Structural identification is crucial for implementing active vibration suppression concepts which are under widespread study in the large space structures community. Near the heart of the identification problem lies the necessity of making a large number of spatially distributed measurements of the structure's free and/or forced vibratory response, with sufficient spatial and frequency resolution, and without introducing unwieldy sensor and actuator calibration requirements which are potentially more difficult than the structural identification problem.

We discuss herein a stereo-optical triangulation approach to making a large number of spatially distributed structural response measurements. A close-range photogrammetric triangulation has already been demonstrated on-orbit with the 1984 Shuttle mission in which a ten story solar panel was deployed from the orbiter bay and vibration tests were imaged by four cameras mounted in the orbiter bay. The concept we propose is a sophistication of these ideas, primarily in the incorporation of unique subsystems for analog edge detection and video processing algorithms. Tens of active or passive (retro-reflecting) targets on the structure are tracked simultaneously in the focal planes of two or more video cameras mounted on an adjacent platform. Triangulation (optical ray intersection) of the conjugate image centroids yield inertial trajectories of each target on the structure. This approach remains in a research stage of development, but have successfully tracked and stereo triangulated 20 targets (on a vibrating cantilevered grid structure) at a sample frequency of 200HZ, and have established conclusively the feasibility and desirability of this approach.

A small number of easy-to-calibrate optical sensors tracking inertial motions of many points on the structure is an attractive concept vis-a-vis practical implementation, as compared to mounting numerous motion measuring sensors on the structure, in which case each sensor must be individually calibrated and its environmental stability established. Our approach brings recent advances in video camera hardware, analog and digital video process-

ing methodology to bear on the structural sensing problem. The present paper includes a discussion of our experimental hardware and some recent experimental results which support the practical feasibility of this structural vibration sensing approach.

## 2.0 OPTICAL MEASUREMENT GEOMETRY AND STEREO TRIANGULATION

We summarize the idealized (zero measurement and model errors) geometric equations for triangulation of video camera imagery. With reference to Figure 1, the image coordinates  $(x, y)$ , measured in the *positive* focal plane of a single lens camera, are related [1, 2] to the object space coordinates  $(X, Y, Z)$  of the imaged point, the camera's principal point  $(X_c, Y_c, Z_c)$ , orientation angles  $(\phi, \theta, \psi)$ , principal point offset  $(x_o, y_o)$ , and focal length  $(f)$ , by the *colinearity equations*

$$\begin{aligned} x &= x_o - f \left[ \frac{C_{11}(X-X_c) + C_{12}(Y-Y_c) + C_{13}(Z-Z_c)}{C_{31}(X-X_c) + C_{32}(Y-Y_c) + C_{33}(Z-Z_c)} \right] \equiv F(X, Y, Z; X_c, Y_c, Z_c; \phi, \theta, \psi; x_o, y_o, f) \\ y &= y_o - f \left[ \frac{C_{21}(X-X_c) + C_{22}(Y-Y_c) + C_{23}(Z-Z_c)}{C_{31}(X-X_c) + C_{32}(Y-Y_c) + C_{33}(Z-Z_c)} \right] \equiv G(X, Y, Z; X_c, Y_c, Z_c; \phi, \theta, \psi; x_o, y_o, f) \end{aligned} \quad (1)$$

where the direction cosine matrix  $[C]$  is parameterized in terms of 3-2-1 Euler angles as

$$[C] = \begin{bmatrix} C_{11} & C_{12} & C_{13} \\ C_{21} & C_{22} & C_{23} \\ C_{31} & C_{32} & C_{33} \end{bmatrix} = \begin{bmatrix} 1 & 0 & 0 \\ 0 & \cos\psi & \sin\psi \\ 0 & -\sin\psi & \cos\psi \end{bmatrix} \begin{bmatrix} \cos\theta & 0 & -\sin\theta \\ 0 & 1 & 0 \\ \sin\theta & 0 & \cos\theta \end{bmatrix} \begin{bmatrix} \cos\phi & \sin\phi & 0 \\ -\sin\phi & \cos\phi & 0 \\ 0 & 0 & 1 \end{bmatrix}$$

For the case of two cameras simultaneously imaging the same structure, we generalize the discussion to briefly discuss how the stereo triangulation calculations are made. We adopt a double subscript notation for Eqs. (1), to denote the image coordinates of the  $i^{\text{th}}$  point measured in the  $j^{\text{th}}$  camera's image space as

$$\begin{aligned} x_{ij} &= F(X_i, Y_i, Z_i; X_{c_j}, Y_{c_j}, Z_{c_j}; \phi_j, \theta_j, \psi_j; x_{o_j}, y_{o_j}, f_j) \\ y_{ij} &= G(X_i, Y_i, Z_i; X_{c_j}, Y_{c_j}, Z_{c_j}; \phi_j, \theta_j, \psi_j; x_{o_j}, y_{o_j}, f_j) \end{aligned} \quad j = 1, 2; i = 1, 2, \dots, N \quad (2)$$

In the event that the camera position, orientation, and calibration constants are considered known, and for measurement of discretely visible images of object space points at unknown locations, it is evident that Eqs. (2) provide 4 equations for the 3 unknown coordinates of each point. Equations (2) can be inverted by least squares to determine the object space coordinates.

The dynamic triangulation process should be preceded by a static calibration to determine the camera calibration constants, and for the case of fixed cameras, the position and orientation coordinates of the cameras. The calibration should use at least three fixed targets which will subsequently be visible in the dynamic experiments. These three points serve to define the object space coordinate system. The points are numbered in some arbitrary (but systematic!) fashion. Point 1 is arbitrarily adopted as the origin:  $(X_1, Y_1, Z_1) = (0, 0, 0)$ . Point 2 is used to define the  $X$  axis:  $(X_2, Y_2, Z_2) = (X_2, 0, 0)$ . Point 3 is used to define the  $X, Y$  plane:  $(X_3, Y_3, Z_3) = (X_3, Y_3, 0)$ . Thus the first 3 points have a total of 3 unknowns  $(X_2, X_3, Y_3)$ , and each additional point introduces 3 unknowns  $(X_i, Y_i, Z_i)$ , for a total of  $3N - 6$  unknown object space coordinates. Notice that each object space point has four associated measurements (two measured coordinates in each of the two image planes). Thus, in the most general case, we have the  $3N - 6$  unknown object space coordinates plus the 18 unknowns associated with the cameras  $(X_{c_i}, Y_{c_i}, Z_{c_i}; \phi_i, \theta_i, \psi_i; x_{o_i}, y_{o_i}, f_i; \text{ for } i = 1, 2)$ . We conclude that we have a total of  $4N$  equations and  $3N + 12$  unknowns; if  $N \geq 12$  conjugate images are measured, we have enough equations to determine all of the  $3N$  object space coordinates and the 18 camera position, orientation, and calibration parameters. Also of significance, when using Charged Coupled Device (CCD) focal plane arrays (as in the present application) the effective focal length is different for the  $x$  and  $y$  axes (actually, there is a ratio of the  $x$  and  $y$  dimensions of the array as a consequence of the rectangular pixels, which can be absorbed into effective focal lengths which are determined during calibration) thereby increasing the number of unknowns by one for each camera and one additional object space point is required. The calibration is very well behaved and can be accomplished in fifteen minutes of real time.

The calibration process is strengthened, of course, by making redundant measurements and using other a priori measurements of object space points and/or camera calibration parameters. The details of the calculations underlying the above are discussed in [1-2, 7]. The precision of the results is dependent most heavily upon the accuracy with which the image coordinates are measured and, of course, the geometric strength of the triangulation process. Upon completing a satisfactory static calibration, the subsequent dynamic triangulation process need consider only four of Eqs. (2) at a time to sequentially accomplish the least square solution for the object space coordinates  $(X_i, Y_i, Z_i)$  of the points imaged on the flexible structure.

The particular scheme adopted to extract the improved structural model from the triangulated measurements of inertial structural motion is not central to the present discussion, but we briefly review below the approach we are taking.

### 3.0 STRUCTURAL IDENTIFICATION

We consider the class of linear elastic structures suitably modeled by a finite element or similar discretization approach, leading to a finite system of 2nd order differential equations

of the form

$$M\ddot{x} + C\dot{x} + Kx = Bu \quad (3)$$

where  $x$  is an  $n \times 1$  configuration vector,  $u$  is an  $m \times 1$  excitation function (or control force) vector,  $M$ ,  $C$ , and  $K$  are the mass, damping, and stiffness matrices, respectively, and  $B$  is the control influence matrix. It is clear that the results of the triangulation process gives the time history of a finite set of points on the structure; these are typically a subset of the  $x$  vector.

Since we are considering stable systems, the fourier transform can be obtained from the Laplace transform by setting  $s = j\omega$ . To outline some of the details, we consider a special case. For harmonic excitation  $u = r \exp(j\omega t)$ , zero damping, and an identity  $B$  matrix, the *frequency response* is given by taking the fourier transform of Eq. (3) to obtain

$$X(i\omega) = [-\omega^2 M + K]^{-1} r = H(i\omega) r, \quad H_{jk}(i\omega) \equiv \sum_{r=1}^n \frac{\phi_{jr} \phi_{kr}}{\omega_r^2 - \omega^2} \quad \left( \begin{array}{c} \text{spectral} \\ \text{decomposition} \\ \text{theorem} \end{array} \right) \quad (4)$$

where  $\{\omega_k, \phi_k\}$  are the free vibration eigenvalues (natural frequencies) and eigenvectors (mode shapes) satisfying  $\det [K - \omega^2 M] = 0$ ,  $\Rightarrow \{\omega_1^2, \dots, \omega_n^2\}$ , and  $[K - \omega_i^2 M]\phi_i = 0$  with the orthonormality conditions

$$\Phi^T M \Phi = I, \quad \Phi^T K \Phi = \text{diag}(\omega_1^2, \dots, \omega_n^2), \quad \Phi = [\phi_1 \dots \phi_n] \quad (5)$$

Of course, we are interested in the case of damped systems, the generalization of Eqns. (4), (5) are classical developments which are the basis of the approach under discussion. Based upon experimental determination of a subset of the eigenvalues, eigenvectors and one or more elements of the frequency response function matrix  $H(i\omega)$ , Creamer and Junkins[3, 4] have developed an identification process whereby linearly parameterized mass, stiffness and damping properties can be estimated to bring the computed eigenvalues, eigenvectors, and frequency response functions into least square agreement with the corresponding measurements, over a prescribed range of sample frequencies. Given triangulated motion of a sufficient number of points on the structure, the eigenstructure realization method of [5] can be used to find the minimum rank linear discrete-time model which represents the measured motion, from this linear model, eigenvalues and eigenvectors can be determined.

The structural parameterization adopted for the present discussion is of the form

$$M = M_0 + \sum_{r=1}^p \mu_r M_r, \quad K = K_0 + \sum_{r=1}^q \kappa_r K_r, \quad C = C_0 + \sum_{r=1}^s \chi_r C_r \quad (6)$$

where  $\mu_r, \kappa_r, \chi_r$  are scalars determined to bring the calculated and measured eigenvalues, eigenvectors, and frequency response functions into least square agreement. Notice that the

structure has been subjectively divided into substructures whose contributions to the nominal mass, stiffness, and damping matrices are scaled in unison;  $M_r$ ,  $K_r$ ,  $C_r$  are the nominal contributions of the prescribed substructures to the global assembly of  $M$ ,  $K$ ,  $C$ . These do not necessarily conform to physical substructures, but can be based upon collections of nominally identical members, and/or members made of the same material, etc. In the limit, of course, the sub-structures could be the finite elements themselves, but we usually find a much coarser parameterization to be highly satisfactory. The subjectivity involved in selecting substructures should not be viewed as a weakness of this approach, it is in fact a strength. The parameterization of Eq. (6) is essentially a "parameter linking" method [5] in which the engineer is permitted convenient latitude in modifying the dimensionality of the parameter estimation process to achieve accuracy and computational efficiency. Based upon partitioning the energy for each mode associated with each substructure [6], it is possible to revise the substructuring decisions and define reduced order structural identification problems. We refer to [3, 4] for further discussion of the identification discussion, including details of the generalizations to identify systems with damping, closed-loop, non-self-adjoint systems.

#### 4.0 OVERVIEW OF THE HARDWARE AND EXPERIMENTAL CONFIGURATION

The optical sensor system depicted in Figure 2 has the advantages of non-contact measurement, high-coverage measurements, excellent large amplitude and low frequency response, ease of calibration, and reflective targets can be placed anyplace on the visible surface of the structure. These advantages make the system extremely attractive for laboratory use; and it is easy to extrapolate that an on-orbit realization of analogous systems should be attractive for identification of large flexible structures. The current laboratory system requires that the motion of a structure of interest be viewed from two different positions by the NAC 200HZ cameras. The stereo pair of images are recorded simultaneously by synchronization of the cameras and recorders. The two recorded images are played back using a standard 60HZ video recorder to the Motion Analysis VP-110 video processor (analog) for the filtering, masking, edge detection and A/D conversion processes.

The VP-110 allows a user interaction to establish a gray scale threshold so the edges of the target image boundaries are reliably determined; only the pixel locations which correspond to the edge-detected image boundary are A/D converted for subsequent digital processing in the SUN 2/120 computer. Thus near-circular image boundaries are digitized and their centroids can be calculated to an uncertainty of about .5 pixel for the present implementation (a sophistication of the present analog/digital processing is presently under study which should result in a resolution of about .1 pixel). The VP-110 processor makes use of several tuneable analog features to filter, window, and mask the imagery to remove unwanted information and improve the signal-to-noise ratio before digitizing the imagery.

In the SUN computer, we make use of the Expertvision software package (developed by

Motion Analysis) to centroid the image boundaries and connect them in time to form a sequence of focal plane coordinates along the time trajectory of each image centroid. By virtue of the fact that the two cameras have been synchronized, each target's inertial motion will correspond to a stereo pair of focal plane trajectories whose centroids are measured by the output of the Expertvision digital processing. We then make use of algorithms and software we have developed, based upon least square inversion of Eqns. (2), to complete the stereo triangulation and thereby determine the laboratory (object space) 3-D trajectories for each marker on the structure. These target trajectories then provide the response measurements for estimation of eigenvalues, eigenvectors, frequency response functions, and structural model parameters. Clearly these digital processes are not executed in real time, but they can be performed post-experiment in less than 1/2 hour of real time.

The test article used in the present discussion is a 5' x 5' grid, with 12.5"x2"x1/8" members. The grid was cut from a single sheet of 3003.H14 aluminum, to eliminate modeling problems associated with bolted or riveted joints. The structure is designed to accommodate accelerometer, strain gauge, as well as optical data acquisition. Excitation of the test structure is accomplished by an impulse hammer or by a harmonic shaker. The resulting motion can be processed to determine frequency, mode shape, and frequency response information which can then be used as input to structural parameter identification methods such as those discussed in Section 3 above.

## 5.0 DISCUSSION OF RESULTS: CONCLUDING REMARKS

In Figure 3, we show typical image centroids, image space trajectories, and inertial trajectories for one of 20 targets tracked in a typical transient response. In Figure 4, the finite element modeled mode shapes[8,9] and the modeled and experimentally determined values the first six natural frequencies (determined from the free response to an impulsive excitation, using the Eigenstructure Realization Algorithm [5]) for the first six modes. The rightmost column shows the natural frequencies of the a model for which three stiffness parameters (EI, GJ, and a gravitational stiffening effect) are adjusted by the method of Creamer and Junkins. Excellent agreement exists between the identified model and the experimental results. Figure 5 provides a comparison between video-measured deflections with accelerometer measurements. It is apparent that the video data has more information in the low frequency portion of the spectrum than the accelerometer, but the accelerometer measures the high frequency motions. In this case, the accelerometer measurements are nearly useless below 1 Hz, and the optical measurements are useless above 15 Hz.

In summary, we have presented a novel approach for structural identification. The approach is a stereo triangulation method wherein conjugate images (measured by a combination of analog and digital processing) of tens of passive targets' images can be measured by a pair of video cameras. The result is a non-contacting measurement and structural identification approach which is an attractive candidate for implementation.

## 6.0 REFERENCES

1. Manual of Photogrammetry (4th Edition), published by the American Society of Photogrammetry, Falls Church, VA(1980).
2. Junkins, J. L. Optimal Estimation of Dynamical Systems, Sijthoff-Noordhoff, Leyden, the Netherlands (1978).
3. Creamer, N. G., Identification of Flexible Structures., Ph. D. Dissertation, Engineering Mechanics, Virginia Tech, 1987.
4. Creamer, N. G., and J. L. Junkins, "An Identification Method for Flexible Structures", to appear, AIAA J. of Guidance , Control, and Dynamics, also presented at the AIAA/ASME/ASCE/AHS 28th Structures, Structural Dynamics, and Materials (SDM) Conference, Monterey, CA, April 6-8, 1987.
5. Deneman, E., Hasselman, T., Sun, C., Juang, J., Junkins, J., Udawadia, F., Venkayya, V., Kamat, M., "Identification of Large Space Structures on Orbit", Final report under Air Force Contract F04611-85-C-0092 with the American Society of Civil Engineering, Air Force Rocket Propulsion Laboratory Report No. AFRPL TR-86-054, 342 pp, August 1986.
6. White, C. W. and Maytum, B. D., "Eigensolution Sensitivity to Parametric Model Perturbations," Shock and Vibration Bulletin, Bulletin 46, Part 5, August 1976, pp123-133.
7. James, G. H., "An Optical Sensor System for Measuring Structural Dynamics with applications to System Identification," final report under 1987 USAF-UES Summer Faculty/Graduate Student Research Program Contract No. F49620-85-C-0013, Texas A&M University, Department of Aerospace Engineering, August 28, 1987.
8. Das, A., Srange, W. T., Schlaegel, and Ward, J. M., "Experiment in Modeling and Parameter Estimation of Flexible Structures", Second NASA/DOD Control-Structure Interaction Conference, Colorado Springs, Co., November 17-19, 1987.
9. Paz, M., Structural Dynamics Theory and Computation, 2nd Ed., Van Nostrand Reinhold Co., New York, (1985).

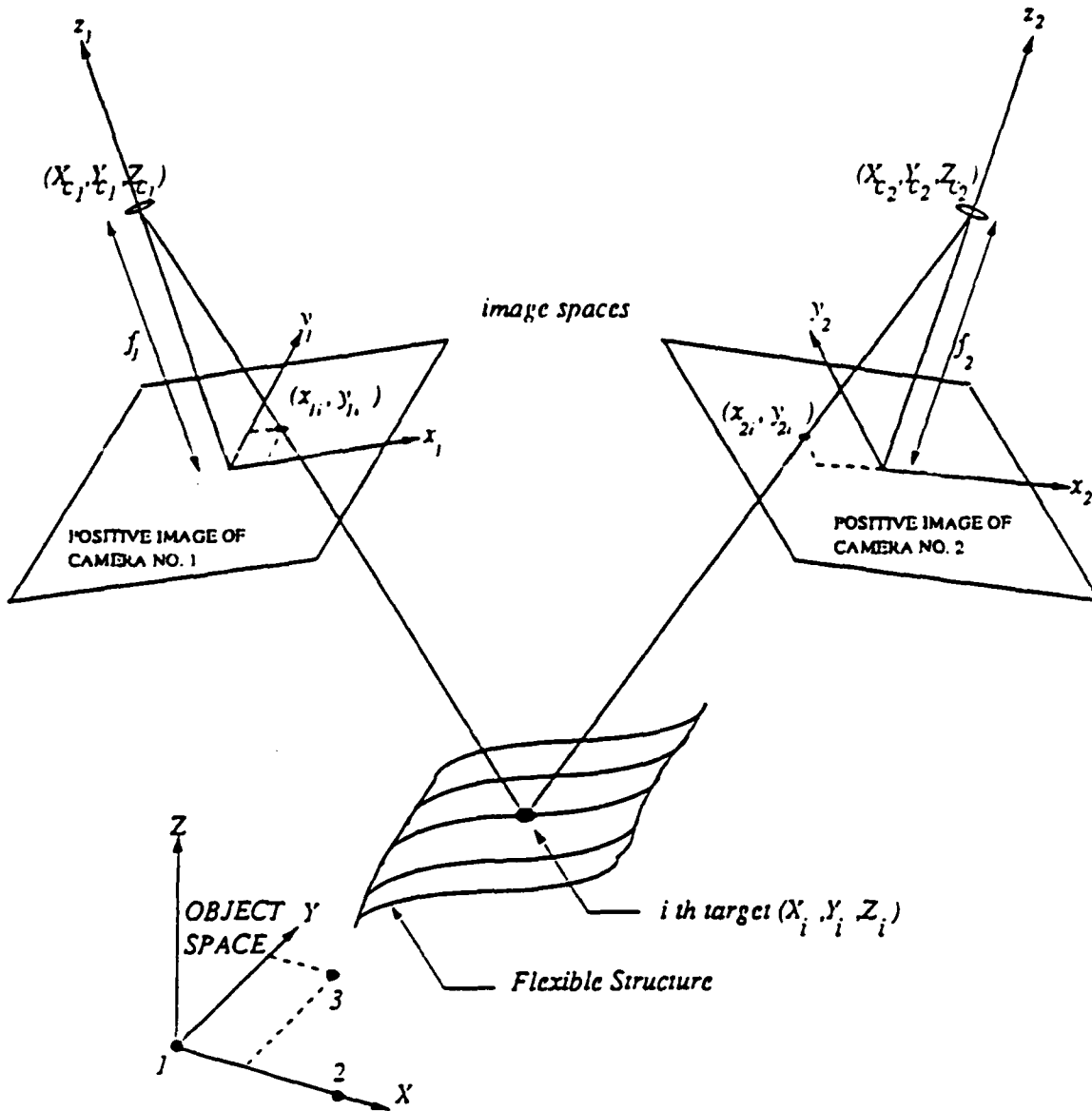
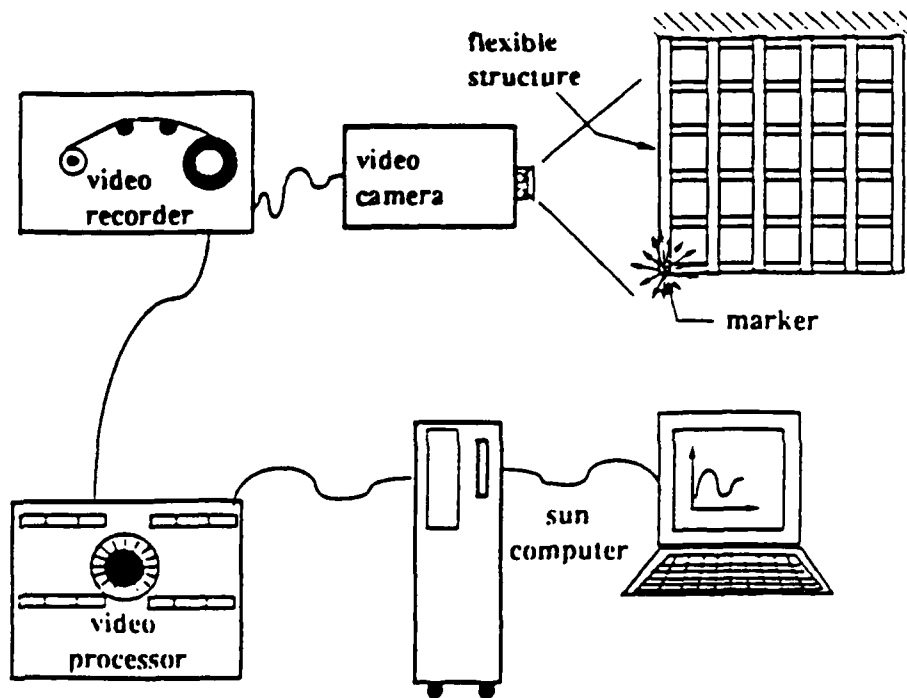


Figure 1. Stereo Triangulation Geometry



MAJOR HARDWARE ITEMS	
ITEM	DESCRIPTION
Flexible Structure	monolithic 3003 H14 aluminum grid (5'x5') cantilevered in the vertical plane (clamped-free boundary conditions)
markers (targets)	3M Scotchlite Reflective Sheeting #3290
Video Cameras(2)	NAC model V-14B, 200/60 IZ, 2/3" MOS imaging CCD array with 320x244 pixels
Video Recorder(2)	NAC model VTR V-32, 200IZ, configured for VHS cassettes
Video Processor	Motion Analysis model VP-310 for threshold-based edge detection, hardware editing and filtering, digitizing image boundaries, and data transfer
Computer	SUN 1/120 with 42 megabyte hard disk and UNIX operating system

Figure 2. Motion Analysis Hardware

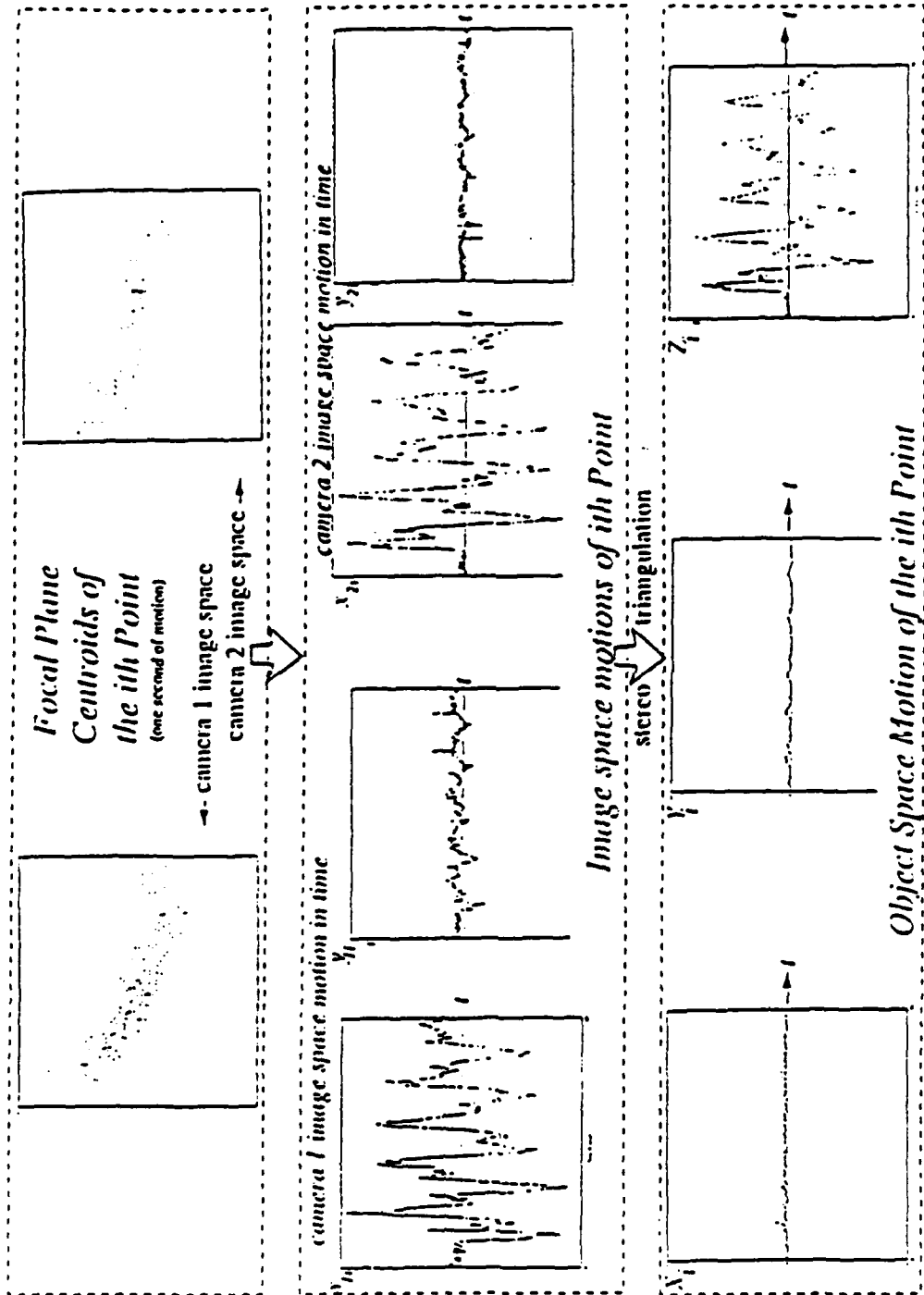
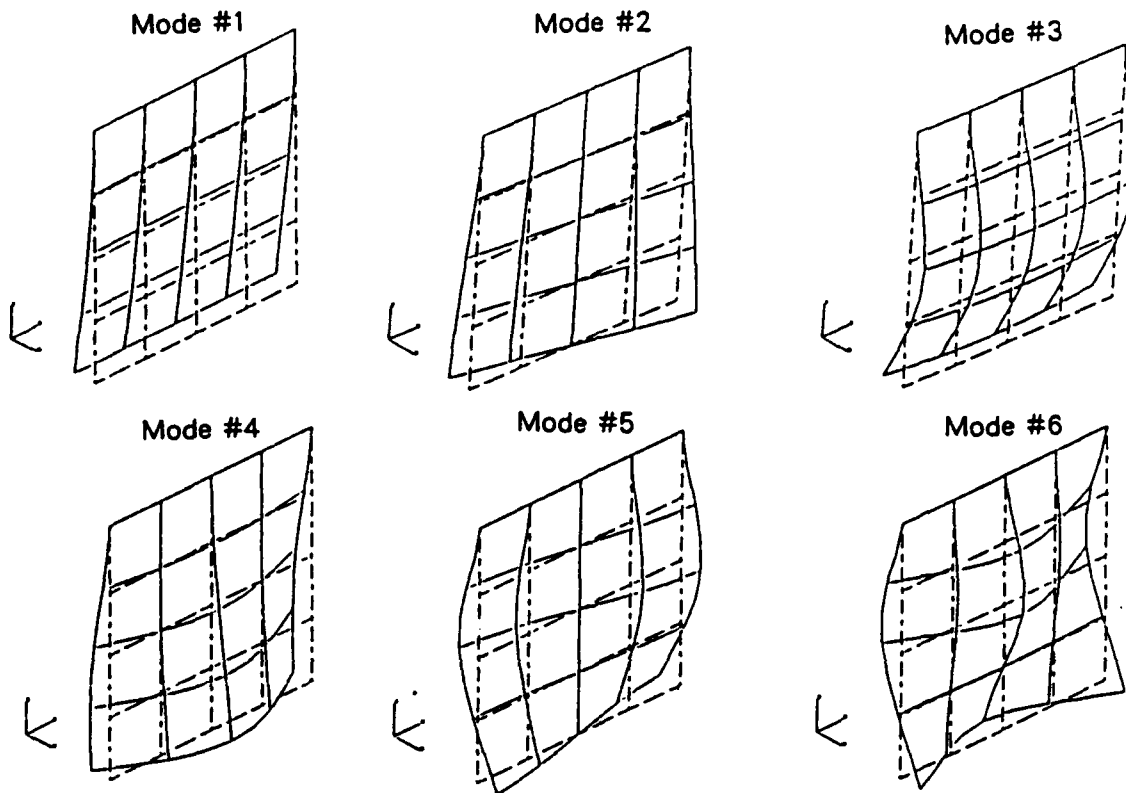


Figure 3. Typical Trajectory of Target Motion in Image Spaces and in Object Space

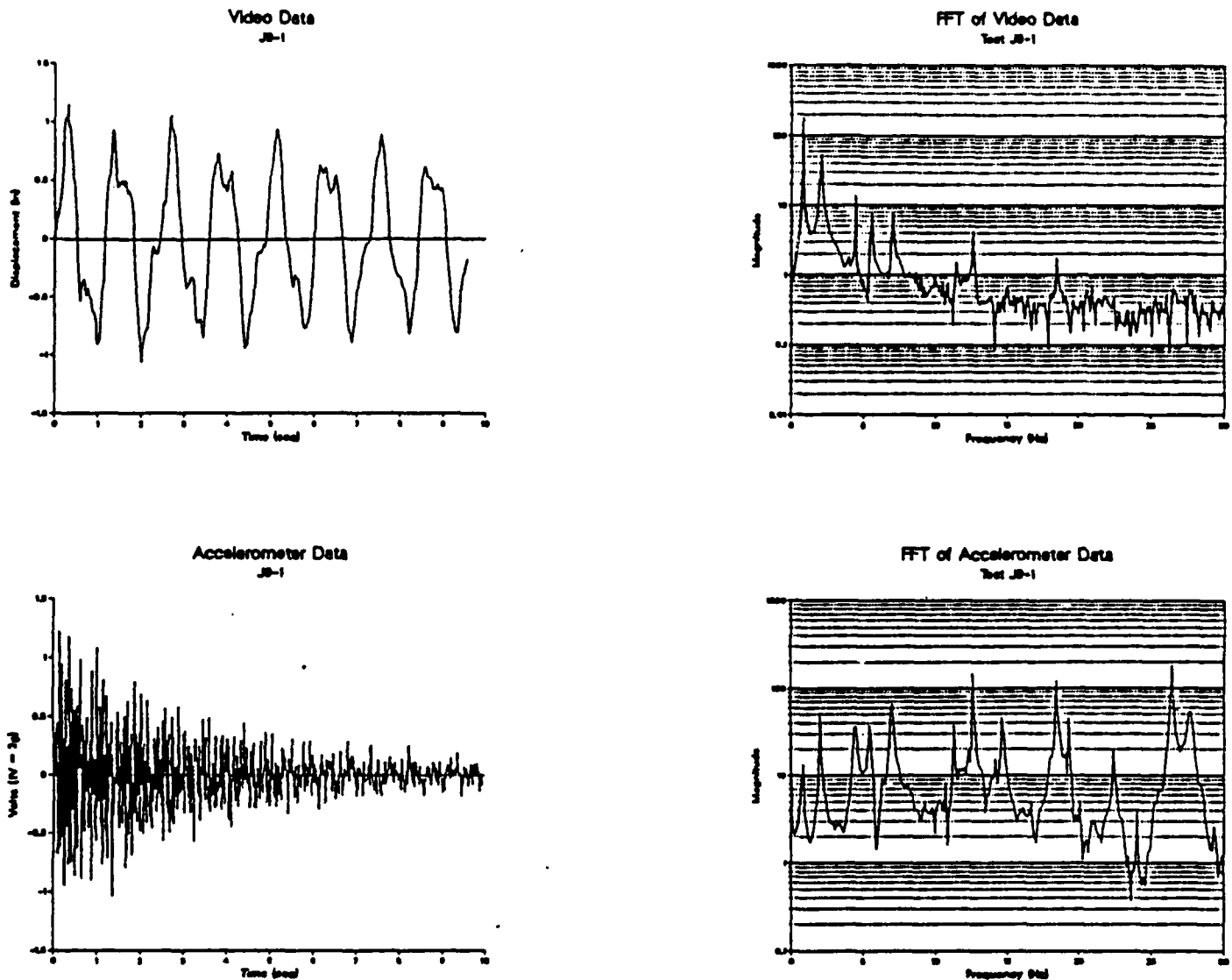
**Figure 4. Modeled, Measured, and Identified Natural Frequencies of the Frame Structure**



The finite element model mode shapes as reported by Das et al are shown above. The first six finite element natural frequencies are given below as well as the first six experimentally determined natural frequencies. These natural frequencies were determined by the eigenstructure realization algorithm using free response to an impulsive loading. Preliminary results of the structural identification method of Creamer and Junkins are given. These results were obtained by holding the mass matrix constant and using three stiffness submatrices to match the natural frequencies.

Mode No.	Modeled Value	Measured Value	Value after Initial Identification
1	.90 Hz	.91 Hz	.92 Hz
2	2.34	2.07	2.06
3	4.85	4.76	4.76
4	6.05	5.14	5.58
5	7.78	6.57	7.09
6	12.84	10.86	11.57

# Figure 5. Comparison of Video-Derived Position Measurements with Accelerometer Measurements



The graphs shown above provide some insight into the advantages and disadvantages of the camera system versus an accelerometer. The video data is very useful at the low frequency large amplitude end of the spectrum. The accelerometer response is most reliable at the high frequency end of the spectrum. This data was taken on the AFAL structural identification test article which is similar to the TAMU structure. The video data was taken with a TAMU RCA TC2811 60 Hz video camera. An AFAL Endevco model 7751-500 accelerometer was also used.

IDENTIFICATION OF FLEXIBLE STRUCTURES  
USING STEREO TRIANGULATION

*J.L. JUNKINS*  
*G.H. JAMES, III*  
*T.C. POLLOCK*

TEXAS A&M UNIVERSITY

Sixth AFOSR Forum of Space Structures

Hyatt Regency Hotel  
Atlanta, Georgia  
April 7-8, 1988

# OUTLINE

- **STRUCTURAL IDENTIFICATION**
  - *modal* parameters (free response)
    - $\Rightarrow \{\omega's, \xi's, \text{ and } \phi's\}$
  - *model* parameters (free or forced response)
    - $\Rightarrow \{EI's, GJ's, \text{ geometric, mass, stiffness, and damping parameters}\}$
  - **time domain identification**
    - (e. g., ERA balanced realization)
  - **frequency domain identification (FRF fitting)**
    - **Creamer/Junkins method** {simultaneous fit of measured subset of modal parameters and the FRF}
    - **connection between identification & order reduction**
- **STEREO TRIANGULATION METHOD FOR SENSING VIBRATION OF LARGE FLEXIBLE STRUCTURES**

# Structural Model Identification

## Parameterization Schemes

- Physical / Geometrical Parameters

$\{EI's, GJ's, \rho's, etc.\}$

- Equivalent Continuum Parameters

$\{\bar{EI}'s, \bar{GJ}'s, \bar{\rho}'s, etc.\}$

- Submatrix Scale Factors

$$M = M_o + \sum_i \mu_i M_i, \quad K = K_o + \sum_j \kappa_j K_j, \quad C = C_o + \sum_i \chi_i C_i$$

where  $\{M_i, K_i, C_i\}$  are prescribed and the scalars  $\{\mu_i, \kappa_i, \chi_i\}$  are estimated.

- Matrix Element Modifications

$$M_{ij} = M_{oij} + m_{ij}, \quad K_{ij} = K_{oij} + k_{ij}, \quad C_{ij} = C_{oij} + c_{ij}$$

# A Novel Identification Method for Linear Elastic Structures

Equations of Motion:  $M\ddot{x} + Kx = f$

Free Vibration Eigensolution:  $[K - \omega_i^2 M]\phi_i = 0 \Rightarrow \{\omega_i^2, \phi_i\}, i = 1, 2, \dots, n$

$\Phi^T M \Phi = I, \Phi^T K \Phi = \text{diag}(\omega_1^2, \dots, \omega_n^2) \equiv \Lambda, \Phi = [\phi_1, \dots, \phi_n]$

Frequency Response:  $X(j\omega) = [K - \omega^2 M]^{-1} F(j\omega) \equiv H(j\omega) F(j\omega)$

*spectral decomposition:*

$$H(j\omega) = [K - \omega^2 M]^{-1} \equiv \Phi^T (\Lambda - \omega^2 I)^{-1} \Phi, H_{pq}(j\omega) = \sum_{r=1}^n \frac{\phi_{pr} \phi_{qr}}{\omega_r^2 - \omega^2}$$

Measurements:

*a subset of free vibration modes:  $\{\tilde{\omega}_r, \tilde{\phi}_r\}, r = 1, 2, \dots, m (\leq n)$*

*frequency response elements:  $\tilde{H}_{pq}(j\omega), \text{ for } \omega_{\min} \leq \omega \leq \omega_{\max}$*

## QUALITATIVE PROBLEM STATEMENT:

*Find optimum estimates of  $M, K$  parameterization which is simultaneously consistent with the measured the free vibration eigensolution and the frequency response function.*

## Creamer's Three Step Identification Process

**Step 1:** Identify a subset of the measured frequencies and mode shapes which correlate well with the corresponding modeled frequencies and mode shapes, do a least square correction of the stiffness parameterization to improve correlation if necessary.

**Step 2:** Find the normalization of the eigenvectors (mode shapes) which results in the best least square fit for the FRF, i. e., find  $\{a_0, a_1, a_2, \dots, a_{m+1}\}$  to minimize

$$\int_{\omega_{min}}^{\omega_{max}} (\tilde{H}_{pq}(j\omega) - H_{pq_{model}}(j\omega))^2 d\omega, \text{ or } \sum_{\omega_{min}}^{\omega_{max}} (\tilde{H}_{pq}(j\omega_k) - H_{pq_{model}}(j\omega_k))^2$$

where

$$H_{pq_{model}}(j\omega) = \frac{a_0}{\omega^2} + \sum_{r=1}^m \frac{\tilde{\Phi}_{pr} \tilde{\Phi}_{qr}}{\omega_r^2} a_r + a_{m+1}$$

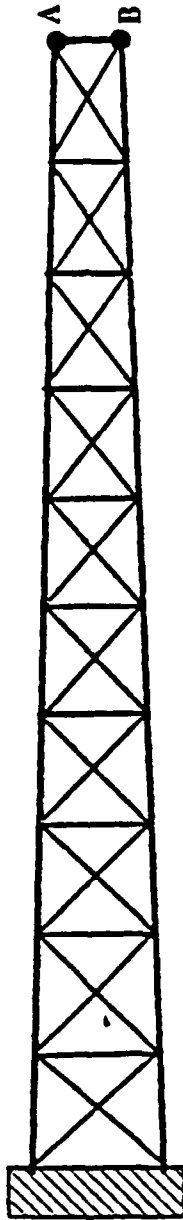
**Step 3:** Estimate values for the linear mass and stiffness parameterization to satisfy the orthonormality conditions in a least square sense; this leads to the following pair of linear equations for  $\mu_r$ , and  $\kappa_r$  in  $M = M_0 + \sum_i \mu_i M_i$ ,  $K = K_0 + \sum_i \kappa_i K_i$  :

$$\begin{bmatrix}
 {}^T\Phi_1 M_1 \Phi_1 & {}^T\Phi_1 M_2 \Phi_1 & \dots & {}^T\Phi_1 M_P \Phi_1 \\
 \vdots & \vdots & \dots & \vdots \\
 {}^T\Phi_m M_1 \Phi_m & {}^T\Phi_m M_2 \Phi_m & \dots & {}^T\Phi_m M_P \Phi_m \\
 {}^T\Phi_1 M_1 \Phi_2 & {}^T\Phi_1 M_2 \Phi_2 & \dots & {}^T\Phi_1 M_P \Phi_2 \\
 \vdots & \vdots & \dots & \vdots \\
 {}^T\Phi_{m-1} M_1 \Phi_m & {}^T\Phi_{m-1} M_2 \Phi_m & \dots & {}^T\Phi_{m-1} M_P \Phi_m
 \end{bmatrix}
 \begin{Bmatrix}
 \mu_1 \\
 \mu_2 \\
 \vdots \\
 \mu_P
 \end{Bmatrix}
 =
 \begin{Bmatrix}
 1/a_1 - \Phi_1 M_0 \Phi_1 \\
 \vdots \\
 1/a_m - \Phi_m M_0 \Phi_m \\
 -\Phi_1 M_0 \Phi_2 \\
 \vdots \\
 -\Phi_{m-1} M_0 \Phi_m
 \end{Bmatrix}$$

and

$$\begin{bmatrix}
 {}^T\Phi_1 K_1 \Phi_1 & {}^T\Phi_1 K_2 \Phi_1 & \dots & {}^T\Phi_1 K_Q \Phi_1 \\
 \vdots & \vdots & \dots & \vdots \\
 {}^T\Phi_m K_1 \Phi_m & {}^T\Phi_m K_2 \Phi_m & \dots & {}^T\Phi_m K_Q \Phi_m \\
 {}^T\Phi_1 K_1 \Phi_2 & {}^T\Phi_1 K_2 \Phi_2 & \dots & {}^T\Phi_1 K_Q \Phi_2 \\
 \vdots & \vdots & \dots & \vdots \\
 {}^T\Phi_{m-1} K_1 \Phi_m & {}^T\Phi_{m-1} K_2 \Phi_m & \dots & {}^T\Phi_{m-1} K_Q \Phi_m
 \end{bmatrix}
 \begin{Bmatrix}
 \kappa_1 \\
 \kappa_2 \\
 \vdots \\
 \kappa_Q
 \end{Bmatrix}
 =
 \begin{Bmatrix}
 \omega_1^2/a_1 - \Phi_1 K_0 \Phi_1 \\
 \vdots \\
 \omega_m^2/a_m - \Phi_m K_0 \Phi_m \\
 -\Phi_1 K_0 \Phi_2 \\
 \vdots \\
 -\Phi_{m-1} K_0 \Phi_m
 \end{Bmatrix}$$

# IDENTIFICATION OF A DAMPED TRUSS STRUCTURE



Measurements: 8 open-loop eigenvalues  
 8 closed-loop eigenvalues  
 Longitudinal FRF between A and B  
 Transverse FRF between A and B

## EIGENVALUES

measured                      a priori                      identified model

MODE	$\bar{\lambda}$	$\lambda_0$	$\lambda_f$
1	-0.0872 + 6.731i	6.111	-0.0872 + 6.931i
2	-0.0890 + 34.591i	31.451	-0.0888 + 35.461i
3	-0.0891 + 87.581i	78.891	-0.0898 + 88.291i
4	-0.1042 + 117.111i	106.671	-0.1039 + 119.391i
5	-0.0907 + 156.491i	142.121	-0.0906 + 157.861i
6	-0.0914 + 240.331i	217.541	-0.0915 + 240.051i
7	-0.0929 + 332.091i	302.001	-0.0925 + 331.391i
8	-0.1039 + 359.291i	325.251	-0.1042 + 363.281i

# Damped Truss Structure Identification

*Frequency Response Function: Measured vs Initial Model vs Identified Model*

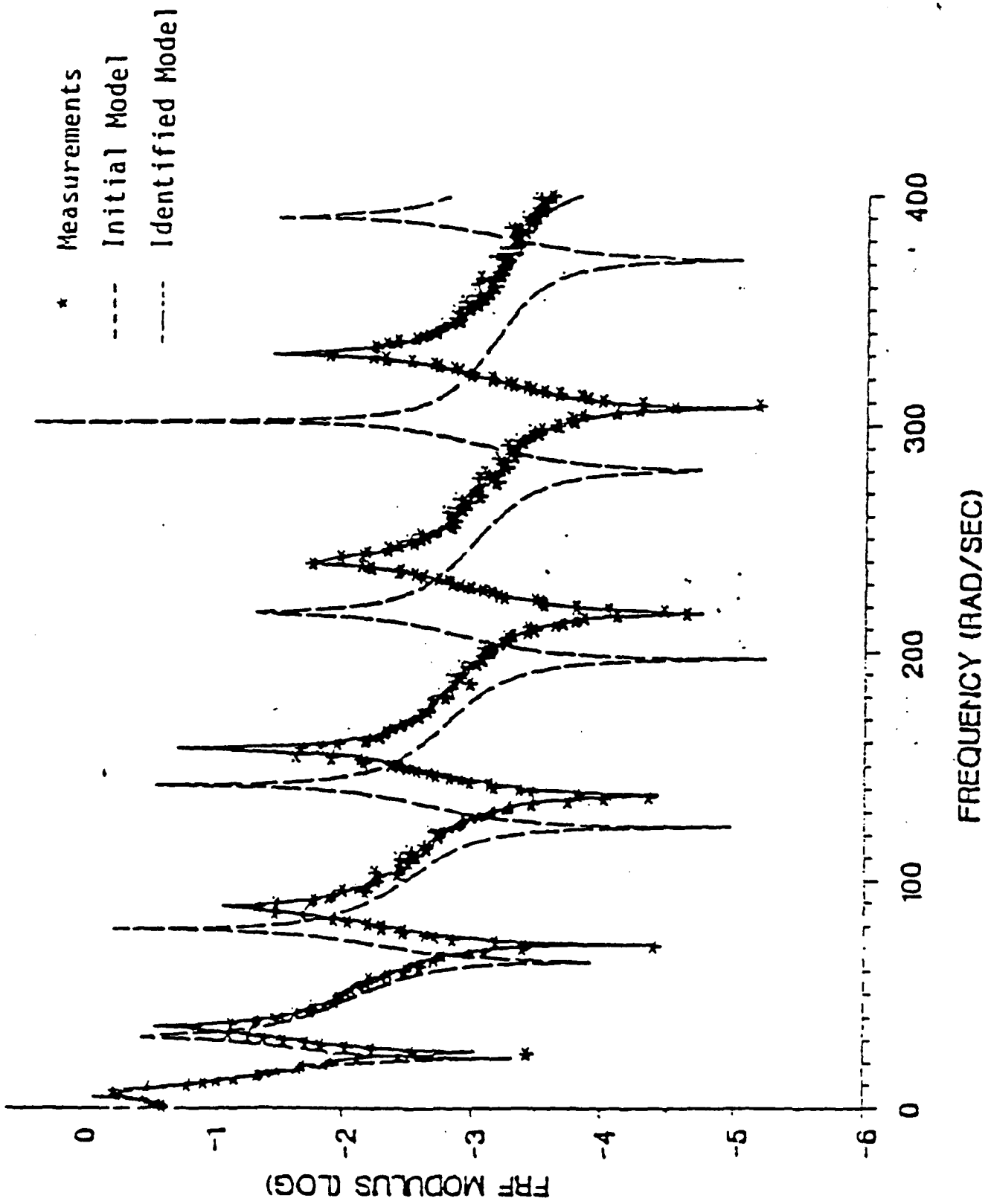


# Figure 1. Stereo Triangulation Geometry

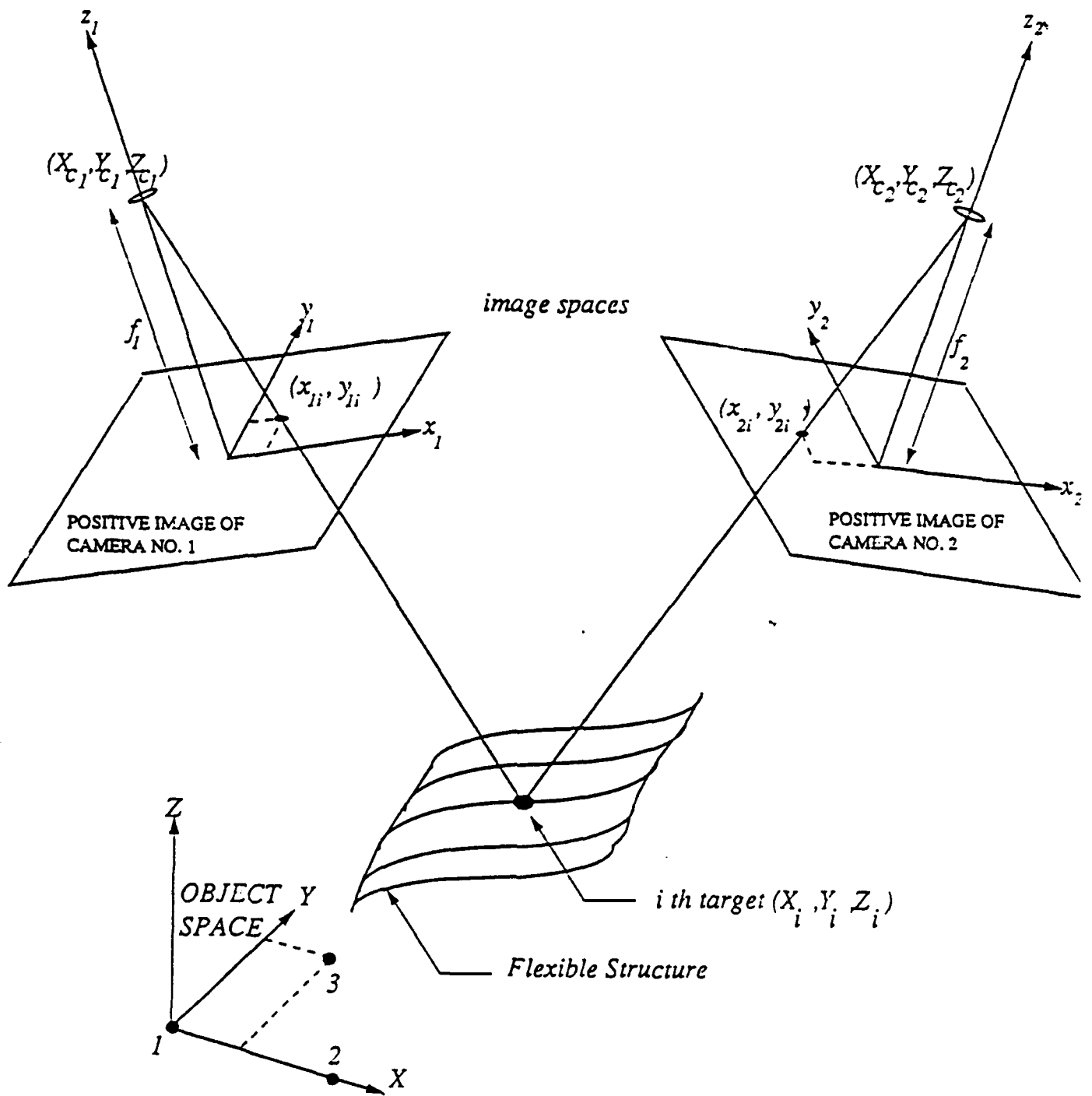
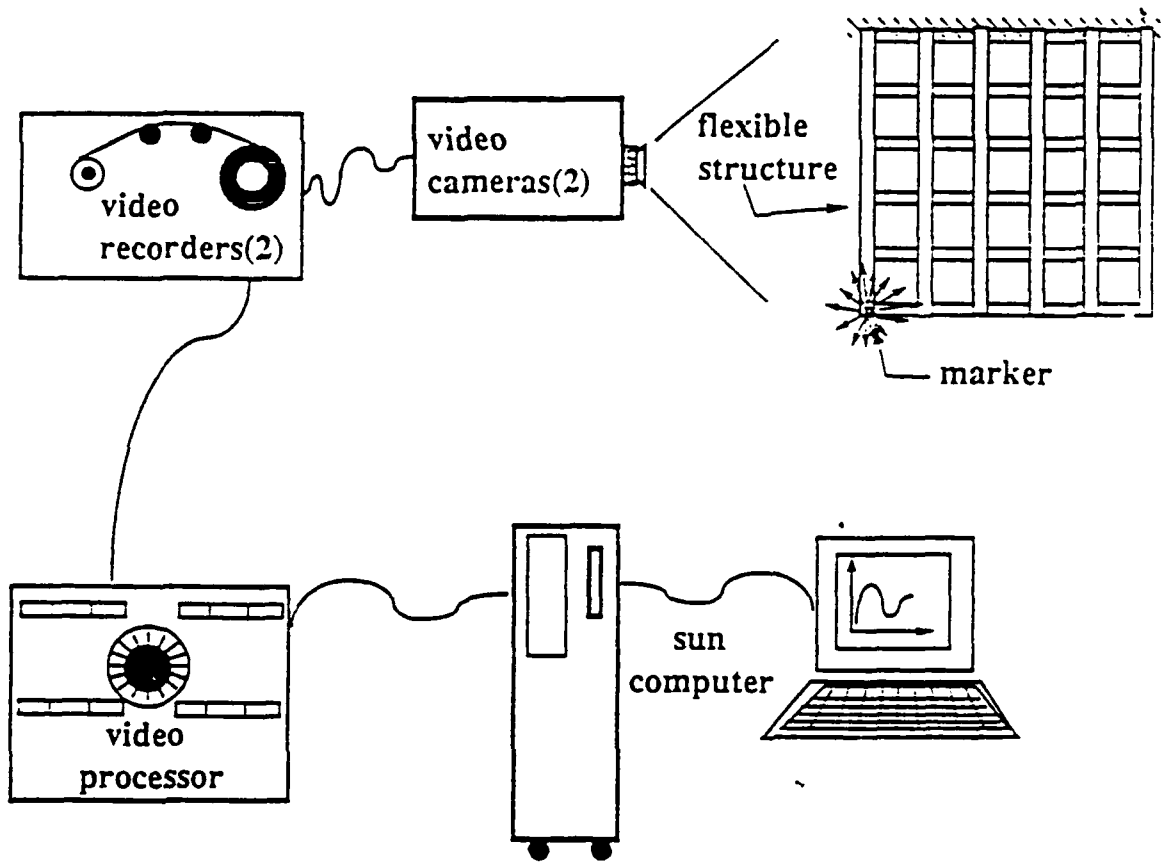


# Figure 2. Motion Analysis Hardware



MAJOR HARDWARE ITEMS	
ITEM	DESCRIPTION
Flexible Structure	monolithic 3003 H14 aluminum grid (5'x5') cantilevered in the vertical plane (clamped-free boundary conditions)
markers (targets)	3M Scotchlite Reflective Sheeting #3290
Video Cameras(2)	NAC model V-14B, 200/60 HZ, 2/3" MOS imaging CCD array with 320x244 pixels
Video Recorder(2)	NAC model VTR V-32, 200HZ, configured for VHS cassettes
Video Processor	Motion Analysis model VP-310 for threshold-based edge detection, hardware editing and filtering, digitizing image boundaries, and data transfer
Computer	SUN 2/120 with 42 megabyte hard disk and UNIX operating system

## Measurement Geometry and Stereo Triangulation

The object-to image space transformation for a single lens camera is given by the *colinearity equations*

$$x = x_o - f \left[ \frac{C_{11}(X-X_c) + C_{12}(Y-Y_c) + C_{13}(Z-Z_c)}{C_{31}(X-X_c) + C_{32}(Y-Y_c) + C_{33}(Z-Z_c)} \right] \equiv F(X, Y, Z; X_c, Y_c, Z_c; \phi, \theta, \psi; x_o, y_o, f)$$

$$y = y_o - f \left[ \frac{C_{21}(X-X_c) + C_{22}(Y-Y_c) + C_{23}(Z-Z_c)}{C_{31}(X-X_c) + C_{32}(Y-Y_c) + C_{33}(Z-Z_c)} \right] \equiv G(X, Y, Z; X_c, Y_c, Z_c; \phi, \theta, \psi; x_o, y_o, f)$$

where

$$\{C\} = \begin{bmatrix} C_{11} & C_{12} & C_{13} \\ C_{21} & C_{22} & C_{23} \\ C_{31} & C_{32} & C_{33} \end{bmatrix} = \begin{bmatrix} 1 & 0 & 0 \\ 0 & \cos\psi & \sin\psi \\ 0 & -\sin\psi & \cos\psi \end{bmatrix} \begin{bmatrix} \cos\theta & 0 & -\sin\theta \\ 0 & 1 & 0 \\ \sin\theta & 0 & \cos\theta \end{bmatrix} \begin{bmatrix} \cos\phi & \sin\phi & 0 \\ -\sin\phi & \cos\phi & 0 \\ 0 & 0 & 1 \end{bmatrix}$$

For the case of two cameras simultaneously imaging the same structure, we adopt a subscript notation to denote the image coordinates of the  $i^{th}$  point measured in the  $j^{th}$  camera's image space as

$$x_{ij} = F(X_i, Y_i, Z_i; X_{cj}, Y_{cj}, Z_{cj}; \phi_j, \theta_j, \psi_j; x_{oj}, y_{oj}, f_j)$$

$$y_{ij} = G(X_i, Y_i, Z_i; X_{cj}, Y_{cj}, Z_{cj}; \phi_j, \theta_j, \psi_j; x_{oj}, y_{oj}, f_j), \quad j = 1, 2; i = 1, 2, \dots, N$$

## TWO PHOTOGRAMMETRIC ESTIMATION PROBLEMS

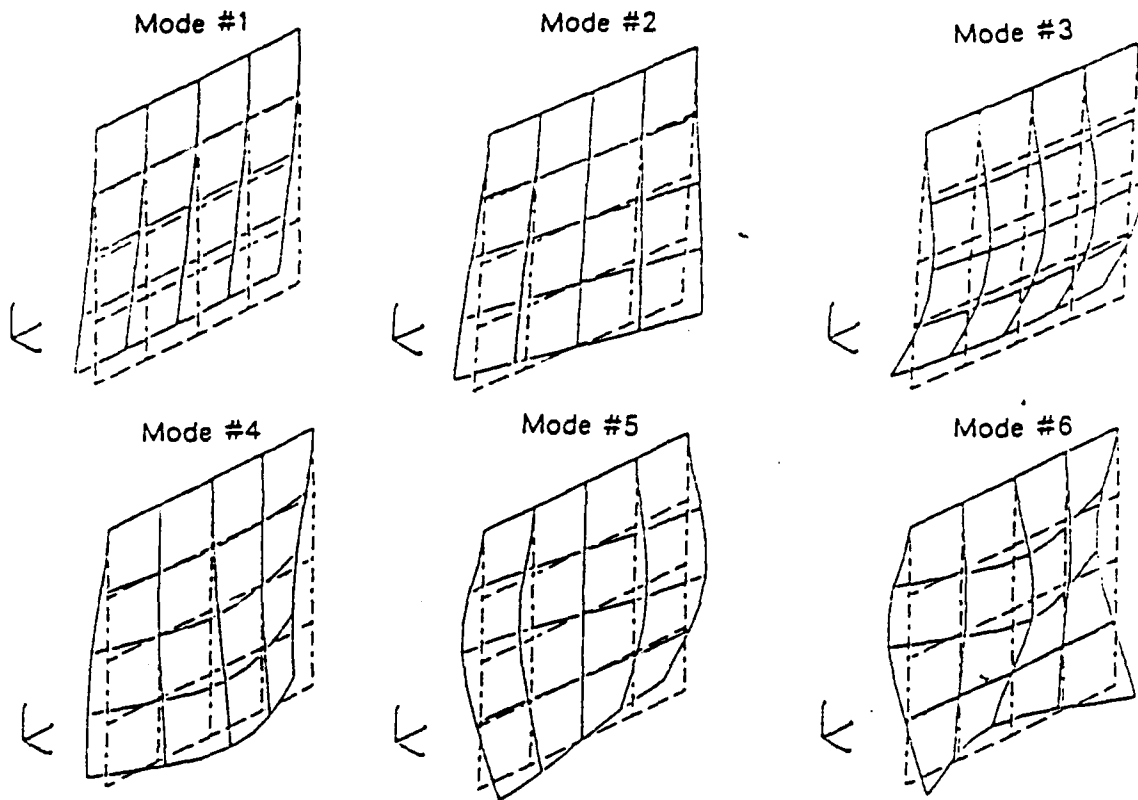
### **Problem One: *Static Calibration***

Each object space point imaged generates four measurements, these measurements can be combined with other a priori calibration information to determine the camera positions, orientation angles, focal lengths, and principle point offsets. Least square differential correction converges to yield estimates and associated covariance for camera geometric parameters.

### **Problem Two: *Dynamic Triangulation to Measure Deflections***

Given the results of the static calibration, the four equations for stereo images of each object space point can be solved for estimates of the object space coordinates; this can be done for each of several images, for each instant in time (e. g. at 200 HZ)

Figure 4. Modeled, Measured, and Identified Natural Frequencies of the Frame Structure

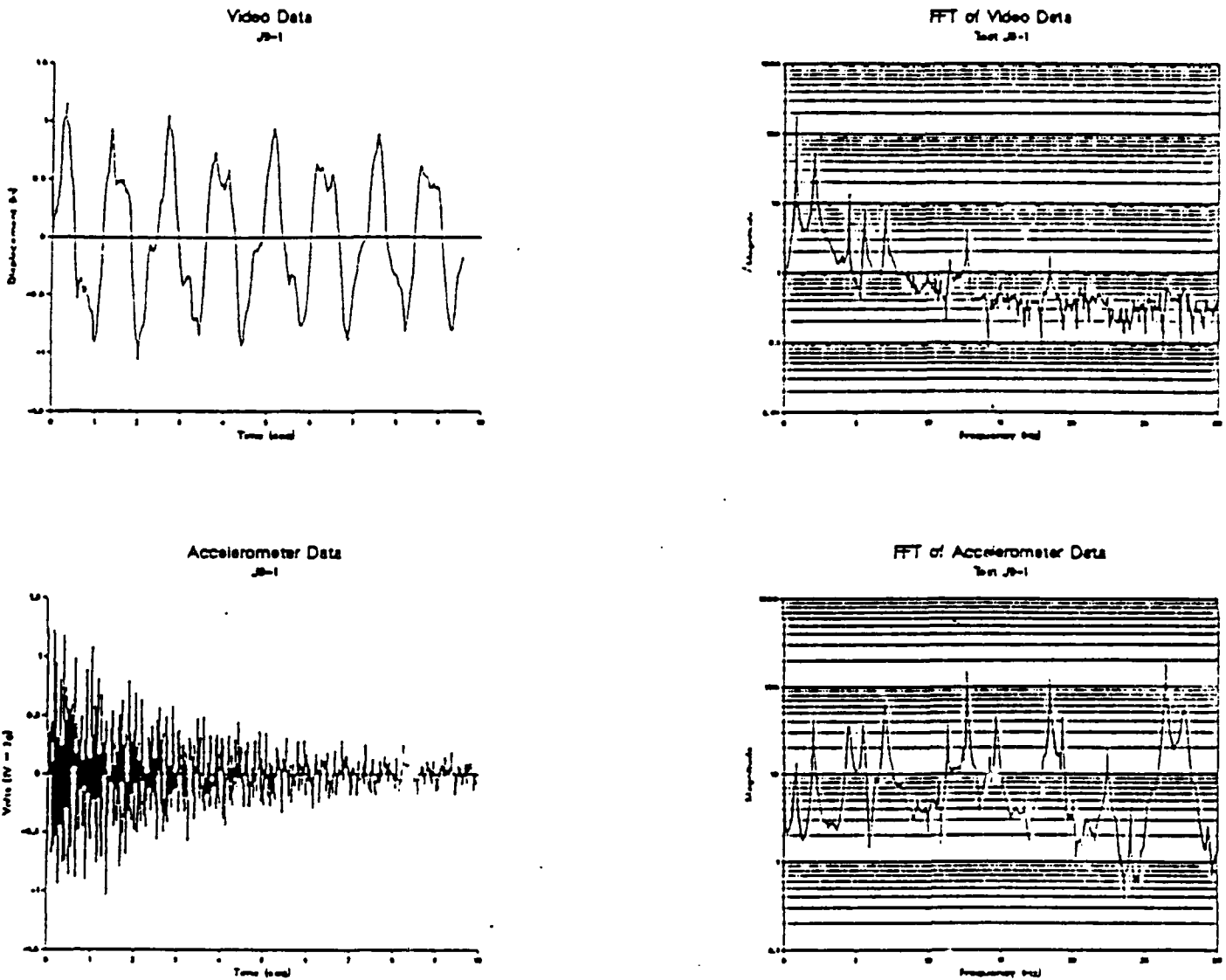


The finite element model mode shapes as reported by Das et al are shown above. The first six finite element natural frequencies are given below as well as the first six experimentally determined natural frequencies. These natural frequencies were determined by the eigenstructure realization algorithm using free response to an impulsive loading. Preliminary results of the structural identification method of Creamer and Junkins are given. These results were obtained by holding the mass matrix constant and using three stiffness submatrices to match the natural frequencies.

Mode No.	Modeled Value	Measured Value	Identified Value *
1	.90 Hz	.92 Hz	.91 Hz
2	2.34	2.32	2.32
3	4.85	4.93	4.93
4	6.05	6.38	6.38
5	7.78	7.27	7.26

\* - Element submatrices used

# Figure 5. Comparison of Video-Derived Position Measurements with Accelerometer Measurements



The graphs shown above provide some insight into the advantages and disadvantages of the camera system versus an accelerometer. The video data is very useful at the low frequency large amplitude end of the spectrum. The accelerometer response is most reliable at the high frequency end of the spectrum. This data was taken on the AFAL structural identification test article which is similar to the TAMU structure. The video data was taken with a TAMU RCA TC2811 60 Hz video camera. An AFAL Endevco model 7751-500 accelerometer was also used.

## CONCLUDING REMARKS

■ A Stereo Triangulation Approach has been developed for measuring vibratory structural deformation.

*Motion of many points measured simultaneously*

*Easy to calibrate (two cameras, no moving parts)*

*> 20 passive targets have been tracked @ 200HZ*

*Analog and digital processing is semi-automated*

■ *The Structural Identification Approach of Junkins and Creamer has been applied to obtain an updated model which matches experimental natural frequencies, mode shapes and freq. response.*

■ *The feasibility of the central ideas has been established, main shortcoming is the moderate spatial resolution (about 1 part in 900) of the optical system and edge detection methodology used.*

■ *Enhancement of the hardware and the image processing concepts promises an order of magnitude of resolution improvement*

**ATTACHMENT 10**

**A Stereo Triangulation System for Structural Identification:  
Analytical and Experimental Results**

*J. L. Junkins  
G. H. James III  
T. C. Pollock  
Z. H. Rahman*

Department of Aerospace Engineering  
Texas A&M University  
College Station, Texas, USA 77843

USAF/NASA Workshop on Model Determination  
for Large Space Structures  
Jet Propulsion Laboratory  
March 22-24, 1988

## ABSTRACT

Identification of large space structures' distributed mass, stiffness, and energy dissipation characteristics poses formidable analytical, numerical, and implementation difficulties. Development of reliable on-orbit structural identification methods is important for implementing active vibration suppression concepts which are under widespread study in the large space structures community. Near the heart of the identification problem lies the necessity of making a large number of spatially distributed measurements of the structure's vibratory response and the associated force/moment inputs with sufficient spatial and frequency resolution. In the present paper, we discuss a method whereby tens of active or passive (retro-reflecting) targets on the structure are tracked simultaneously in the focal planes of two or more video cameras mounted on an adjacent platform. Triangulation (optical ray intersection) of the conjugate image centroids yield inertial trajectories of each target on the structure. Given the triangulated motion of the targets, we apply and extend methodology developed by Creamer, Junkins and Juang to identify the frequencies, mode shapes and updated estimates for the mass/stiffness/damping parameterization of the structure. The methodology is semi-automated, for example the post experiment analysis of the video imagery to determine the inertial trajectories of the targets typically requires less than thirty minutes of real time.

Using methodology discussed herein, the frequency response of a large number of points on the structure (where reflective targets are mounted) on the structure can be determined from optical measurements alone. For comparison purposes, we also utilize measurements from accelerometers and a calibrated impulse hammer. While our experimental work remains in a research stage of development, we have successfully tracked and stereo triangulated 20 targets (on a vibrating cantilevered grid structure) at a sample frequency of 200HZ, and have established conclusively the feasibility and desirability of this approach.

We discuss, in summary, recent advances in analog and digital video processing methodology, and actuation methods, and bring them to bear on the structural identification problem. We include a brief discussion of our experimental hardware and some recent experimental results which support the practical feasibility of this structural vibration sensing approach.

## Measurement Geometry and Stereo Triangulation

The object-to image space transformation for a single lens camera is given by the *colinearity equations*

$$x = x_0 - f \left[ \frac{C_{11}(X-X_c) + C_{12}(Y-Y_c) + C_{13}(Z-Z_c)}{C_{31}(X-X_c) + C_{32}(Y-Y_c) + C_{33}(Z-Z_c)} \right] \equiv F(X, Y, Z; X_c, Y_c, Z_c; \phi, \theta, \psi; x_0, y_0, f)$$

$$y = y_0 - f \left[ \frac{C_{21}(X-X_c) + C_{22}(Y-Y_c) + C_{23}(Z-Z_c)}{C_{31}(X-X_c) + C_{32}(Y-Y_c) + C_{33}(Z-Z_c)} \right] \equiv G(X, Y, Z; X_c, Y_c, Z_c; \phi, \theta, \psi; x_0, y_0, f)$$

where

$$[C] = \begin{bmatrix} C_{11} & C_{12} & C_{13} \\ C_{21} & C_{22} & C_{23} \\ C_{31} & C_{32} & C_{33} \end{bmatrix} = \begin{bmatrix} 1 & 0 & 0 \\ 0 & \cos\psi & \sin\psi \\ 0 & -\sin\psi & \cos\psi \end{bmatrix} \begin{bmatrix} \cos\theta & 0 & -\sin\theta \\ 0 & 1 & 0 \\ \sin\theta & 0 & \cos\theta \end{bmatrix} \begin{bmatrix} \cos\phi & \sin\phi & 0 \\ -\sin\phi & \cos\phi & 0 \\ 0 & 0 & 1 \end{bmatrix}$$

(205)

For the case of two cameras simultaneously imaging the same structure, we adopt a subscript notation to denote the image coordinates of the  $i^{th}$  point measured in the  $j^{th}$  camera's image space as

$$x_{ij} = F(X_i, Y_i, Z_i; X_{cj}, Y_{cj}, Z_{cj}; \phi_j, \theta_j, \psi_j; x_{0j}, y_{0j}, f_j)$$

$$y_{ij} = G(X_i, Y_i, Z_i; X_{cj}, Y_{cj}, Z_{cj}; \phi_j, \theta_j, \psi_j; x_{0j}, y_{0j}, f_j), \quad j = 1, 2; i = 1, 2, \dots, N$$

## TWO PHOTOGRAMMETRIC ESTIMATION PROBLEMS

### **Problem One: *Static Calibration***

Each object space point imaged generates four measurements, these measurements can be combined with other a priori calibration information to determine the camera positions, orientation angles, focal lengths, and principle point offsets. Least square differential correction converges to yield estimates and associated covariance for camera geometric parameters.

### **Problem Two: *Dynamic Triangulation to Measure Deflections***

Given the results of the static calibration, the four equations for stereo images of each object space point can be solved for estimates of the object space coordinates; this can be done for each of several images, for each instant in time (e. g. at 200 HZ)

# Figure 1. Stereo Triangulation Geometry

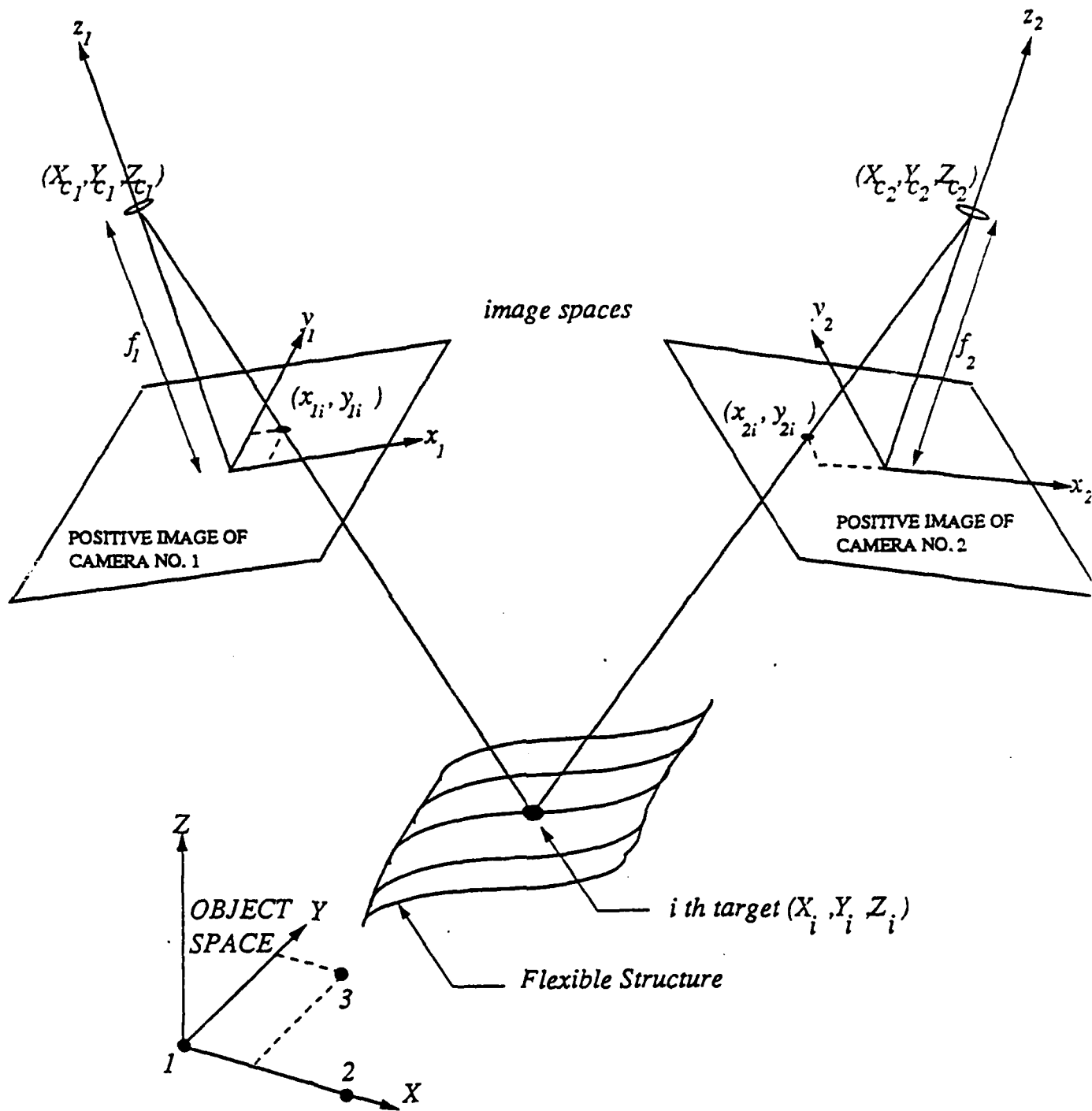
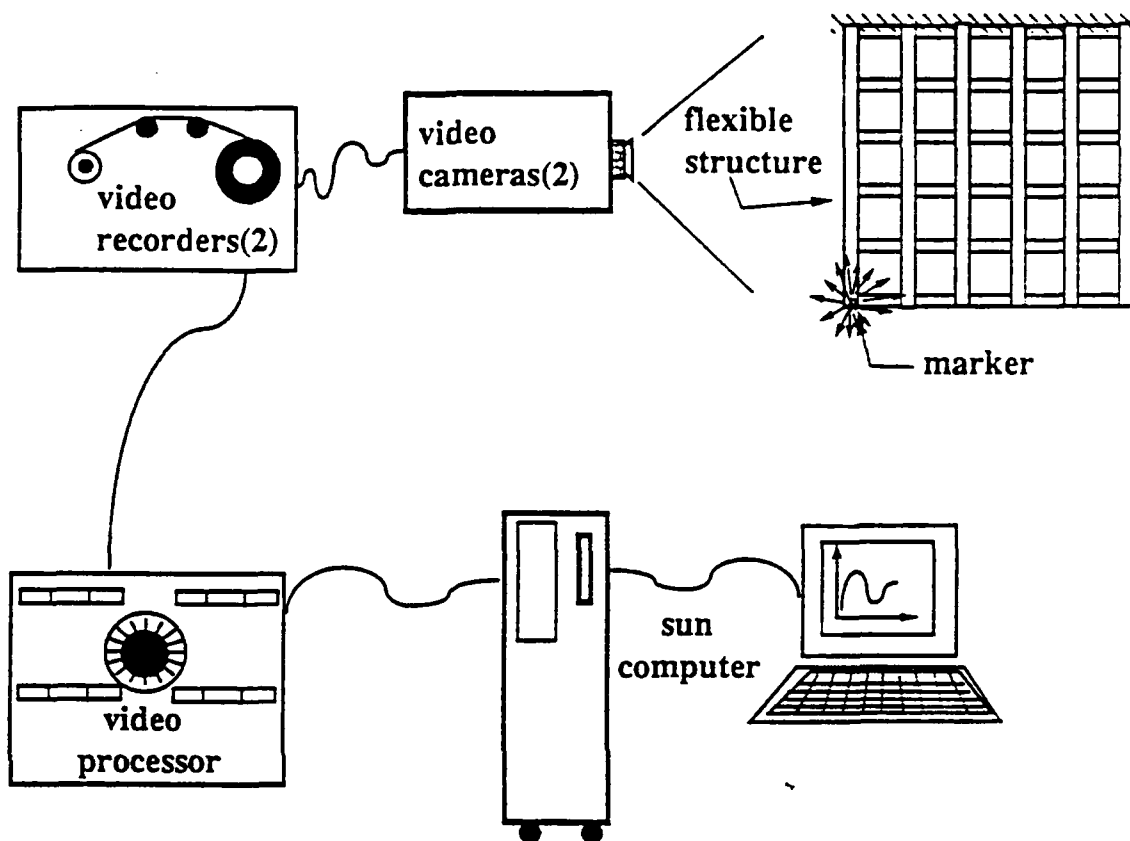


# Figure 2. Motion Analysis Hardware



MAJOR HARDWARE ITEMS	
ITEM	DESCRIPTION
Flexible Structure	monolithic 3003 H14 aluminum grid (5'x5') cantilevered in the vertical plane (clamped-free boundary conditions)
markers (targets)	3M Scotchlite Reflective Sheeting #3290
Video Cameras(2)	NAC model V-14B, 200/60 HZ, 2/3" MOS imaging CCD array with 320x244 pixels
Video Recorder(2)	NAC model VTR V-32, 200HZ, configured for VHS cassettes
Video Processor	Motion Analysis model VP-310 for threshold-based edge detection, hardware editing and filtering, digitizing image boundaries, and data transfer
Computer	SUN 1/120 with 42 megabyte hard disk and UNIX operating system

# STRUCTURAL IDENTIFICATION

We consider the class of linear elastic structures suitably modeled by

$$M\ddot{x} + C\dot{x} + Kx = Bu$$

To outline some of the details of our structural identification approach, we consider a special case. For harmonic excitation  $u = r \exp(j\omega t)$ , zero damping, and an identity  $B$  matrix, the *frequency response* is given by taking the Fourier transform of the equations of motion to obtain

$$X(i\omega) = [-\omega^2 M + K]^{-1} r \equiv H(i\omega) r; \quad H_{jk}(i\omega) \equiv \sum_{l=1}^n \frac{\phi_{jl} \phi_{kl}}{\omega_l^2 - \omega^2} \quad \left( \begin{array}{l} \text{spectral} \\ \text{decomposition} \\ \text{theorem} \end{array} \right)$$

where  $\det [K - \omega^2 M] = 0, \Rightarrow \{\omega_1^2, \dots, \omega_n^2\}$ , and  $[K - \omega_i^2 M]\phi_i = 0, \Rightarrow \{\phi_1, \dots, \phi_n\}$

$$\Phi^T M \Phi = I, \quad \Phi^T K \Phi = \text{diag}(\omega_1^2, \dots, \omega_n^2), \quad \Phi = [\phi_1 \dots \phi_n]$$

Cremer and Junkins[3, 4] developed an identification process whereby linearly parameterized mass, stiffness and damping properties can be estimated; the parameterization adopted for the present discussion is of the form

$$M = M_0 + \sum_{r=1}^p \mu_r M_r, \quad K = K_0 + \sum_{r=1}^q \kappa_r K_r, \quad C = C_0 + \sum_{r=1}^s \chi_r C_r$$

where  $\mu_r, \kappa_r, \chi_r$  are scalars determined to bring the calculated and measured eigenvalues, eigenvectors, and frequency response functions into least square agreement. Notice that the coupling pattern of the original structural model is preserved and that both the free vibration and forced vibration measurements are taken into account.

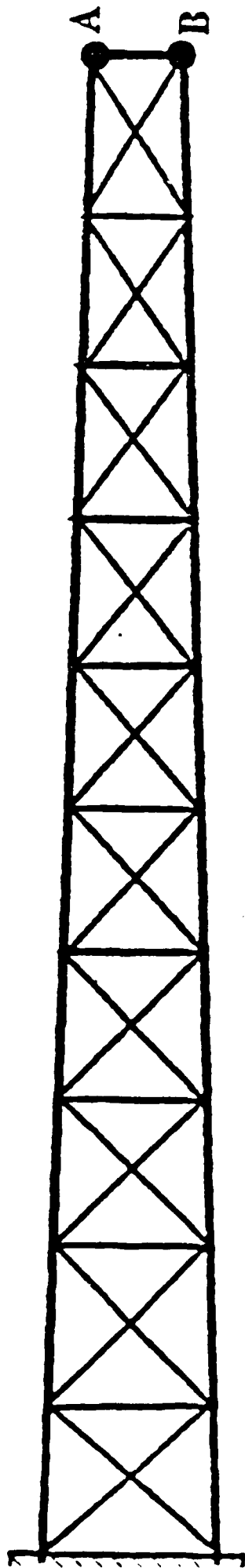
**Table 1. Modeled, Measured, and Identified  
Natural Frequencies of the Grid Structure**

<b>Mode No.</b>	<b>Modeled Value</b>	<b>Measured Value</b>	<b>Identified Value *</b>	<b>Identified Value **</b>
1	.90 Hz	.92 Hz	.91 Hz	.92 Hz
2	2.34	2.32	2.32	2.32
3	4.85	4.93	4.93	4.93
4	6.05	6.38	6.38	6.38
5	7.78	7.27	7.26	7.27

\* - Element submatrices used

\*\* - Modal submatrices used (coupling and sparsity may not be retained)

# IDENTIFICATION OF A DAMPED TAPERED TRUSS



(211)

**From Video and Force Measurements:**

- first 8 open-loop eigenvalues**
- first 8 closed-loop eigenvalues**
- longitudinal FRF between A and B**
- transverse FRF between A and B**



# Eigenvalues for Damped Truss Structure

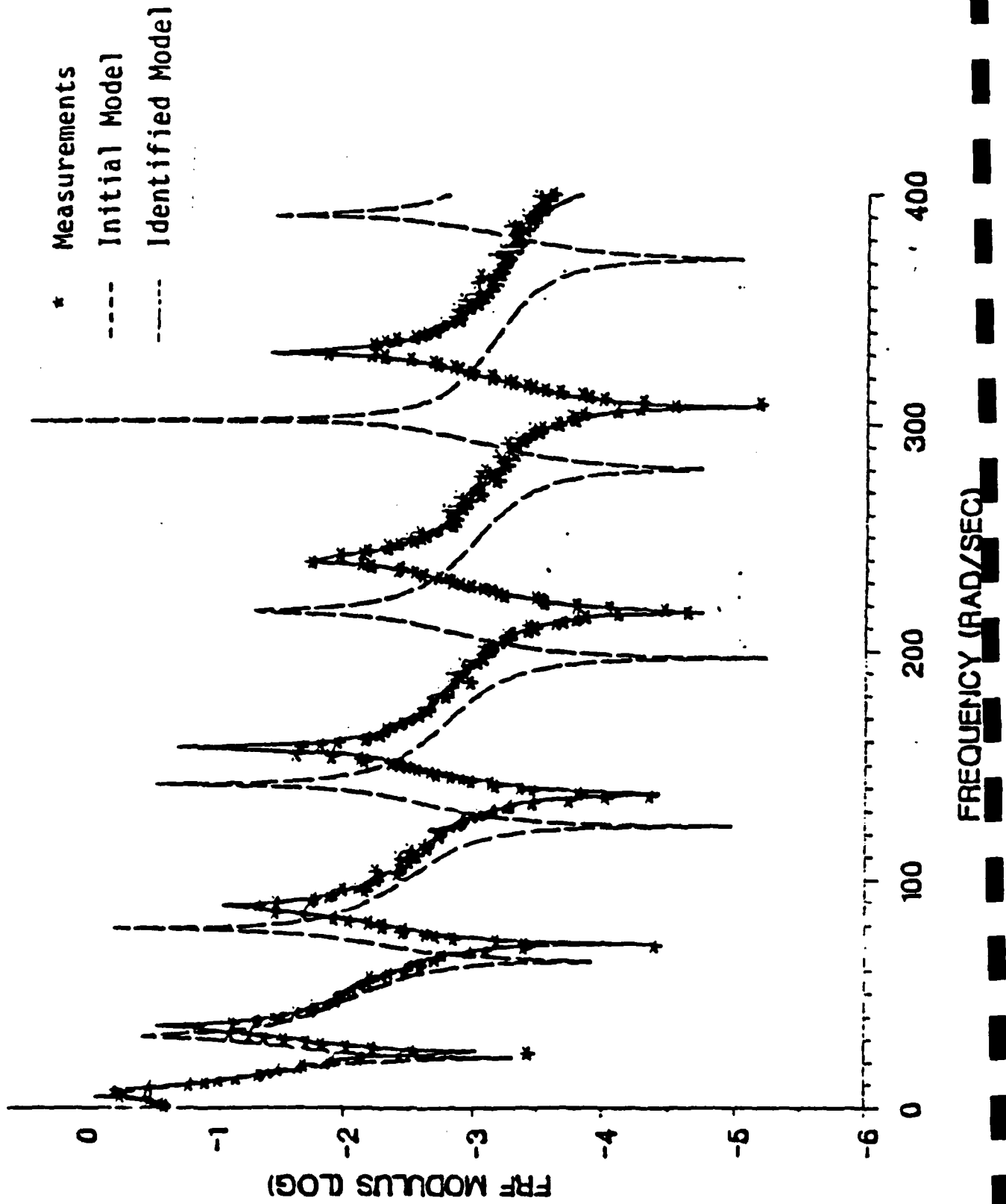
*Measured vs Initial Model vs Identified Model*

MEASURED INITIAL IDENTIFIED MODEL

MODE	$\bar{\lambda}$	$\lambda_0$	$\lambda_f$
1	-0.0872 + 6.731	6.111	-0.0872 + 6.931
2	-0.0890 + 34.591	31.451	-0.0888 + 35.461
3	-0.0891 + 87.581	78.891	-0.0898 + 88.291
4	-0.1042 + 117.111	106.671	-0.1039 + 119.391
5	-0.0907 + 156.491	142.121	-0.0906 + 157.861
6	-0.0914 + 240.331	217.541	-0.0915 + 240.051
7	-0.0929 + 332.091	302.001	-0.0925 + 331.391
8	-0.1039 + 359.291	325.251	-0.1042 + 363.281

# Damped Truss Structure Identification

*Frequency Response Function: Measured vs Initial Model vs Identified Model*



## CONCLUDING REMARKS

■ A Stereo Triangulation Approach has been developed for measuring vibratory structural deformation.

*Motion of many points measured simultaneously*

*Easy to calibrate (two cameras, no moving parts)*

*> 20 passive targets have been tracked @ 200HZ*

*Analog and digital processing is semi-automated*

■ *The Structural Identification Approach of Jenkins and Creamer has been applied to obtain an updated model which matches experimental natural frequencies, mode shapes and freq. response.*

■ *The feasibility of the central ideas has been established, main shortcoming is the moderate spatial resolution (about 1 part in 900) of the optical system and edge detection methodology used.*

■ *Enhancement of the hardware and the image processing concepts promises an order of magnitude of resolution improvement*

*CSI Sensing and Control:  
Analytical and Experimental Results*

J. L. Junkins  
T. C. Pollock  
Z. H. Rahman

Texas A&M University

3rd Annual NASA/DoD Control/Structure Interaction Conference  
San Diego, CA  
January 29 - February 2, 1989

## *Acknowledgments*

*The following graduate research assistants made significant contributions to the analytical, numerical and experimental results reported herein:*

*G. James, III*

*S. Morgan*

*Y. Kim*

*D. Anderson*

*M. McVay*

*This research is supported by the Air Force Office of Scientific Research and the Texas Advanced Technology Research Program. The liasion of Dr. A. K. Amos is appreciated.*

# *OUTLINE*

- TAMU Flexible Grid Experiments
  - Configuration & Objectives
  - System Identification
  - Approach and Formulation
  - Stereo-Triangulation Deflection Measurements
  - Other Sensor & Actuators
  - Experimental Results
  - Minimum Sensitivity Control Law Design
  
- Large Angle Maneuver Experiment
  - Configuration & Objectives
  - Torque-Shaped, Near-minimum-time maneuvers
  - Liapunov-Stable Feedback Control
  - Experimental Results
  
- Concluding Remarks

# Structural Model Identification

## *Parameterization Schemes*

- Physical / Geometrical Parameters

$\{EI's, GJ's, \rho's, etc.\}$

- Equivalent Continuum Parameters

$\{\bar{E}I's, \bar{G}J's, \bar{\rho}'s, etc.\}$

- Submatrix Scale Factors

$$M = M_o + \sum_i \mu_i M_i, \quad K = K_o + \sum_i \kappa_i K_i, \quad C = C_o + \sum_i \chi_i C_i$$

where  $\{M_i, K_i, C_i\}$  are prescribed and the scalars  $\{\mu_i, \kappa_i, \chi_i\}$  are estimated.

- Matrix Element Modifications

$$M_{ij} = M_{oij} + m_{ij}, \quad K_{ij} = K_{oij} + k_{ij}, \quad C_{ij} = C_{oij} + c_{ij}$$

## STRUCTURAL IDENTIFICATION:

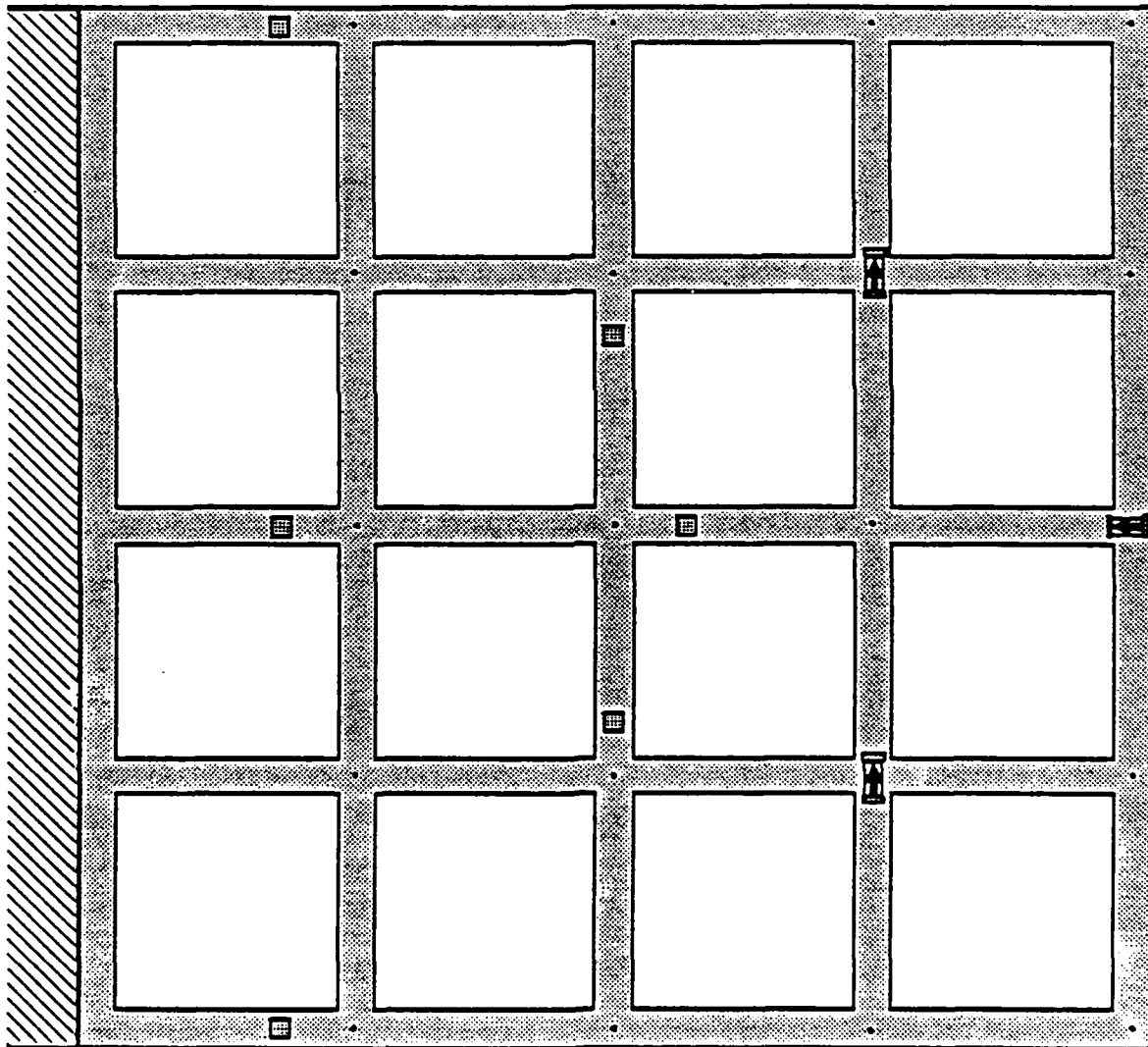
### Ingredients of Our Approach

- ▶ *modal* parameters (free response)  $\Rightarrow$   $\{\omega$ 's,  $\xi$ 's, and  $\phi$ 's $\}$
- ▶ *model* parameters (free or forced response)  
 $\Rightarrow$   $\{EI$ 's,  $GJ$ 's, *geometric, mass, stiffness, and damping parameters* $\}$
- ▶ **time domain identification** (e. g., ERA balanced realization)
- ▶ **frequency domain identification (Freq. Resp. Fct. fitting)**
  - Creamer/Junkins method {simultaneous best-fit of free-vibration derived modal parameters and the forced response derived Freq. Resp. Function}

### Optical Vibration Sensing System & Identification Methods

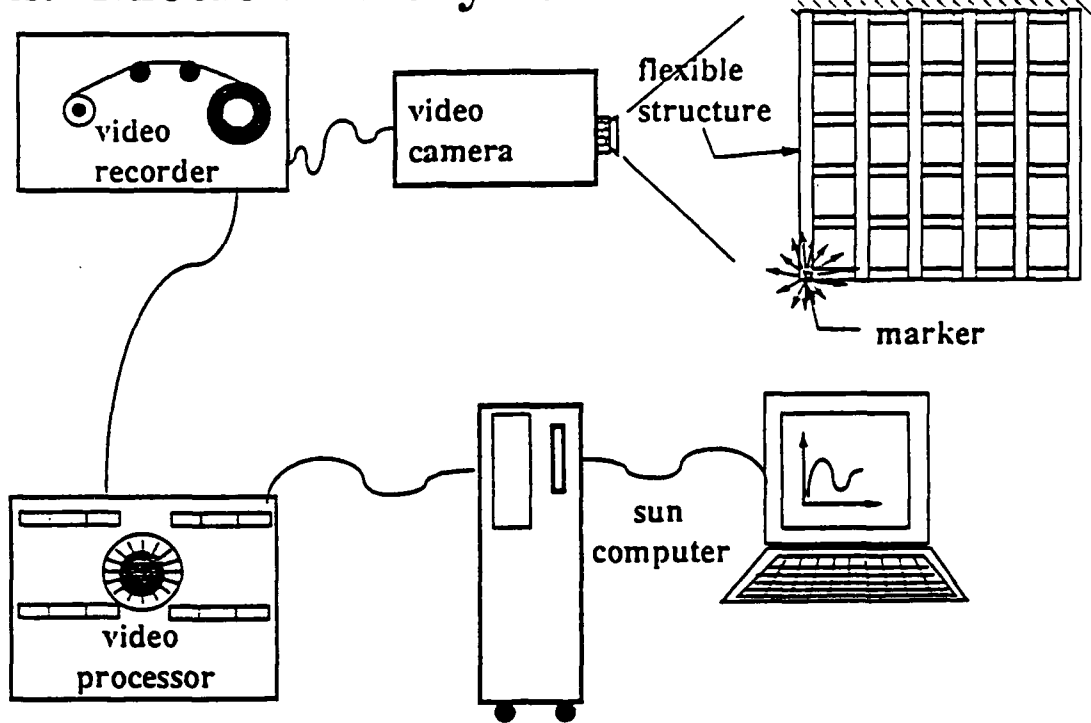
- ▶ *Experimental results on a grid structure*

# Flexible Grid Sensor and Actuator Locations



■ strain gauge location  
• fiber optic light source  
⚙ reaction wheel actuator

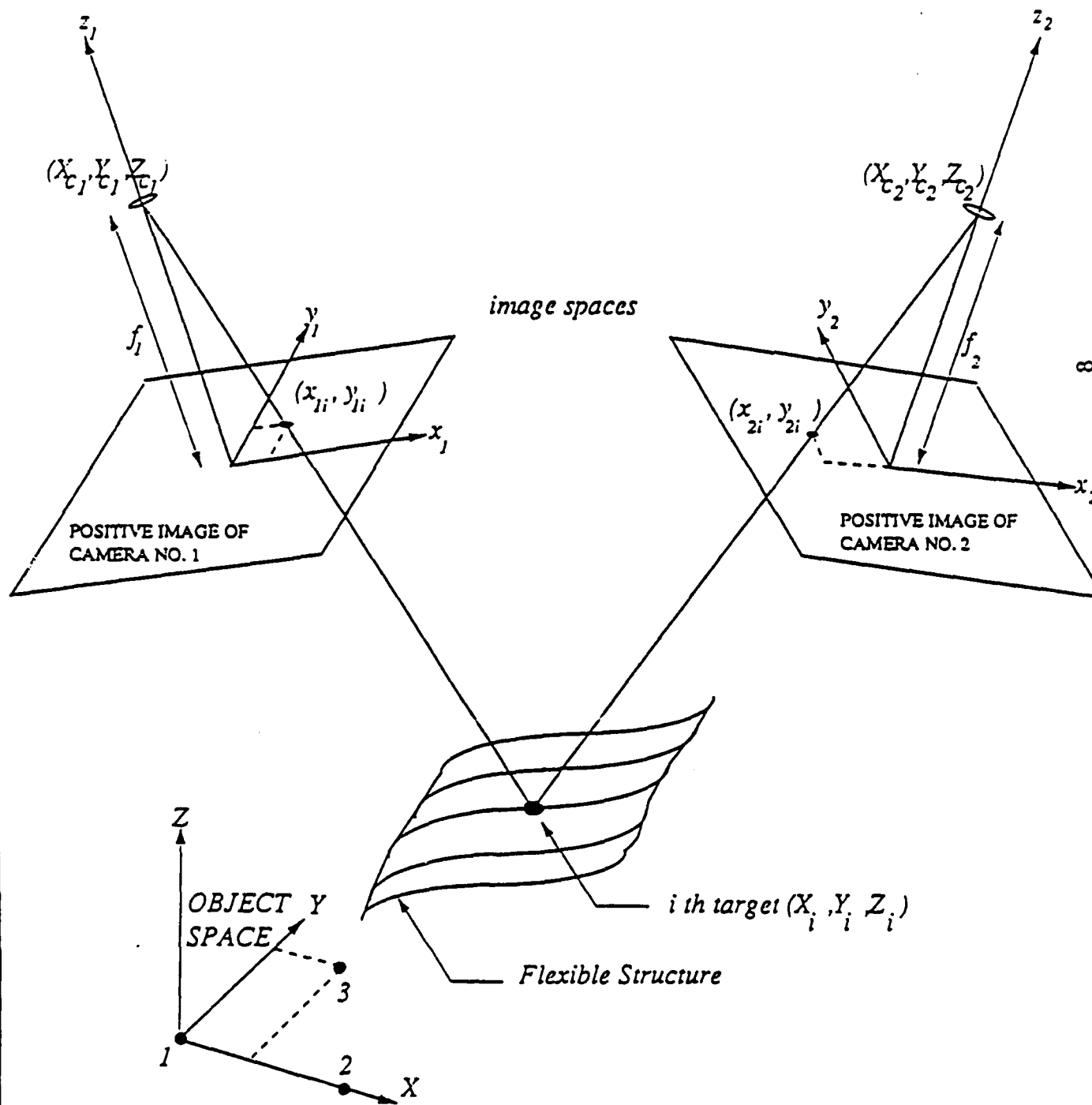
# Figure 1. Motion Analysis Hardware



7

MAJOR HARDWARE ITEMS	
ITEM	DESCRIPTION
Flexible Structure	monolithic 3003 H14 aluminum grid (5'x5') cantilevered in the vertical plane (clamped-free boundary conditions)
markers (targets)	3M Scotchlite Reflective Sheeting #3290
Video Cameras(2)	NAC model V-14B, 200/60 HZ, 2/3" MOS imaging CCD array with 320x244 pixels
Video Recorder(2)	NAC model VTR V-32, 200HZ, configured for VHS cassettes
Video Processor	Motion Analysis model VP-110 for threshold-based edge detection, hardware editing and filtering, digitizing image boundaries, and data transfer
Computer	SUN 2/120 with 42 megabyte hard disk and UNIX operating system

Figure 1. Stereo Triangulation Geometry



## Measurement Geometry and Stereo Triangulation

The object-to image space transformation for a single lens camera is given by the *colinearity equations*

$$x = x_0 - f \left[ \frac{C_{11}(X - X_c) + C_{12}(Y - Y_c) + C_{13}(Z - Z_c)}{C_{31}(X - X_c) + C_{32}(Y - Y_c) + C_{33}(Z - Z_c)} \right] \equiv F(X, Y, Z; X_c, Y_c, Z_c; \phi, \theta, \psi; x_0, y_0, f)$$

$$y = y_0 - f \left[ \frac{C_{21}(X - X_c) + C_{22}(Y - Y_c) + C_{23}(Z - Z_c)}{C_{31}(X - X_c) + C_{32}(Y - Y_c) + C_{33}(Z - Z_c)} \right] \equiv G(X, Y, Z; X_c, Y_c, Z_c; \phi, \theta, \psi; x_0, y_0, f)$$

where

$$[C] = \begin{bmatrix} C_{11} & C_{12} & C_{13} \\ C_{21} & C_{22} & C_{23} \\ C_{31} & C_{32} & C_{33} \end{bmatrix} = \begin{bmatrix} 1 & 0 & 0 \\ 0 & \cos\psi & \sin\psi \\ 0 & -\sin\psi & \cos\psi \end{bmatrix} \begin{bmatrix} \cos\theta & 0 & -\sin\theta \\ 0 & 1 & 0 \\ \sin\theta & 0 & \cos\theta \end{bmatrix} \begin{bmatrix} \cos\phi & \sin\phi & 0 \\ -\sin\phi & \cos\phi & 0 \\ 0 & 0 & 1 \end{bmatrix}$$

For the case of two cameras simultaneously imaging the same structure, we adopt a subscript notation to denote the image coordinates of the  $i^{\text{th}}$  point measured in the  $j^{\text{th}}$  camera's image space as

$$x_{ij} = F(X_i, Y_i, Z_i; X_{cj}, Y_{cj}, Z_{cj}; \phi_j, \theta_j, \psi_j; x_{0j}, y_{0j}, f_j)$$

$$y_{ij} = G(X_i, Y_i, Z_i; X_{cj}, Y_{cj}, Z_{cj}; \phi_j, \theta_j, \psi_j; x_{0j}, y_{0j}, f_j), \quad j = 1, 2; i = 1, 2, \dots, N$$

## TWO PHOTOGRAMMETRIC ESTIMATION PROBLEMS

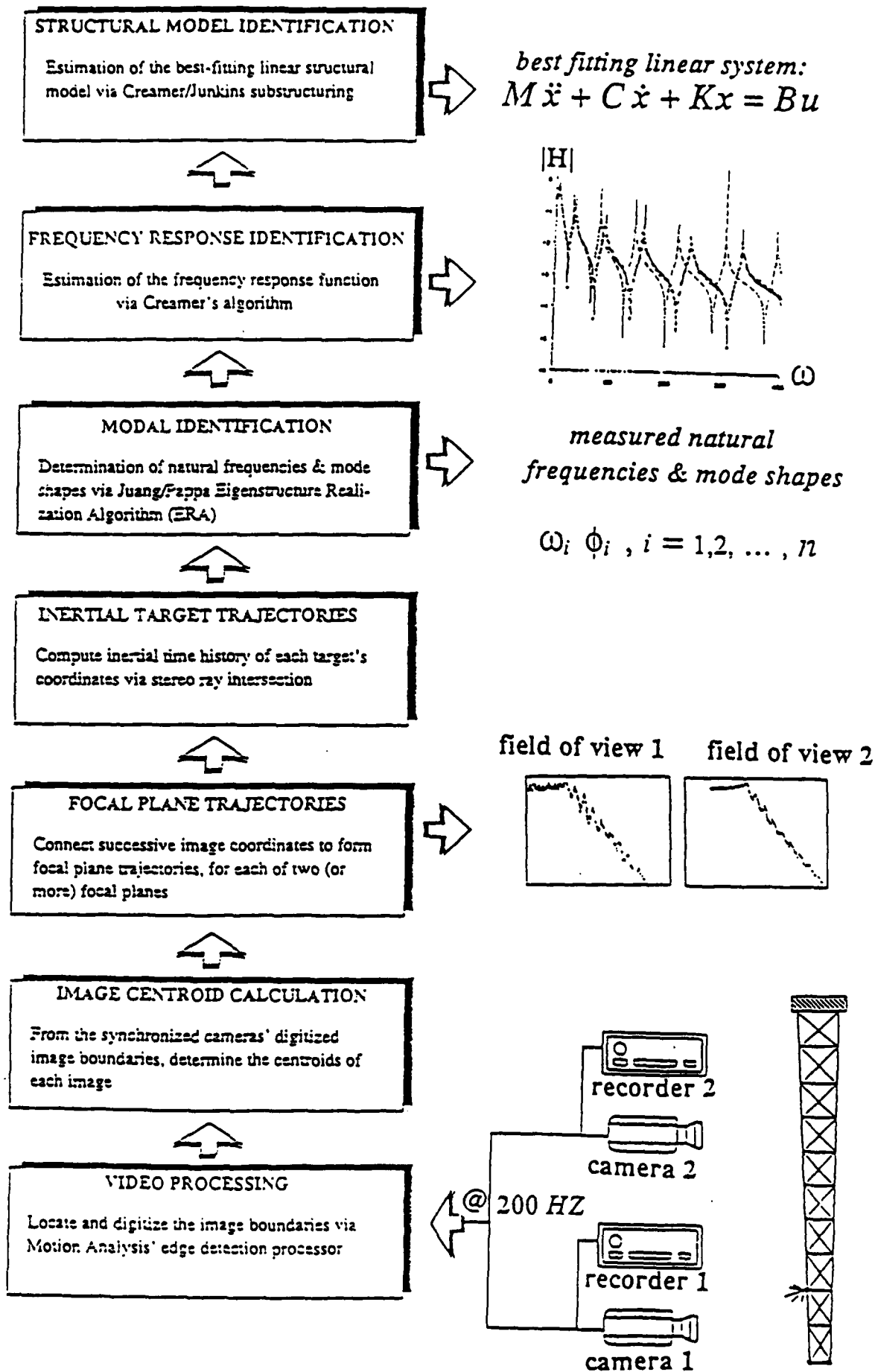
### **Problem One: *Static Calibration***

Each object space point imaged generates four measurements, these measurements can be combined with other a priori calibration information to determine the camera positions, orientation angles, focal lengths, and principle point offsets. Least square differential correction converges to yield estimates and associated covariance for camera geometric parameters.

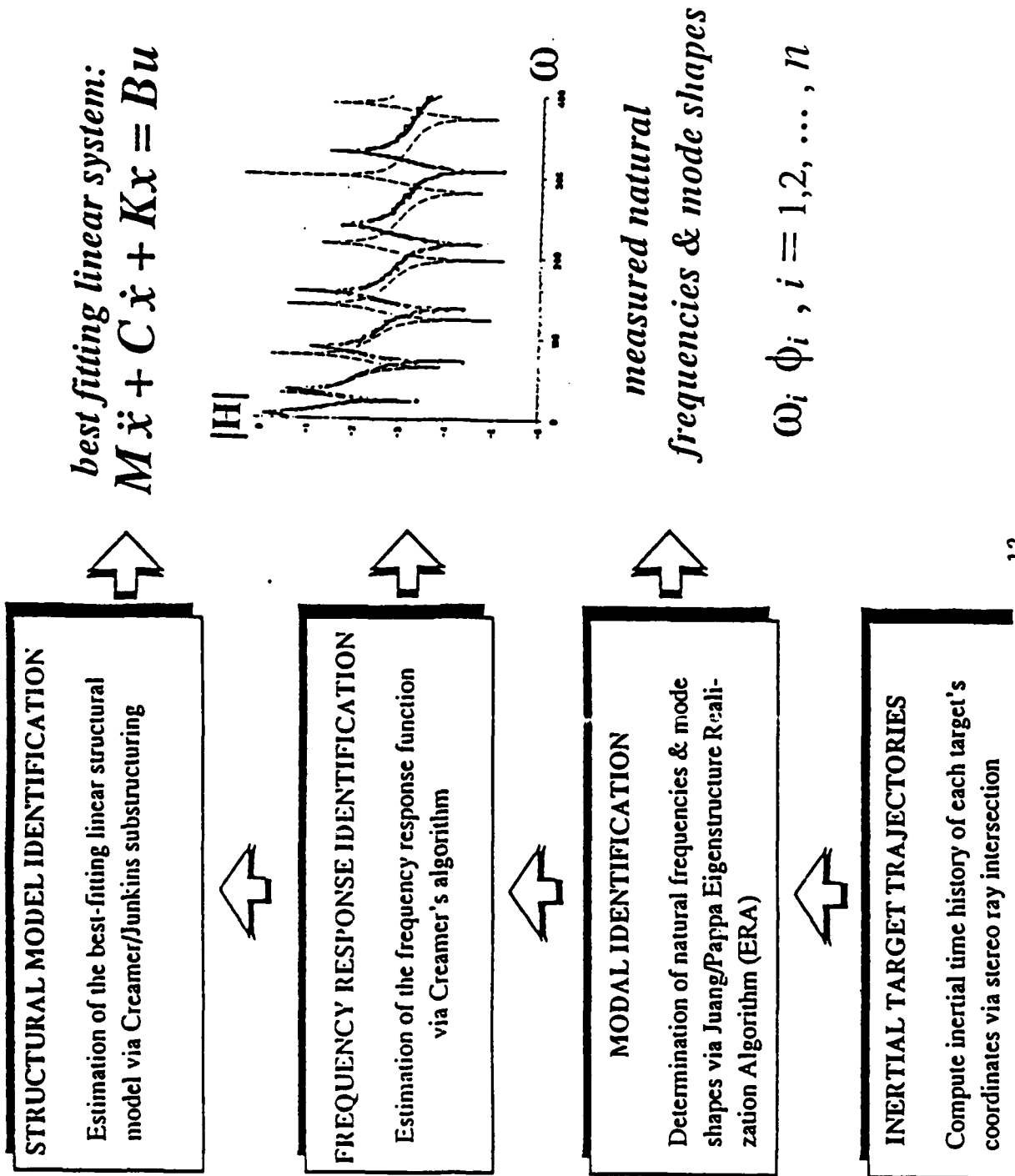
### **Problem Two: *Dynamic Triangulation to Measure Deflections***

Given the results of the static calibration, the four equations for stereo images of each object space point can be solved for estimates of the object space coordinates; this can be done for each of several images, for each instant in time (e. g. at 200 HZ)

# A Novel Approach to Structural Identification



# A Novel Approach to Structural Identification



### INERTIAL TARGET TRAJECTORIES

Compute inertial time history of each target's coordinates via stereo ray intersection



### FOCAL PLANE TRAJECTORIES

Connect successive image coordinates to form focal plane trajectories, for each of two (or more) focal planes



field of view 1      field of view 2

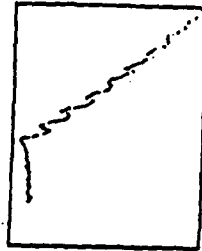


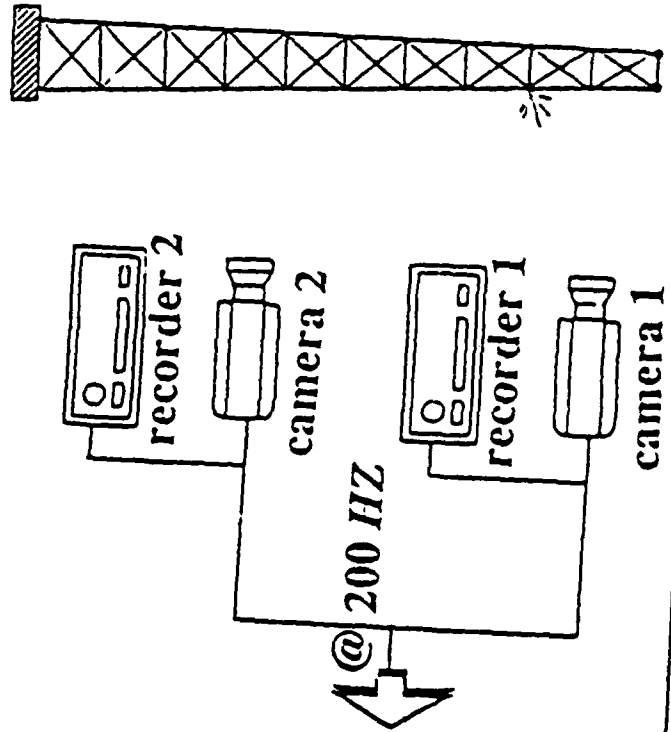
### IMAGE CENTROID CALCULATION

From the synchronized cameras' digitized image boundaries, determine the centroids of each image



### VIDEO PROCESSING

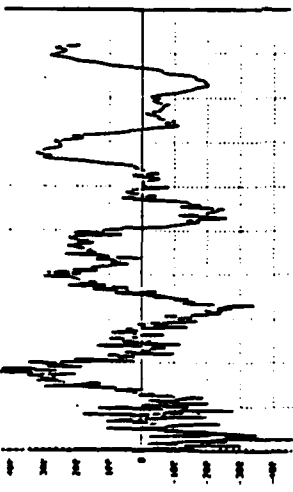
Locate and digitize the image boundaries via Motion Analysis' edge detection processor



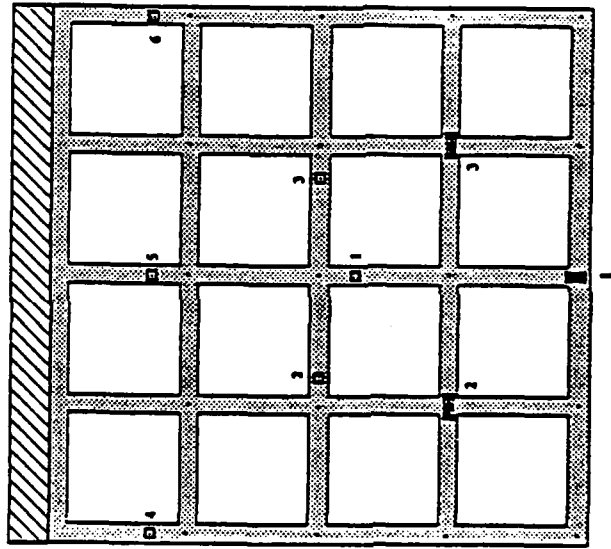
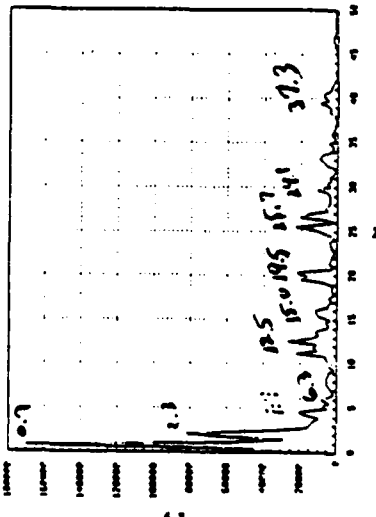
# Response of the Grid to Impulsive Excitation

Strain Gauge # 4 Response:

Time response history:

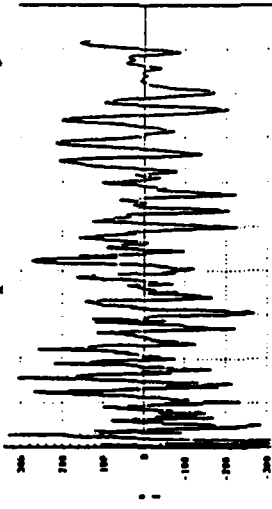


FFT of measured strain history:

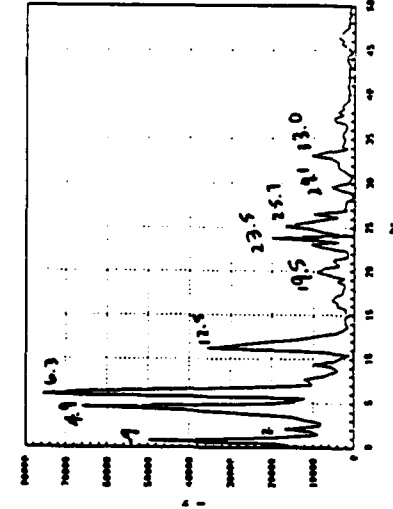


Strain Gauge # 1 Response:

Time response history:



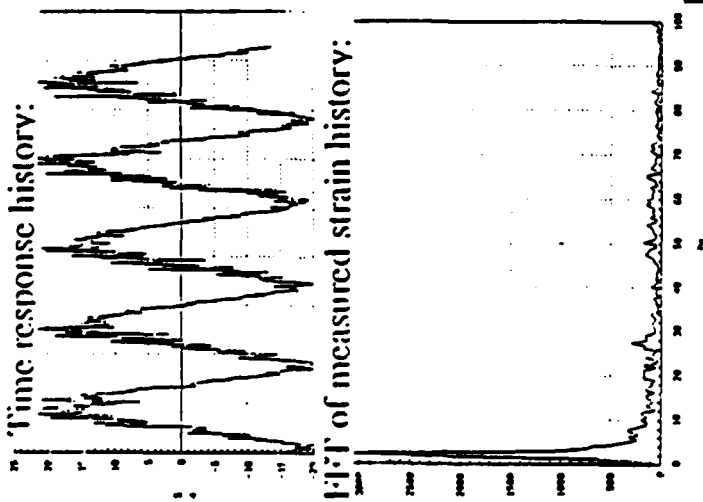
FFT of measured strain history:



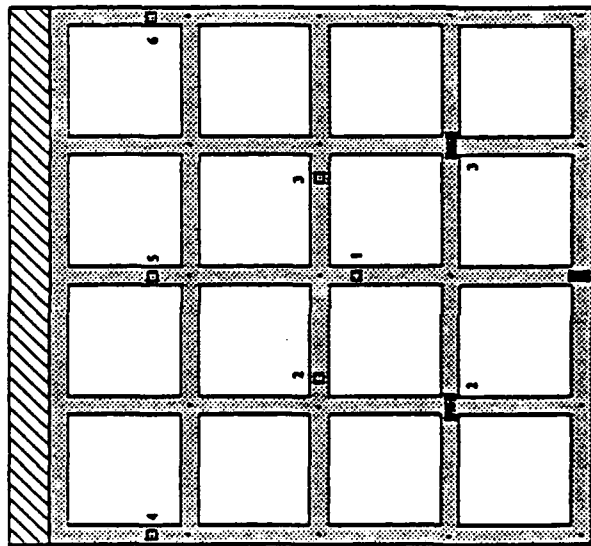
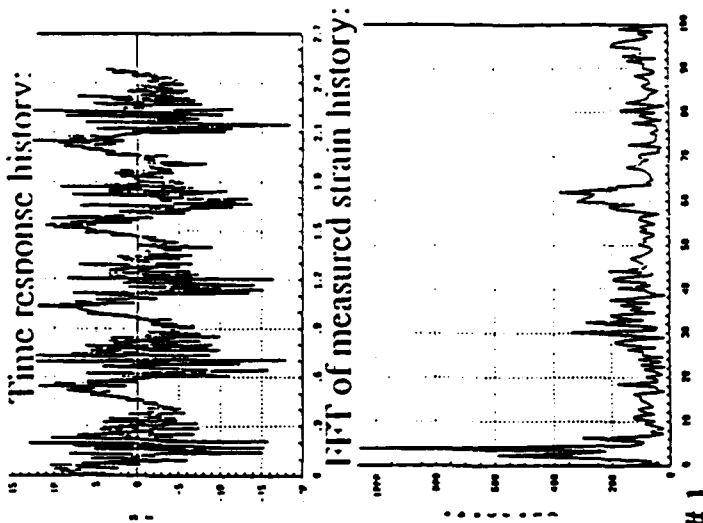
[calibrated initial impulse applied at lower left corner of the grid]

# Response of the Grid to Harmonic Excitation

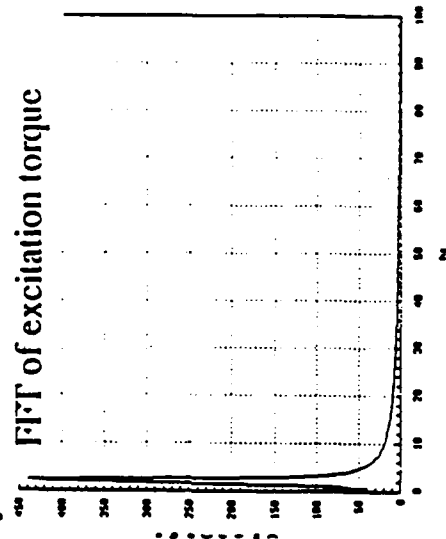
Strain Gauge # 4 Response:



Strain Gauge # 1 Response:



Harmonic Excitation Torque by Reaction Wheel # 1



Time history of excitation torque

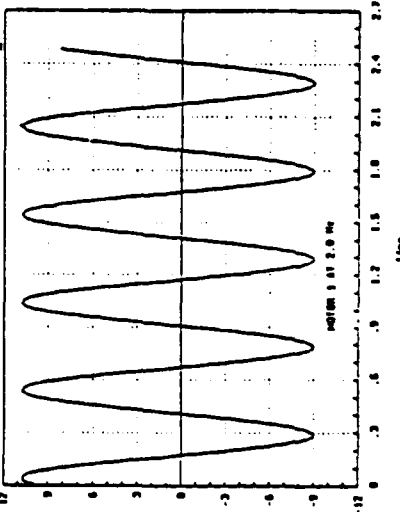
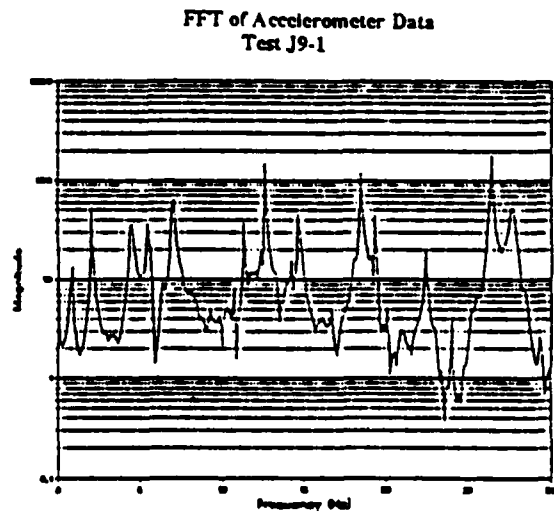
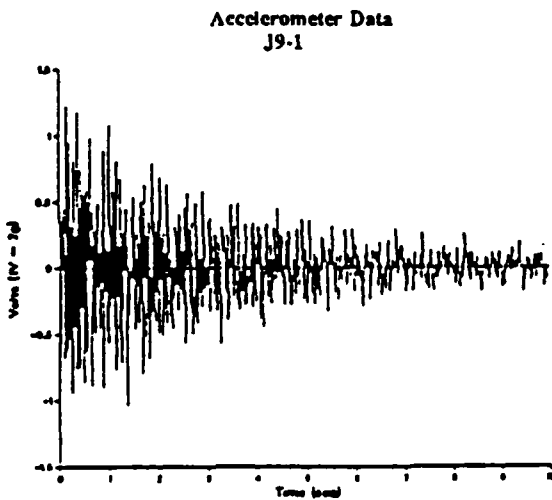
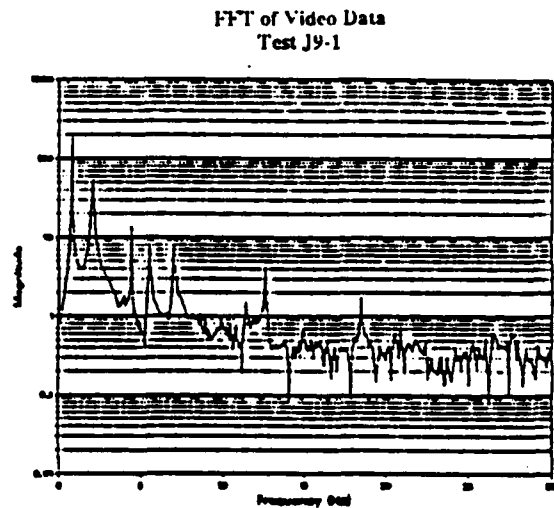
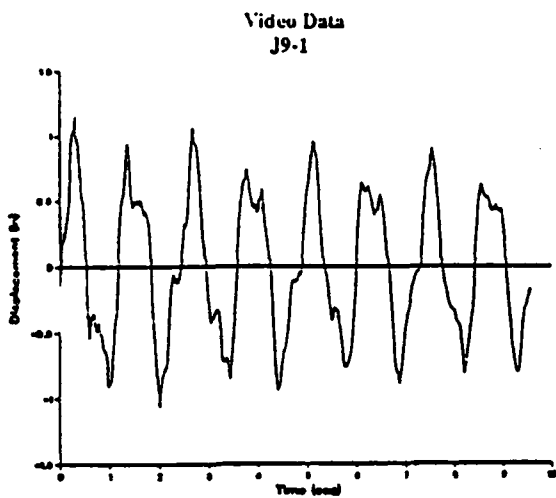


Figure 4. Comparison of Video-Derived Position Measurements with Accelerometer Measurements



# Basic System Realization Concepts

Linear Autonomous System

$$\dot{x} = Ax + Bu$$

$$y = Cx$$

Time Response

$$x(t) = e^{At} x(t_0) + \int_{t_0}^t e^{A(t-\tau)} Bu(\tau) d\tau$$

$$y(t) = C e^{At} x(t_0) + \int_{t_0}^t C e^{A(t-\tau)} Bu(\tau) d\tau$$

Laplace Transform

$$x(s) = (sI - A)^{-1} Bu(s)$$

$$y(s) = Cx(s) = C(sI - A)^{-1} Bu(s)$$

$$y(s) = G(s) u(s)$$

Transfer Function

$$G(s) = C(sI - A)^{-1} B$$

Freq. Response Function

$$G(j\omega) = C(j\omega I - A)^{-1} B$$

Notes

The triple  $(A, B, C)$  is not unique.

But  $G(s)$  is unique.

$(A_1, B_1, C_1)$  and  $(A_2, B_2, C_2)$  are said to be equivalent if any of the following statements are true:

- The transfer functions are equal:

$$G_1(s) = G_2(s), \text{ for all } s$$

- The weighting patterns are the same:

$$C_1 e^{A_1 t} B_1 = C_2 e^{A_2 t} B_2$$

- $C_1 A_1^k B_1 = C_2 A_2^k B_2$ , for all  $k$ .

$\Rightarrow$  Any  $(A, B, C)$  which produces the correct transfer function  $G(s) = C(sI - A)^{-1} B$  is said to be a "realization" of the system.

## A Novel Identification Method for Linear Elastic Structures

Equations of Motion:

$$M\ddot{x} + Kx = f$$

Free Vibration Eigensolution:  $[K - \omega_i^2 M]\phi_i = 0 \Rightarrow \{\omega_i^2, \phi_i\}, i = 1, 2, \dots, n$

$$\Phi^T M \Phi = I, \quad \Phi^T K \Phi = \text{diag}(\omega_1^2, \dots, \omega_n^2) \equiv \Lambda, \quad \Phi = [\phi_1, \dots, \phi_n]$$

Frequency Response:  $X(j\omega) = [K - \omega^2 M]^{-1} F(j\omega) \equiv H(j\omega) F(j\omega)$

*spectral decomposition:*

$$H(j\omega) = [K - \omega^2 M]^{-1} \equiv \Phi^T (\Lambda - \omega^2 I)^{-1} \Phi, \quad H_{pq}(j\omega) = \sum_{r=1}^n \frac{\phi_{pr} \phi_{qr}}{\omega_r^2 - \omega^2}$$

Measurements:

*a subset of free vibration modes:  $\{\tilde{\omega}_r, \tilde{\phi}_r\}, r = 1, 2, \dots, m (\leq n)$*

*frequency response elements:  $\tilde{H}_{pq}(j\omega), \text{ for } \omega_{\min} \leq \omega \leq \omega_{\max}$*

### QUALITATIVE PROBLEM STATEMENT:

*Find optimum estimates of  $M, K$  parameterization which is simultaneously consistent with the measured the free vibration eigensolution and the frequency response function.*

## Cremer's Three Step Identification Process

**Step 1:** Identify a subset of the measured frequencies and mode shapes which correlate well with the corresponding modeled frequencies and mode shapes, do a least square correction correction of the stiffness parameterization to improve correlation if necessary.

**Step 2:** Find the normalization of the eigenvectors (mode shapes) which results in the best least square fit for the FRF, i. e., find  $\{a_0, a_1, a_2, \dots, a_{m+1}\}$  to minimize

$$\int_{\omega_{\min}}^{\omega_{\max}} (\tilde{H}_{pq}(j\omega) - H_{pq_{model}}(j\omega))^2 d\omega, \text{ or } \sum_{\omega_{\min}}^{\omega_{\max}} (\tilde{H}_{pq}(j\omega_k) - H_{pq_{model}}(j\omega_k))^2$$

where

$$H_{pq_{model}}(j\omega) = \frac{a_0}{\omega^2} + \sum_{r=1}^m \frac{\tilde{\Phi}_{pr} \tilde{\Phi}_{qr}}{\tilde{\omega}_r^2 - \omega^2} a_r + a_{m+1}$$

**Step 3:** Estimate values for the linear mass and stiffness parameterization to satisfy the orthonormality conditions in a least square sense; this leads to the following pair of linear equations for  $\mu_r$ , and  $\kappa_r$  in  $M = M_0 + \sum_i \mu_i M_i$ ,  $K = K_0 + \sum_i \kappa_i K_i$ :

$$\left\{ \begin{array}{l} 1/a_1 - \overset{T}{\phi}_1 M_0 \bar{\phi}_1 \\ \vdots \\ 1/a_m - \overset{T}{\phi}_m M_0 \bar{\phi}_m \\ - \overset{T}{\phi}_1 M_0 \bar{\phi}_2 \\ \vdots \\ - \overset{T}{\phi}_{m-1} M_0 \bar{\phi}_m \end{array} \right\} =$$

$$\left\{ \begin{array}{l} \mu_1 \\ \mu_2 \\ \vdots \\ \mu_P \end{array} \right\}$$

$$\left[ \begin{array}{cccc} \overset{T}{\phi}_1 M_1 \bar{\phi}_1 & \overset{T}{\phi}_1 M_2 \bar{\phi}_1 & \dots & \overset{T}{\phi}_1 M_P \bar{\phi}_1 \\ \vdots & \vdots & \dots & \vdots \\ \overset{T}{\phi}_m M_1 \bar{\phi}_m & \overset{T}{\phi}_m M_2 \bar{\phi}_m & \dots & \overset{T}{\phi}_m M_P \bar{\phi}_m \\ \overset{T}{\phi}_1 M_1 \bar{\phi}_2 & \overset{T}{\phi}_1 M_2 \bar{\phi}_2 & \dots & \overset{T}{\phi}_1 M_P \bar{\phi}_2 \\ \vdots & \vdots & \dots & \vdots \\ \overset{T}{\phi}_{m-1} M_1 \bar{\phi}_m & \overset{T}{\phi}_{m-1} M_2 \bar{\phi}_m & \dots & \overset{T}{\phi}_{m-1} M_P \bar{\phi}_m \end{array} \right]$$

and

$$\left\{ \begin{array}{l} \omega_1^2/a_1 - \overset{T}{\phi}_1 K_0 \bar{\phi}_1 \\ \vdots \\ \omega_m^2/a_m - \overset{T}{\phi}_m K_0 \bar{\phi}_m \\ - \overset{T}{\phi}_1 K_0 \bar{\phi}_2 \\ \vdots \\ - \overset{T}{\phi}_{m-1} K_0 \bar{\phi}_m \end{array} \right\} =$$

$$\left\{ \begin{array}{l} \kappa_1 \\ \kappa_2 \\ \vdots \\ \kappa_Q \end{array} \right\}$$

$$\left[ \begin{array}{cccc} \overset{T}{\phi}_1 K_1 \bar{\phi}_1 & \overset{T}{\phi}_1 K_2 \bar{\phi}_1 & \dots & \overset{T}{\phi}_1 K_Q \bar{\phi}_1 \\ \vdots & \vdots & \dots & \vdots \\ \overset{T}{\phi}_m K_1 \bar{\phi}_m & \overset{T}{\phi}_m K_2 \bar{\phi}_m & \dots & \overset{T}{\phi}_m K_Q \bar{\phi}_m \\ \overset{T}{\phi}_1 K_1 \bar{\phi}_2 & \overset{T}{\phi}_1 K_2 \bar{\phi}_2 & \dots & \overset{T}{\phi}_1 K_Q \bar{\phi}_2 \\ \vdots & \vdots & \dots & \vdots \\ \overset{T}{\phi}_{m-1} K_1 \bar{\phi}_m & \overset{T}{\phi}_{m-1} K_2 \bar{\phi}_m & \dots & \overset{T}{\phi}_{m-1} K_Q \bar{\phi}_m \end{array} \right]$$

## STRUCTURAL IDENTIFICATION: A FRONTAL ASSAULT

Consider the case that a force or moment is applied at a point, but the response at many measurement stations are available. For this case  $B$  and therefore  $G(\omega)$  are vectors. Suppose that the frequency response function (vector) is measured over a frequency range  $\{\omega_{\min} < \omega < \omega_{\max}\}$  at the frequencies  $\{\omega_1, \omega_2, \dots, \omega_m\}$ . Use the notation:

$$\bar{G} = \left\{ \begin{array}{c} \bar{G}(\omega_1) \\ \vdots \\ \bar{G}(\omega_m) \end{array} \right\} = \text{measured FRF}, \quad G(p) = \left\{ \begin{array}{c} G(\omega_1, p) \\ \vdots \\ G(\omega_m, p) \end{array} \right\} = \text{computed FRF using model vector } p \quad (8)$$

and

$$\bar{\Omega} = \{\bar{\Omega}_1 \bar{\Omega}_2 \dots\}^T = \text{measured free vibration } \Omega\text{'s}, \quad \Omega(p) = \{\Omega_1 \Omega_2 \dots\}^T = \text{computed } \Omega\text{'s using } p. \quad (9)$$

We seek the optimal estimate of the model parameter vector  $p$  which minimizes

$$J = \frac{1}{2} \int_{\omega_{\min}}^{\omega_{\max}} \Delta G^T(p, \omega) W_G(\omega) \Delta G(p, \omega) d\omega + \frac{1}{2} \Delta \Omega^T W_\Omega \Delta \Omega, \quad \Delta G(p, \omega) \equiv G(\omega) - G(\omega, p), \quad \Delta \Omega \equiv \bar{\Omega} - \Omega(p) \quad (10)$$

For FRF measurements available at discrete frequencies, the integral can be replaced by a discrete summation; we seek to minimize a weighted sum square of the residuals between all measured and modeled FRF's and  $\Omega$ 's:

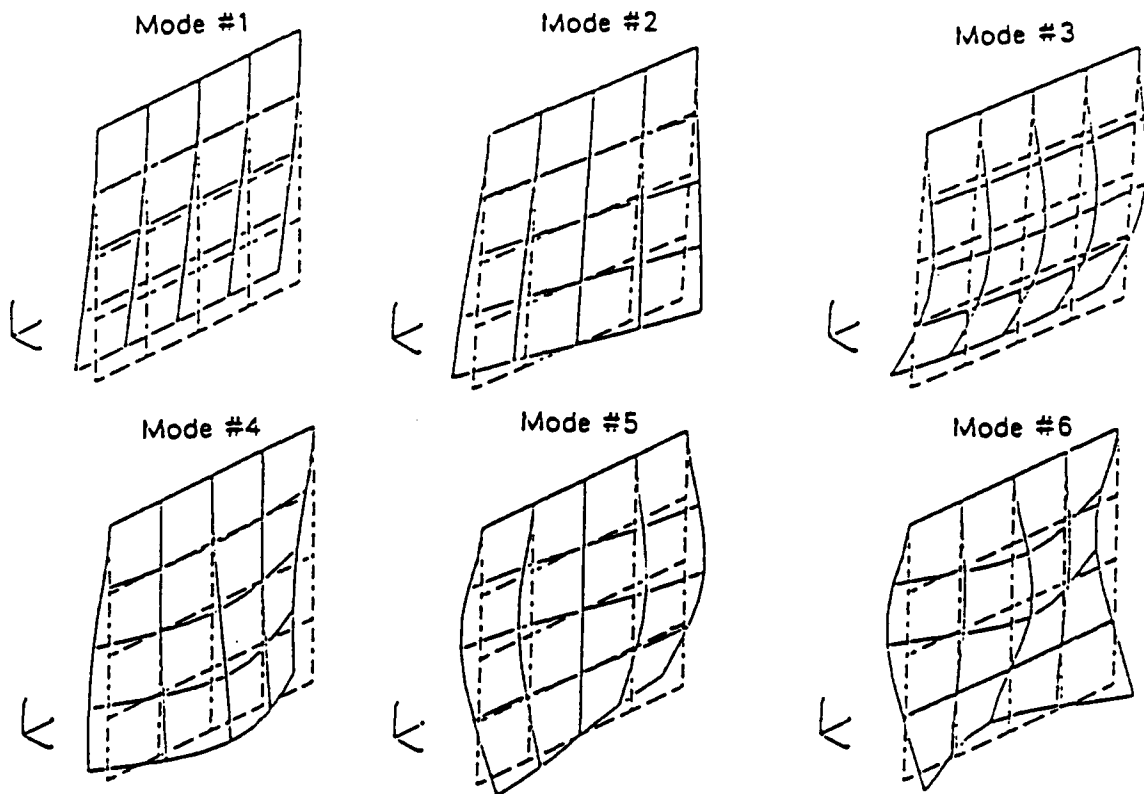
$$\Delta G \equiv \left\{ \begin{array}{c} \hat{G}(\omega_1) - G(\omega_1, p) \\ \vdots \\ \hat{G}(\omega_m) - G(\omega_m, p) \end{array} \right\} = \text{FRF residuals}, \quad \Delta \Omega \equiv \left\{ \begin{array}{c} \bar{\Omega}_1 - \Omega_1(p) \\ \bar{\Omega}_2 - \Omega_2(p) \\ \vdots \end{array} \right\} = \text{free vib. frequency residuals} \quad (11)$$

and we are led to the least squares differential correction algorithm:

$$\left\{ \begin{array}{c} \Delta G \\ \Delta \Omega \end{array} \right\} = A \Delta p + \dots \Rightarrow \Delta p = A^\dagger \left\{ \begin{array}{c} \Delta G \\ \Delta \Omega \end{array} \right\}, \quad \text{where } A \equiv \left[ \begin{array}{c} \frac{\partial G}{\partial p} \\ \frac{\partial \Omega}{\partial p} \end{array} \right], \quad \text{and } p_{\text{new}} = p_{\text{old}} + \Delta p \quad (12)$$

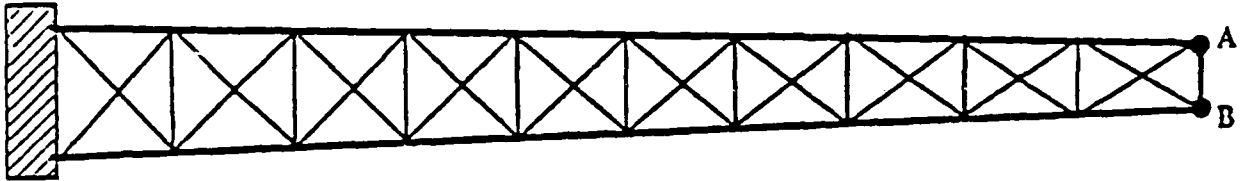
*Potential trouble in toyland!! This approach works great, but only if: (i) the model is "good" & (ii)  $p_{\text{start}}$  is "close" to  $p$ .*

Figure 4. Modeled, Measured, and Identified Natural Frequencies of the Frame Structure



Mode No.	Modeled Value	Measured Value	Identified Value
1	.90 Hz	.92 Hz	.91 Hz
2	2.34	2.32	2.32
3	4.85	4.93	4.93
4	6.05	6.38	6.38
5	7.78	7.27	7.26

## IDENTIFICATION OF A DAMPED TRUSS STRUCTURE



Measurements: 8 open-loop eigenvalues  
 8 closed-loop eigenvalues  
 Longitudinal FRF between A and B  
 Transverse FRF between A and B

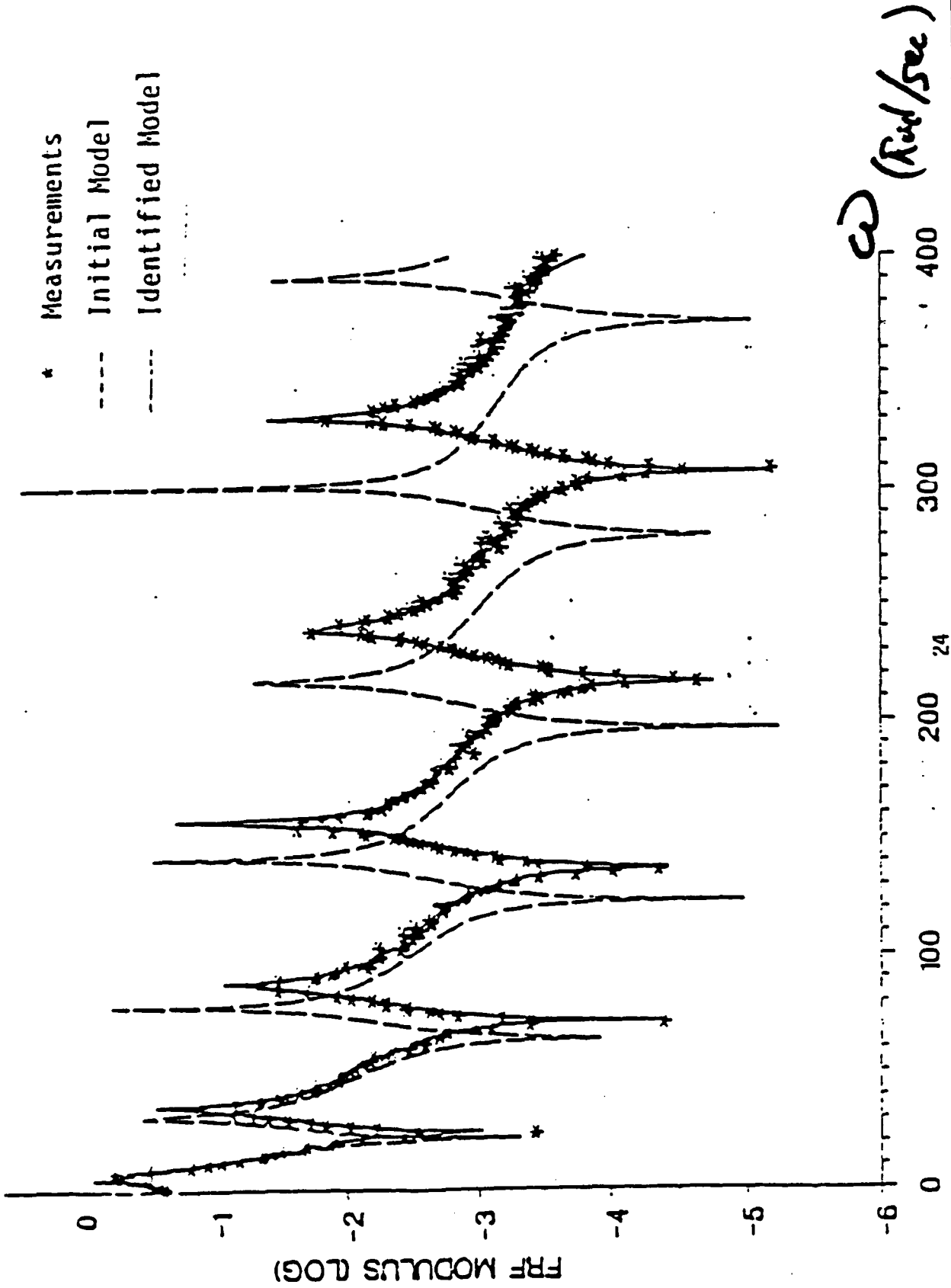
23

### EIGENVALUES

measured                  apriori                  identified model

MODE	$\bar{\lambda}$	$\lambda_0$	$\lambda_f$
1	-0.0872 + 6.73i	6.11i	-0.0872 + 6.93i
2	-0.0890 + 34.59i	31.45i	-0.0888 + 35.46i
3	-0.0891 + 87.58i	78.89i	-0.0898 + 88.29i
4	-0.1042 + 117.11i	106.67i	-0.1039 + 119.39i
5	-0.0907 + 156.49i	142.12i	-0.0906 + 157.86i
6	-0.0914 + 240.33i	217.54i	-0.0915 + 240.05i
7	-0.0929 + 332.09i	302.00i	-0.0925 + 331.39i
8	-0.1039 + 359.29i	325.25i	-0.1042 + 363.28i

*Frequency Response Function: Measured vs Initial Model vs Identified Model*

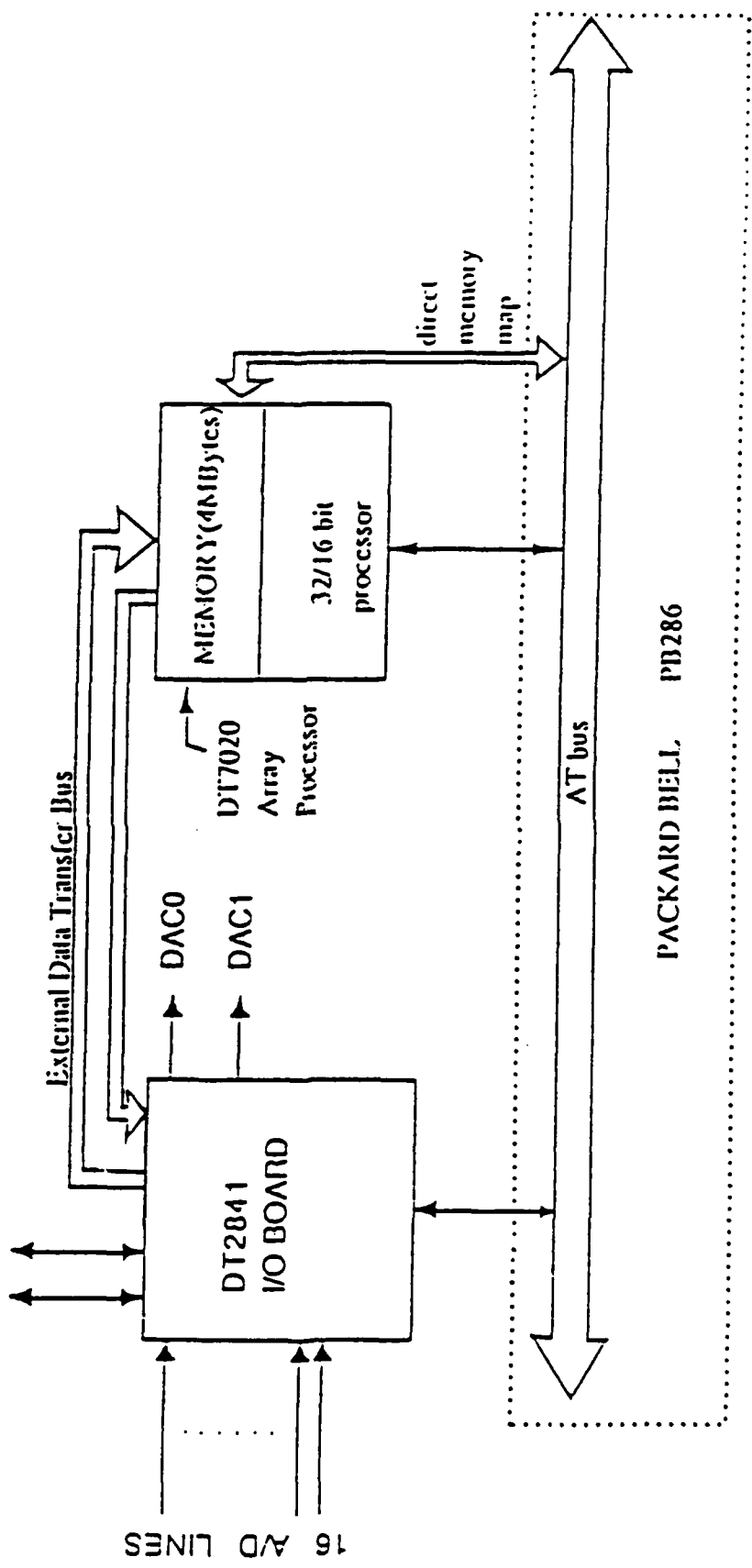


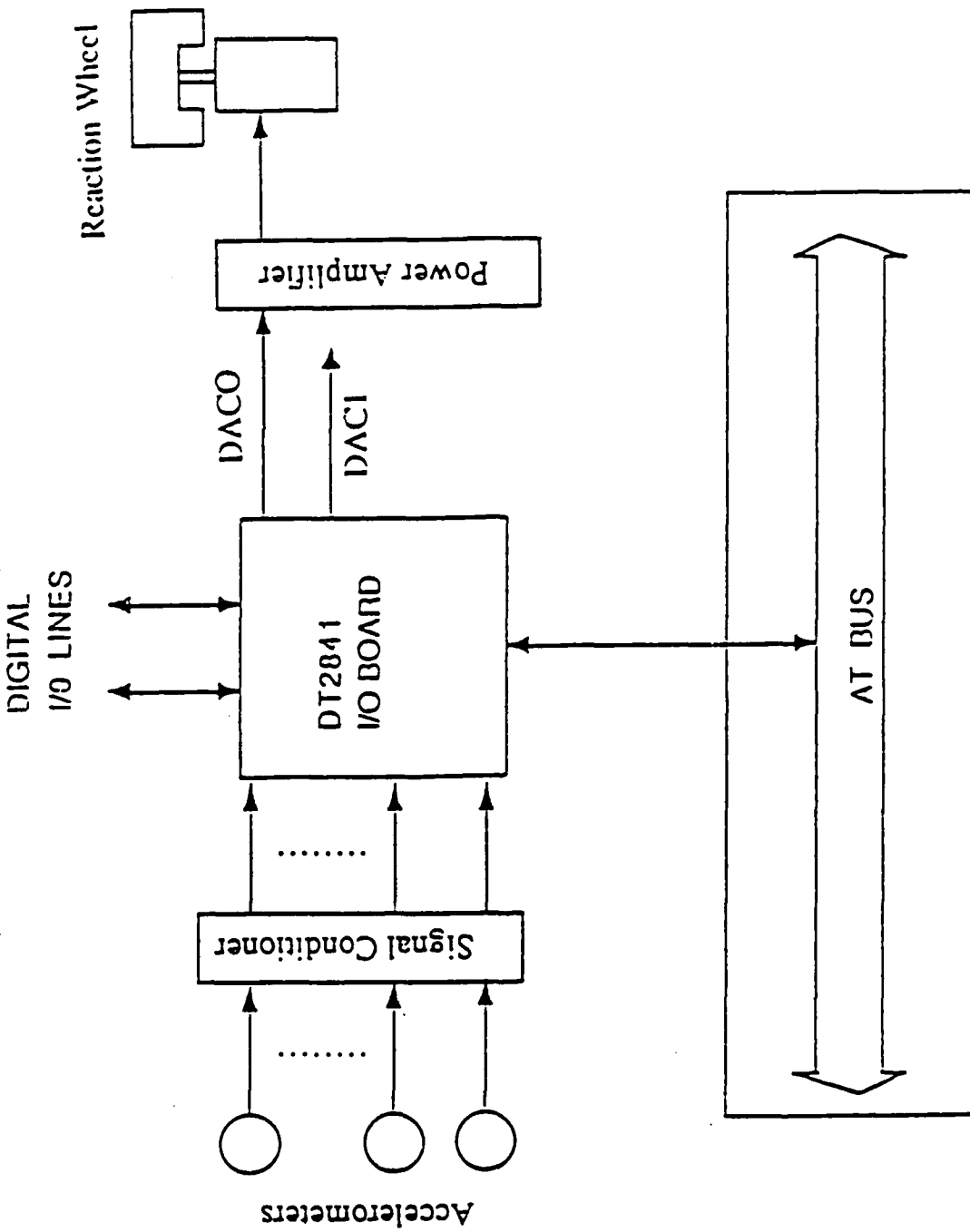
*Data Acquisition Systems  
and Control Computer Configuration*

B.

DIGITAL I/O LINES

16 AD LINES





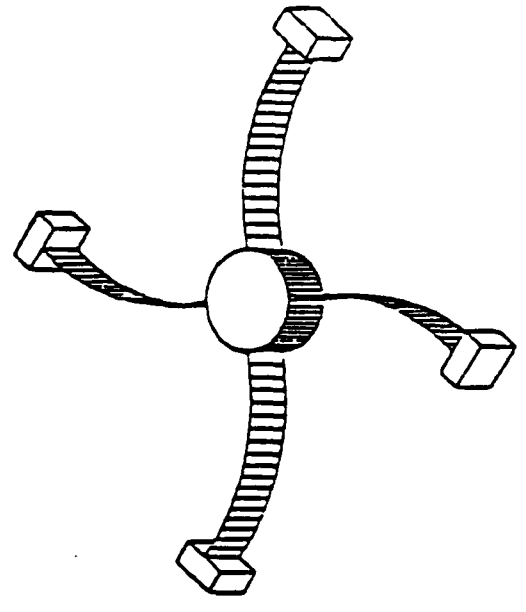
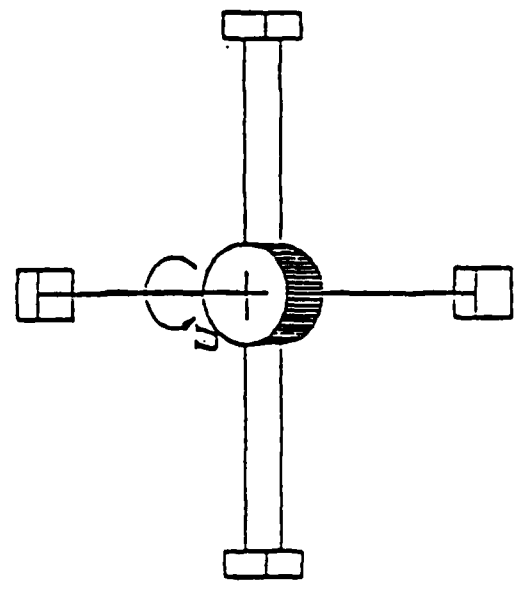
PACKARD BELL PB286

Λ.

- Data transfer rate between DT2841 and DT7020 is 250 KHz (without the use of AT bus).
- DT 2841-G-165E I/O Board
  - i) 16 A/D channels: conversion rate up to 250 KHz (12 bit accuracy)
  - ii) 2 DAC channels: conversion rate up to 260 KHz (12 bit accuracy)
  - iii) 2 8 bit digital I/O lines
- DT7020 Array Processor
  - i) 32 bit floating point processor
  - ii) 8 million operations/sec (addition, subtraction, multiplication)
  - iii) 2K x 64 bit program memory
  - iv) 4 Mb data memory
  - v) No AT bus loading while receiving/transmitting from/to DT2841 or processing on board.
  - vi) Supports up to 10 MHz data transfer rate

# APPENDAGE/HUB STRUCTURE DEVELOPMENT

The appendage/hub structure was designed, fabricated and assembled so as to produce a structure that is symmetric with respect to physical and geometric parameters and that is also subject to a minimal dynamic asymmetry. Phasing problems that exist between appendages are apparent only after free vibrations are allowed to continue for several minutes. This permits free and forced vibration data to be recorded for a structure that exhibits an initial dynamic symmetry.



PRIMARY SENSORS

TORQUE SENSOR

Sensor Developments  
custom unit with  
signal conditioner

STRAIN GAGES

Micromasurements Div.  
Measurements Group  
Std. metal film

ANGLE ENCODER

Teledyne Gurley 8708  
36000 counts / rev  
C-TEK counter  
mod. LIN-101-5021418E

SECONDARY SENSORS

TACHOMETER

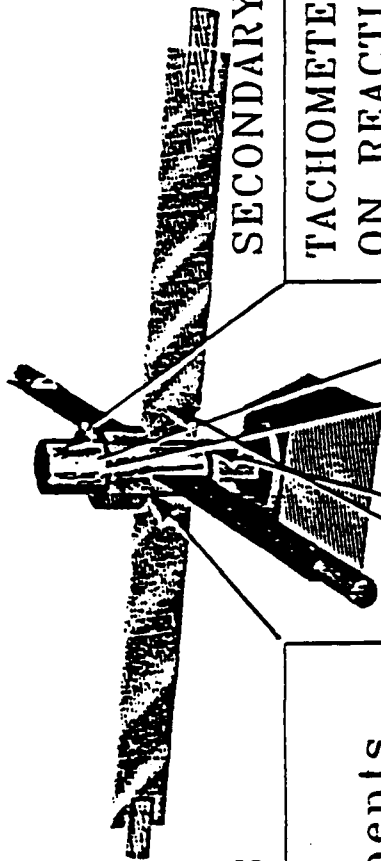
ON REACTION WHEEL  
PMI Motion Technologies

MOTOR CURRENT MONITOR

hard wired to  
A/D board

MOTOR VOLTAGE MONITOR

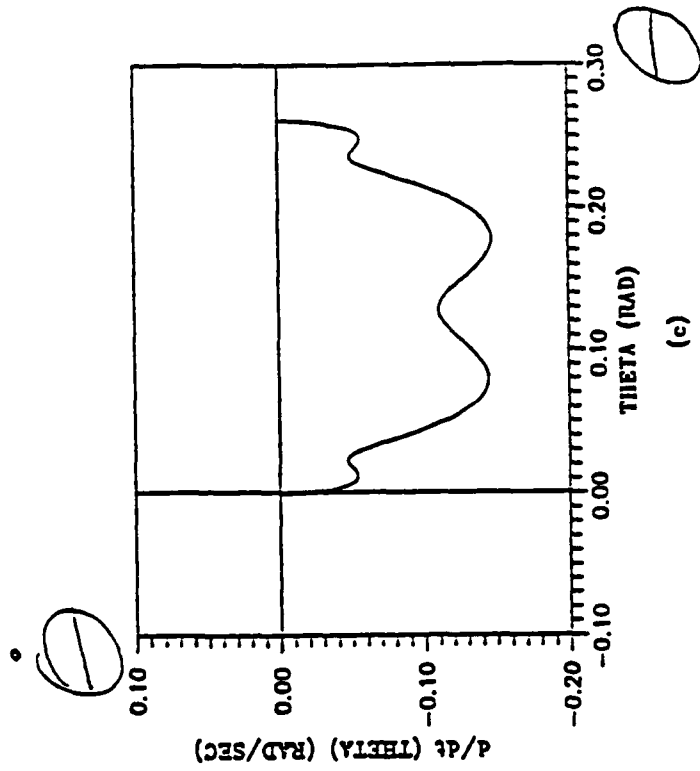
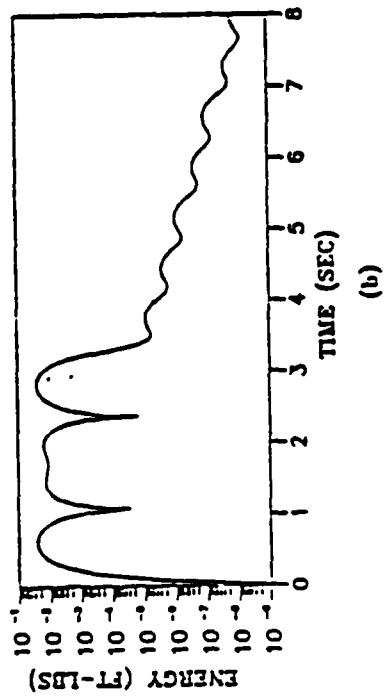
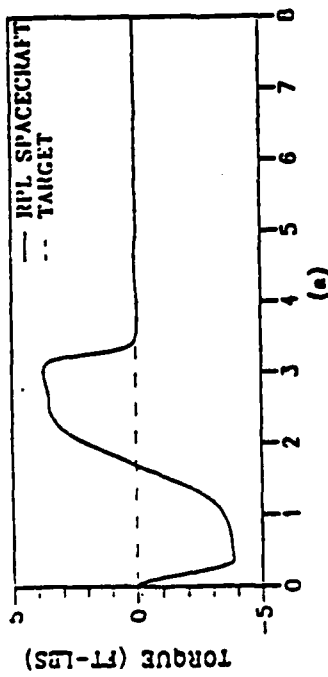
hard wired to  
A/D board



# Texas A&M Maneuverable Space Structure Experiment

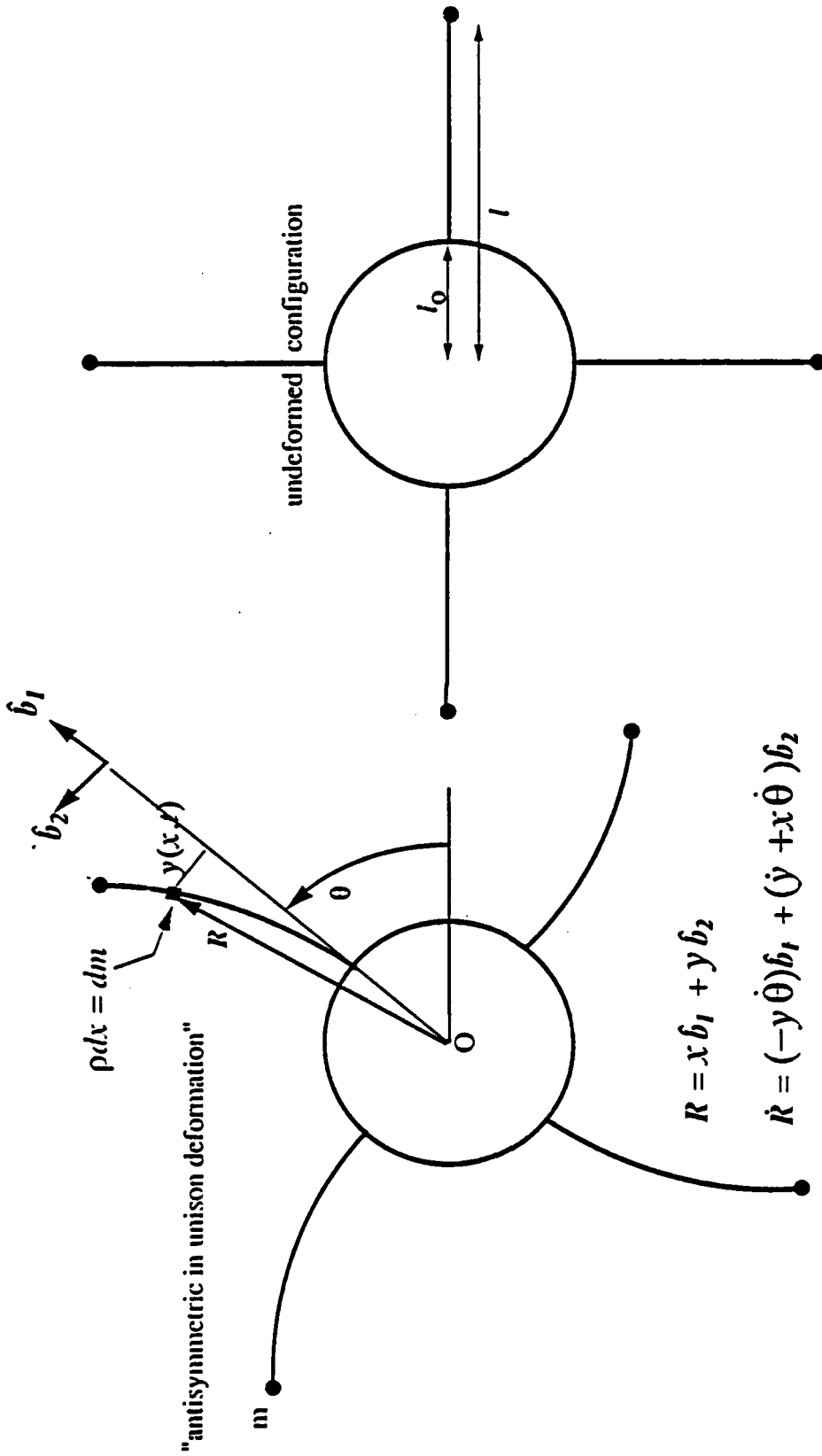
15° Rest-to-Rest Maneuver

$$T_1 = .35 \text{ sec}, \alpha = .93, \beta = .97, \psi = \varphi = 0$$



(a) control profile, (b) flexible mode energy,  
(c) state space trajectory

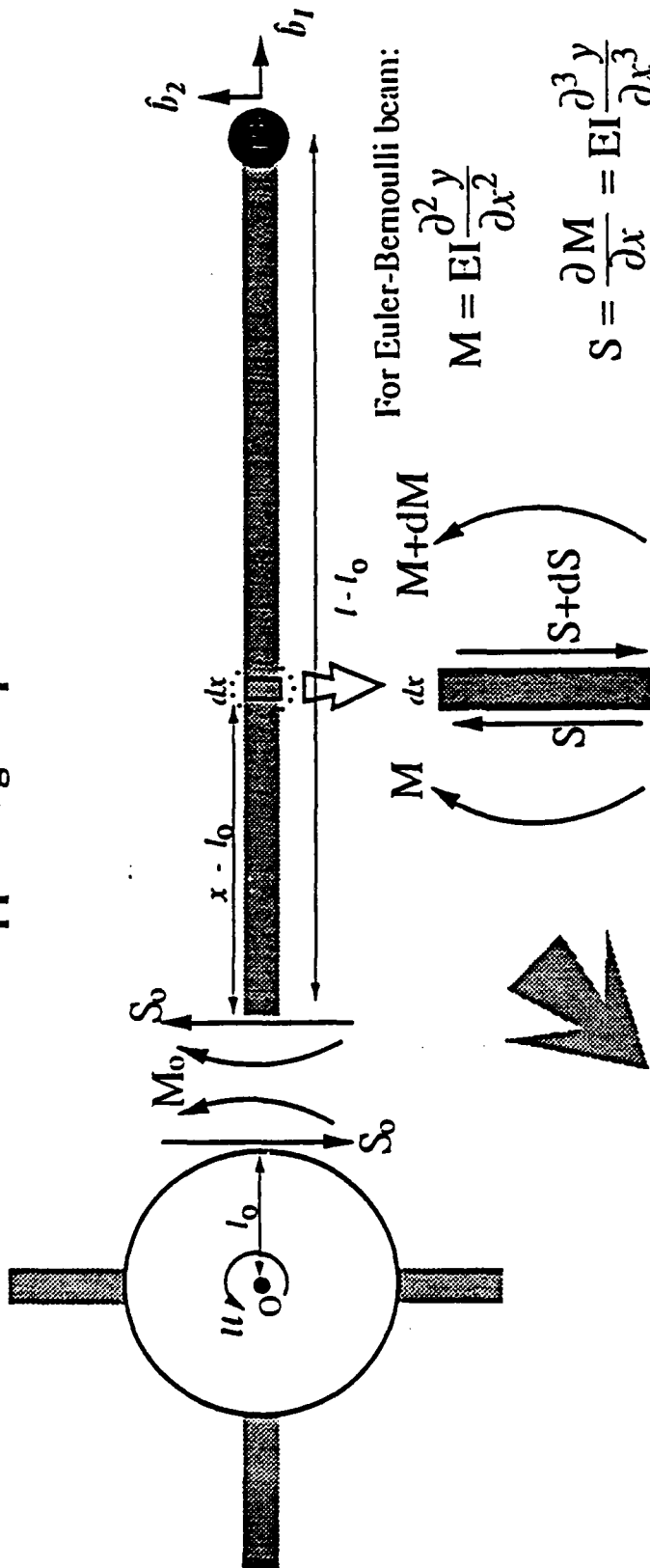
# TAMU Hub/Appendage Formulation of Equations of Motion



$$L = T - V = T_{hub} + T_{beam} + T_{tip} - V_{beam} = \frac{1}{2} I_{hub} \dot{\theta}^2 + 4 \left[ \frac{1}{2} \int_{l_0}^l \dot{R} \cdot \dot{R} \rho dx + \frac{1}{2} m \dot{R}_{tip} \cdot \dot{R}_{tip} - \frac{1}{2} \int_{l_0}^l EI \left( \frac{\partial^2 y}{\partial x^2} \right)^2 \rho dx \right]$$

Apply the Extended Hamilton's Principle:  $\int_{t_1}^{t_2} (\delta L + \delta W) dt + BCs \Rightarrow PDE \text{ equations of motion} \Rightarrow$

# TAMU Hub/Appendage Equations of Motion



Equations of motion:

$$I_{hub} \frac{d^2 \theta}{dt^2} = u + 4(M_0 - S_0 l_0) + H_0 T$$

$$-(M_0 - S_0 l_0) = \int_{l_0}^l \rho x \left( \frac{\partial^2 y}{\partial t^2} + x \frac{d^2 \theta}{dt^2} \right) dx + ml \left( l \frac{d^2 \theta}{dt^2} + \frac{d^2 y}{dt^2} \Big|_l \right) + H_0 T$$

$$\rho \left( \frac{\partial^2 y}{\partial t^2} + x \frac{d^2 \theta}{dt^2} \right) + EI \frac{\partial^4 y}{\partial x^4} = 0 + H_0 T$$

Boundary conditions:

at  $x = l_0$ :  $y = \frac{\partial y}{\partial x} = 0$

at  $x = l$ :

(moment)  $\frac{\partial^2 y}{\partial x^2} = 0$

(shear)  $\frac{\partial^3 y}{\partial x^3} = \frac{m}{EI} \left( l \frac{d^2 \theta}{dt^2} + \frac{d^2 y}{dt^2} \Big|_l \right)$

## In Search of a Judicious Liapunov Function & a Stabilizing Control Law ...

Motivated by the total system energy

$$2E = 2(T+V) = I_{hub} \left(\frac{d\theta}{dt}\right)^2 + 4 \int_{l_0}^l \left[ \rho \left(\frac{\partial y}{\partial t} + x \frac{d\theta}{dt}\right)^2 dx + \int_{l_0}^l EI \left(\frac{\partial^2 y}{\partial x^2}\right)^2 dx + m \left(l \frac{d\theta}{dt} + \frac{dy}{dt} \Big|_l\right)^2 \right]$$

and the recent work of Fujii, we "investigate the wisdom" of the candidate Liapunov fct.:

$$2U = a_1 I_{hub} \dot{\theta}^2 + a_2 (\theta - \theta_0)^2 + 4a_3 \left[ \int_{l_0}^l \rho \left(\frac{\partial y}{\partial t} + x \dot{\theta}\right)^2 dx + \int_{l_0}^l EI \left(\frac{\partial^2 y}{\partial x^2}\right)^2 dx + m \left(l \dot{\theta} + \frac{dy}{dt} \Big|_l\right)^2 \right] \quad (4)$$

It is obvious by inspection that choosing  $a_i > 0$  guarantees that  $U > 0$ , and that  $U=0$  is the desired state. Differentiation, substitution of the Eqs of motion & some calculus lead to

$$\dot{U} = \frac{dU}{dt} = \dot{\theta} \left[ a_1 u + a_2 (\theta - \theta_0) + 4(a_3 - a_1)(l_0 S_0 - M_0) \right] \quad (5)$$

Since we require that  $\dot{U} < 0$  to guarantee stability, we choose the control torque  $u$  as

$$u = - \frac{1}{a_1} \left[ a_2 (\theta - \theta_0) + a_4 \dot{\theta} + 4(a_3 - a_1)(l_0 S_0 - M_0) \right]$$

or, we see that the following *linear, discrete* feedback law globally stabilizes this system:

$$u = - \left[ g_1 (\theta - \theta_0) + g_2 \dot{\theta} + g_3 (l_0 S_0 - M_0) \right], \quad g_i \geq 0 \text{ for stability} \quad (6)$$

## Discussion

The control law:  $u = - [g_1 (\theta - \theta_0) + g_2 \dot{\theta} + g_3 (I_0 S_0 - M_0)]$ ,  $g_i \geq 0$  for stability (6)

is very attractive because it is linear and controls the distributed system without requiring distributed sensing. This law has been experimentally demonstrated by Fujii and in our work at Texas A&M.

It is of significance that this law maintains its globally stabilizing character even when the above Euler/Bernoulli formulation is generalized to include the following *nonlinear* effects:

rotational stiffening and coriolis effects (kinematic/inertial nonlinearities)  
aerodynamic damping/drag

as well as a more general accounting for the following linear effects:

modifications of the formulation to include shear deformation and rotary inertia  
finite inertia of the tip mass.

*In short, closed-loop stability using this law is very forgiving of modeling assumptions!*

## Control Law Design for Flexible Body Maneuvers Using Lyapunov's Second Method

Consider the candidate error energy function

$$\begin{aligned}
 2U = & a_1 I_{hub} (\dot{\theta} - \dot{\theta}_r)^2 + a_2 (\theta - \theta_r)^2 \\
 & + 4a_3 \left[ \int_{l_0}^l \rho \left[ \left( \frac{\partial y}{\partial t} - \frac{\partial y_r}{\partial t} \right) + x(\dot{\theta} - \dot{\theta}_r) \right]^2 dx \right. \\
 & \left. + \int_{l_0}^l EI \left( \frac{\partial^2 y}{\partial x^2} - \frac{\partial^2 y_r}{\partial x^2} \right)^2 dx + m \left[ l(\dot{\theta} - \dot{\theta}_r) + \left( \frac{\partial y}{\partial t} \Big|_l - \frac{\partial y_r}{\partial t} \Big|_l \right) \right]^2 \right]
 \end{aligned} \tag{18}$$

We have investigated the time derivative of  $U$  of Eq. (18) and found that it is given exactly by the following equation

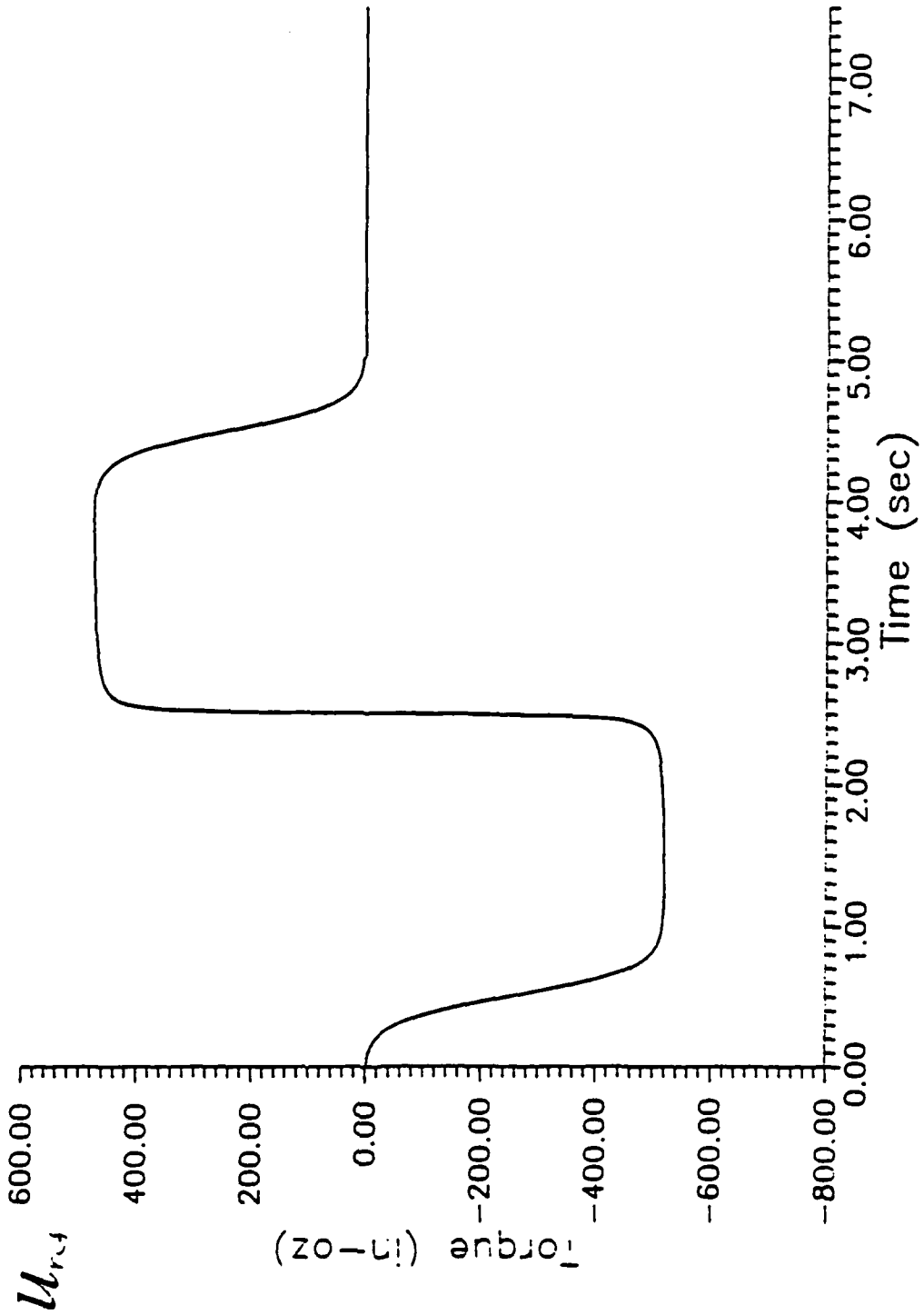
$$\dot{U} = -a_1 (\dot{\theta} - \dot{\theta}_r) \left[ u - u_{ref} + \frac{a_2}{a_1} (\theta - \theta_r) + 4 \frac{a_3 - a_1}{a_1} [(l_0 S_0 - M_0) - (l_0 S_0 - M_0)_r] \right] \tag{19}$$

We see that setting the bracketed term to a positive quantity ( $g_2$ ) times  $(\dot{\theta} - \dot{\theta}_r)$  makes  $\dot{U}$  negative definite. This condition gives the control law

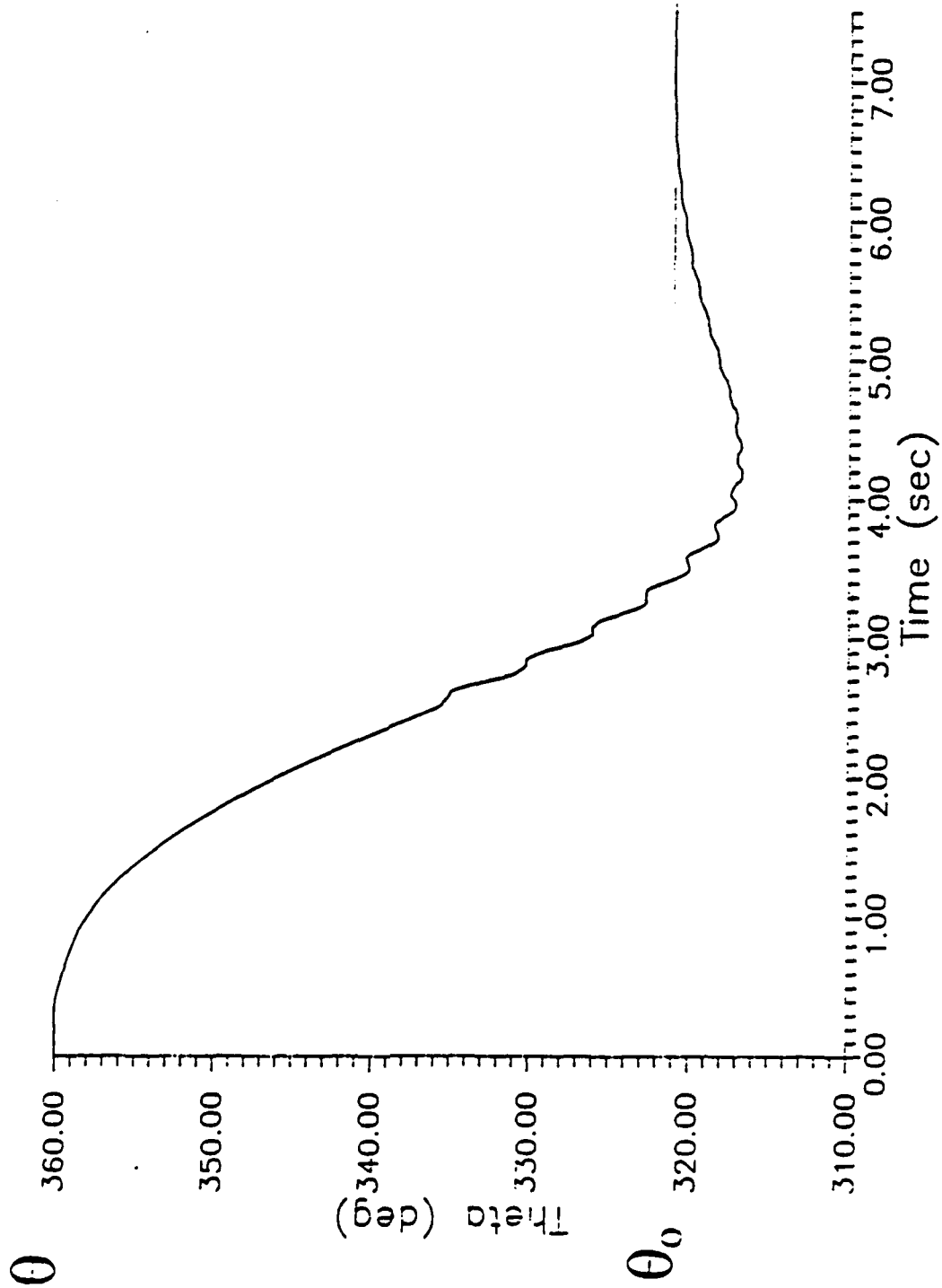
$$u = u_{ref}(t) - [g_1 (\theta - \theta_r) + g_2 (\dot{\theta} - \dot{\theta}_r) + g_3 ((l_0 S_0 - M_0) - (l_0 S_0 - M_0)_r)] \tag{20}$$

with  $\dot{U} = -a_1 g_2 (\dot{\theta} - \dot{\theta}_r)^2$  and we introduced  $g_1 = \frac{a_2}{a_1}$ ,  $g_3 = \frac{a_3 - a_1}{a_1}$ .

# A Large Angle Maneuver of the TAMU Flexible Structure (Test Run No. 3 of 01/25/89)



# A Large Angle Maneuver of the TAMU Flexible Structure (Test Run No. 3 of 01/25/89)



## CONCLUDING REMARKS

■ A Stereo Triangulation Approach has been developed for measuring vibratory structural deformation.

*Motion of many points measured simultaneously  
Easy to calibrate (two cameras, no moving parts)  
> 20 passive targets have been tracked @ 200HZ  
Analog and digital processing is semi-automated*

■ *The Structural Identification Approach of Jenkins and Creamer has been applied to obtain an updated model which matches experimental natural frequencies, mode shapes and freq. response.*

■ *The feasibility of the central ideas has been established, main shortcoming is the moderate spatial resolution (about 1 part in 900) of the optical system and edge detection methodology used.*

■ *Enhancement of the hardware and the image processing concepts promises an order of magnitude of resolution improvement*

## **Concluding Remarks**

- **Novel Vibration Sensing and System Identification Methods have been Developed and Demonstrated**
- **Minimum Sensitivity Output Feedback Controller Design Methodology Developed and Demonstrated**
- **Large Angle Maneuver Feedback Control Approaches have been Developed and Tested**

**ATTACHMENT 12**

**Feedback Control of Tethered Satellites Using  
Liapunov Stability Theory**

*S. R. Vadali  
E. S. Kim*

Texas A&M University  
Dept. of Aerospace Engineering  
College Station, Texas 77843

*AIAA Paper No. 90-1197*

**FEEDBACK CONTROL OF TETHERED SATELLITES USING  
LIAPUNOV STABILITY THEORY**

S. R. Vadali\* and E-S. Kim\*\*  
Texas A&M University  
College Station, Texas

**Abstract**

This paper treats the three dimensional aspects of tethered satellite deployment and retrieval. Feedback control laws with guaranteed closed loop stabilizability are obtained using the second method of Liapunov. Tether mass and aerodynamic effects are not included in the design of the control laws. First, a coordinate transformation is presented that partially uncouples the in-plane and out-of-plane dynamics. A combination of tension control as well as out-of-plane thrusting is shown to be adequate for a speedy retrieval. Next, a unified control design method based on an integral of motion (for the coupled system) is presented. It is shown that the controller designed by the latter method is superior to that of the former primarily from the out-of-plane thrust usage point of view. A detailed analysis of stability of the closed loop system is presented and existence of limit cycles is ruled out if out-of-plane thrusting is used in conjunction with tension control. Finally a tether rate control law is also developed using the integral of motion mentioned above. The control laws developed in the paper can also be used for stationkeeping.

\* Assistant Professor, Aerospace Engineering, Member AIAA.

\*\* Graduate Student.

## Introduction

Currently many space missions involving tethers are being planned. One of these is the Tether Dynamics Explorer (TDE-1) mission scheduled for July 1991. TDE-1 will deploy a 22.7 kg, rectangular subsatellite attached to the spent second stage of a Delta-II using a 20 km tether<sup>1</sup>. The main aim of this mission is to validate tether deployment performance of various control laws proposed to date. The TSS-1 (Tethered Satellite System) mission is also being planned for 1991 for conducting electrodynamic research. Space tethers can also be utilized for study of the lower atmosphere, micro and variable "g" experiments, space construction, and gravity gradient stabilization.

One of the primary issues in tether utilization is fast deployment/retrieval of attached payloads. Rupp<sup>2</sup> provided the impetus for the study of tether dynamics and control law development and since then a vast body of literature has come to exist. An excellent survey of the literature has been conducted by Misra and Modi<sup>3</sup>. Rupp's control law was originally designed for in-plane deployment and utilized a feedforward tether length command as well as linear feedback of length and length rate. Later studies have proposed control laws for deployment and retrieval involving additional linear/nonlinear feedback of in-plane pitch angle and its rate, the out-of-plane roll angle and its rate, and tether extensional as well as flexural modes<sup>4,6</sup>. Liangdong and Bainum<sup>6</sup> also investigate the effect of tether mass and flexibility and the gains of the tension control law on the (in-plane) stability of stationkeeping. They show that the stability conditions involving the length and rate gains for a flexible tether are qualitatively similar to those for a rigid tether.

It has been concluded that deployment can be controlled with relative ease but retrieval is more difficult to control as large amplitude in-plane as well as out-of-plane tether librations are excited and sufficient tension can not be maintained during terminal retrieval phases. Thruster augmentation has been suggested to overcome these difficulties by Banerjee and Kane<sup>7</sup>. Retrieval utilizing tether-normal thrusting and based on shuttle orbiter maneuvering and sliding mode control

has been proposed by Pines, von Flotow, and Redding<sup>8</sup>. A mechanism by which the subsatellite crawls on the tether has also been proposed by Kane<sup>9</sup>. A comparison of tension controlled retrieval and retrieval using the crawler mechanism has been conducted by Glickman and Rybak<sup>10</sup> and it is shown that the latter technique has several advantages including low levels of libration amplitudes and fast terminal retrieval rates. The disadvantage of this method is that if the tether is not retrieved, it may have to be jettisoned. This will add to the already serious space debris problem.

Even if characteristics such as tether flexibility and atmospheric effects are neglected, the equations of motion are highly nonlinear, nonautonomous, and coupled. A Liapunov (mission function) approach has been used for tether deployment and retrieval by Fujii and Ishijima<sup>11</sup>. Tether mass and flexibility as well as aerodynamic effects are neglected in this study. The proposed nonlinear tension control law has been designed for controlling deployment and retrieval in the orbital plane. It is based on feedback of tether length, length rate, pitch angle, and pitch rate. A feedforward length command is not needed. An alternate treatment of the same problem by Vadali<sup>12</sup> concludes that under similar assumptions, a linear feedback of tether length and its rate is sufficient to guarantee asymptotic stability of the closed loop system to the desired equilibrium point. Fast retrieval is possible if the pitch angle is not actively controlled to be near its equilibrium value but allowed to deviate sufficiently either in the mid or terminal phases of retrieval.

This paper treats the three dimensional aspects of tethered satellite deployment and retrieval. Feedback control laws with guaranteed closed loop stabilizability are obtained using the second method of Liapunov. Tether mass and aerodynamic effects are not included in the design of the control laws. First, a coordinate transformation is presented that partially uncouples the in-plane and out-of-plane dynamics. A combination of tension control as well as out-of-plane thrusting is shown to be adequate for a speedy retrieval. Next, a unified control design method based on an integral of motion (for the coupled system) is presented. It is shown that the controller designed by the latter method is superior to that of the former primarily from the out-of-plane thrust usage point of view. A detailed analysis of stability of the closed loop system is presented and existence

of limit cycles is ruled out if out-of-plane thrusting is used in conjunction with tension control. Finally a tether rate control law is also developed using the integral of motion mentioned above. The control laws developed in the paper can also be used for stationkeeping.

### The Liapunov Approach

In many instances, one can consider control and stabilization to be equivalent. Global asymptotic stability can be ascertained by using Liapunov's second method<sup>13</sup>. Choosing the right Liapunov function is a difficult task but one can sometimes find suitable positive definite energy or Hamiltonian functions based on the principles of Analytical Dynamics<sup>14</sup>. The beauty of the method is that it is not based on linearization.

The Liapunov approach is briefly outlined next. Let the dynamic system be described by the system of nonlinear ordinary differential equations

$$\dot{\mathbf{x}} = \mathbf{f}(\mathbf{x}, \mathbf{u}, t) \quad (1)$$

where  $\mathbf{x}$  is the state vector,  $\mathbf{u}$  is the control vector, and  $t$  denotes time. The desired final state is assumed to be the origin of the state space. This framework is still valid if a nontrivial equilibrium point is desired, for the origin can be placed there by a suitable coordinate transformation. Let  $V$  be a positive definite function. The time derivative of  $V$  can be written as

$$\dot{V} = \left[ \frac{\partial V}{\partial \mathbf{x}} \right]^T \mathbf{f} + \frac{\partial V}{\partial t} \quad (2)$$

If the above identity can be solved for  $\mathbf{u}$  as a function of  $\mathbf{x}$  and  $t$ , such that  $\dot{V}$  is globally negative definite, a feedback control law is obtained that globally, asymptotically stabilizes the closed loop system. Of course, the nature of the control law depends on the type of  $V$  chosen. If  $\dot{V}$  can only be made negative semidefinite, it must be verified that this  $\dot{V}$  remains zero only at the desired final state.

The earliest work utilizing this method has been presented by Kalman and Bertram<sup>15</sup>. Since then many applications of this method for controlling spacecraft attitude maneuvers can be found in References 16-22. A different approach is followed by Lee and Grantham<sup>23</sup>, in which the directional derivative of  $V$  in the direction of  $f$  is minimized using the method of steepest descent. This procedure has benefits of optimality but it typically involves on-line computation of roots of a polynomial/transcendental equation.

### Equations of Motion

Assuming that the tether remains straight, the equations of motion of the tether and the attached satellite<sup>4</sup> are

$$\begin{aligned} \ddot{l} - l[\dot{\phi}^2 + \cos^2 \phi (\dot{\theta} + \Omega)^2 - \Omega^2 + 3\Omega^2 \cos^2 \phi \cos^2 \theta] &= -T/m \\ \ddot{\theta} + 2\left(\frac{\dot{l}}{l} - \dot{\phi} \tan \phi\right)(\dot{\theta} + \Omega) + 3\Omega^2 \cos \theta \sin \theta &= 0 \\ \ddot{\phi} + 2\frac{\dot{l}}{l}\dot{\phi} + \cos \phi \sin \phi [(\dot{\theta} + \Omega)^2 + 3\Omega^2 \cos^2 \theta] &= F/(ml) \end{aligned} \quad (3)$$

where  $l$  indicates the instantaneous tether length;  $\theta$ , the pitch angle(in-plane);  $\phi$ , the yaw angle(out-of-plane);  $\Omega$ , the orbital rate;  $T$ , the tension;  $F$ , the out-of-plane thrust; and  $m$ , the mass of the subsatellite. These equations can be nondimensionalized by defining the following nondimensional variables:

$$\tau = \Omega t, \quad \lambda = \frac{l}{L}, \quad \hat{T} = \frac{T}{[m\Omega^2 L]}, \quad \text{and} \quad \hat{F} = \frac{F}{[m\Omega^2 L]}$$

where  $L$  is the reference tether length. The nondimensional equations are

$$\begin{aligned}\lambda'' - \lambda[\phi'^2 + \cos^2 \phi(1 + \theta')^2 - 1 + 3 \cos^2 \phi \cos^2 \theta] &= -\hat{T} \\ \theta'' + 2\left(\frac{\lambda'}{\lambda} - \phi' \tan \phi\right)(1 + \theta') + 3 \cos \theta \sin \theta &= 0 \\ \phi'' + 2\frac{\lambda'}{\lambda}\phi' + \cos \phi \sin \phi[(1 + \theta')^2 + 3 \cos^2 \theta] &= \hat{F}/\lambda\end{aligned}\quad (4)$$

where superscript (') indicates the derivative with respect to nondimensional time.  $\hat{T}$  and  $\hat{F}$  are treated as the control variables and methods for designing control laws are discussed in the following sections. A tether rate control law is also developed by treating  $\lambda'$  as the control variable instead of  $\hat{T}$ .

### In-plane Control Law

A control law for in-plane deployment and retrieval is first reviewed for completeness. If  $\phi$  and  $\dot{\phi}$  are assumed to be zero at the initial time and  $\hat{F}$  is zero, only the in-plane equations are needed to describe the motion of the tether. This is also true if the out-of-plane motion is actively controlled. The in-plane equations of the tether are

$$\begin{aligned}\lambda'' - \lambda[(1 + \theta')^2 - 1 + 3 \cos^2 \theta] &= -\hat{T} \\ \theta'' + 2\left(\frac{\lambda'}{\lambda}\right)(1 + \theta') + 3 \cos \theta \sin \theta &= 0\end{aligned}\quad (5)$$

If downward deployment and upward retrieval are considered, the desired final boundary conditions on the pitch angle and its rate are  $\theta = \theta' = 0$ . A simple control law applicable in this situation is based on the following Liapunov function<sup>12</sup>:

$$V = 1/2 [\lambda'^2 + K_1(\lambda - \lambda_f)^2 + (K_2 + \lambda^2)(\theta'^2 + 3 \sin^2 \theta)] \quad (6)$$

where  $\lambda_f > 0$ , is the desired final value of  $\lambda$ .  $K_1$  is a positive constant and  $K_2$  can either be positive or zero. The nature of the Liapunov function is such that the undesirable conditions  $\theta = \pi$  and  $\theta' = 0$  can also be reached. This Liapunov function has some similarity to that used by Fujii and Ishijima<sup>11</sup>.

It is primarily a quadratic function; the quartic terms have been included to obtain mathematical simplifications. The nondimensional tension control law is

$$\hat{T} = 3\lambda + K_1(\lambda - \lambda_f) - 2K_2\theta'(1 + \theta')/\lambda + K_3\lambda' \quad (7)$$

It can be verified that this feedback control law locally asymptotically stabilizes the closed loop system in the neighborhood of the desired final conditions. Care must be exercised in selecting the gains as the tension must remain positive and the undesirable equilibrium point must be avoided. A particularly interesting special case is obtained if  $K_2$  is set to zero. The control law then feeds back the instantaneous tether length and its rate. This is a continuous equivalent of Rupp's control law without the discrete feedforward commands. It is observed that the stability conditions derived by Liangdong and Bainum<sup>6</sup> for Rupp's control law ( $K_1 > 0$ ,  $K_2 = 0$  and  $K_3 > 0$ ) are clearly satisfied by the above control law. A nonzero  $K_2$  is effective in suppressing the pitch deviations but the tether length response slows down considerably. For nondimensional tether lengths below 0.01, better performance is obtained with  $K_2$  set to zero.

### An Integral of Motion

Before proceeding with a choice of a Liapunov function, the existence of integrals of motion should be examined. Such integrals for the linearized in-plane motion have been derived by Rajan and Anderson<sup>24</sup> using Noether's theorem. Integrals of motion of the nonlinear system of equations are of interest here. Consider the differential equations (4) and the following positive definite function:

$$V_1 = 1/2 (\theta'^2 \cos^2 \phi + 3 \sin^2 \theta \cos^2 \phi + \phi'^2 + 4 \sin^2 \phi) \quad (8)$$

It can be shown that if  $\hat{F}$  is assumed to be zero,

$$V_1' = -2 \frac{\lambda'}{\lambda} [\theta'(1 + \theta') \cos^2 \phi + \phi'^2] \quad (9)$$

Thus, if the tether length is held constant then  $V_1$  is an integral of motion. This is an important result as it can be used to determine maximum libration amplitudes analytically and even more, it can be said that if  $\lambda'/\lambda$  is extremely small, the tether librations will closely resemble limit cycles. Figure 1 shows a roll angle versus pitch angle plot for a constant tether length ( $\lambda = 1.0$ ) and initial conditions  $\theta = \phi = 5^\circ$ , and  $\theta' = \phi' = 0$ .

A tether rate control law can easily be developed to damp the pitch and roll librations. The tether rate may be oscillatory depending on the initial conditions. A stationkeeping strategy based on modulating the tether length has been proposed by Davis and Banerjee<sup>25</sup>. It is also seen from Eq. (9) that for the function  $V_1$  to decrease,  $\lambda'$  has to be positive for  $\theta' \geq 1$ . On the other hand, for very small values of  $\phi$  and  $\phi'$  and small negative values of  $\theta'$ ,  $\lambda'$  has to be negative for  $V_1$  to decrease. This suggests that if  $\theta$  is allowed to increase initially in a positive sense and  $\phi$  and  $\phi'$  are small, a unidirectional retrieval is possible without tether oscillations. This further implies that a unidirectional retrieval is possible if out-of-plane thrust is utilized to control roll and roll rate.

Presence of pitch as well as roll motions is considered next. Out-of-plane thrust is utilized to keep roll motion bounded. Tension, rate, and out-of-plane thrust control laws are developed in the following sections using the Liapunov approach.

### **Tension Control Law Design Based on Decoupled Equations of Motion**

The first method is based on a coordinate transformation that nearly uncouples the in-plane and out-of-plane motions. If we define  $z = \lambda \cos \phi$  and  $y = \lambda \sin \phi$ , the differential equations (4) transform to

$$z'' - z[(1 + \theta')^2 - 1 + 3 \cos^2 \theta] = -\frac{\hat{T}}{\lambda} z - \frac{\hat{F}}{\lambda} y$$

$$\theta'' + 2\left(\frac{z'}{z}\right)(1 + \theta') + 3 \cos \theta \sin \theta = 0 \quad (10)$$

$$y'' + y = -\frac{\hat{T}}{\lambda} y + \frac{\hat{F}}{\lambda} z$$

It will be useful to note the following relationships:

$$yy' + zz' = \lambda\lambda' \quad (11)$$

$$zy' - yz' = \lambda^2\phi' \quad (12)$$

The nonhomogeneous part of each of the above equations can be treated as a generalized force. It is interesting to note that the first two of Eqs. (10) are similar to Eqs. (5). The third of Eqs. (10) has the form of a linear oscillator with a forcing function. Thus, the in-plane motion can be controlled by using a modified version of the tension control law given by Eq. (7) and it is a simple matter to control the out-of-plane motion using derivative feedback for the generalized out-of-plane force. Hence the following control laws are chosen:

$$\begin{bmatrix} z & y \\ y & -z \end{bmatrix} \begin{bmatrix} \frac{\hat{T}}{\lambda} \\ \frac{\hat{F}}{\lambda} \end{bmatrix} = \begin{bmatrix} 3z + K_1(z - z_f) - 2K_2\theta'(1 + \theta')/z + K_3z' \\ K_3y' \end{bmatrix} \quad (13)$$

Equation (13) can always be solved for  $\hat{T}$  and  $\hat{F}$  because the determinant of the matrix to be inverted is  $-\lambda^2$ . The control laws can be written in terms of the original variables using Eqs. (11) and (12), as

$$\hat{T} = (3 + K_1)\lambda \cos^2 \phi - K_1\lambda_f \cos \phi - 2K_2\theta'(1 + \theta')/\lambda + K_3\lambda' \quad (14)$$

and

$$\hat{F} = (3 + K_1)\lambda \cos \phi \sin \phi - K_1\lambda_f \sin \phi - 2K_2\theta'(1 + \theta')/\lambda \tan \phi + K_3\lambda\phi' \quad (15)$$

In what follows, retrieval of a tethered satellite is considered. The primary body is the space shuttle assumed to be in a circular orbit at an altitude of 220 km, with an orbital rate of .07068

rad/min. The orbital period is nearly 1.48 hours. The tether is assumed to be 20 km long. The initial conditions for the motion of the tether are  $\lambda = 1.0$ ,  $\lambda' = 0$ ,  $\theta = \phi = 5^\circ$ , and  $\theta' = \phi' = 0$  and the final conditions are  $\lambda = .01$  and  $\lambda' = \theta = \theta' = \phi = \phi' = 0$ . Note that if an exponential feedforward command is used, the initial velocity has to be finite.

Figure 2 shows the variations of tether length, pitch angle, and tension and Fig. 3 shows the roll angle and out-of-plane thrust variations during retrieval for gain settings  $K_1 = 1.0$ ,  $K_2 = 0$ , and  $K_3 = 3$ . The results indicate that the tether length and pitch angle reach their respective final values in nearly *two orbits* but the roll angle response is slower. The reason for this uncoupled behaviour can be explained as a result of the decoupled control design. The pitch angle undergoes a sharp change near the end of the retrieval. The initial nondimensional tension is 4, the equilibrium initial value being 3. In dimensional form, assuming a satellite mass of 22.7 kg, the initial tension is 2.52 N. This value will be higher if tether mass is included. It should be noted that this example depicts a fast retrieval. The initial value of tension can be decreased further for a slower retrieval. Thrust usage has been quantified by evaluating the index  $\int |\hat{F}| d\tau$  over two orbits. This nondimensional index is 0.9 which amounts to an average thrust impulse of 481 N-s.

### Tension Control Law Design Based on the Coupled Equations of Motion

The second method is based on the following candidate Liapunov function:

$$V = 1/2 [\lambda'^2 + K_1(\lambda - \lambda_r)^2 + (K_2 + \lambda^2) (\theta^2 \cos^2 \phi + 3 \sin^2 \theta \cos^2 \phi + \phi^2 + 4 \sin^2 \phi)] \quad (16)$$

A significant part of the above function is the integral of motion obtained previously. Note that this choice of  $V$  automatically admits the possibility of existence of multiple equilibria. They are given by

- 1)  $\lambda = \lambda_r, \lambda' = 0, \text{ and } \theta = \theta' = \phi = \phi' = 0$
- 2)  $\lambda = \lambda_r, \lambda' = 0, \theta = \theta' = 0, \phi = \pi, \text{ and } \phi' = 0$
- 3)  $\lambda = \lambda_r, \lambda' = 0, \theta = \pi, \theta' = 0, \text{ and } \phi = \phi' = 0$

The last two equilibria are one and the same and also undesirable for downward deployment/ upward retrieval. Besides these, other equilibria might exist. This possibility will be investigated subsequently.

The time derivative of  $V$  is given by

$$V' = \lambda' \{3\lambda - \hat{T} + K_1(\lambda - \lambda_r) - 2K_2[\theta'(1 + \theta') \cos^2 \phi + \phi'^2] / \lambda\} + \phi'(k_2 + \lambda^2)\hat{F} / \lambda \quad (17)$$

If we assume that out-of-plane thrust is not utilized, the tension control law can be selected as

$$\hat{T} = 3\lambda + K_1(\lambda - \lambda_r) - 2K_2[\theta'(1 + \theta') \cos^2 \phi + \phi'^2] / \lambda + K_3\lambda' \quad (18)$$

so that

$$V' = -K_3\lambda'^2 \quad (19)$$

Simulations using the above control law reveal that there is a significant interplay between the tether length and swing motion. If  $K_2$  is set to zero, the pitch and roll libration amplitudes become alarmingly high. Even with a positive  $K_2$ , the tether retrieval rate is oscillatory and convergence to the desired equilibrium point is extremely slow.

If out-of-plane thrust is utilized, the tension control law need not be changed. Simple rate feedback thrust control is sufficient to enhance the stability of the closed loop system significantly.

The out-of-plane control law is selected to be

$$\hat{F} = -K_4\lambda\phi' \quad (20)$$

Roll angle feedback can also be included in the out-of-plane thrust control law by adding a quadratic term in  $\phi$  to the Liapunov function. The usage of the tension as well as the out-of-plane control law leads to

$$V' = -K_3\lambda'^2 - (K_2 + \lambda^2)K_4\phi'^2 \quad (21)$$

It is easy to verify the stability of the closed loop system. If  $\lambda'$  and  $\phi'$  are both zero, the closed loop system is given by the following equations:

$$\begin{aligned} -\lambda[\cos^2\phi(1+\theta')^2 - 1 + 3\cos^2\phi\cos^2\theta] &= -3\lambda - K_1(\lambda - \lambda_r) + 2K_2[\theta'(1+\theta')\cos^2\phi]/\lambda \\ \theta''\cos\phi + 3\cos\phi\cos\theta\sin\theta &= 0 \\ \cos\phi\sin\phi((1+\theta')^2 + 3\cos^2\theta) &= 0 \end{aligned} \quad (22)$$

It can be shown that a local equilibrium point is  $\lambda = \lambda_r$  and  $\lambda' = \theta = \theta' = \phi = \phi' = 0$ . Other undesirable equilibria do exist but can be avoided by properly selecting the control gains.

Simulation results using this control law with gains  $K_1 = 1.0$ ,  $K_2 = 0$ ,  $K_3 = 3$ , and  $K_4 = 2.0$  are shown in Figs. 4 and 5. It is observed that the retrieval process is unidirectional and quite similar to the previous example. However, the required out-of-plane thrust is much less and the roll response is faster. The nondimensional thrust impulse index, defined earlier, evaluated over two orbits is 0.24 which is 128.4 N-s. If  $K_4$  is selected as 3 instead in the above example, the thrust impulse index amounts to 0.258.

The desired nondimensional final length of the tether in the above examples has been 0.01. The effect of a smaller desired final length (0.001) on the performance of the control laws is investigated next. The control parameters are  $K_1 = 1.0$ ,  $K_2 = 0$ ,  $K_3 = 3$ , and  $K_4 = 2.0$ . The initial conditions are the same as before. The tether length, pitch angle, and tension are shown in Fig. 6. The pitch angle is too large and an undesirable equilibrium point is reached. A slight change in the gain  $k_1$  from 1.0 to 0.9 produces a nice retrieval as shown in Fig. 7. The maximum value of the pitch angle is  $21.9^\circ$  in Fig. 7 as compared to  $29.3^\circ$  in Fig. 4. An increase in the gain  $K_2$  also serves the same purpose as decreasing  $K_1$ .

## A Tether Rate Control Law

A tether rate control law can easily be developed using the integral of motion given by Eq. (8). Out-of-plane thrust is utilized for this application also. Based on the previous developments, the following candidate Liapunov function is chosen:

$$V = 1/2 [K_1(\lambda - \lambda_f)^2 + K_2 V_1] \quad (23)$$

The rate control law and the out-of-plane thrust law can be obtained following the usual process as

$$\lambda' = -K_1(\lambda - \lambda_f) + K_2[\theta'(1 + \theta') \cos^2 \phi + \phi'^2] / \lambda \quad (24)$$

and

$$\hat{F} = -K_3 \lambda \phi' \quad (25)$$

If  $K_2$  is very small, the retrieval process is nearly exponential. This leads to a nearly constant (slow decay) pitch angle during the terminal phases of retrieval. Figure 8 shows the tether length and pitch and roll angles for  $K_1 = 0.25$ ,  $K_2 = 0.01$ , and  $K_3 = 1.0$ . The initial conditions on the tether motion are the same as before and  $\lambda_f = .01$ . The value of  $K_1$  dictates the initial tether retrieval rate for this example as the initial pitch and roll rates are zero. The above choice of  $K_1$  results in an initial dimensional retrieval rate of 30 m/s which is moderate. The pitch angle behavior for this example is oscillatory unlike that for the previous examples. The slow decay of the pitch angle is also noted.

## Conclusions

Liapunov feedback control design methods have been presented for deployment and retrieval of tethered satellites. The first method is based on partial decoupling of the equations of motion and utilization of a two-dimensional control law developed previously using Liapunov stability theory. The second method uses a Liapunov function based on a first integral of motion of the original set of differential equations. Controllers designed by both the methods work very well but the second controller has the advantage of using lesser out-of-plane thrust. These control laws are

quite simple and utilize tether tension control as well as out-of-plane thrusting. Liapunov stability analysis is used to rule out the possibility of limit cycles. It is recommended that the control gains be chosen such that the pitch angle does not exceed  $\pm 30^\circ$ . This will ensure that undesirable equilibrium points are not reached. The gains in the tension control law should be adjusted according to the desired final tether length. A rate control law derived using the integral of motion is also presented. Finally, it is apparent that controlling the roll librations is essential for retrieval.

Further validation of the effectiveness of these control laws in the presence of tether flexibility and extension and aerodynamic effects is necessary.

#### Acknowledgments

The support of the Texas Advanced Research and Technology Program ( Projects 4193/1987 and 231/1989 ) and AFOSR (Contract No. F49620-87-C-0078) are gratefully acknowledged.

#### References

1. DeLoach, R., Private Communication.
2. Rupp, C.C., "A Tether Tension Control Law for Tethered Satellites Deployment Along the Local Vertical," *NASA TM X-64963*, 1975.
3. Misra, A.K. and Modi, V.J., "A Survey on the Dynamics and Control of Tethered Satellite Systems," *Tethers in Space, Advances in the Astronautical Sciences*, Vol. 62, Published by The American Astronautical Society, 1987, pp. 667-720.
4. Modi, V.J., Chang-Fu, G., Misra, A.K., and Xu, D.M., "On the Control Of The Space Shuttle Based Tethered Systems," *Acta Astronautica*, Vol. 9, June-July 1982, pp. 437-443.
5. Bainum, P.M. and Kumar, V.K., "Optimal Control of the Shuttle-Tethered-Subsatellite System," *Acta Astronautica*, Vol. 7, May 1980, pp. 1333-1348.
6. Liangdong, L. and Bainum, P.M., "Effect of Tether Flexibility on the Tethered Shuttle Subsatellite Stability and Control," *Journal of Guidance, Control, and Dynamics*, Vol. 12, November-December 1989, pp. 866-873.

7. Banerjee, A.K. and Kane, T.R., "Tethered Satellite Retrieval with Thruster Augmented Control," *Journal of Guidance, Control, and Dynamics*, Vol. 7, January-February 1984, pp. 45-50.
8. Pines, D.J., von Flotow, A.H., and Redding, D.C., "Two Non-Linear Control Approaches for Retrieval of a Thrusting Tethered Sub-Satellite," AIAA Paper No. 88-4171-CP, *Proceedings of the AIAA Guidance, Navigation, and Control Conference*, August 15-17, 1988, Minneapolis, Minnesota, pp. 975-983.
9. Kane, T.R., "A New Method for the Retrieval of the Shuttle-Based Tethered Satellite," *The Journal Of Astronautical Sciences*, Vol. 32, No. 3, July-September 1984, pp. 351-354.
10. Glickman, R.E. and Rybak, S.C., "Gravity Gradient Enhancement During Tethered Payload Retrieval," *The Journal Of Astronautical Sciences*, Vol. 35, No. 1, January-March 1987, pp. 57-74.
11. Fujii, H. and Ishijima, S., "Mission Function Control for Deployment and Retrieval of a Subsatellite," *Journal of Guidance, Control, and Dynamics*, Vol. 12, No. 2, March-April 1989, pp. 243-247.
12. Vadali, S.R., "Feedback Tether Deployment and Retrieval," *Journal of Guidance, Control, and Dynamics*, to appear.
13. Vidyasagar, M., *Nonlinear Systems Analysis*, Prentice-Hall, Englewood Cliffs, New Jersey, 1978.
14. Meirovitch, L., *Methods of Analytical Dynamics*, McGraw-Hill, New York, New York, 1970.
15. Kalman, R.E. and Bertram, J.E., "Control System Analysis and Design Via the Second Method of Lyapunov," *Journal of Basic Engineering*, June 1960, pp. 371-400.
16. Mortenson, R.E., "A Globally Stable Linear Attitude Regulator," *International Journal of Control*, Vol. 8, No. 3, 1968, pp. 297-302.
17. Vadali, S.R. and Junkins J.L., "Optimal Open loop and Stable Feedback Control of Rigid Spacecraft Attitude Maneuvers," *The Journal Of Astronautical Sciences*, Vol. 32, No. 2, April-June 1984, pp. 105-122.
18. Wie, B. and Barba, P.M., "Quaternion Feedback for Spacecraft Large Angle Maneuvers," *Journal of Guidance, Control, and Dynamics*, vol. 8, No. 3, May-June 1985, pp. 360-365.
19. Vadali, S.R., "Feedback Control of Flexible Spacecraft Large-Angle Maneuvers Using Liapunov Theory," *Proceedings of the American Control Conference*, Vol. 3, 1984, pp. 1674-1678.
20. Oh, H-S. and Vadali, S.R., "Feedback Control and Steering Laws for Spacecraft Using Single Gimbal Control Moment Gyros," AIAA paper 89-3475, presented at the AIAA Guidance, Navigation, and Control Conference, Boston, to appear in *The Journal Of Astronautical Sciences*.
21. Fujii, H. and Ishijima, S., "Mission Function Control applied to Slew Maneuvers," IAF paper 87-354, presented at the 38th Congress of the IAF, October 1987, Brighton, U.K.

22. Junkins, J.L., Rahman, Z., Bang, H., "Near-Minimum-Time Maneuvers of Flexible Vehicles: A Liapunov Control Law Design Method," *Mechanics and Control of Large Space Structures*, Edited by J.L. Junkins, Published by AIAA, 1990.
23. Lee, B. and Grantham, W.J., "Aeroassisted Orbital Maneuvering Using Lyapunov Optimal Feedback Control," *Journal of Guidance, Control, and Dynamics*, Vol. 12, No. 2, March-April 1989, pp. 237-242.
24. Rajan, M. and Anderson, T.J., "First Integrals of Motion in the Dynamics of Tethered Satellites," *The Journal Of Astronautical Sciences*, Vol. 34, No. 3, July-September, 1986, pp. 331-339.
25. Davis, W.R. and Banerjee, A.K., "Libration Damping of a Tethered Satellite Using Rate Only Control," AIAA Paper No. 88-4172-CP, *Proceedings of the AIAA Guidance, Navigation, and Control Conference*, August 15-17, 1988, Minneapolis, Minnesota, pp. 984-994.

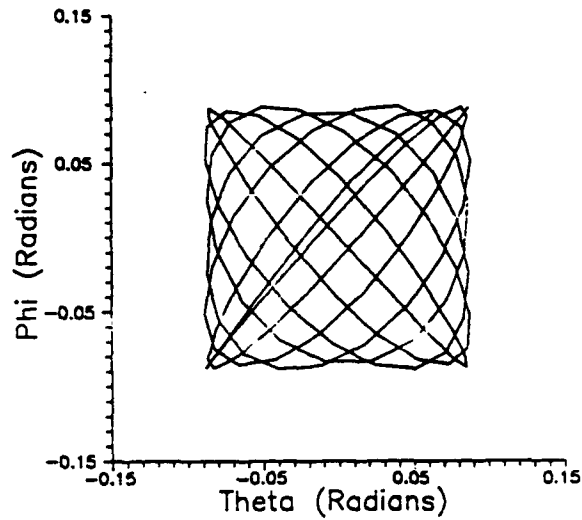


Fig. 1 Pitch-Roll Librations ( Constant Length Tether).

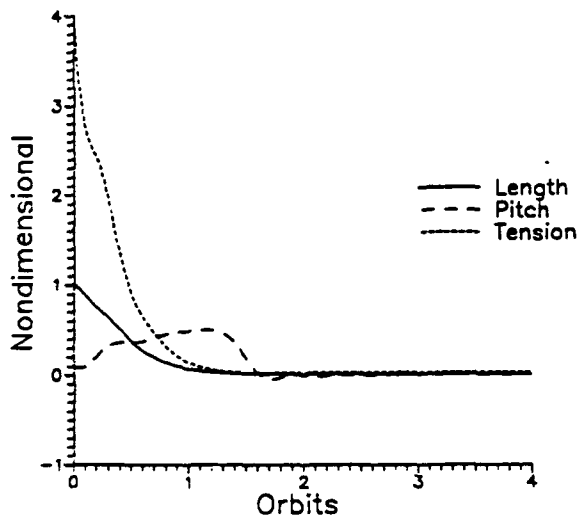


Fig. 2 Retrieval Using Controller-1.

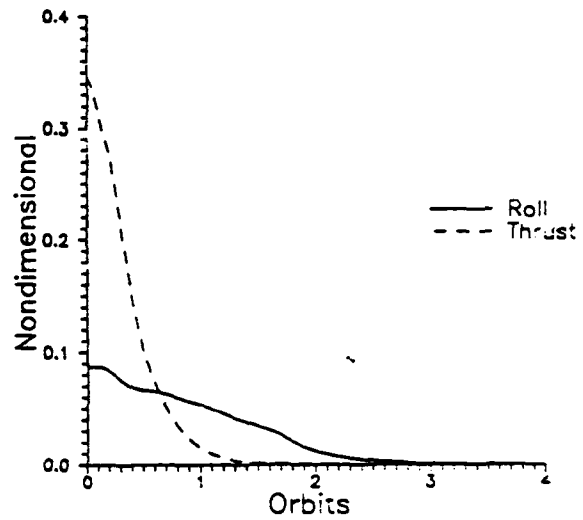


Fig 3. Retrieval Using Controller-1.

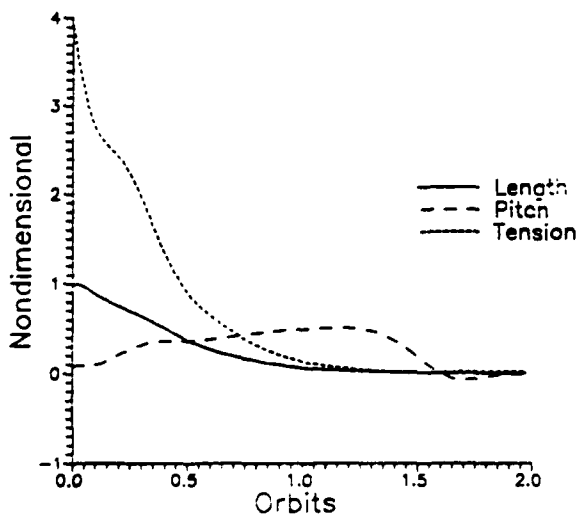


Fig. 4 Retrieval Using Controller-2.

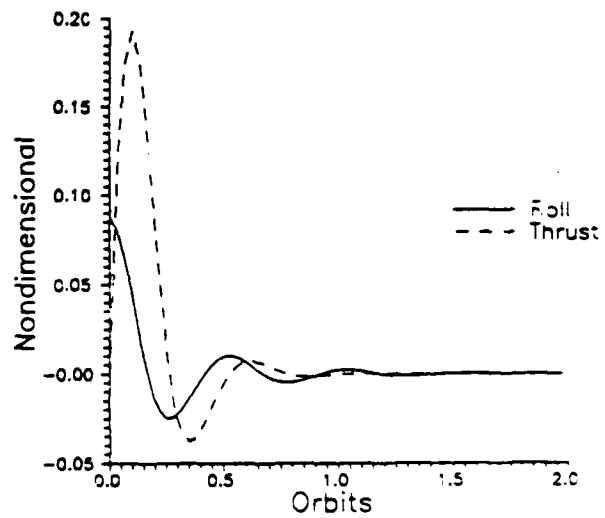


Fig 5. Retrieval Using Controller-2.

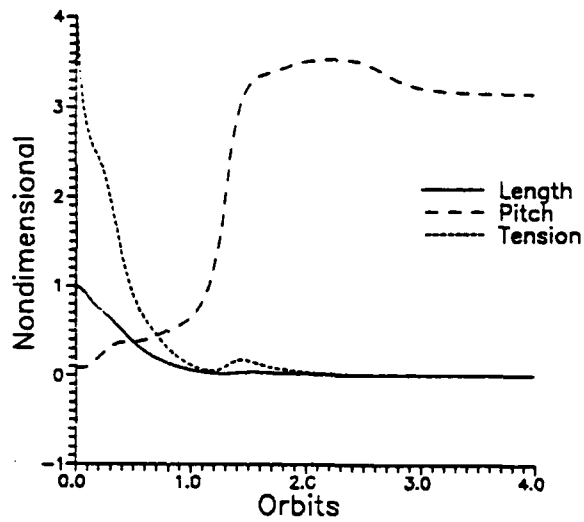


Fig. 6 Undesirable Retrieval Using Controller-2 ( $\lambda_r = .001$ ).

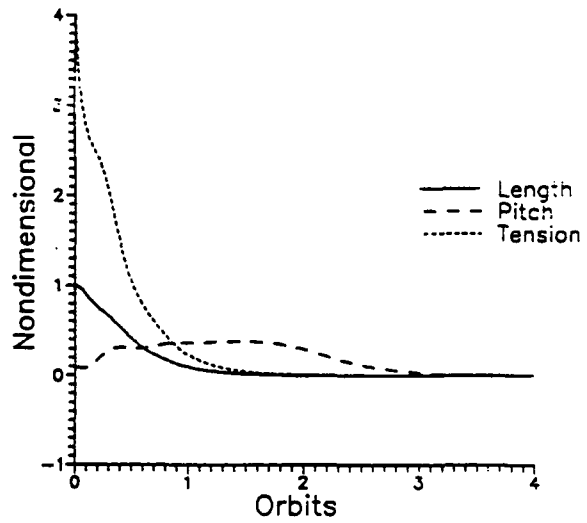


Fig. 7 Desirable Retrieval Using Controller-2 ( $\lambda_r = .001$ ).

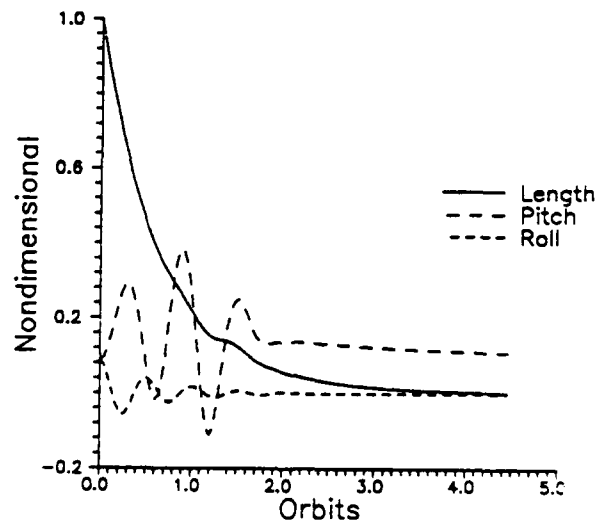


Fig. 8 Retrieval Using the Rate Control Law.

**Preferred Gimbal Angles for  
Single Gimbal Control Moment Gyros**

S. R. Vadali and H-S Oh  
Texas A&M University  
Dept. of Aerospace Engineering  
College Station, Texas

S. R. Walker  
Rockwell Shuttle Operations  
Houston, Texas

*accepted for publication in  
The Journal of Guidance, Control and Dynamics  
American Institute of Aeronautics and Astronautics*

## **PREFERRED GIMBAL ANGLES FOR SINGLE GIMBAL CONTROL MOMENT GYROS**

***S. R. Vadali<sup>1</sup>, H-S. Oh<sup>2</sup>, and S. R. Walker<sup>3</sup>***

***Texas A&M University  
College Station, Texas 77843***

### **ABSTRACT**

This paper deals with torque command generation using Single Gimbal Control Moment Gyros. The angular momentum and torque envelopes are assumed to be known a priori. A method based on back integration of the gyro torque equation from desired final conditions is utilized to determine a family of initial gimbal angles that avoid singularities. Each member of this family is defined as a preferred initial gimbal angle set. The pseudo-inverse steering law is used during the numerical integrations. This procedure is demonstrated by means of numerical examples which include attitude control and momentum management of the space station "Freedom". A feedback control scheme based on "null motion" is also developed to position the gimbals at preferred locations.

1. Assistant Professor of Aerospace Engineering, Member AIAA
2. Graduate Student, Student Member AIAA
3. Currently Engineer, Rockwell Shuttle Operations, Houston, Texas

## INTRODUCTION

Control Moment Gyros (CMGs) are attractive spacecraft attitude control devices. They require no expendable propellant, which is a limited resource and can contaminate the spacecraft environment. Their fixed rotor speeds minimize structural dynamic excitations. They can be used for rapid slewing maneuvers and precision pointing. For low earth orbiting spacecraft, momentum dumping can be easily achieved by gravity gradient torques. From the steering law viewpoint, it is widely accepted that double-gimbal CMGs (DCMGs) are preferable to single-gimbal CMGs (SCMGs). For DCMGs, steering laws proposed by Kennel<sup>1,2</sup> have been well accepted. The SCMGs have the advantages of possessing relative mechanical simplicity and producing amplified torques (for low spacecraft angular velocities) on the spacecraft. However, development of gimbal steering laws for their use is made difficult by the existence of internal singular states. For any system of  $n$  CMGs and any direction in space, there exist  $2^n$  sets of gimbal angles<sup>3</sup> for which no torque can be produced in that direction, and these sets are called internal singularities. External singular states correspond to directional angular momentum saturation. DCMG's have internal singularities also, but they are easier to avoid.

Margulies and Aubrun<sup>3</sup> present a geometric theory of SCMG systems. They characterize the momentum envelope of a cluster of SCMGs and identify the internal singular states. Yoshikawa<sup>4</sup> presents a steering law for a roof-type configuration with four SCMGs. His steering law is based on making all the internal singular states unstable by providing two jumps with hystereses around the singularities. Cornick<sup>5</sup> develops singularity avoidance control laws for the pyramid configuration. His technique is based on the ability to calculate the instantaneous locations of all singularities. Hefner and McKenzie<sup>6</sup> develop a technique for maximizing the minimum torque capability of a cluster of SCMGs in the pyramid configuration. Bauer<sup>7</sup> concludes that it is impossible to avoid some singularities and in general, no global singularity avoidance steering law can exist.

Consequently, there will be instances when torque demand can not be met exactly.

Meffe<sup>8</sup> presents a parametric trade-off study between CMG systems (type and number) for the space station. Specifically, the indicators are reliability, weight, power, volume, maintenance, safety, control law, and life cycle cost. The conclusions are in favor of either the 4/6 or 5/6 SCMG clusters. The numbers 4/6 indicate a total of six CMGs with four being active. The Soviet space station MIR uses the 4/6 SCMG cluster. The DCMG clusters are found superior to SCMG clusters only from power consumption view point. In a recent paper, Blondin, et al.<sup>9</sup> discuss the selection of a prototype DCMG for the space station. One of the reasons behind this choice is that the space station does not have requirements to perform rapid maneuvers.

The requirements for the space station are to control the attitude in the presence of disturbance torques due to environmental effects, motion of sun tracking devices, and shuttle docking. Besides the attitude constraints of Torque Equilibrium Attitude (TEA) reference within 10 degrees of Local Vertical Local Horizontal (LVLH) and rates less than 0.02 deg/sec, the CMG momentum must be restricted<sup>8</sup> to a spherical storage radius (initial phase) of 20,000 ft-lbs-sec. The torque is limited to 400 ft-lbs (spherical). These figures are subject to change. An active momentum management and attitude controller for the space station has been developed by Wie, et al.<sup>10,11</sup>. This scheme seeks TEA and provides periodic-disturbance rejection. The design of the pitch axis controller is decoupled from that of roll-yaw. Periodic-disturbance rejection filters are developed to reject disturbances in the attitude or angular momentum at the orbital rate and multiples of the orbital rate. CMG dynamics and steering laws have not been considered in this work.

In the present paper, we consider the determination of initial gimbal angles for SCMG systems to avoid internal singularities. Throughout the study, four SCMGs in a pyramid configuration shown in Fig. 1 are used. The motivation for this study came from earlier works mentioned above, wherein it has been shown that many singularity avoidance steering laws are

not capable of avoiding singularities consistently even for unidirectional torque demands. We approach the torque generation problem from a more conservative view point. Rather than trying to develop a singularity avoidance law, we present a simple procedure for determining the preferred initial gimbal angles for specific torque and momentum envelopes. In many instances, these can be obtained by performing attitude control simulations without including the CMG dynamics for a variety of initial conditions, parameter variations, etc. The proposed method is based on back integration of the CMG torque equation, typically starting near the saturation envelope (to utilize the entire envelope) and going to the specified initial angular momentum state. The pseudo-inverse steering law is used during the numerical integration. It is shown by means of examples given in the literature that the preferred initial gimbal angles do avoid internal singularities. Finally, the attitude control and momentum management of the Phase-I space station is considered as an additional example. This example clearly shows the advantage of using a preferred set of initial gimbal angles.

An important issue is the reorientation of the gimbals from arbitrary values to a preferred set. A feedback scheme for performing such reorientations while minimizing output torques on the spacecraft is also discussed.

### CMG STEERING

We consider CMG gimbal steering for four SCMG's mounted in the pyramid configuration shown in Fig. 1. It is assumed that the  $x,y,z$  axes (roll, pitch, and yaw, respectively) shown in the figure coincide with the vehicle body axes and the center of the pyramid base is assumed to be located at the center of mass of the vehicle. Only the axial angular momentum of each CMG is included in the mathematical model.

The angular momentum vector  $\mathbf{h}$  and its derivative  $\dot{\mathbf{h}}$  in the body axes can be written as

$$\mathbf{h} = h \begin{Bmatrix} -\text{Cos}\delta\text{Sin}\sigma_1 & -\text{Cos}\sigma_2 + \text{Cos}\delta\text{Sin}\sigma_3 + \text{Cos}\sigma_4 \\ \text{Cos}\sigma_1 - \text{Cos}\delta\text{Sin}\sigma_2 - \text{Cos}\sigma_3 + \text{Cos}\delta\text{Sin}\sigma_4 \\ \text{Sin}\delta\text{Sin}\sigma_1 + \text{Sin}\delta\text{Sin}\sigma_2 + \text{Sin}\delta\text{Sin}\sigma_3 + \text{Sin}\delta\text{Sin}\sigma_4 \end{Bmatrix} \quad (1)$$

and

$$\dot{\mathbf{h}} \triangleq \mathbf{C}\dot{\boldsymbol{\sigma}} = h \begin{bmatrix} -\text{Cos}\delta\text{Cos}\sigma_1 & \text{Sin}\sigma_2 & \text{Cos}\delta\text{Cos}\sigma_3 & -\text{Sin}\sigma_4 \\ -\text{Sin}\sigma_1 & -\text{Cos}\delta\text{Cos}\sigma_2 & \text{Sin}\sigma_3 & \text{Cos}\delta\text{Cos}\sigma_4 \\ \text{Sin}\delta\text{Cos}\sigma_1 & \text{Sin}\delta\text{Cos}\sigma_2 & \text{Sin}\delta\text{Cos}\sigma_3 & \text{Sin}\delta\text{Cos}\sigma_4 \end{bmatrix} \begin{Bmatrix} \dot{\sigma}_1 \\ \dot{\sigma}_2 \\ \dot{\sigma}_3 \\ \dot{\sigma}_4 \end{Bmatrix} \quad (2)$$

where  $h$  is the constant magnitude of the axial angular momentum of each CMG,  $\sigma_i$  are the gimbal angles, and  $\delta$  is the pyramid angle as shown in Fig. 1.

The Euler equations for a system consisting of a spacecraft and a CMG cluster can be written as

$$[\mathbf{I}] \dot{\boldsymbol{\omega}} + \dot{\mathbf{h}} + \boldsymbol{\omega} \times \{[\mathbf{I}] \boldsymbol{\omega} + \mathbf{h}\} = \mathbf{0} \quad (3)$$

where  $[\mathbf{I}]$  is the inertia matrix of the spacecraft,  $\boldsymbol{\omega}$  is the angular velocity vector. We can write Eq. (3) as

$$[\mathbf{I}] \dot{\boldsymbol{\omega}} + \boldsymbol{\omega} \times [\mathbf{I}] \boldsymbol{\omega} = -\dot{\mathbf{h}} - \boldsymbol{\omega} \times \mathbf{h} \triangleq -\mathbf{u} \quad (4)$$

where  $\mathbf{u}$  is the internal torque vector. The CMG steering equation is written, using Eqs. (2) and (4) as

$$\mathbf{C} \dot{\boldsymbol{\sigma}} = \mathbf{T} \quad (5)$$

where

$$\mathbf{T} \triangleq -\boldsymbol{\omega} \times \mathbf{h} + \mathbf{u} \quad (6)$$

The usual procedure for obtaining the gimbal rates from Eq. (6) is to use the Pseudo-inverse of  $\mathbf{C}$ . Thus we have

$$\boldsymbol{\sigma} = \mathbf{C}^T (\mathbf{C} \mathbf{C}^T)^{-1} \mathbf{T} \quad (7)$$

Determinant of the matrix  $\mathbf{C} \mathbf{C}^T$  can be thought of as the average gain of the cluster. It is well known that if Rank  $(\mathbf{C} \mathbf{C}^T)$  is less than three, the pseudo-inverse does not exist. The sets of states at which this happens are called singular states or singularities. Many steering laws have been developed to avoid singular states, yet, none has been proven to do so consistently. A factor common to these schemes is the addition of "null motion" - motion of the gimbals such that no torque is produced on the spacecraft. In many situations, it is difficult to anticipate the approaching singular states fast enough to add sufficient null motion. The scheme proposed by Kurokawa, et al.<sup>12</sup> is based on off-line calculation and table look-up of gimbal angles which globally maximize the gain for a given momentum. This scheme also has not been able to provide singularity-free steering. As mentioned above, our objective is to develop a systematic approach for determining a set of initial gimbal angles that can avoid singular states for a given torque and momentum envelopes. This is discussed in the next section.

## DETERMINATION OF PREFERRED INITIAL GIMBAL ANGLES

Perhaps the most severe demand on the CMGs is a secular torque. ( $\mathbf{T}$  in Eq. (6)). Bauer<sup>7</sup> shows that for the present CMG configuration ( $\delta = 54.74^\circ$ ), with the pseudo-inverse steering law, starting with all the gimbal angles at zero, for a constant positive torque about the x-axis, an internal singularity is encountered at a momentum value of 1.15h. This corresponds to an antiparallel situation, i.e., two of the CMG angular momentum vectors are pointed in opposite directions. The gimbal angles at the singularity are  $\boldsymbol{\sigma} = [-90^\circ, 0^\circ, -90^\circ, 0^\circ]^T$ .

The gimbal rates, without imposed constraints, are large near a singularity. It is noted that for the same torque demand, multiple trajectories can exist from one momentum state to another, in the gimbal angle space. A set of initial gimbal angles that allows smooth gimbal rates throughout, up to saturation is termed "a preferred set". In order to investigate the existence of preferred sets, a backward integration of Eq. (7) was attempted, for specified torque demands.

At saturation along the positive x-axis, all the momentum vectors are maximally projected along the x-axis, i.e.,  $\sigma = [-90^\circ, 180^\circ, 90^\circ, 0^\circ]^T$  and  $h = [h(2\cos\delta + 2), 0, 0]^T = [3.1545 h, 0, 0]^T$ . The saturation gimbal angles for a given direction are unique. Since saturation is an external singularity, we can not start the integration process exactly there. Hence, the gimbal angles were perturbed slightly. For example, we selected the near-saturation angles as  $\sigma = [-89^\circ, 177^\circ, 90^\circ, -1^\circ]^T$ . This choice is arbitrary and forces the selection of one of the many trajectories leading toward the zero momentum state. On back integration of Eq. (7), with a unit torque along the x-axis, the following gimbal angles were obtained near the zero angular momentum state:  $[-59.6^\circ, 60.7^\circ, 118^\circ, -121^\circ]^T$ . The angular momentum vector at this point was  $[.003, -.023, .029]^T$ . It is interesting to note that singularities were not encountered during this process. The nearest gimbal angles for zero angular momentum state are  $\sigma = [-60^\circ, 60^\circ, 120^\circ, -120^\circ]^T$ . These initial gimbal angles provide a local maximum for the CMG gain for zero momentum, which is 1.1854. The gimbal angles and rates with these preferred settings (forward integration with pseudo inverse steering law) are shown in Figs. (2 - 3). Figure 4 shows the CMG gain and it is clear that the gain margin is quite high throughout except near saturation. Moreover, near the x-axis momentum of 1.15, the gain is increasing. It can be verified that a pseudo-inverse steering law with this initial gimbal angle set does indeed avoid all singular states for torques along the x-axis.

Several sets of initial gimbal angles for null momentum were obtained for other desired torques as shown in Table 1. It should be noted that due to symmetry of the configuration, the set  $[-120^\circ, -60^\circ, 60^\circ, 120^\circ]$  is admissible for a torque demand of  $[0 \ 1 \ 0]^T$ .

**TABLE 1. INITIAL GIMBAL ANGLES FOR NULL MOMENTUM**

Torque Demand	Initial Gimbal Angles				
[1 0 0]	[-60°	60°	120°	-120°]	[45° -45° 45° -45°]
[0 1 0]	[-120°	-60°	60°	120°]	[45° -45° 45° -45°]
[0 0 1]	[ 0°	0°	0°	0°]	
[1 1 1]	[ 0°	0°	0°	0°]	[45° -45° 45° -45°]
[4 2 0]	[-60°	60°	120°	-120°]	[45° -45° 45° -45°]
[2 4 0]	[-120°	-60°	60°	120°]	[45° -45° 45° -45°]

Preferred gimbal angles for nonzero momentum states can also be obtained by this procedure. It is also interesting that the set  $[45^0, -45^0, 45^0, -45^0]$  provided singularity-free operation for all the examples in Table 1, except for the uniaxial z-torque example.

Kurokawa, et al.<sup>12</sup> consider the following torque demand:

$$T_x = 0.2 \sin(4\pi t)$$

$$T_y = 0.3$$

$$T_z = 0.0$$

Our simulations were performed with gimbal angles initially set at  $[-120^0, -60^0, 60^0, 120^0]$  as well as  $[45^0, -45^0, 45^0, -45^0]$ . These choices were made because the torque lies in the x-y plane. No internal singular gimbal states were encountered and saturation occurred at about ten seconds.

The next example is similar to that considered by Bedrossian<sup>13</sup>. The required angular momentum distribution is shown in Fig. 5. The momentum envelope can be extended to the saturation limit to obtain initial conditions for back integration. The absolute values of the x- and y-components of the torque are both held constant at 0.707. Gimbal rates with zero initial angles are shown in Fig. 6. It is clear that a singularity is encountered at 1.5 seconds. Figure 7 shows the gimbal rates with the preferred set  $[45^\circ, -45^\circ, 45^\circ, -45^\circ]$ . It is evident that no singularities are encountered. Figure 8 shows the gain along the trajectory and again we see that there is sufficient gain margin and the gain is increasing near the region where a singularity was encountered during the previous simulation (Fig. 6).

### SPACE STATION EXAMPLE

We now consider the attitude control and momentum management of the space station. This study also includes input disturbances which are not used in the control design model. The space station data are given in Table 2. Although the angular momentum storage capability of 20,000 ft-lb-sec dictates the use of 5/6 CMG's, we only use four. The following assumptions are made to obtain linearized equations:

- i) Products of inertia are neglected.
- ii)  $\theta_1$ ,  $\theta_2$  and  $\theta_3$  are small excursions from LVLH: roll, pitch, and yaw respectively.
- iii) The effect of CMG gimbal and rotor transverse inertia are neglected.

The linearized equations are

$$\begin{aligned}
 I_1 \dot{\omega}_1 + n (I_2 - I_3) \omega + 3n^2 (I_2 - I_3) \theta_1 &= -u_1 + w_1 \\
 I_2 \ddot{\theta}_2 + 3n^2 (I_1 - I_3) \theta_2 &= -u_2 + w_2 \\
 I_3 \dot{\omega}_3 - n (I_2 - I_1) \omega_1 &= -u_3 + w_3
 \end{aligned}
 \tag{8}$$

$$\begin{aligned}
 \dot{\theta}_1 - n\theta_3 &= \omega_1 \\
 \dot{\theta}_3 + n\theta_1 &= \omega_3
 \end{aligned}
 \tag{9}$$

$$\begin{aligned}
 \dot{h}_1 - nh_3 &= u_1 \\
 \dot{h}_1 &= u_2 \\
 \dot{h}_3 + nh_1 &= u_3
 \end{aligned}
 \tag{10}$$

where  $I_1$ ,  $I_2$ , and  $I_3$  are moments of inertia,  $\omega$  is the angular velocity vector of the space station,  $n$  is the orbital rate,  $h$  is the CMG angular momentum vector along the body axes of the space station,  $u$  is the torque vector, and  $w$  is the vector of disturbance torques.

$I_1$	5.28E6	slug-ft <sup>2</sup> (roll)
$I_2$	10.80E6	slug-ft <sup>2</sup> (pitch)
$I_3$	58.57E6	slug-ft <sup>2</sup> (yaw)
$n$	.0011	r/sec
$h$	3500	ft-lb-sec

The design disturbance model<sup>10</sup> is

$$\begin{aligned}
 w_1 &= 1 + \text{Sin}(nt) + 0.5 \text{Sin}(2nt) \text{ ft-lb} \\
 w_2 &= 4 + 2 \text{Sin}(nt) + 0.5 \text{Sin}(2nt) \text{ ft-lb} \\
 w_3 &= 1 + \text{Sin}(nt) + 0.5 \text{Sin}(2nt) \text{ ft-lb}
 \end{aligned}
 \tag{11}$$

One filter for each frequency of the model disturbance is used in each channel. The filter equations for pitch attitude disturbance rejection are of the form<sup>10</sup>

$$\begin{aligned}\ddot{\alpha} + n^2 \alpha &= \theta \\ \ddot{\beta} + (2n)^2 \beta &= \theta\end{aligned}\tag{12}$$

Similar filters can be incorporated for momentum management. A more refined disturbance model (AERO1 disturbance)<sup>14</sup> which includes variable aerodynamic drag characteristics is also included. The AERO1 disturbances are shown in Fig. 9. This model includes disturbances at higher frequencies than twice the orbit rate as well as orbit decay. In principle, one can filter out disturbances at three and four times the orbit rate using filters defined above<sup>11</sup>; we have chosen not to do this, as our main aim is to assess CMG steering performance.

The pitch axis controller is designed using LQR techniques<sup>10</sup>. The states are

$$\bar{x} = [\theta_2, \dot{\theta}_2, h_2, \int h_2 dt, \text{ and filter states}]$$

The states for the roll-yaw controller are

$$x = [\theta_1, \omega, h_1, \int h_1 dt, \theta_3, \omega_3, h_3, \int h_3 dt, \text{ and filter states}]$$

The state weighting matrix  $Q$  is selected to be diagonal and each entry is chosen such that  $x_i Q_{ii} x_i = 1$ , where  $x_i$  is the anticipated maximum value of the  $i^{\text{th}}$  state. The control weighting matrix is selected to be the unity matrix. For the purpose of simulation, the initial attitude errors are selected to be  $1^\circ$  about each axis.

As  $h$  and  $u$  are known approximately after the controller design simulation,  $\dot{h}$  can be thought of as a known quantity to determine steering histories for the gimbals. In flight operation, the CMG loop will be driven in parallel with the attitude control loop. In the present context, the two loops have been separated for ease of simulation. This can be justified as the attitude control bandwidth is low, of the order of .01 r/sec. For convenience, Eq. (5) is written as

$$C \dot{\sigma} = T$$

where 
$$T = \begin{Bmatrix} u_1 + nh_3 \\ u_2 \\ u_3 - nh_1 \end{Bmatrix}$$

Starting with initial conditions of  $\sigma = [0, 0, 0, 0]^T$ , simulation of the Pseudo-inverse steering law shows that a singularity is encountered quite early in the first orbit (in about 720 seconds), as shown in Fig. 10.

From initial simulations with out including CMG dynamics, we see that during the initial phases (less than one orbit) the pitch and roll momenta are much higher than the the yaw momentum. Figure 11 shows the gimbal angle histories with the initial gimbal angles selected as  $\sigma = [45^\circ, -45^\circ, 45^\circ, -45^\circ]^T$ . No singular states are encountered and the momentum magnitudes show near periodic variations within limits. A small secular component is noticeable in the pitch aerodynamic torque due to orbit decay. This will lead to saturation of the CMG's if uncompensated for.

### GIMBAL REORIENTATION USING NULL MOTION

CMG momentum vectors can be repositioned at desired orientations by a feedback scheme using null motion. Let  $\sigma_f$  be the desired gimbal angle set and  $\sigma$  the current gimbal angle set. The relative error between the two is  $e = \sigma_f - \sigma$ . We define a candidate Liapunov function

$$V = \frac{1}{2} e^T e$$

The time derivative of V can be written as

$$\dot{V} = e^T \dot{e} = -(\sigma_f - \sigma)^T \sigma \quad (12)$$

If the reorientation process is to be performed without producing torques on the spacecraft, null motion equation for  $\sigma$  must be used. That is, let

$$\dot{\sigma} = [I - C^T (C C^T)^{-1} C] d \quad (13)$$

where  $d$  is any non zero vector and  $I$ , the identity matrix. Equation. (13) can be written as

$$\dot{\sigma} = \tau d \quad (14)$$

where  $\tau = [I - C^T (CC^T)^{-1} C]$ . It is easy to verify that if we premultiply Eq. (13) by  $C$ , the result is  $C \dot{\sigma} = 0$ . It is also important to note that  $\tau^2 = \tau$ , i.e.,  $\tau$  is a projection matrix. From Eqs. (12) and (14), it is clear that  $\dot{V}$  is at least locally negative if

$$d = k (\sigma_f - \sigma) \quad (15)$$

where  $k$  is a scalar and

$$\dot{V} = -k (\sigma_f - \sigma)^T \tau (\sigma_f - \sigma) \quad (16)$$

Even though this scheme seems simple, there exists one drawback. If an internal singularity is encountered during the transit,  $\tau$  becomes undefined. To avoid this problem, near a singularity, the following modification is made by using the so-called singular robustness inverse<sup>13,15</sup>:

$$\dot{\sigma} = [I - C^T (C C^T + \alpha I)^{-1} C] d \quad (17)$$

where  $\alpha$  is a small positive constant of the order of 0.001. It is true that with this modification, it is unavoidable that during the gimbal transit, small torques could act on the spacecraft. Figure 12 shows the gimbal reorientation using the above scheme. The initial gimbal angles are  $\sigma = [0^\circ, 0^\circ, 0^\circ, 0^\circ]^T$  and the final gimbal angles are  $\sigma = [45^\circ, -45^\circ, 45^\circ, -45^\circ]^T$ . The gimbal rates are shown in Fig. 13. It is evident that as the singularity is reached, the gimbal rates approach zero and it becomes necessary to use the correction. Figure 14 shows the gain variation and it is clear that for this example, the output torque on the spacecraft is negligible.

## CONCLUSIONS

A new methodology for determining preferred initial gimbal angle sets for SCMG clusters is presented. It is assumed that torque and angular momentum envelopes are known apriori. These need not be known exactly but in a qualitative sense. The basic element of this procedure is back integration of the CMG torque equation from the final conditions to the initial conditions. The procedure can be applied to any number of CMGs (more than three) in a cluster.

Several examples, including active momentum management and attitude control of the space station are presented. It is shown that singularity avoidance for a variety of problems can be easily achieved by selecting proper initial gimbal angles. Except in one instance, the gimbal angle set  $\sigma = [45^\circ -45^\circ 45^\circ -45^\circ]^T$  has been found to be applicable in all the examples considered. Data regarding the preferred gimbal angle sets for various torque and momentum conditions have to be stored to use this procedure in practice. A feedback scheme for positioning the gimbals is also discussed. If this is done slowly, the disturbance on the spacecraft is negligible, and can be compensated for by a feedback control law. For this reason, the gimbal reorientation control law may have to be active along with the torque producing control law.

It is true that there are many preferred sets for a given problem and one may be better than the others. To determine this, a meaningful performance index such as integral sum squares of the gimbal rates can be utilized and an optimal control problem solved.

### ACKNOWLEDGMENTS

We thank Mr. Eric Ring and Mr. David Geller of NASA Johnson Space Center for many useful discussions. We are grateful for the support of the Texas Advanced Research and Technology Program (Project 4193/1987) and AFOSR (Contract No. F49620-87-C-0078). Critical reviews by the reviewers are appreciated.

### REFERENCES

1. Kennel, H. F., "Steering Law for Parallel Mounted Double-Gimballed Control Moment Gyros" Revision A, NASA TM - 82390.
2. Kennel, H. F., "A Control Law for Double-Gimballed Control Moment Gyros Used For Space Vehicle Attitude Control", NASA TM - 64536, Aug. 7, 1970.

3. Margulies, G. and Aubrun, J. N., "Geometric Theory of Single Gimbal Control Moment Gyro Systems," Journal of Astronautical Sciences, Vol. XXVI, No. 2, Apr. - Jun. 1978, pp. 159-191.
4. Yoshikawa, T., "Steering Law for Roof Type Configuration Control Moment Gyro System," Automatica, Vol. 13, pp. 359-368, 1977.
5. Cornick, D. E., "Singularity Avoidance Control Laws for Single Gimbal Control Moment Gyros," AIAA paper 79-1698, AIAA Guidance and Control Conference, Boulder, Colorado, Aug. 6-8, 1979.
6. Hefner, R. D. and McKenzie, C. H., "A Technique for Maximizing the Torque Capability of Control Moment Gyro Systems," AAS paper 83-387, presented at the AAS Guidance and Control Conference.
7. Bauer, S. R., "Single Gimbal CMG Steering Laws," Charles Stark Draper Laboratory, Inc., Space Guidance and Navigation Memo 10E-87-06, May 1987.
8. Meefe, M., "Control Moment Gyroscope Configurations for the Space Station, AAS 88-040, presented at the 11th AAS Guidance and Control Conference, February 1988, Keystone, Colorado.
9. Blondin, J., et. al., "Design, Fabrication, and Test of a Prototype Double Gimbal Control Moment Gyroscope for the NASA Space Station", AAS 89-006, presented at the 12th annual AAS Guidance and Control Conference, February 1989, Keystone, Colorado.

10. Wie, B., Byun, K., Warren, W. Geller, D., Long, D., Sunkel, J., "A New Momentum Management Controller from the Space Station", AIAA paper 88-4132, presented at the AIAA Guidance and Control Conference, 1988, Minneapolis, Minnesota.
11. Warren, W., Wie, B., and Geller, D., "Periodic-Disturbance Accomodating Control of the Space Station for Asymptotic Momentum Management", AIAA paper 89-3476, Guidance, Navigation, and Control Conference, August 1989, Boston.
12. Kurokawa, H., Yajima, N., and Usui, S., "A New Steering Law of a Single Gimbal CMG System of Pyramid Configuration, "Proceeding of the Xth IFAC Symposium on Automatic Control in Space, Toulouse, France, June 25 - 28, 1985, P. 249.
13. Bedrossian, N. S., "Steering Law Design for Redundant Single Gimbal Control Moment Gyro Systems," M.S. Thesis, Mechanical Engineering, Massachusetts Institute of Technology, Aug. 1987.
14. Geller, D., Private Communication.
15. Nakamura, Y. and Hanafusa, H., "Inverse Kinematic Solutions with Singularity Robustness for Robot Manipulator Control,"Journal of Dynamic Systems, Measurement, and Control, Vol. 108, Sep. 1986, pp.163-171.

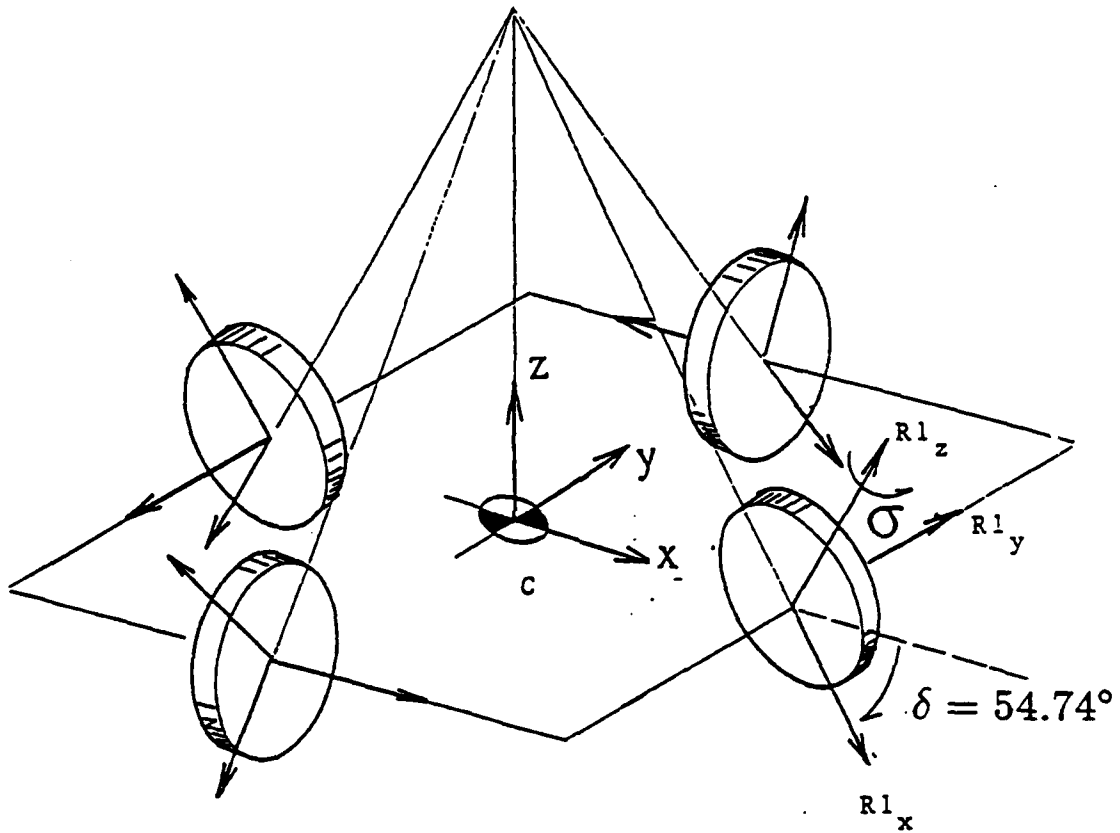


FIG. 1 Pyramid configuration.

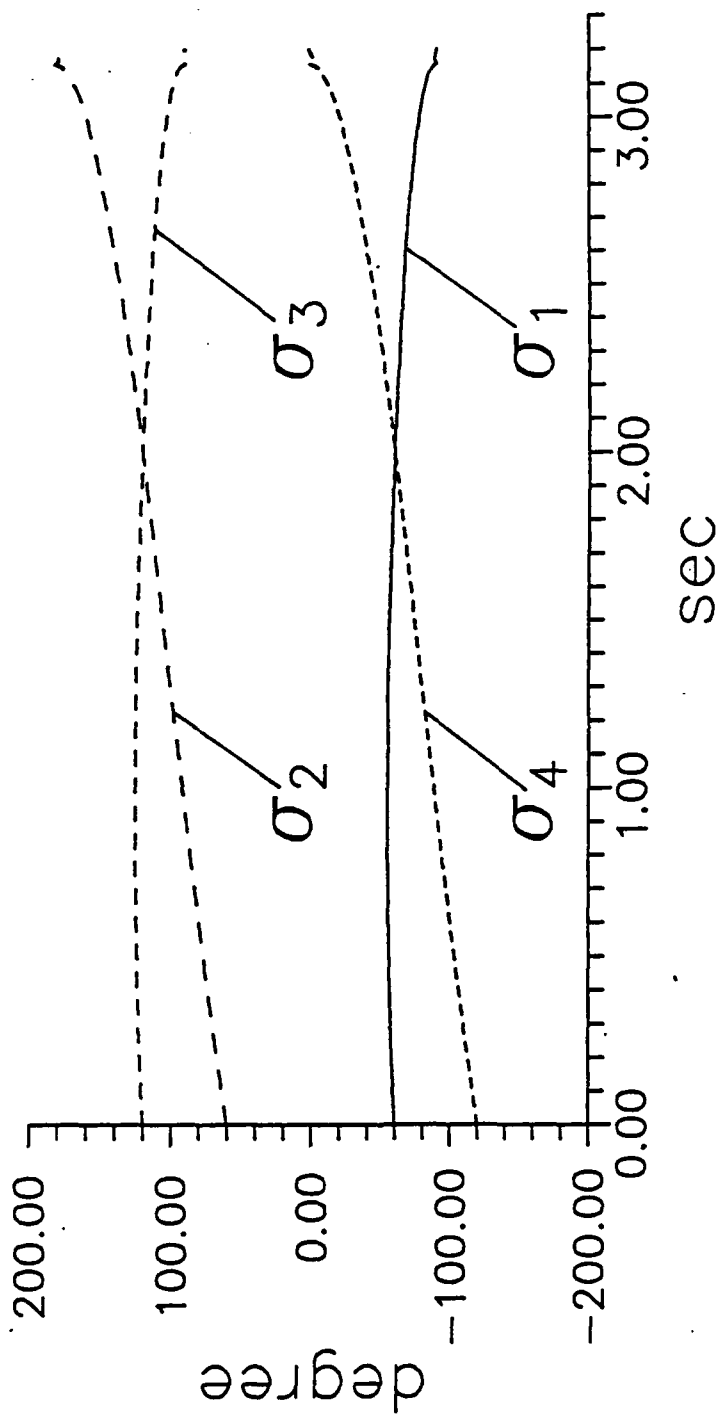


FIG. 2 Gimbal angles for unit x-axis torque  $\sigma(0) = [-60^\circ, 60^\circ, 120^\circ, -120^\circ]^T$ .

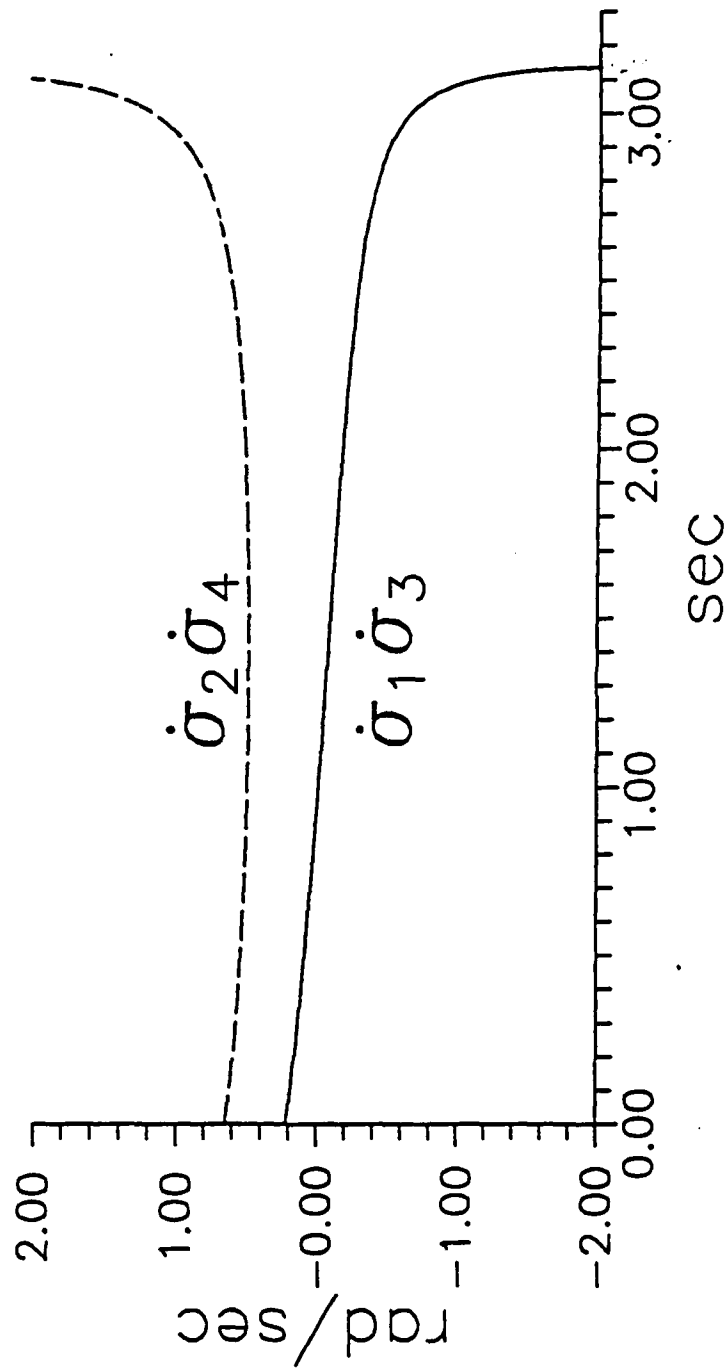


FIG. 3 Gimbal rates for unit x-axis torque  $\sigma(0) = [-60^\circ, 60^\circ, 120^\circ, -120^\circ]^T$ .

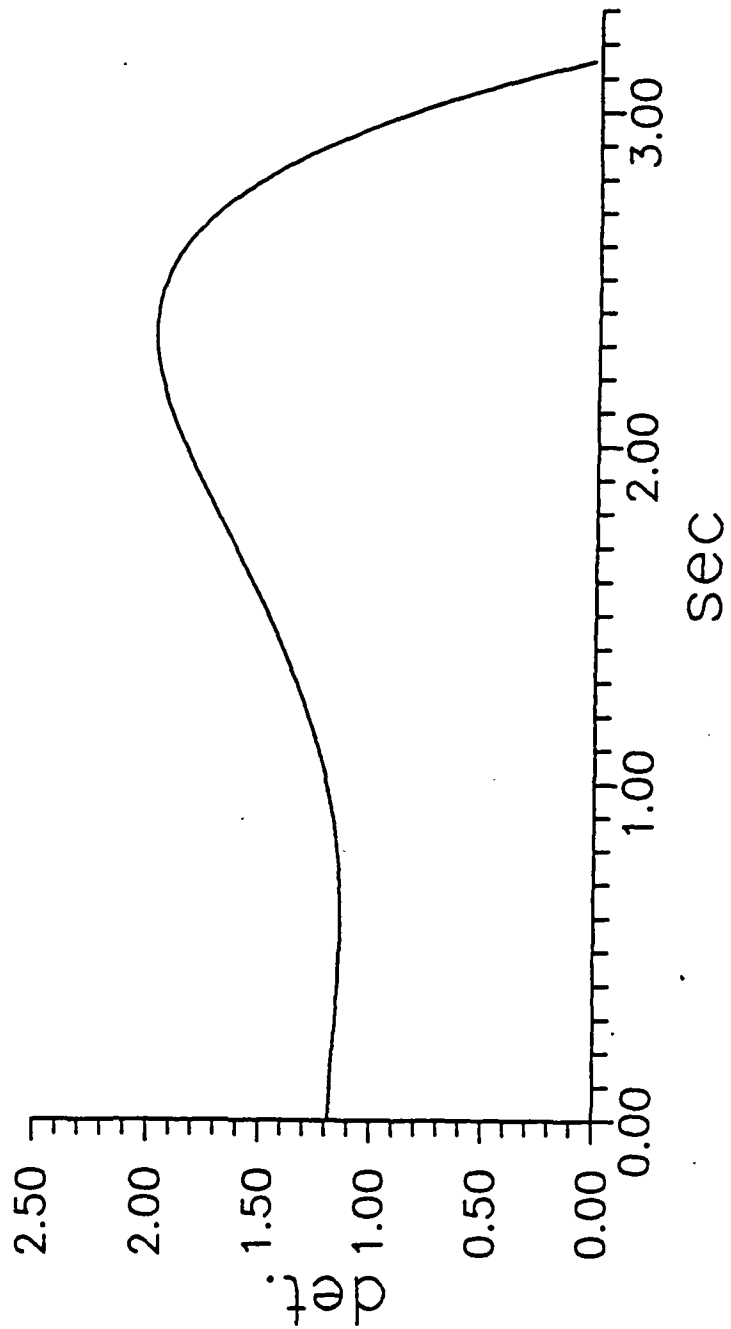


FIG. 4 Gain for unit x-axis torque.

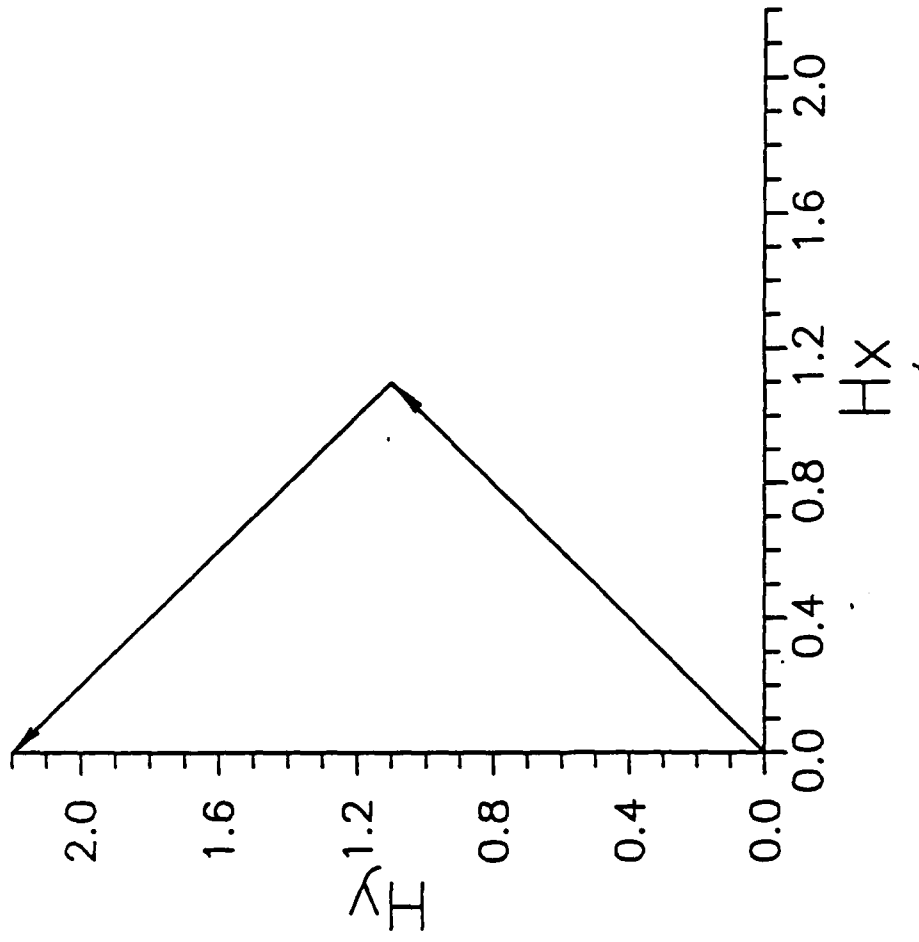


FIG. 5 Angular momentum requirement for Bedrossian example.

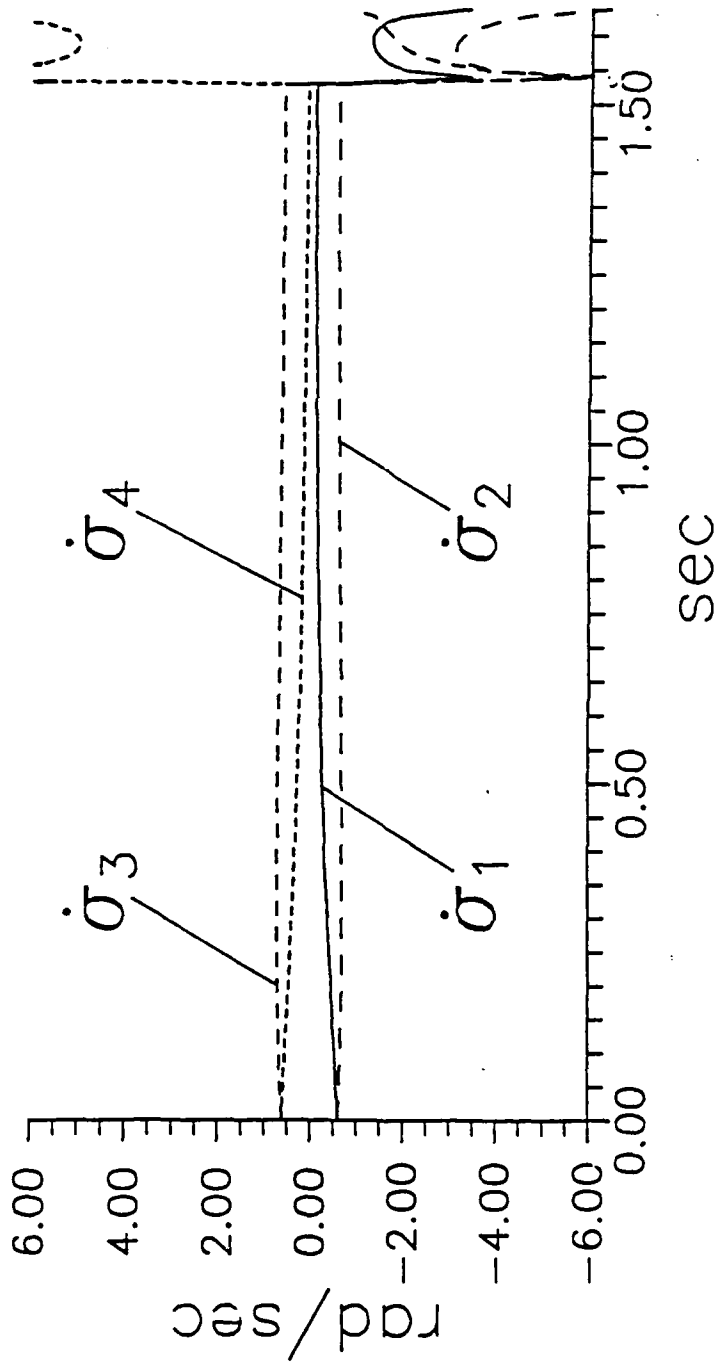


FIG. 6 Gimbal rates with  $\sigma(0) = [0^\circ, 0^\circ, 0^\circ, 0^\circ]^T$ .

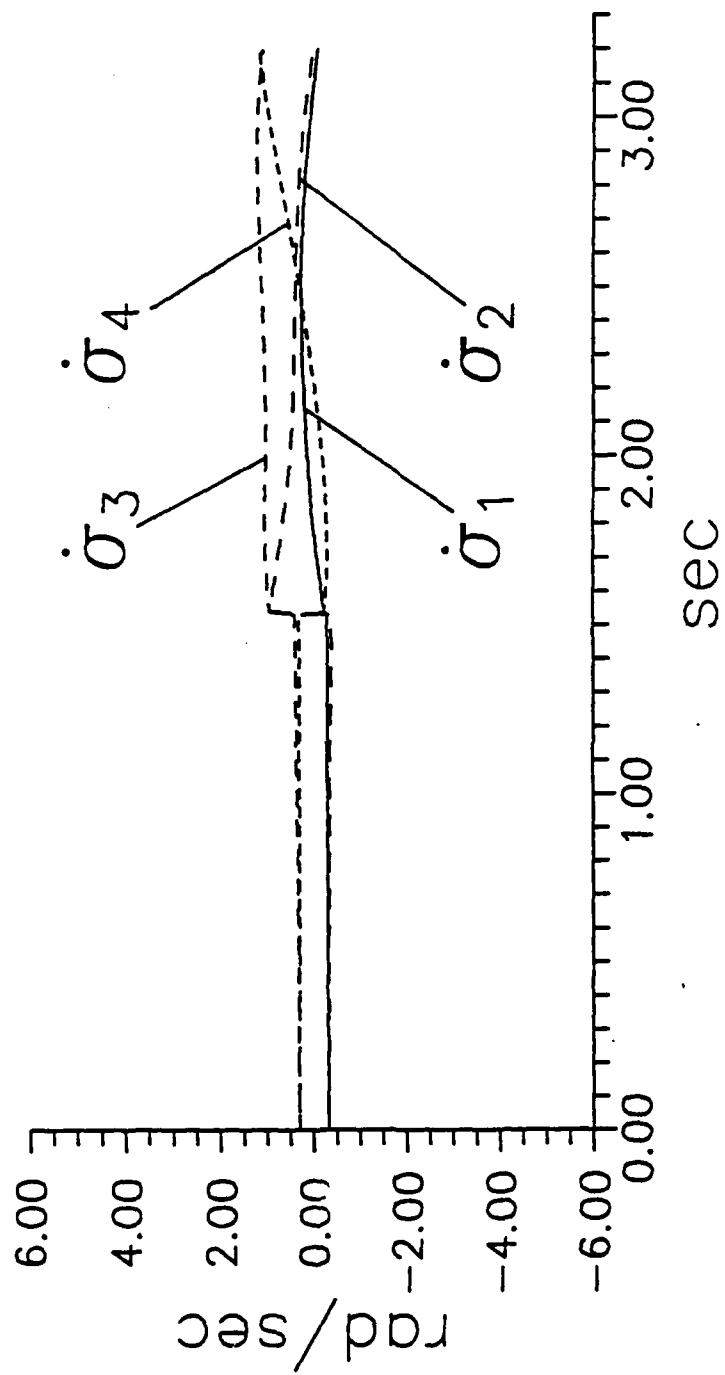


FIG. 7 Gimbal rates with  $\sigma(0) = [45^\circ, -45^\circ, 45^\circ, -45^\circ]^T$ .

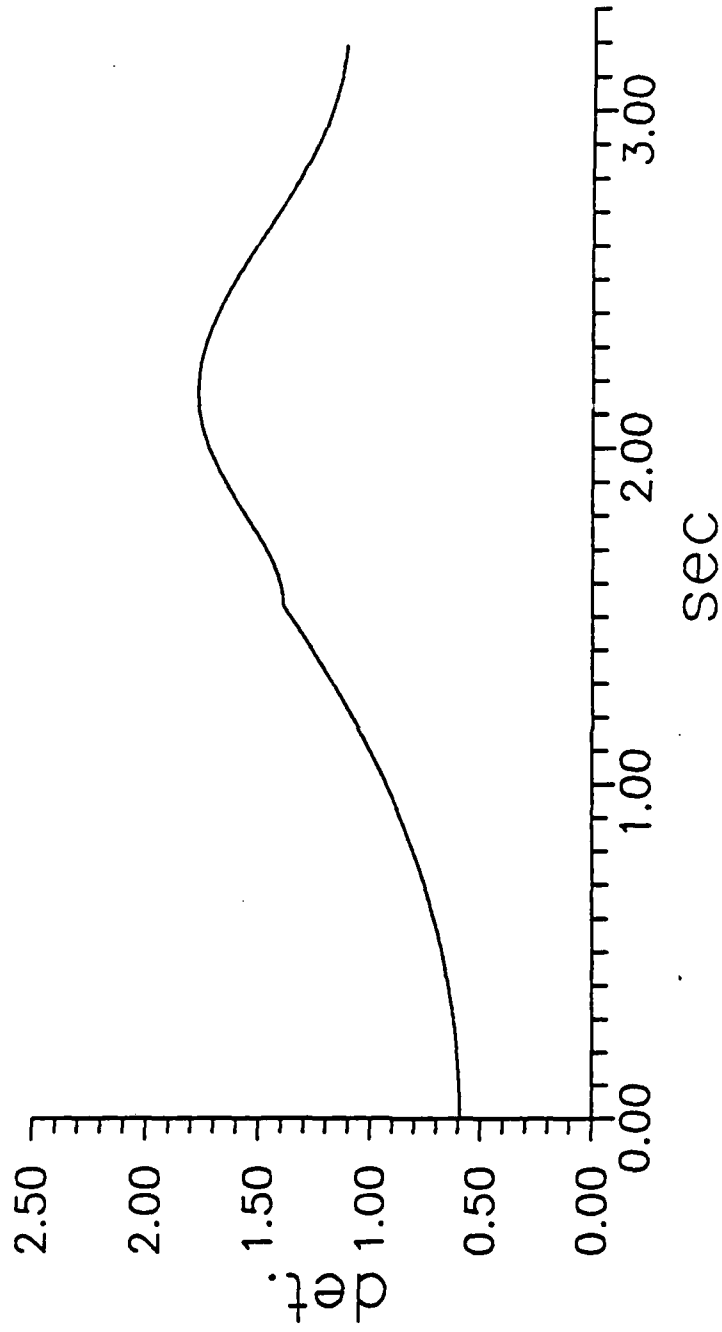


FIG. 8 Gain with  $\sigma(0) = [45^\circ, -45^\circ, 45^\circ, -45^\circ]^T$ .

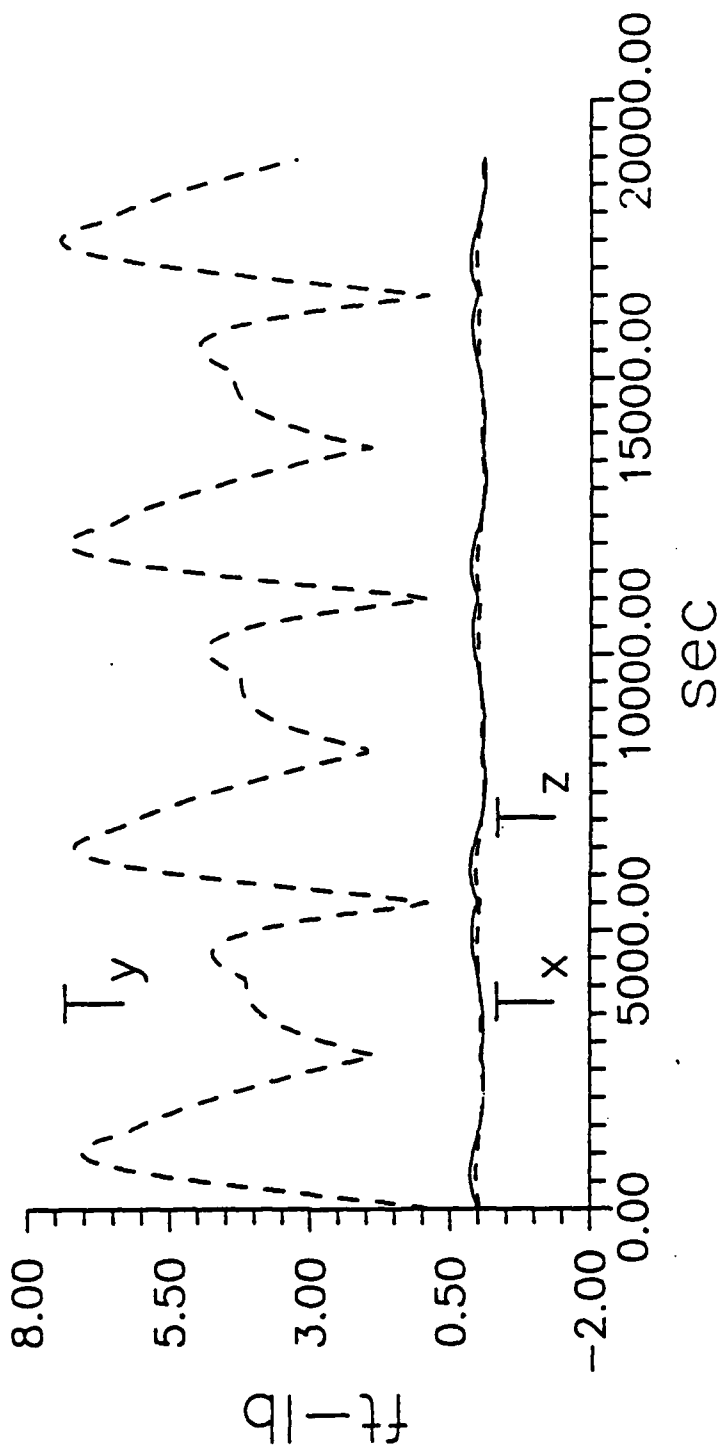


FIG. 9 Aerodynamic torques on the space station.

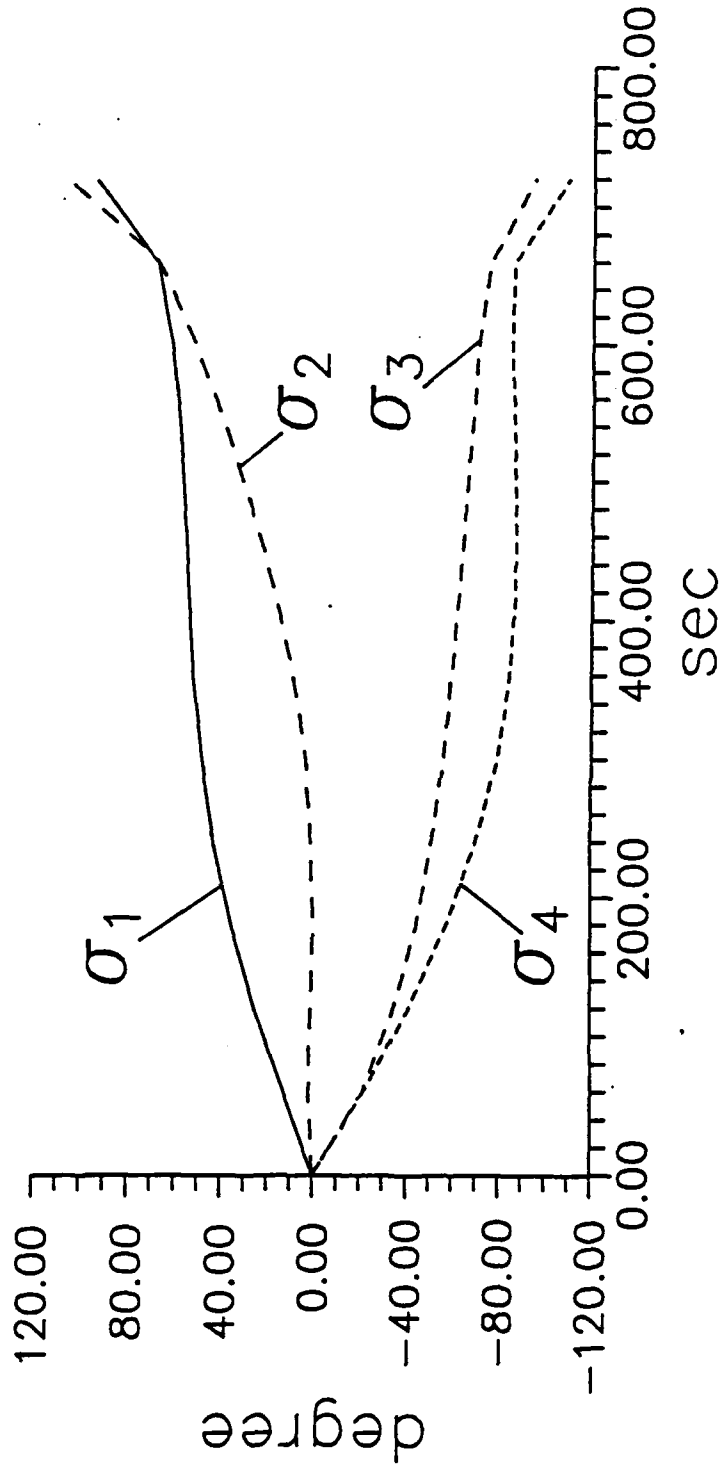


FIG. 10 Gimbal angles with  $\sigma(0) = [0^\circ, 0^\circ, 0^\circ, 0^\circ]^T$ .

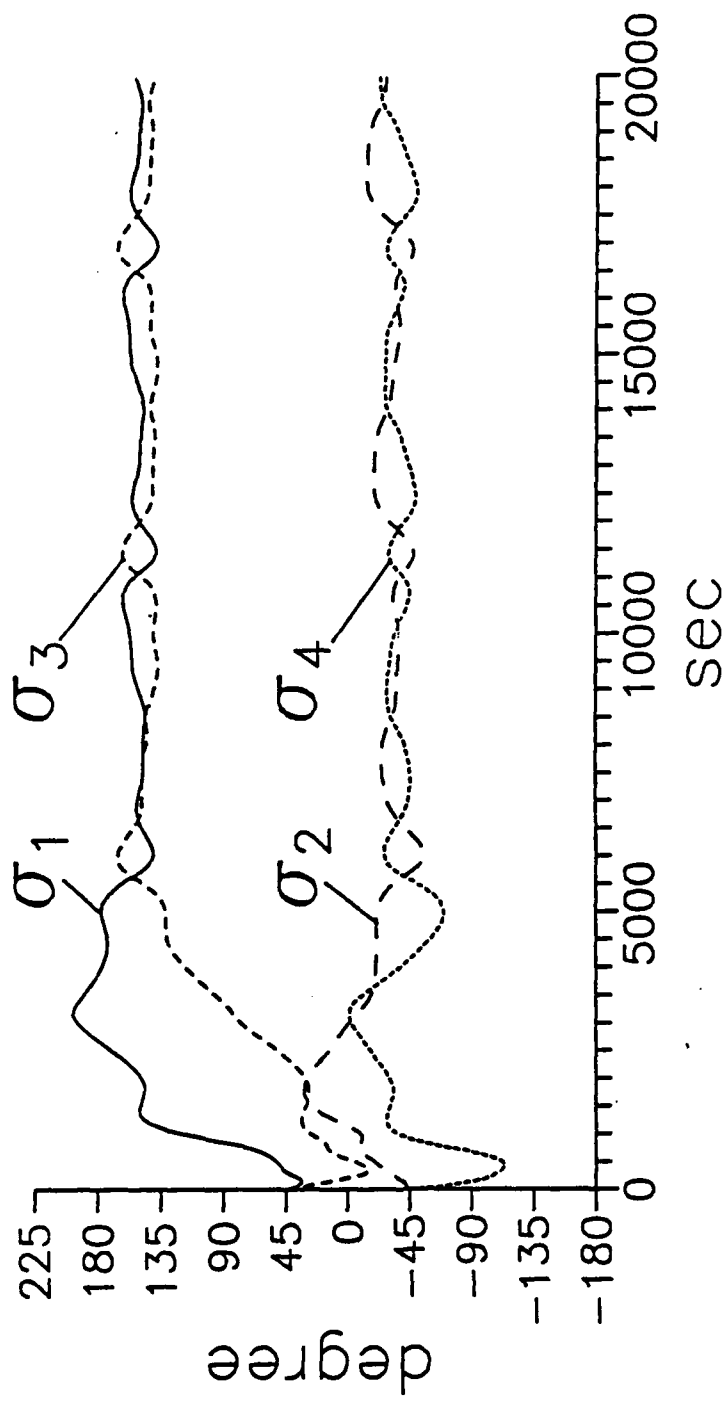


FIG. 11 Gimbal angles with  $\sigma(0) = [45^\circ, -45^\circ, 45^\circ, -45^\circ]^T$ .

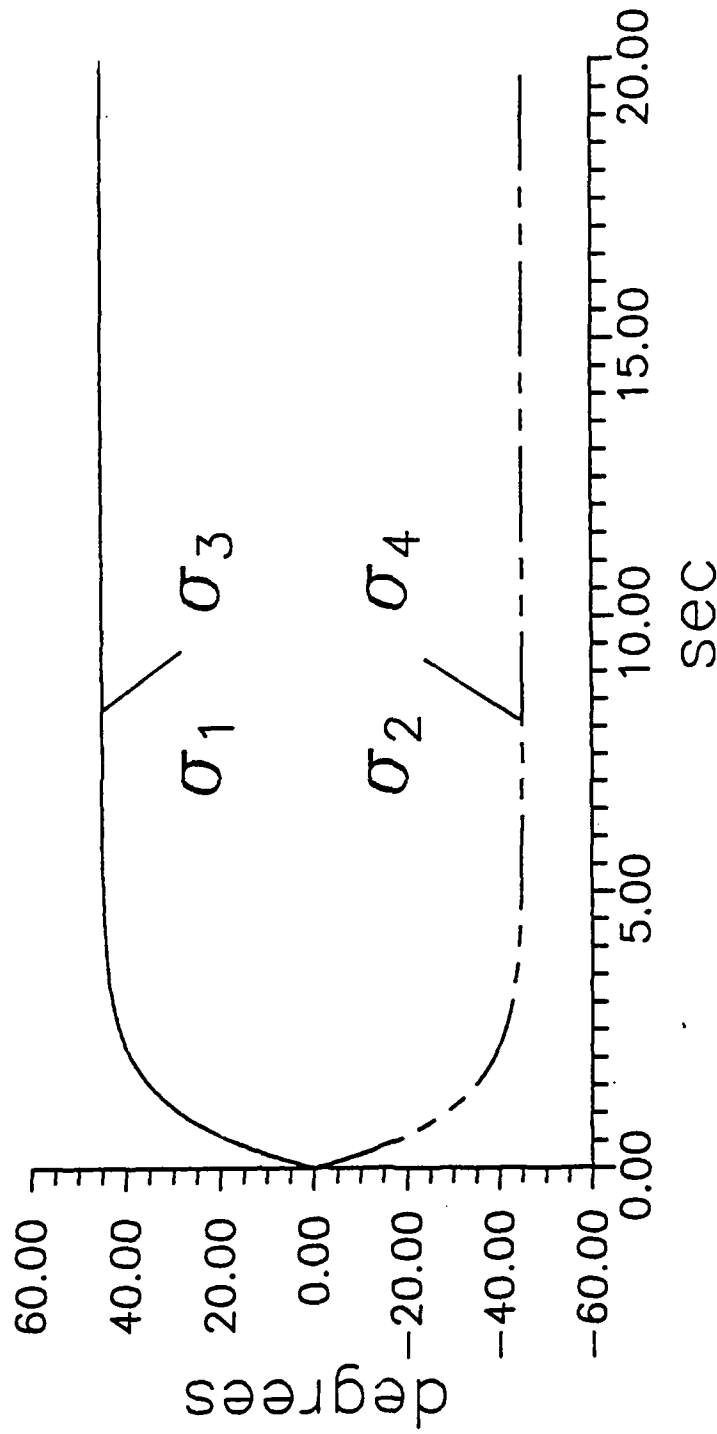


FIG. 12 Gimbal angles during reorientation.

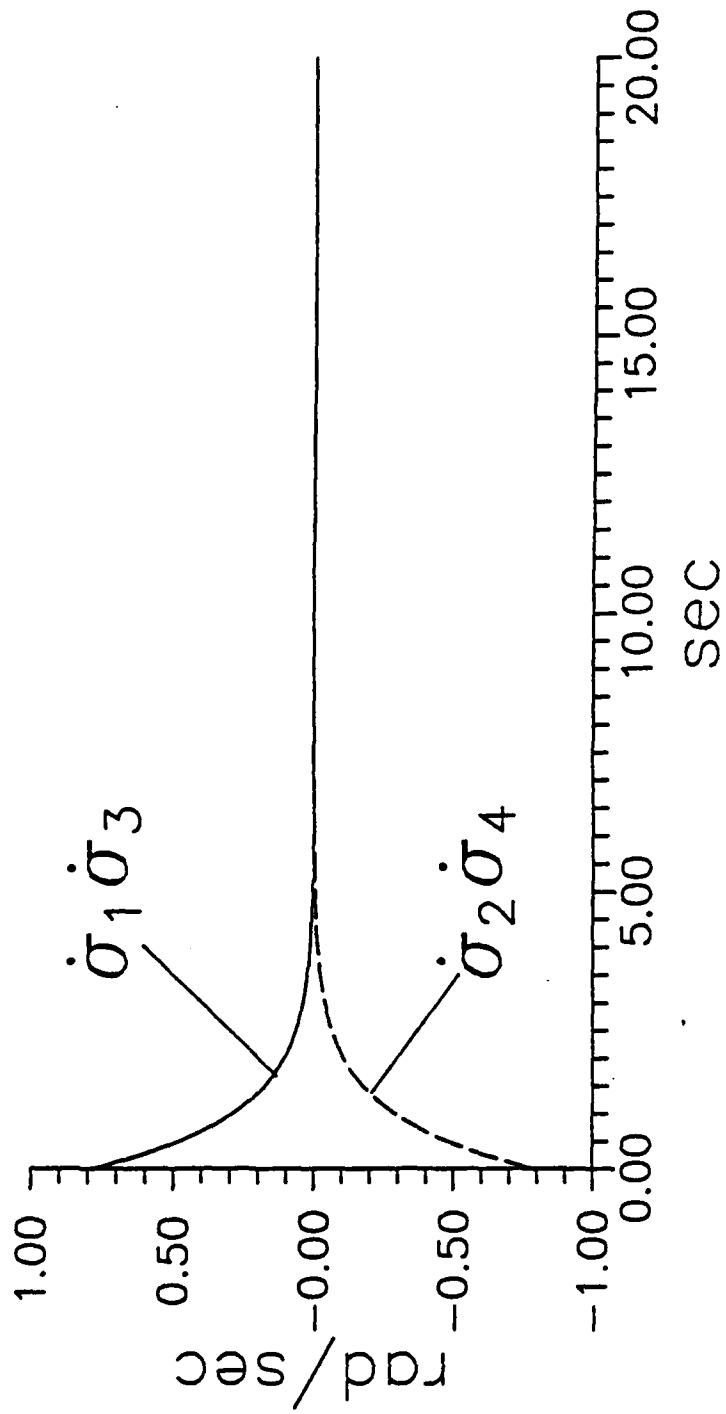


FIG. 13 Gimbal rates during reorientation.

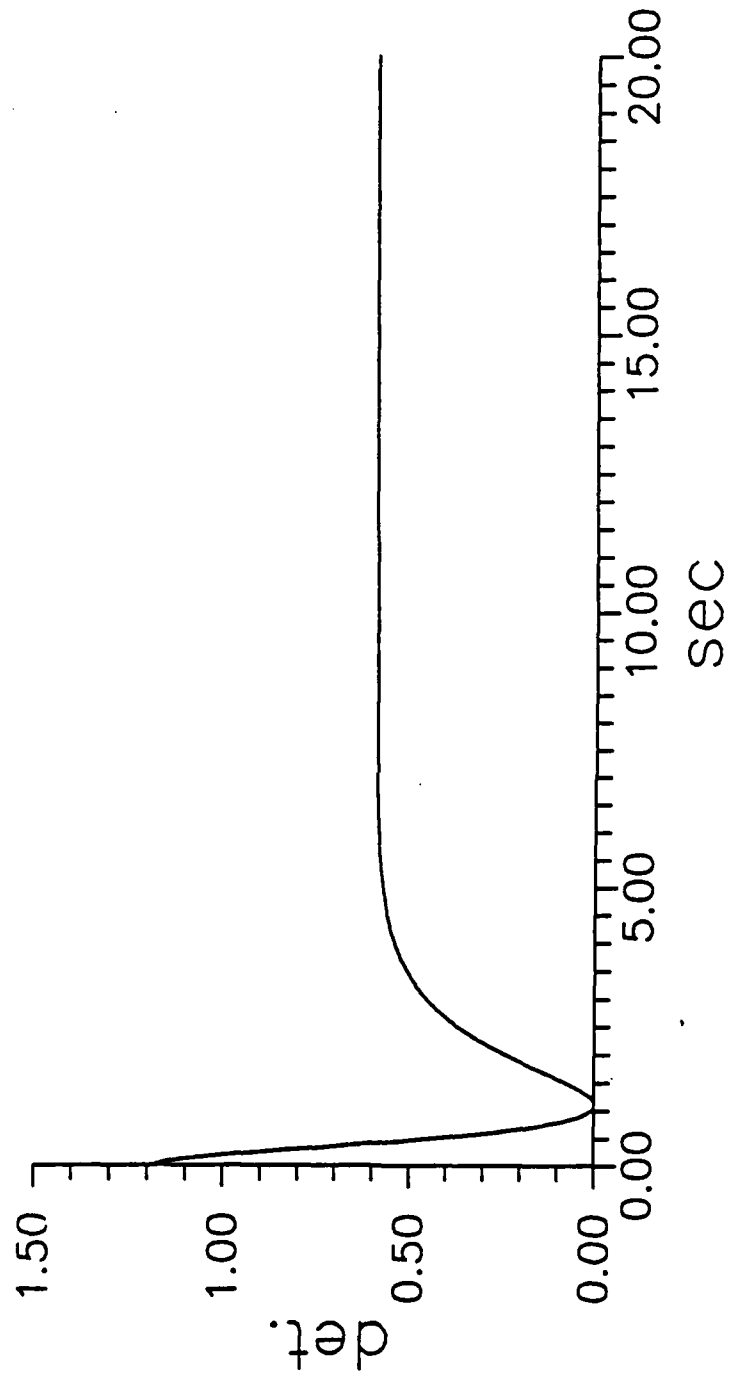


FIG. 14 Determinant ( $CC^T$ ) during reorientation.

**ATTACHMENT 14**

**Dynamics and Controls  
Laboratory Facilities and Equipment**

*T. C. Pollock*

Texas A&M University  
Department of Aerospace Engineering  
College Station, Texas

# Dynamics and Controls Laboratory Facilities and Equipment

Department of Aerospace Engineering  
Texas A&M University

Facilities for experimental studies in control structure interaction (CSI) have been developed during the past four years. Located in the newly completed Engineering Sciences Building are several equipment systems which represent an investment of more than \$1.1M in new equipment over that time span. Presented below is a brief description of each system.

## **The Fine Pointing System**

The central component of the Fine Pointing System is a Contraves Goerz single axis air bearing table capable of pointing an 800 pound experimental apparatus to better than arc second accuracy. This table can be controlled remotely from a computer workstation or directly from an in-line microprocessor. At the present time, the table is partially surrounded by a simulated star field composed of more than one hundred light emitting diodes set into a curved plastic substrate. This configuration is used in the study of spacecraft attitude position sensing by star tracking. Supporting this experiment is a dedicated 80286-based workstation carrying add-in cards which perform frame grabbing and array processing functions. These cards, supplied by Data Translation, Inc., receive pixel information from a high resolution CCD video camera and perform most of the data reduction tasks. The table is also equipped with a second axis capable of supporting small experiments. This device, designed and fabricated in house, can be pointed to an accuracy of 10 arc seconds.

## **The Stereo Triangulation System**

The Stereo Triangulation System consists of four video cameras (two high speed NAC200 and two high resolution (NEC TI23A) linked to two high speed recorders. These recorders can accept data from the cameras at rates up to 200 frames per second. A Motion Analysis (VP110) analog video processor is linked to a Sun workstation to reduce pixel information and perform the triangulation calculations in a user-interactive environment. This system also performs a number of structural identification tasks using data from the stereo camera pair.

## **Single Axis Maneuvering Structure**

A structure consisting of a hub with four flexible appendages has been fabricated for performing large angle maneuvers with active vibration control. This unit rests on a low friction bearing system of our design. The actuator is a reaction wheel powered by a permanent magnet dc motor chosen for very low cogging torque. A variety of sensors are attached to this experiments, which are listed later.

## **Dynamic Testing and Structural Identification**

### **Test Articles and Fixtures**

Several test articles have been fabricated to provide a capability for making precise measurements of dynamic response. Some of the structures investigated to date include simple cantilever beams, a 5' x 5' aluminum grid of monolithic (jointless) construction and aircraft propeller blades.

When the Engineering Science Building was erected, anchor points were placed in the floors of two rooms. Large, steel spaceframes attached to these points support experiments such as the ones mentioned above, and provide fully clamped constraints where desired. The anchor points and support frames were designed to allow quick reconfiguration so that several experiments can proceed in parallel. Test articles as long as 26 feet or as tall as 13 feet can be tested in these laboratories.

### **Actuators**

A variety of actuators are used. Several reaction wheel torquers have been built in our laboratory. These range in size from 2 oz-in to 10 lb-ft, and are currently used on the hub appendage experiment and the monolithic grid experiment. Larger units are currently being designed for implementation on the ASTREX flexible structure at the Air Force Astronautics Laboratory. Power to these actuators is provided by a bank of eight 400 watt linear operational amplifiers. These class A amplifiers (Kepco BOP series) can be controlled from the workstation in either a commanded voltage (wheel speed) mode or a commanded current (torque) mode.

Two shakers are used as linear actuators. These are B&K vibration exciters powered by matching B&K amplifiers. The larger unit provides 380 N rated peak force and 2060 m/sec<sup>2</sup> (210 g) maximum acceleration, and the smaller unit is about one tenth of that size. The primary use for the shakers at the present time is to provide identification excitation.

A Kistler Instruments instrumented hammer is also used as an actuator in certain free response experiments.

### **Sensors**

The stereo triangulation system previously described is one of the sensor systems used for structural identification. In the near future, we expect the fine pointing / star tracker system to be utilized as a sensor for control feedback. There are several other types of sensors in use, as well, which are listed below.

Angular position sensing is accomplished digitally, using Teledyne Gurley optical sensors having a resolution of 36,000 counts per revolution.

Angular rate sensors from Watson Industries are used on the grid experiment, and are being evaluated for other applications.

Linear accelerometers are used on several experiments. In current use are Kistler piezoelectric units, and servoaccelerometers have been ordered in an effort to expand our measurement capability to frequencies below 0.5 Hz.

Force sensors include two linear piezoelectric devices (Kistler) and one torque sensor (Sensor Developments, Inc.)

Conventional strain gages are used on the hub / appendage experiment and the grid experiment.

#### **Data Acquisition and Processing**

Data acquisition boards have been installed in three 80286 - class microcomputers running under MS DOS. The boards are Data Translation 28xx series which may be used in an interactive control mode or a high speed direct memory access (DMA) mode. The fastest of these boards performs 250,000 conversions per second in single channel DMA mode. Two digital oscilloscope cards with FFT capability are also available for general data reduction chores.